Image and Shape Reconstruction Methods in Magnetic Induction and Electrical Impedance Tomography

A thesis submitted to the University of Manchester
for the degree of Doctor of Philosophy in
Faculty of Engineering and Physical Sciences
School of Mathematics

Manuchehr Soleimani

August 22, 2005

Abstract

The main topics of this thesis are forward and inverse problems in electromagnetic imaging. While the main focus is on magnetic induction tomography, other modalities including, electrical resistance tomography, electrical capacitance tomography and magnetostatic permeability tomography are treated. Regularized Gauss-Newton method is used as a nonlinear inverse solver and applied to both simulated and experimental data. Finite element programs using nodal and edge elements have been developed for the forward problems. For the large scale forward problems of resistance tomography we employed algebraic multigrid method to improve the speed of the solution. Sensitivity formulae are derived for all these modalities, where the change in measurement due to small change in material properties can be calculated efficiently. This thesis reports some of the first results of using nonlinear reconstruction for electrical capacitance tomography and magnetic induction tomography for simulated and experimental data. The monotonicity method, a pixel based shape reconstruction method, and the level set method, an interface based shape method, have been implemented for two phase materials. The contribution of this thesis in monotonicity is to apply the method to the electrical resistance tomography with the complete electrode model and apply it to the electrical capacitance tomography with simulated data. In the level set method a narrowband technique is implemented to reconstruct the interfaces between two phases. Reconstruction of two phase materials with experimental electrical resistance and capacitance tomography data in two dimension and simulated data for electrical resistance tomography in three dimension by using the level set method are presented thesis for the first time.

Acknowledgement

I would like to say many thanks to my supervisor Prof. Bill Lionheart. It was an honor and great pleasure to study my PhD with him. He is an amazing applied mathematician and one of the most respected and best member of the inverse problem and EIT communities. Prof. Antony Peyton, it was so interesting to be able to collaborate with him in the area of magnetic induction tomography. Dr Oliver Dorn, he is a fantastic scientist and I was lucky to collaborate with him. I would like to thanks Dr Antonello Tamburrino for his communications and helps. Dr Frank Podd and Dr John Parkinson and Dr Catherine E. Powell thanks for your friendship and helps. I am very pleased that Prof. Simon Arridge accepted to be the external examiner, thanks for that. I gratefully say thanks for the support of the UK Engineering and Physical Sciences Research Council (EPRSC) and Corus RD&T, Teesside Technology Centre.

I would like to say thanks to all my family members especially my father and my mother because of giving me so much freedom and support.

Contents

List of Figures

List of Tables

Chapter 1

INTRODUCTION

Low frequency electromagnetic tomography techniques (less than 20 MHz) are used to non-invasively create cross sectional images of the objects with contrasts in one or more of the passive electromagnetic properties (PEP) including conductivity, permittivity and permeability. Magnetic induction tomography (MIT) [58], [78], [116], [145], [131] is a relatively new member of the electromagnetic imaging family, which works based the eddy current in conductive objects. Image reconstruction of MIT and the three other members of this family, including magnetostatic permeability tomography (MPT) [88], electrical impedance tomography (EIT) [32], [168] and electrical capacitance tomography (ECT) [175] have been studied in this thesis.

EIT is the oldest member and was introduced in a medical context by Barber and Brown [8]. ECT has been used for industrial process tomography applications mainly for materials with low permittivity and negligible conductivity. This thesis will study MIT in conductivity imaging mode and MPT for permeability imaging. EIT considered here works in electrical conductivity mode, so it is referred to as electrical resistance tomography (ERT).

In MIT and MPT a magnetic field from an excitation coil is applied to the object. MIT is based on concept of the eddy current that originates with Michael Faraday's discovery of electromagnetic induction in 1831. In MIT, a time varying magnetic field is induced in the sample material using a magnetic coil with alternating current. This magnetic field causes an eddy current to be generated in conducting materials. These currents, in turn, produce small magnetic fields around the conducting materials. The smaller magnetic fields generally oppose the original field, which changes the transimpedance between excitation and sensing coils. Thus, by measuring the changes in transimpedance between magnetic coils as it traverses the sample, we can identify different characteristics of the sample. In MPT there is no eddy current and changes in magnetostatic fields due to the presence of a permeable object can be detected by sensing coils. The mutual inductances between excitation and sensing coil is the measurement data in MIT. In ERT electrical current is applied to the conductive body via excitation electrodes and resulting electric voltages are measured in peripheral electrodes. In ECT electric potential is applied to the excitation electrodes and capacitances are measured between pairs of electrodes. ERT requires direct contact between the imaging area and the electrodes, but MIT and MPT are fully contactless, and ECT can be used without direct contacts.

All these modalities are inherently complex. They need energization of target region, sensors, electronics, data acquisition and data processing. Induced voltages in MPT and MIT, measured voltages in ERT electrodes and measured capacitances between ECT electrodes are the data for the image reconstruction.

There have been extensive studies of the image reconstruction for EIT including many past PhD theses designated only to the EIT image reconstruction (see for example [17], [121],[160], [20], [101], [178]). Image reconstruction in EIT is more advanced

than for ECT and MIT. For instance, nonlinear image reconstruction methods, including most commonly used regularized Gauss-Newton, are now widely adapted for EIT imaging but not for ECT or MIT. The area of image reconstruction in ECT and MIT is still very underdeveloped. In the past few years many interesting works have been done in the area of sensor design [132], electronic design [162], [78] and basic understanding of the sensitivity maps in MIT [143]. Various types of linear reconstruction methods were used for the image reconstruction of ECT and MIT [176], [79], [11]. In ECT the main focus was to generate images by fast methods, so the computational time and complexity of a nonlinear solver could be a reason why it has not been exploited. Non-phenomenological methods (methods that do not consider and thus are not benefiting from the knowledge of the underlying physics of the measurement system) such as Neural Network and Genetic algorithm were used for ECT and MIT [50], [80], [103]. In phenomenological methods such as regularized Gauss-Newton methods one needs to numerically model the underlying physical problem. Modelling of the electric fields in ECT and ERT involves solving a Laplacian elliptic partial differential equation and scalar fields. The finite element method (FEM) [179] is a powerful tool to solve such a problem. In MIT, further development of the image reconstruction (phenomenological method) requires computation of the general eddy current problem involving vector fields. Some simplified models were used earlier by using scalar fields in MIT [51], which were not accurate to model for higher frequency cases. Edge FEM are developed for the eddy current problem to enhance the computation of vector fields. In the past decade finite element solution of the eddy current problem has been an active area of research [12], [19], [30], [48]. In this thesis we have implemented nodal and edge finite elements for the forward problem in ECT, MPT and MIT.

Recently, shape based reconstruction techniques have become more popular in EIT.

The shape reconstruction method is intended to be applied in situations where approximate values of the parameters inside non-smooth, high-contrast structures are available, but the sizes, shapes, locations and geometry of these structures are unknown. For example, shape reconstruction method has been studied in [76], monotonicity based shape reconstruction in [155], linear sampling methods in [26], and level set method in [31]. Further study of the monotonicity method is considered in this thesis. So far most of these schemes have been applied to simulated data. The linear sampling method was applied to real measurement data in EIT and the results were reported in [61]. In this thesis we have designed a narrowband level set method for the shape reconstruction. The method was applied successfully to experimental data in ECT and ERT. This shape reconstruction algorithm is a nonlinear inversion scheme, which makes use of a numerical shape propagation technique, the so-called level set technique, which originally was developed for the modelling of moving interfaces [112], [113], [140].

1.1 Aims and objectives

The main objective of this thesis is to design suitable algorithms and create corresponding computer programs for image reconstruction of various types of electrical impedance and magnetic induction tomography systems. This thesis mainly concentrates on forward and inverse problems of electromagnetic tomography systems. The forward problem is to simulate the observed measurements given the internal structure (and excitation fields). Image reconstruction here is an inverse problem. Inverse problems are to determine the internal structure of a system using some measurement data from the outside of the object. In this thesis we are interested in reconstruction

of two or three dimensional image of the PEP parameters. The inverse problems are ill-posed, which makes them sensitive to the inevitable measurement noise. Regularization schemes are required to stabilize the ill-posed inverse problem. In general, the inverse problems of PEP are nonlinear as well. Iterative methods are the most commonly used techniques to solve nonlinear inverse problems. In this thesis the forward problems are solved using nodal and edge FEM method for scalar and vector fields. An efficient sensitivity formula has been derived in each case to calculate the sensitivity map as well as the Jacobian matrix. Then the regularized Gauss-Newton method is used to solve the inverse problem. This inverse finite element technique is applied to MIT, MPT, ECT and ERT using simulated and experimental data.

An important part of the study of the inverse problem is the regularization and incorporation of a priori information. For example Tikhonov regularization imposes smooth constraints on the solution. A priori information is different in different applications. In many applications one knows in advance that there is only a two phase material to be reconstructed. The knowledge of the two phase material prepares the ground for some interesting shape reconstruction methods. In this thesis we have studied the monotonicity based method and a level set method for the shape reconstruction problem.

As it can be seen in the course of this thesis, these imaging modalities have many common aspects in the forward problem, sensitivity formula and the inverse problems. So the idea of this thesis can be used to develop reconstruction techniques in a more generic way. However, there are important details and differences in each system that requires special attention.

1.2 Thesis organization

In chapter 2 we briefly overview some mathematical settings required for linear and nonlinear inverse problems. It also includes a brief introduction to the linear solvers arising from the FE discretization.

In chapter 3 we study inverse and forward problems of MIT. The goal is to reconstruct electrical conductivity images based on MIT measurement data and inverse finite element techniques. There are two major application areas we have in mind, medical and industrial applications. In medical applications we are dealing with low contrast conductivity imaging whilst in the industrial application studied in this thesis (molten steel flow visualization in continuous casting) the conductivity contrast is very high. We derive a sensitivity formula with some theoretical study of a simplified coil model for a general eddy current problem. The forward problem was implemented by edge finite elements. The sensitivity maps are studied and a nonlinear inverse solver has been implemented for the conductivity imaging.

Chapter 4 considers an MPT system, and similar to chapter 3 the forward problem has been solved using an edge FEM formulation of magnetic vector potential $\boldsymbol{A}$. The sensitivity formula for magnetic permeability and sensitivity maps have been obtained. The sensitivity map for two opposite coils in MPT is different from the one for MIT for electrical conductivities. A numerical study of the inverse permeability problem with potential applications in detecting reinforced steel bars in concrete has been conducted.

Chapter 5 describes the implementation of an efficient numerical scheme for the large scale forward problem of electrical resistance tomography. In many practical applications, especially in medical ERT, a large scale forward problem occurs. In ERT the

accuracy of the external shape is an important issue for the image reconstruction. For a complicated geometry such as the human brain the number of nodes in the FEM mesh increases substantially. Therefore, the computational time for the forward problem increases. Algebraic multigrid is used as a preconditioner for an iterative solver (Conjugate Gradient (CG)), and the computational time for the forward problem has been reduced substantially.

Chapter 6 deals with numerical modelling of the inverse and forward problems of ECT using some experimental data. The implementation of a suitable forward solver for ECT and validation of the forward problem with experimental data were studied. An efficient formulation for the Jacobian matrix has been derived based on an adjoint field formulation. Linear inverse solvers were used for low contrast permittivity, and nonlinear schemes were used for the high contrast permittivity imaging.

Chapter 7 is dedicated to an extension of a two phase material reconstruction using the monotonicity technique. The technique is a very fast nonlinear method that requires only computation of eigenvalues of small matrices (resistance or capacitance matrix). The technique has potential to be used in real time monitoring of many industrial process tomography applications. Monotonicity method is an interesting pixel based binary reconstruction algorithm for two component mixtures.

Chapter 8 is designated to a narrowband level set method, implemented to reconstruct the interfaces between two conductivity phases. Compared with more traditional pixel based image reconstruction, the level set method can provide more accurate solution for the interfaces. The computational time to solve the inverse problem reduces as one only needs to solve the inverse problem in a narrow band area surrounding the interfaces. In this chapter we show some improvements for real ERT data using the level set scheme and some three dimensional ERT test examples.

Chapter 9 is dedicated to the conclusions and future works. Future works includes some modelling and mathematical studies as well as some simulation work. A selected list of the author's publications is given in appendix A.

Chapter 2

DETERMINISTIC INVERSE PROBLEMS

In this chapter the inverse problem theory necessary for this thesis is reviewed. A more detailed study of general inverse problems can be found in [62], [161]. The background knowledge of low frequency electromagnetic imaging systems and their applications [168], [64], electromagnetic theory, computational electromagnetic [87], [92], [152] FEM modelling [179] and knowledge of edge FEM [19] are assumed. We also assume background in linear algebra [49]. The main bases of the regularization and the inverse problems can be described in terms of statistical methods for such study we refer to [160], [121], [17].

2.1 Forward and inverse problems

The formulation of image reconstruction for one or more internal PEP characteristics from a set of boundary measurements is an example of an inverse boundary value

problem. The definition of the the forward problem [5] is *"Given some boundary conditions on the boundary $\partial\Omega$ of an object $\Omega \subset \mathbb{R}^3$, and a distribution of parameter p within Ω, find the resulting measurement set y on $\partial\Omega$"*.

The solution to the forward problem can be expressed in the form of a general non-linear forward operator $y = F(p)$, where $F : P \to Y$ and $F \in C^{\infty}(P,Y)$, where $p \in P$ and $y \in Y$. Similarly, the inverse problem may be stated as follows *"Given a distribution of PEP characteristics p and a distribution of measurements y on $\partial\Omega$ derive the PEP parameter p within Ω. This can be represented by $y = F^{-1}(p)$."*

If we have an estimated p_0 that is close to ideal solution, then the resulting forward solution $y_0 = F(p_0)$ is close to y. Under suitable conditions one can expand the forward operator in a Taylor series. We now state sufficient conditions for the existence of a Taylor expansion [20]. A general map $F : P \to Y$ between two Banach space is considered. The Fréchet definition of F at a point p in a subset $U \subset P$ is defined as a bounded linear map by $F^{'}$ such that

$$\lim_{h \to 0} \frac{F(p+h) - F(p) - F^{'}(p)}{h} = 0 \tag{2.1}$$

If $F^{'}$ exists F is differentiable at p and if $F^{'}$ is continuous of p, then F is called continuously differentiable ($F \in C^1(P,Y)$). If the second derivative of F, described by $F^{''}_p$, exists we say it is twice differentiable at p, and we say $F \in C^r(P,Y)$ if $F^{(r)}_p$ is continuous. If $F \in C^r(P,Y)$ for all r we say F is smooth or $F \in C^{\infty}(P,Y)$. For $F \in C^r(P,Y)$ Taylor's theorem states [47]

$$F(p+h) = F(p) + F^{'}_p(h) + (\frac{1}{2!})F^{''}_p(h,h) + \ldots (\frac{1}{r!})F^{(r)}_p(h,h,\ldots,h) + o(h^r) \tag{2.2}$$

For $r = 1$ this reduces to (2.1). Here $o(h^r)$ is the Landau symbol stands for any map de-

fined in a neighborhood of the origin of a Banach space P satisfying $\lim_{h\to 0} \frac{o(h^r)}{\| h \|^r} = 0$. If p_0 is an estimate close to the actual solution, the forward map can be extended by the Taylor series

$$y = F(p_0) + F_p^{'}(p_0)(p - p_0) + (p - p_0)^T F_p^{''}(p_0)(p - p_0) + o(\| p - p_0 \|^2) \qquad (2.3)$$

In the discrete case the matrix representation of $F^{'}$ in standard basis is $\boldsymbol{J} \in \mathbb{R}^{m\times n}$ the Jacobian matrix and $F^{''}$ represented by $\boldsymbol{H} \in \mathbb{R}^{m\times n}$, the Hessian (the discrete representation of Hessian is a matrix for a single multivariable function, but for vector value function it is a tensor). Here $\boldsymbol{p} \in \mathbb{R}^n$ and $\boldsymbol{y} \in \mathbb{R}^m$ are finite number of the parameter to be estimated and measurements respectively. Putting $\Delta\boldsymbol{y} = \boldsymbol{y} - \boldsymbol{y}_0$ and $\Delta\boldsymbol{p} = \boldsymbol{p} - \boldsymbol{p}_0$ leads to

$$\Delta\boldsymbol{y} = \boldsymbol{J}\Delta\boldsymbol{p} + \Delta\boldsymbol{p_0}^T \boldsymbol{H}\Delta\boldsymbol{p} + o(\| \boldsymbol{p} - \boldsymbol{p}_0 \|^2) \qquad (2.4)$$

Neglecting terms after the first, linear term constitutes the perturbation approach and the problem reduces to inversion of the matrix representation of $\boldsymbol{J}$ at $\boldsymbol{p}_0$. This is therefore a linear problem which may well be ill-posed, and is amenable to standard matrix inversion methods. Its success is largely dependent on how closely the initial estimate is to the correct solution, and how little effect is played by higher-order terms in equation (2.4). The linear methods require a different experiment that measures $\Delta\boldsymbol{y}$ as the difference between two states. This approach provides a means of imaging which is sensitive to the change in PEP.

2.2 Linear inverse problems

Linear reconstruction relies on the fact that for small changes, the measurement $\Delta \boldsymbol{y}$ can be approximated in a linear fashion with the parameter $\Delta \boldsymbol{p}$, which may be expressed using the Jacobian matrix $\boldsymbol{J}$ as

$$\Delta \boldsymbol{y} = \boldsymbol{J} \Delta \boldsymbol{p} + o(\| \Delta \boldsymbol{p} \|) \tag{2.5}$$

This could be interpreted as seeking either a difference image from the difference between two sets of measurement data, or it could be a step in a non-linear iterative algorithm in which the voltage difference is taken between calculated and measured data. If the number of unknowns is smaller or bigger than the number of the measurements, then the matrix $\boldsymbol{J}$ is not square. In such a case we can use the Moore-Penrose generalized inverse, however we must also consider the stability of the solution. In particular, measurement noise and computational errors that occur during the forward modelling means that the perturbations in object properties that can be reconsted have also to be big enough, in order to create sufficient signal changes above the noise and computation errors. Mathematically this is described as ill-posedness of the inverse problem. This means that the minimization of misfit between data and model is difficult, and that small errors in the measurements or simulations can lead to large errors in the solution. For this reason, some assumptions, which incorporate as much prior information as is practical, are required.

2.2.1 Singular value decomposition

The inverse problems of finding PEP using electromagnetic tomography are ill-posed. Hadmard [60] gives a definition of ill-posed problem saying that the solution does not

exist or is not unique or is not a continuous function of the data. The third condition is one of the biggest problems in electromagnetic tomography. An arbitrary small perturbation of the data can create an arbitrarily large perturbation of the solution. Singular value decomposition (SVD) provides a means to study the ill-posedness of an inverse problem.

In equation (2.5) in our definition of a linear inverse problem. SVD of $\boldsymbol{J}$ is

$$\boldsymbol{J} = \boldsymbol{U}\boldsymbol{\Sigma}\boldsymbol{V}^T = \sum_{i=1}^{n} \boldsymbol{u}_i \sigma_i \boldsymbol{v}_i^T \tag{2.6}$$

here $\boldsymbol{U} = (\boldsymbol{u}_1, \boldsymbol{u}_2, ..., \boldsymbol{u}_n) \in \mathbb{R}^{m\times n}$ and $\boldsymbol{V} = (\boldsymbol{v}_1, \boldsymbol{v}_2, ..., \boldsymbol{v}_n) \in \mathbb{R}^{n\times n}$ are matrices with orthonormal columns called singular vectors, $\boldsymbol{U}^T\boldsymbol{U} = \boldsymbol{V}^T\boldsymbol{V} = \boldsymbol{I}_n$, and the diagonals of $\boldsymbol{\Sigma}$ includes the singular values, which are positive numbers $(\sigma_1, \sigma_2, ...\sigma_n)$ sorted in non-increasing order.

If matrix $\boldsymbol{J}$ is invertible then $\Delta\boldsymbol{p} = \sum_{i=1}^{n} \frac{\boldsymbol{u}_i^T \Delta\boldsymbol{y}}{\sigma_i} \boldsymbol{v}_i$ is the solution to our linear problem.

A plot of singular values will tell us, how ill-posed a particular inverse problem is. In next chapters logarithmic plots of singular values of the Jacobian matrix in our low frequency electromagnetic imaging techniques shows almost a linear decay which means the problem is very ill-posed. If we include dependent measurements, there will be a distinguishable gap between large and small singular values which shows linearly dependent measurements. Figure 2.1.a shows the singular values of 64 measurements of an 8 electrode ECT system (to be discussed later on in this thesis in the next chapters). The plot shows this inverse problem is rank deficient meaning some of those measurements are linearly dependent and can not be used for the inverse solution, this is called effectively rank deficient. Figure 2.1.b shows the same problem with 28 independent measurement. This problem is ill-posed and including some small singular values will produce errors in the reconstructed image.

[a]

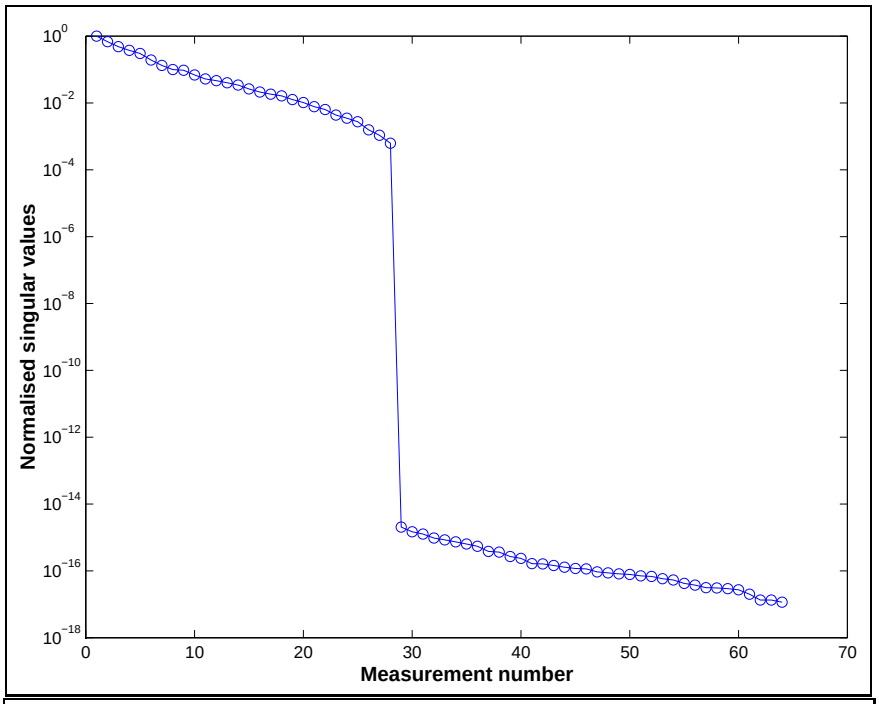

[b]

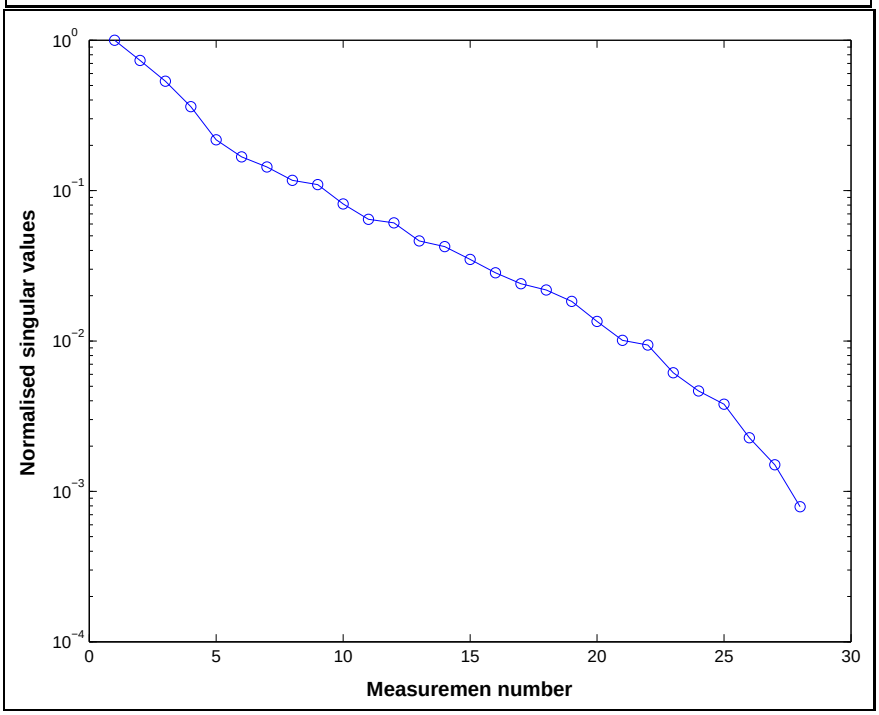

Figure 2.1: (a): Singular values for 64 ECT measurement, shows rank deficiency and (b): Singular values for 28 independent measurement, shows ill-posedness

Truncated SVD (TSVD) can be used to solve an ill-posed problem by ignoring $n-k$ number of small singular values in $\Delta \boldsymbol{p}_{\text{ls}} = \sum_{i=1}^{k} \frac{\boldsymbol{u}_i^T \Delta \boldsymbol{y}}{\sigma_i} \boldsymbol{v}_i$ giving a least square solution $\Delta \boldsymbol{p}_{\text{ls}}$. TVSD was used for the MIT image reconstruction and was reported in [28].

A comparison between the decay of $\|\boldsymbol{u}_i \Delta \boldsymbol{y}\|$ and σ_i's is the basis for the Picard criterion [62]. If the decay of $\|\boldsymbol{u}_i \Delta \boldsymbol{y}\|$ is faster than the decay of σ_i's then $\Delta \boldsymbol{p}_{\text{ls}}$ will be an acceptable solution. For the inverse problem described before, assume that we are very close to the actual solution, the level of the noise in the data is the error level and it is $\Delta \boldsymbol{y}$. Different measurement strategies can be compared based on Picard criteria, given one can estimate the noise level for each measurement strategy and also able to calculate the SVD for that particular measurement strategy. Polydorides et al. [119] investigated optimum number of electrodes and electrode arrangements in EIT based on Picard criteria.

If we can reduce large decay of the singular values, in other words increase the condition number of the system of equations artificially we can have an approximation solution for the problem. By doing that we regularize the ill-posed problem. For example replacing σ_i by $\sigma_i^{\text{new}} = \frac{\sigma_i^2 + \alpha^2}{\sigma_i}$ we have $\boldsymbol{\Delta p}_{\text{ls}} = \sum_{i=1}^{n} \frac{\boldsymbol{u}_i^T \Delta \boldsymbol{y}}{\sigma_i^{\text{new}}} \boldsymbol{v}_i$ that can be solved in a stable manner. Choosing small value of α has small effect on lager singular values, whilst at the same time smaller singular values are contributing in the solution in an stabilized way. Because of the regularization the contribution of the smaller singular values in the solution is not the exact reflection of those singular values of the components in the measurements.

2.2.2 Underdetermined and overdetermined

We are looking to find $\Delta\boldsymbol{p}$ in the interior given a measurement data $\Delta\boldsymbol{y}$ on the boundary. Solving the inverse problem by minimizing

$$\Delta\boldsymbol{p}_{ls} = \text{argmin}\,(\parallel \Delta\boldsymbol{y} - \boldsymbol{J}\Delta\boldsymbol{p} \parallel^2) \tag{2.7}$$

This is the so called *output least squares* approach [82]. If $\boldsymbol{J}$ is a square matrix $\Delta\boldsymbol{p} = \boldsymbol{J}^{-1}\Delta\boldsymbol{y}$. When $\boldsymbol{J}$ is not square we need

$$\Delta\boldsymbol{p} = \boldsymbol{J}^{+}\Delta\boldsymbol{y} \tag{2.8}$$

Where $\boldsymbol{J}^{+} = \boldsymbol{J}^{T}(\boldsymbol{J}\boldsymbol{J}^{T})^{-1}$ in the underdetermined case and $\boldsymbol{J}^{+} = (\boldsymbol{J}^{T}\boldsymbol{J})^{-1}(\boldsymbol{J}^{T})$ for the overdetermined case. In many cases the image reconstruction problem is an underdetermined problem.

2.2.3 Tikhonov regularization

A big change in $\Delta\boldsymbol{p}$ makes a small change on the measurements. This means that the optimization in (2.7) fails to produce a correct result. In order to overcome the ill-posedness we need to regularize, imposing additional information about the solution. A penalty term can be added to the optimization problem

$$\Delta\boldsymbol{p}_{GT} = \text{argmin}\ \parallel \Delta\boldsymbol{y} - \boldsymbol{J}\Delta\boldsymbol{p} \parallel^2 + \alpha^2 \parallel \boldsymbol{R}(\Delta\boldsymbol{p} - \Delta\boldsymbol{p}_{\boldsymbol{0}}) \parallel^2 \tag{2.9}$$

A simple choice for the regularization penalty term is Tikhonov regularization. The aim of this regularization is to dampen the contribution of smaller singular values in solution. The matrix $\boldsymbol{R}$ is a regularization matrix which penalizes extreme changes in

parameter $\boldsymbol{p}$ removing the instability in the reconstruction, at the cost of producing artificially smooth images. TSVD achieves this goal by explicitly removing those smaller singular values. In Tikhonov regularization by adding a penalty term the effect of smaller singular values are dampened in an implicit way. The parameter α controls the trade-off between fitting the data and violating the prior assumption. For Tikhonov regularization we reformulate the optimization problem. The function to be minimized can be expanded as a quadratic form.

$$\begin{aligned} g(\Delta\boldsymbol{p}) = \| \Delta\boldsymbol{y} - \boldsymbol{J}\Delta\boldsymbol{p} \|^2 + \alpha^2 \| \boldsymbol{R}(\Delta\boldsymbol{p} - \Delta\boldsymbol{p}_0 \|^2 = \Delta\boldsymbol{p}^T\boldsymbol{J}^T\boldsymbol{J}\Delta\boldsymbol{p} - 2\Delta\boldsymbol{p}^T\boldsymbol{J}^T\Delta\boldsymbol{y} + \\ \Delta\boldsymbol{y}^T\Delta\boldsymbol{y} + \alpha^2\Delta\boldsymbol{p}^T\boldsymbol{R}^T\boldsymbol{R}\Delta\boldsymbol{p} - 2\alpha^2\Delta\boldsymbol{p}^T\boldsymbol{R}^T\boldsymbol{R}\Delta\boldsymbol{p}_0 + \alpha^2\Delta\boldsymbol{p_0}^T\boldsymbol{R}^T\boldsymbol{R}\Delta\boldsymbol{p_0} \end{aligned} \tag{2.10}$$

The regularization would mean making the resulting linear system better conditioned. But it does not necessarily mean having a solution that is acceptable. An acceptable solution can be achived by considering the realistic situation in the measurement as well as the material side. In the measurement side we would like to include the reality of the electronic noise and any other sources of errors either in the measurement or in the model. In the parameter side, a good initial guess is a good regularization which means $\| \Delta\boldsymbol{p} - \Delta\boldsymbol{p}_0 \|$ is small.

Differentiating $g(\Delta\boldsymbol{p})$ with respect to $\Delta\boldsymbol{p}$ in the $\boldsymbol{z}$ direction we get

$$\boldsymbol{z}^T\nabla g(\Delta\boldsymbol{p}) = 2\boldsymbol{z}^T\boldsymbol{J}^T\boldsymbol{J}\Delta\boldsymbol{p} - 2\boldsymbol{z}^T\boldsymbol{J}^T\Delta\boldsymbol{y} + 2\alpha^2\boldsymbol{z}^T\boldsymbol{R}^T\boldsymbol{R}\Delta\boldsymbol{p} - 2\alpha^2\boldsymbol{z}^T\boldsymbol{R}^T\boldsymbol{R}\Delta\boldsymbol{p}_0 \tag{2.11}$$

If this is zero for all z we have

$$\Delta\boldsymbol{p} = (\boldsymbol{J}^T\boldsymbol{J} + \alpha^2\boldsymbol{R}^T\boldsymbol{R})^{-1}(\boldsymbol{J}^T\Delta\boldsymbol{y} + \alpha^2\boldsymbol{R}^T\boldsymbol{R}\Delta\boldsymbol{p}_0) \tag{2.12}$$

A simple form is the standard Tikhonov where $\boldsymbol{R} = \boldsymbol{I}$ and assuming $\Delta p_0 = 0$

$$\Delta \boldsymbol{p} = (\boldsymbol{J}^T \boldsymbol{J} + \alpha^2 \boldsymbol{I})^{-1} (\boldsymbol{J}^T \Delta \boldsymbol{y}) \tag{2.13}$$

2.2.4 Generalized SVD

Generalized SVD (GSVD) of pair of matrices $\boldsymbol{J} \in \mathbb{R}^{m \times k}$ and $\boldsymbol{R} \in \mathbb{R}^{n \times k}$. As singular values of $\boldsymbol{J}^T \boldsymbol{J}$ and $\boldsymbol{R}^T \boldsymbol{R}$ are square of singular values of $\boldsymbol{J}$ and $\boldsymbol{R}$, GSVD is a good tool to analyze the regularized system. Here $m < k$ and $n = k$, then the pair can be decomposed to $\boldsymbol{U}, \boldsymbol{V}, \boldsymbol{\Theta}, \boldsymbol{C}, \boldsymbol{S} \in \mathbb{R}^{k \times k}$ where $[\boldsymbol{J},\ \boldsymbol{0}] = \boldsymbol{U}\boldsymbol{C}\boldsymbol{\Theta}^{-1}$, $\boldsymbol{R} = \boldsymbol{V}\boldsymbol{S}\boldsymbol{\Theta}^{-1}$, here $\boldsymbol{U}$ and $\boldsymbol{V}$ are orthogonal and $\boldsymbol{\Theta}$ is square and nonsingular and $\boldsymbol{C}$ and $\boldsymbol{S}$ are diagonal matrices of the singular values of $\boldsymbol{J}$ and $\boldsymbol{R}$. Given $\lambda_i = \dfrac{\boldsymbol{C}_{ii}}{\boldsymbol{S}_{ii}}$ for $i = 1, 2 \ldots k$, and $\Delta \boldsymbol{y}^f = [\Delta \boldsymbol{y},\ 0] \in \mathbb{R}^k$ the general Tikhonov solution can be written as $\Delta \boldsymbol{p} = \sum_{i=k-n}^{k} \xi_i \dfrac{\boldsymbol{u}_i^T \Delta \boldsymbol{y}^f}{\lambda_i} \theta_i$, and ξ_i is the filter factor and $\xi_i = \dfrac{\lambda_i^2}{\lambda_i^2 + \alpha^2}$. This factor tend to zero when λ_i is very small compared to α, which means rejecting the effect of smaller singular values in the solution. The filter factor in TSVD is 1 for selected singular values and zero for the rejected ones. And for standard Tikhonov the filter factor is $\xi_i = \dfrac{\sigma_i}{\sigma_i^2 + \alpha^2}$ where σ_i is *i-th* singular value of matrix $\boldsymbol{J}$. The Picard criteria from GSVD information is also useful for analyzing the regularized system with the expected noise level in measurement data [119], [62].

2.2.5 Other methods

In Newton one step reconstruction (NOSER) [33] the regularization matrix is $\boldsymbol{R}^T \boldsymbol{R} = \text{diag}(\boldsymbol{J}^T \boldsymbol{J})$. Replacing σ_i to $\sigma_i^{\text{new}} = \dfrac{\sigma_i^2 + \alpha^2 l_i}{\sigma_i}$, and l_i is diagonal elements of $\boldsymbol{J}$. We have $\Delta \boldsymbol{p}_{ls} = \sum_{i=1}^{n} \dfrac{\boldsymbol{u}_i^T \Delta \boldsymbol{y}}{\sigma_i^{\text{new}}} v_i$ that can be solved in a stable manner.

Krylov subspace methods such as preconditioned conjugate gradient (PCG) [122] also act as an implicit regularization for the ill-posed inverse problem and can be efficient when used for the large scale problems.

A simpler iterative algorithm is the Landweber iteration scheme used in ECT image reconstruction [176]. Let us consider Landweber's iterations as give by the formulation

$$\Delta \boldsymbol{p}_{i+1} = \Delta \boldsymbol{p}_i + \lambda \boldsymbol{J}^T (\Delta \boldsymbol{y} - \boldsymbol{J} \Delta \boldsymbol{p_i}) \tag{2.14}$$

where the fixed parameter λ is a relaxation parameter. If $\| \boldsymbol{I} - \lambda \boldsymbol{J}^T \boldsymbol{J} \|_2^2 < 1$ or $0 << 2\|\boldsymbol{J}^T \boldsymbol{J}\|_2^2$ the method will converge. The method can be expressed as an SVD filter with the filter factor for iteration i is $\xi_i = \dfrac{(1-(1-\lambda\sigma_i^2))^i}{\sigma_i}$.

In [93] a hybrid method is used for ECT image reconstruction. Hybrid method is

$$\Delta \boldsymbol{p}_{i+1} = \Delta \boldsymbol{p}_i + \lambda (\boldsymbol{J}^T \boldsymbol{J} + \alpha^2 \boldsymbol{R}^T \boldsymbol{R})^{-1} (\boldsymbol{J}^T)(\Delta \boldsymbol{y} - \boldsymbol{J} \Delta \boldsymbol{p}_i) \tag{2.15}$$

An algorithm for finding the nearest local minimum of a function which presupposes that the gradient of the function can be computed. The method of steepest descent [98], also called the gradient descent method. Steepest descent method is given by iteration $\Delta \boldsymbol{p}_{i+1} = \Delta \boldsymbol{p}_i + \lambda_i \boldsymbol{J}^T (\Delta \boldsymbol{y} - \boldsymbol{J} \Delta \boldsymbol{p_i})$ and in iteration i we calculate $\lambda_i = \dfrac{\| \boldsymbol{J}^T (\Delta \boldsymbol{y} - \boldsymbol{J} \Delta \boldsymbol{p_i}) \|}{\| \boldsymbol{J}\boldsymbol{J}^T (\Delta \boldsymbol{y} - \boldsymbol{J} \Delta \boldsymbol{p_i}) \|}$.

2.3 Nonlinear inverse problems

Nonlinear methods are suitable to reconstruct the absolute values where as linear methods are useful for difference imaging. First we begin from minimization of the

residual error

$$g(p) = \frac{1}{2} \| y - F(p) \|^2 \tag{2.16}$$

Consider $D(p) = y - F(p)$. Here gradient of g is $\nabla g(p) = F^{'}(p)(y - F(p))$.

$$D(p+h) = D(p) + D'(p)h + \left(\frac{1}{2}\right) F^{''}(p)h^2 + o(\| h^2 \|) \tag{2.17}$$

Newton's method began as a method to approximate roots of functions, equivalently, here solutions to equation $g(p) = 0$. A Newton-Raphson iteration is $p_{i+1} = p_i + \nabla g(p_i)$, gradient of g can be used to optimize $g(p)$ by $D(p+h) \approx 0$. By ignoring second order term we have $D(p+h) = D(p) + D^{'}(p)h$ so $D^{'}(p)h = D(p+h) - D(p)$. The iterations are in a way that $D(p+h) \to 0$, which means $h = D^{'}(p)^{-1}D(p)$. Therefore Newton-Raphson iterations can be written $p_{i+1} = p_i + F'(p_i)^{-1}(y - F(p_i))$.

Hessian for the function g can be calculated

$$H(p) = D^{'}(p)^T D^{'}(p) + D^{''}(p)D(p) = F^{'}(p)^T F^{'}(p) + \sum_{j=1}^{k} F_j^{''}(p)(F_j(p) - y_j) \tag{2.18}$$

By ignoring second derivative term in Hessian the Gauss-Newton iteration can be written $p_{i+1} = p_i - H(p_i)^{-1}\nabla g(p_i)$. Gauss-Newton method is a standard optimization technique for well-posed problems.

By replacing Hessian with identity, we can build nonlinear conjugate gradient (NLCG) algorithm with regularization [4]

Data: Measurement data

Result: Solution of the nonlinear inverse problem

initialization;

for *i=1,2,...* **do**

  if $\| \nabla g(p_i) \|^2 < tol$ **then**
    break ;

  else

$$\beta_i = \frac{\| \nabla g(p_i) \|^2}{\| \nabla g(p_{i-1}) \|^2} ;$$

$$\Lambda_i = -(W \nabla g(p_i) + \alpha^2 I) + \beta_i \Lambda_{i-1} ;$$

  end

  line search for λ_i ;

  $p_{i+1} = p_i + \lambda_i \Lambda_i$;

end

Algorithm 1: Nonlinear CG algorithm

here tol is the tolerance and α is the regularization parameter.

A weighting function W was proposed by [121], to improve the efficiency of NLCG and was applied to the EIT problem. NLCG does not require calculation of the Hessian and using adjoint formulation one can calculate the g efficiently [121].

A nonlinear Landweber can be described by iteration $p_{i+1} = p_i + \lambda F'(p_i)(y - F(p_i))$ [176].

In the regularized Gauss-Newton method the second order term in the Hessian is approximated. The regularized optimization is to find p, given p_0 as the initial guess, $R(p)$ is the regularization function, we also include regularization parameter α here

$$g(p) = \frac{1}{2} \| y - F(p) \|^2 + \alpha^2 R(p) \tag{2.19}$$

For regularized Gauss-Newton the iteration steps are $p_{i+1} = p_i - H(p_i)^{-1}\nabla g(p_i)$, where $H(p_i) = F'(p_i)^T F'(p_i) + \alpha^2 R''(p_i)$, where H is the modified Hessian here and $R(p)$ is regularization function and $\nabla g(p_i) = F'(p_i)(F(p_i) - y) + \alpha^2 R'(p_i)$. Here $R'(p_i)$ and $R''(p_i)$ are the first and second derivatives of $R(p)$ with respect to p_i. The regularized Gauss-Newton (GN) algorithm is as follows

Data: Measurement data

Result: Solution of the nonlinear inverse problem

Initialization ;

for *i=1,2,...* **do**

  if *Stopping criteria is satisfied* **then**

    break;

  else

    Material distribution $\boldsymbol{p}_i$ *in step i* ;

    Calculate the forward model $\boldsymbol{F}(\boldsymbol{p}_i)$;

    Calculate the sensitivity term $\boldsymbol{F}'(\boldsymbol{p}_i)$;

    Choose regularization parameter α ;

    Compute gradient by $\nabla g(\boldsymbol{p}_i) = \boldsymbol{F}'(\boldsymbol{p}_i)(\boldsymbol{F}(\boldsymbol{p}_i) - \boldsymbol{y}) + \alpha^2 R'(\boldsymbol{p}_i)$;

    Compute G-N approximation of $\boldsymbol{H}$ by

    $\boldsymbol{H}(\boldsymbol{p}_i) = \boldsymbol{F}(\boldsymbol{p}_i)'\boldsymbol{F}(\boldsymbol{p}_i) + \alpha^2 R''(\boldsymbol{p}_i)$;

    Calculate $\delta\boldsymbol{p}_i = -\boldsymbol{H}(\boldsymbol{p}_i)^{-1}\nabla g(\boldsymbol{p}_i)$;

    Update the material distribution $\boldsymbol{p}_{i+1} = \boldsymbol{p}_i + \lambda_i \delta\boldsymbol{p}_i$, here λ_i is the

    step size ;

  end

end

Algorithm 2: G-N algorithm

2.3.1 Linearized Tikhonov steps

Let's consider generalized Tikhonov regularization

$$p = \text{argmin}(\|\boldsymbol{F}(\boldsymbol{p}) - \boldsymbol{Y_m}\|^2 + \alpha^2\|\boldsymbol{R}(\boldsymbol{p} - \boldsymbol{p}_0)\|^2) \tag{2.20}$$

Using iterative method to solve (2.20), $\Delta\boldsymbol{p}_i = \boldsymbol{p}_{i+1} - \boldsymbol{p}_i$, by linear approximation around $\boldsymbol{p}_i$ (the solution of step i) we have

$$\boldsymbol{p}_{i+1} = \text{argmin}(\|\boldsymbol{F}(\boldsymbol{p}_{i+1}) - \boldsymbol{Y}_m\|^2 + \alpha^2\|\boldsymbol{R}(\boldsymbol{p}_{i+1} - \boldsymbol{p}_0)\|^2) \tag{2.21}$$

by linearization around $\boldsymbol{p}_i$ we can reformulate the problem to

$$\Delta\boldsymbol{p}_i = \text{argmin}(\|\boldsymbol{F}(\boldsymbol{p}_i) + \boldsymbol{F}'(\boldsymbol{p}_i)\Delta\boldsymbol{p}_i - \boldsymbol{Y}_m\|^2 + \alpha^2\|\boldsymbol{R}(\Delta\boldsymbol{p}_i + \boldsymbol{p}_i - \boldsymbol{p}_0)\|^2) \tag{2.22}$$

Replacing $\Delta\boldsymbol{p}_0 = \boldsymbol{p}_i - \boldsymbol{p}_0$ and $\Delta\boldsymbol{Y}_m = \boldsymbol{F}(\boldsymbol{p}_i) - \boldsymbol{Y}_m$, this is similar to equation (2.10), so we have

$$\Delta\boldsymbol{p}_i = (\boldsymbol{F}'(\boldsymbol{p}_i)^T\boldsymbol{F}'(\boldsymbol{p}_i) + \alpha^2\boldsymbol{R}^T\boldsymbol{R})^{-1}(\boldsymbol{F}'^T(\boldsymbol{p}_i)(\boldsymbol{F}(\boldsymbol{p}_i) - \boldsymbol{Y}_m) + \alpha^2\Delta\boldsymbol{p}_0) \tag{2.23}$$

In discrete form we have iteration steps such that

$$\Delta\boldsymbol{p}_i = \left(\boldsymbol{J_i}^T\boldsymbol{J_i} + \alpha^2\boldsymbol{L}^T\boldsymbol{L}\right)^{-1}\boldsymbol{J_i}^T\left((\boldsymbol{Y}_m - \boldsymbol{F}\left(\boldsymbol{p_i}\right)) - \alpha^2\boldsymbol{R}^T\boldsymbol{R}(\boldsymbol{p_i} - \boldsymbol{p_0})\right) \tag{2.24}$$

For $i = 1$ this is a linear reconstruction algorithm. Here $\boldsymbol{J_i}$ is the Jacobian calculated for the inverse parameter $\boldsymbol{p_i}$, $\boldsymbol{Y}_m$ is the vector of measurements and the forward solution $\boldsymbol{F}\left(\boldsymbol{p_i}\right)$ is the predicted measurement from the forward model with parameter $\boldsymbol{p_i}$. There are methods to find the best regularization parameter for linear problems, for example *L-Curve* method [62], a review of other methods is given in [160]. Morozov's stopping

criteria has been used to stop the iterations [105]. The iteration will stop when $\| \boldsymbol{F}(\boldsymbol{p}_i) - \boldsymbol{Y}_{\boldsymbol{m}} \| < \varepsilon$, where ε is the noise level estimated in measurement system.

2.4 Semi-linear methods

In the Newton-Kantorovich [77] method the forward problem is solved in each iteration but the Jacobian matrix remains the same in all iterations the same as the Jacobian matrix in first iteration.

With the aim of speeding up Newton types algorithm Broyden Quasi-Newton method has been studied for ERT [86].

In the BQN technique one needs to solve the forward problem in each step and the inverse of the Jacobian matrix can be updated with direct formula as follow. If F is the forward map and $\boldsymbol{Y}_m$ is the measurement capacitance, we define $\boldsymbol{D} = \boldsymbol{F} - \boldsymbol{Y}_m$ and $\boldsymbol{\gamma} = \boldsymbol{D}_{i+1} - \boldsymbol{D}_i$ and $\Delta \boldsymbol{p}_{i+1} = \boldsymbol{p}_i - \boldsymbol{p}_{i+1}$. The material distribution that best describes the actual solution is the one that makes $\boldsymbol{D} \approx 0$. The solution for this particular permittivity can be found using the iterative equation

$$\boldsymbol{p}_{i+1} = \boldsymbol{p}_i + \boldsymbol{H}_i \boldsymbol{D}_i \tag{2.25}$$

We start with an initial guess, and updating the solution for each iteration. $\boldsymbol{H}_i$ is an approximation of the inverse of the Jacobian matrix related to permittivity distribution $\boldsymbol{p}_i$. Instead of calculating the Jacobian matrix and solving a linear system of equation in each iteration, the matrix $\boldsymbol{H}$ can be updated with $O(n^2)$ operations, n is the number

of pixels of the image as follow

$$\boldsymbol{H}_{i+1} = \boldsymbol{H}_i + \frac{(\Delta \boldsymbol{p} - \boldsymbol{H}_i \gamma_i)\Delta \boldsymbol{p}_i^T \boldsymbol{H}_i}{\Delta \boldsymbol{p}^T \boldsymbol{H}_i \gamma_i} \tag{2.26}$$

It is been shown that the method has super-linear convergence [6] and that the set of matrixes $\boldsymbol{H}_i, i = 1,2,3,\ldots$ converges to $\boldsymbol{H}^{true}$(The inverse of the Jacobian matrix at the point $\boldsymbol{p}^{true}$ where $\boldsymbol{D} = 0$ is satisfied). The initial guess for the BQN method is important to the convergence. If we start close to the solution the BQN converges fast. If the initial guess is far from the solution, the BQN may not converge. A mixed regularized Gauss-Newton and BQN for high contrast ERT problem, where the first few steps are using regularized Gauss-Newton and when we are approaching the solution we can benefit from faster BQN iteration [86].

2.5 Linear solvers for FEM

A major part of FEM modelling is the linear solver for the system of equations arising from the discretized model. In real-life applications, where we are dealing with very complicated geometries in three space dimensions, these systems of equations are extremely large. Hence, iterative solution methods outperform direct ones. The CG method is an effective method for symmetric positive definite (SPD) systems. If for any complex vector $\boldsymbol{x}$ we have $\boldsymbol{x}^* \boldsymbol{K} \boldsymbol{x} > 0$ the $\boldsymbol{K}$ is positive definite and $(.)^*$ is the complex conjugate transpose. The method proceeds by generating vector sequences of iterates (i.e., successive approximations to the solution), residuals corresponding to the iterates, and search directions used in updating the iterates and residuals. Although the length of these sequences can become large, only a small number of vectors needs to be kept in memory. In every iteration of the method, two inner products are performed

in order to compute update scalars that are defined to make the sequences satisfy certain orthogonality conditions. On a SPD linear system these conditions imply that the distance to the true solution is minimized in some norm. Here, the CG method is the solver of choice, having the optimal approximation property that the iterate $\boldsymbol{x}_i$ produced at the ith step, has minimal error $\boldsymbol{e}_i = \boldsymbol{x} - \boldsymbol{x}_i$, measured in the norm,

$$\| \boldsymbol{e}_i \|_{\boldsymbol{K}}^2 = \boldsymbol{e}_i{}^T \boldsymbol{e}_i,$$

over all possible choices of $\boldsymbol{x}_i$ belonging to the associated Krylov subspace. Convergence of the method is completely determined by the spread of the eigenvalues of the coefficient matrix, in that,

$$\frac{\| \boldsymbol{e}_i \|_{\boldsymbol{K}}}{\| \boldsymbol{e}_0 \|_{\boldsymbol{K}}} \leq \min_{\varpi_i} \max_{j=1,2,\ldots,n} |\varpi_i(\sigma_j)|, \tag{2.27}$$

where ϖ_i is any polynomial of degree i satisfying $\varpi_i(0) = 1$ and $\{\sigma_j\}_{j=1}^n$ denotes the set of eigenvalues of $\boldsymbol{K} \in \mathbb{R}^{n \times n}$. Simply put, the error on the left hand side of (2.27) can only be reduced to zero with a few iterations of CG if the eigenvalues of $\boldsymbol{K}$ are clustered. As is common in finite element problems, the SPD matrix $\boldsymbol{K}$ in our study does not have this property. Efficient CG convergence can only be achieved by locating a symmetric preconditioner $\boldsymbol{M} \in \mathbb{R}^{n \times n}$, such that the eigenvalues of $\boldsymbol{M}^{-1}\boldsymbol{K}$ are clustered, and iterating, instead, on the preconditioned system, $\boldsymbol{M}^{-1}\boldsymbol{K}\boldsymbol{x} = \boldsymbol{M}^{-1}\boldsymbol{f}$.

2.5.1 Conjugate gradient algorithm

To solve the linear system of equation $\boldsymbol{K}\boldsymbol{x} = \boldsymbol{f}$. The iterates $\boldsymbol{x}_i$ are updated in each iteration by θ_i a multiple of the search direction vector $\boldsymbol{\Lambda}_i$, is

$$\boldsymbol{x}_i = \boldsymbol{x}_{i-1} + \theta_i \boldsymbol{\Lambda}_i \tag{2.28}$$

Correspondingly the residuals $\boldsymbol{r}_i = \boldsymbol{f} - \boldsymbol{K}\boldsymbol{x}_i$ are updated as $\boldsymbol{r}_i = \boldsymbol{r}_{i-1} - \theta_i \boldsymbol{K}\boldsymbol{\Lambda}_i$.

The choice of $\theta_i = \dfrac{\boldsymbol{r}_{i-1}^T \boldsymbol{r}_{i-1}}{\boldsymbol{\Lambda}_i^T \boldsymbol{K}\boldsymbol{\Lambda}_i}$ minimizes $\boldsymbol{r}_i^T \boldsymbol{K}^{-1} \boldsymbol{r}_i$ over all possible choices for θ_i.

The search directions are updated using the residuals $_i = \boldsymbol{r}_i + \kappa_{i-1}\boldsymbol{\Lambda}_{i-1}$ where the choice $\kappa_i = \dfrac{\boldsymbol{r}_i^T \boldsymbol{r}_i}{\boldsymbol{r}_{i-1}^T \boldsymbol{r}_{i-1}}$ ensures that $\boldsymbol{r}_i$ and all $\boldsymbol{r}_j$ are orthogonal ($for \;\; i \neq j$).

Here is a PCG iteration with matrix $\boldsymbol{M}$ as a preconditioner

Data: Linear system of equations and right hand side

Result: Solution of the linear system of equations

Choose an initial guess for $\boldsymbol{x}$, $\boldsymbol{x}_0$;

Compute $\boldsymbol{r}_0 = \boldsymbol{f} - \boldsymbol{K}\boldsymbol{x}_0$;

for *i=1,2,...* **do**

  if *check convergence* **then**

    break

  else

    solve $\boldsymbol{M}\boldsymbol{\zeta}_{i-1} = \boldsymbol{r}_{i-1}$;

    $\rho_{i-1} = \boldsymbol{r}_{i-1}\boldsymbol{\zeta}_{i-1}$;

    if *i=1* **then**

      $\boldsymbol{\Lambda}_1 = \boldsymbol{\zeta}_0$;

    else

      $\beta_{i-1} = \dfrac{\rho_{i-1}}{\rho_{i-2}}$;

      $\boldsymbol{\Lambda}_i = \boldsymbol{\zeta}_{i-1} + \beta_{i-1}\boldsymbol{\Lambda}_{i-1}$;

    end

    $\boldsymbol{q}_i = \boldsymbol{K}_i$;

    $\theta_i = \dfrac{\rho_{i-1}}{\boldsymbol{\Lambda}_i^T \boldsymbol{q}_i}$;

    $\boldsymbol{x}_i = \boldsymbol{x}_{i-1} + \theta_i \boldsymbol{\Lambda}_i$;

    $\boldsymbol{r}_i = \boldsymbol{r}_{i-1} - \theta_i \boldsymbol{q}_i$;

  end

end

Algorithm 3: CG method

If $\boldsymbol{M} = \boldsymbol{I}$ the algorithm is unpreconditioned CG. The convergence of PCG algorithm depends on condition number of $\boldsymbol{M}^{-1}\boldsymbol{K}$. In order to compare total computational time of solving a problem using PCG, one needs to take into account computational time

of generating matrix $\boldsymbol{M}$. Essentially, the new coefficient matrix is $\boldsymbol{M}^{-1}\boldsymbol{K}$. Preconditioning aims to produce a more clustered eigenvalue structure for $\boldsymbol{M}^{-1}\boldsymbol{K}$ and/or lower condition number than for $\boldsymbol{K}$ to improve the relevant convergence ratio. However, preconditioning also adds to the computational effort by requiring that a linear system involving $\boldsymbol{M}$ (namely $\boldsymbol{M}\boldsymbol{\zeta} = \boldsymbol{r}$) be solved at every step. Thus, it is essential for efficiency of the method that $\boldsymbol{M}$ be factored very rapidly in relation to the original $\boldsymbol{K}$. Accurate predictions of the convergence of iterative methods are difficult to make, but useful bounds can often be obtained. For the Conjugate Gradient method, the error can be bounded in terms of the spectral condition number of the matrix $\boldsymbol{M}^{-1}\boldsymbol{K}$. With symmetric positive definite matrix $\boldsymbol{K}$, then for CG with symmetric positive definite preconditioner $\boldsymbol{M}$, it has be shown [53] that

$$\| \boldsymbol{x}_i - \boldsymbol{x}_{tru} \|_{\boldsymbol{K}} < 2\theta_i \| \boldsymbol{x}_0 - \boldsymbol{x}_{\text{true}} \|_{\boldsymbol{K}}$$

where $\theta = \dfrac{\sqrt{\text{cond}(\boldsymbol{M}^{-1}\boldsymbol{K})} - 1}{\sqrt{\text{cond}(\boldsymbol{M}^{-1}\boldsymbol{K})} + 1}$, where cond$(.)$ is the condition number of a matrix, $\boldsymbol{x}_{\text{true}}$ is the exact solution.

The Cholesky factorization expresses a symmetric matrix as the product of a triangular matrix and its transpose $\boldsymbol{K} = \boldsymbol{\Upsilon}^T\boldsymbol{\Upsilon}$ where $\boldsymbol{\Upsilon}$ is an upper triangular matrix. Not all symmetric matrices can be factored in this way; the matrices that have such a factorization are said to be positive definite. If we could have exact Cholesky factorization for matrix $\boldsymbol{K}$ the solution of the linear system of equation could be $\boldsymbol{x} = \boldsymbol{\Upsilon}^{-1}(\boldsymbol{\Upsilon}^T \boldsymbol{f})$. If $\boldsymbol{K}$ is $n \times n$ matrix, the computational complexity of Cholesky factorization of $\boldsymbol{K}$ is $O(n^3)$ and the complexity of the solution of the linear system after that is only $O(n^2)$. For large scale systems of equations this is not an efficient method. But one can use incomplete Cholesky (IC) factorization and use that as preconditioner for the CG algorithm. In IC factorization the matrix $\boldsymbol{K}$ can be written as $\boldsymbol{K} = \boldsymbol{\Upsilon}^T\boldsymbol{\Upsilon} - \boldsymbol{\Xi}$, where $\boldsymbol{\Xi}$

is the error (rest) matrix. To calculate IC factorization of the matrix $\boldsymbol{K}$ we need to set a drop tolerance. Smaller drop tolerance means that the incomplete factorization is closer to the Cholesky factorization. So if Υ calculated with smaller drop tolerance is used as a preconditioner in PCG, the number of iterations of PCG will reduce, but the computational cost of calculating more accurate Υ is higher. It is always difficult to find a balance between the computational time for calculating the IC factorization and PCG iterations.

2.6 conclusion

In this chapter some of the basic concepts in forward and inverse problems have been studied. This study is an abstract study but helps to understand some of the techniques that have been implemented in this thesis. Comprehensive details can be seen in refrences given in each part.

Chapter 3

MAGNETIC INDUCTION TOMOGRAPHY

Magnetic induction tomography (MIT) is relatively new modality for medical and industrial imaging (see for example [58], [145], [116], [78]). The technique operates as follows. Passing an alternating current through excitation coil(s) produces a primary magnetic field. When this magnetic field interacts with a conductive and/or a permeable object, a secondary magnetic field is created. The sensing coils can then detect the resulting magnetic field. As the secondary field depends on the materials present, the measured induced voltages are nonlinear functions of their electromagnetic properties, e.g., conductivity and permeability. The contact-less nature of this type of tomography makes the technique of interest for non-invasive and non-intrusive applications. Potential applications of MIT for medical imaging have been studied earlier (see for example [29], [133],[100], [145]). In [29] the possibility of using MIT for permeability imaging in medical application has been investigated. In addition to the medical applications MIT has some potential applications to the industrial process monitoring

[63],[116], non-destructive testing (NDT) [70], and geophysics [41]. Industrial process applications of MIT especially for the metals industry, such as molten steel flow visualization [116], [11], [94] and solidification monitoring for molten steel [117], [118] are of interest of this study. In particular we are interested in molten metal flow visualization using MIT. The major difference between medical (e.g [78]) and industrial MIT is that in industrial applications conductivity contrast are often high, where as in the medical context small conductivity contrasts are more typical [143].

In this thesis we focus on electrical conductivity imaging using the eddy current concept. The formulation can be easily extended to complex conductivity reconstruction, but we assume the permittivity distribution is given. A mathematically similar problem (crack detection) has been studied extensively for the NDT application. In NDT applications various forward problem formulations, sensitivity formulations and several inverse techniques have been developed [110], [153], [81], [70]. In this thesis the tomographic notion of the inverse eddy current problem (MIT) is considered. Image reconstruction here is a nonlinear ill-posed inverse problem where the measured voltages are given and the spatial distribution of the electromagnetic properties (for purpose of this chapter the electrical conductivity) of the object material need to be found. The idea of regularization has not been explored in NDT application of the inverse eddy current problem. Here we are using regularization methods to stabilize the inverse solver.

In medical MIT, linear back projection [78] and a single step regularized method [28] have been used. In this thesis we demonstrate that the MIT is a so called soft field tomography method, and that the linear back projection cannot be a suitable image reconstruction method. Soft field tomography means that a local change in imaging quantity (here electrical conductivity) has an effect on all measurement data. In this

chapter we present a regularized Gauss-Newton scheme to the inverse problem of MIT. Sensitivity analysis in this thesis shows that the sensitivity map changes with the background conductivity. Because the sensitivity map changes with the background one needs to recalculate the Jacobian matrix at each iterative step of the purposed nonlinear inverse solver. A computationally efficient method to calculate the Jacobian matrix is given in this chapter. Reconstruction of the conductivity requires a forward solver so that predicted data can be compared with measured data. The generalized eddy current form of the Maxwell's equation has been adapted for the forward problem in MIT. The eddy current problem involves the computation of the vector field as well as scalar fields. Edge FEM has advantages over nodal elements for vector field computation of the eddy current problem [12]. We have implemented edge FEM software to simulate the forward problem in MIT. For mesh generation we are using a general purpose mesh generator provided by FEMLAB [46]. The edge finite element method (edge FEM) has been employed for the medical and industrial MIT forward problem [146], [99]. Solving the forward problem of MIT using a scalar field has been reported earlier by [51]. A major simplifying assumption is made by the authors of [51], that the electric field in conductive region can be written in terms of the magnetic vector potential of the primary field and a scalar potential. This assumption is not valid for the general eddy current problem. In order to understand why the assumption is not correct, one can follow the eddy current formulation of $\boldsymbol{A}_r, \boldsymbol{A}_r - V$ by [99], which shows the electric field in the conducting area is the sum of the scalar field and primary magnetic vector potential and a reduced magnetic vector potential. The simplifying assumption of [51] is valid for very low frequency (for example medical conductivity with frequency range smaller than 100kHz), but at higher frequencies one can not ignore the effect of the secondary magnetic field.

In this thesis we present some simulation results with a range of conductivity and frequency of medical MIT.

For the industrial process tomography application we have examined the image reconstruction software with simulation and experimental data. The experimental data was collected from a newly developed industrial MIT system working at frequency 5kHz. Reconstructed results using experimental MIT data are among the first real data reconstruction using an FE based image reconstruction in MIT.

3.1 Inverse eddy current problem

Assuming time-harmonic fields with angular frequency ω Maxwell's equations are

$$\nabla \times E = -i\omega\mu H \tag{3.1}$$

$$\nabla \cdot \mu H = 0 \tag{3.2}$$

$$\nabla \times H = (\sigma + i\omega\varepsilon) E + J_s \tag{3.3}$$

$$\nabla \cdot \varepsilon E = 0 \tag{3.4}$$

Here E and H are the magnetic and electric fields, σ is conductivity, μ magnetic permeability and ε permittivity. The current sources are represented by the current density $\boldsymbol{J}_s$. The inverse boundary value problem for Maxwell's equations is the recovery of the material parameters σ, ε and μ from measurements of the tangential components $n \times H$ and $n \times E$ of the fields on some surface Γ (with normal n) enclosing the region Ω where the material parameters are unknown. Uniqueness of the solution for

this inverse boundary value problem has been proved, provided ω is not a resonant frequency [111] (resonant frequency is a frequency that the capacitive and inductive component of the the impedance cancell each other). In this study they take $J_s = 0$ assuming the sources are included in the boundary conditions. It is worth noticing that in the sensing coil the measurements of induced voltage can be expressed as line integral of the tangential component of E along the coil. It can also be described as surface integral of the normal component of the magnetic flux density B.

The methodology for establishing the derivative of the boundary measurements with respect to a perturbation of a material parameter was established in the fundamental paper of Calderón [27] for the static case $\omega = 0$. The general case for time harmonic Maxwell's equations was treated by [150]. These results require some slight modification for application to MIT. In this case, we are not measuring on an isolated boundary. Typically we have an arrangement of coils on some surface Γ but boundary conditions (such as screening by a conductive or magnetic shield) are applied on some surface containing this. We can think of an idealized excitation coil as imposing a predetermined tangential component of H on Γ, and our idealized measurement as an integral of E around an infinitesimal loop on Γ. This is no worse than the idealization in the low frequency case (EIT) that one can apply arbitrary current patterns to the surface and measure the voltage everywhere.

In practise we measure a finite subset of the idealized data, but it is important to know at least that if we collected ideal data then the material parameters are uniquely determined. This question, called *uniqueness of solution* by mathematicians, is the practical question of *sufficiency of data* for the engineer. The measurement arrangements of MIT using a system of coils does not fit exactly in to this formalism. There is no barrier to electric and magnetic fields on the surface containing the coils so we must

model them by a current source term J_s, and impose boundary conditions on some larger enclosing surface. We will address this in the next section. For the moment, our ideal data is the transfer impedance on the surface Γ, where we have complete control of the tangential component of H and knowledge of the transfer impedance of E (or vice versa). There is of course a parallel impedance due to the region exterior to Γ, which we will assume is known by calibration and has already been subtracted.

It is convenient to recast the data on Γ in an integral of the normal component of the Poynting vector $E \times H$ that represents the power-flux, we obtain

$$\begin{aligned} \int_\Gamma \delta(E \times H) \cdot n \, dx^2 = \\ \int_\Omega \delta\mu H \cdot H + (\delta\sigma + i\omega\delta\varepsilon) E \cdot E \, dx^3 + O(||\delta\sigma||^2) \end{aligned} \tag{3.5}$$

Taking the electric and magnetic fields from two different excitations from coils 1 and 2, but with the same material perturbations, and applying the above to $E = E_1 \pm E_2$ and $H = H_1 \pm H_2$ then subtracting we obtain

$$\begin{aligned} \int_\Gamma \delta(E_1 \times H_2) \cdot n dx^2 = \int_\Omega \delta\mu H_1 \cdot H_2 + (\delta\sigma + i\omega\delta\varepsilon) E_1 \cdot E_2 \, dx^3 \\ + O(\|\delta\sigma\|^2) \end{aligned} \tag{3.6}$$

Now taking the magnetic field on Γ to be prescribed and the tangential magnetic field to be measured, the left hand side reduces to

$$\int_\Gamma \delta E_1 \times H_2 \cdot n \, dx^2. \tag{3.7}$$

Taking H_2 to be the field due to the excitation of measurement coil 2 with a unit current, this reduces to δV_{21} the change of the induced voltage on the measurement coil 2 when coil 1 is excited.

Although one could in principle calculate the sensitivity using a numerical solver for Maxwell's equations by successively making small perturbations to small voxels in

the model, this would result in a large number of field solutions, whereas calculation using this formula requires only one E and H solution for each coil.

3.1.1 Coil Model and Sensitivity

There are a number of ways to model the excitation and measurement coils. As in EIT where the conductive electrodes must be modelled, the presence of the coils can affect the fields. Rather than modelling individual turns of copper wire, we will use a simplified model of a coil as a surface, (topologically at least) an open ended cylinder. When used as an excitation coil this surface carries a tangential current J_s. This is equivalent to a surface that is perfectly conducting in one direction (angular for a cylinder) and an insulator in another (axial) direction, with each loop fed by a perfect current source.

A typical arrangement of the sensors for MIT uses fixed excitation and the measurement coils. There might be an external screen modelled as an electrical conductor, which means that the tangential component of E vanishes. Where shielding is not possible one would nevertheless need to apply far field boundary conditions to Maxwell's equations. It is important to note that the electromagnetic fields inside the sensor area and between the coils and the shield are coupled so that we can no longer apply the above approximation where measurement is made on a surface, which decouples the problem. Instead we apply the boundary condition $n \times E = 0$ on the shield Γ, and include source terms J_s for the coils as above.

In areas (such as the air gap surrounding the coils) the same approximation of ignoring the displacement current results in the magnetostatic approximation $\nabla \times H = 0$. This does not allow wave propagation effects and is valid provided our system is small

compared with the wavelength of electromagnetic waves in air. Our coils are considered as electro-magnets not radio transmitting antennas. Combining (3.1) and (3.3) we obtain

$$\nabla \times \left(\frac{1}{\mu}\nabla \times E\right) + \mathrm{i}\omega\xi E = -\mathrm{i}\omega J_s \tag{3.8}$$

Where ξ is the complex admittivity $\xi = \sigma + i\omega\varepsilon$. We now consider the case where we excite one coil. Suppose that the admittivity is perturbed $\xi \to \xi + \delta\xi$ with the resulting change in the field $E \to E + \delta E$ while the current J_s is held constant. Our aim is to find the linearized change in the voltage measured on some other coil, so in this derivation we will neglect second and higher order terms. A more detailed derivation along the lines of Calderón [27] would prove that this is the Fréchet derivative in suitable normed spaces. Applying (3.8) to E and $E + \delta E$, then subtracting and neglecting higher order terms gives

$$\nabla \times \left(\frac{1}{\mu}\nabla \times \delta E\right) + i\omega(\delta\xi E + \xi\delta E) = 0. \tag{3.9}$$

Taking the dot product with E yields

$$\frac{1}{\mu}E \cdot \nabla \times (\nabla \times \delta E) + i\omega\delta\xi E \cdot E + i\omega\xi E \cdot \delta E = 0 \tag{3.10}$$

from which we seek to remove the term in δE (in the interior). We use the identity

$$\nabla \cdot (E \times \nabla \times \delta E) = E \cdot \nabla \times \nabla \times \delta E + (\nabla \times E) \cdot (\nabla \times \delta E) \tag{3.11}$$

to give

$$\begin{aligned} \nabla \cdot (\delta E \times \nabla \times E) &= \delta E \cdot \nabla \times \nabla \times E + (\nabla \times \delta E) \cdot (\nabla \times E) \\ &= -i\omega\mu\xi\delta E \cdot E - i\omega\mu\delta E \cdot J_s + (\nabla \times \delta E) \cdot (\nabla \times E) \end{aligned} \tag{3.12}$$

using (3.8) and subtracting (3.12) from (3.11) gives

$$\begin{aligned} \nabla \cdot (E \times \nabla \times \delta E - \delta E \times \nabla \times E) = E \cdot \nabla \times \nabla \times \delta E \\ + i\omega\mu\xi E \cdot \delta E + i\omega\mu\delta E \cdot J_s \end{aligned} \tag{3.13}$$

eliminating the δE terms using (3.10) then integrating over the domain and using Gauss' theorem, together with the vanishing of the tangential components of E and δE on Γ finally gives

$$\int_{\Omega} \delta E \cdot J_s dx^3 = \int_{\Omega} \delta\xi E \cdot E dx^3 \tag{3.14}$$

which, unsurprisingly has the same right hand side as terms contained in (3.6). One can calculate the sensitivity of a voltage measured on coil 2 when coil 1 is excited.

$$\int_{\Omega} \delta E_1 \cdot J_{s2} dx^3 = \int_{\Omega} \delta\xi E_1 \cdot E_2 dx^3 \tag{3.15}$$

The left hand side here is now the change in voltage induced on our ideal coil provided a unit current is driven in coil 2. It must be emphasized that with non-zero (for example impedance) boundary conditions on the shield Γ the sensitivity would involve boundary terms that are unknown. The same sensitivity formula (3.14) holds here, and the uniqueness result of [111] can be adapted here. If Ω is a bounded domain in R^3 with a smooth boundary Γ and a connected complement. Suppose the map Λ that assigns the tangential component of E_t to that of H_t is defined. Assume that outside Ω, ε, μ are known constants and σ vanishes. Then, it has been proved by [111] that knowledge of the map Λ uniquely determines these quantities. This applies to the coil model we presented here. The same uniqueness will be applied to the permeability tomography in next chapter.

3.2 MIT system

In this chapter the simulated MIT system is a virtual system, and has been used to generate the data for image reconstruction. The simulated image reconstruction results in this chapter are based on this MIT system. The simulated MIT system here has

8 coils system, used for both excitation and sensing. The coils have 0.04 m inner and 0.05 m outer diameter and 0.02 m length. They are arranged in a circular ring surrounding the object to be imaged. In this example the distance between the centre of two coils on opposite sides is 0.160 m, the centre of the coil ring is at (0,0,0). Figure 3.1 shows the coil arrangement of this virtual MIT system. The system could have a magnetic or electric shield but in this chapter the far field boundary condition $B_n = 0$ is applied to the model and the shield has not been considered. We use the normalized value of the measured voltage. All voltages are normalized with respect to the free space induced voltage and a $1Am^{-2}$ current is applied to the excitation coil for simplicity. The region of interest for the imaging is a cylinder with radius 0.07 m, length 0.10 m centred at (0,0,0) and a relative permeability of 1 (labelled C1). Each coil is excited in turn and the induced voltages are measured in the remaining coils. The real part of the induced voltage (in phase to the excitation) has been used for the conductivity reconstruction in low contrast and the imaginary part has been used in high contrast conductivity and experimental examples.

The purpose of the forward solver in MIT is to predict the measurement by a given material distribution and the excitation currents. As we can see in the next section one needs to calculate the interior electric and magnetic field to be able to calculate the efficient Jacobian matrix. Commercial FEM packages do not provide enough access to the model to enable it to be used for the purpose of the inverse problem. As we will see in this chapter in order to generate sensitivity maps one needs to have access to system matrices, which may not be accessible from a commercial package. For the image reconstruction one needs to have access to the system matrix and all shape functions. For this reason one needs to implement a suitable forward solver for the particular inverse problem.

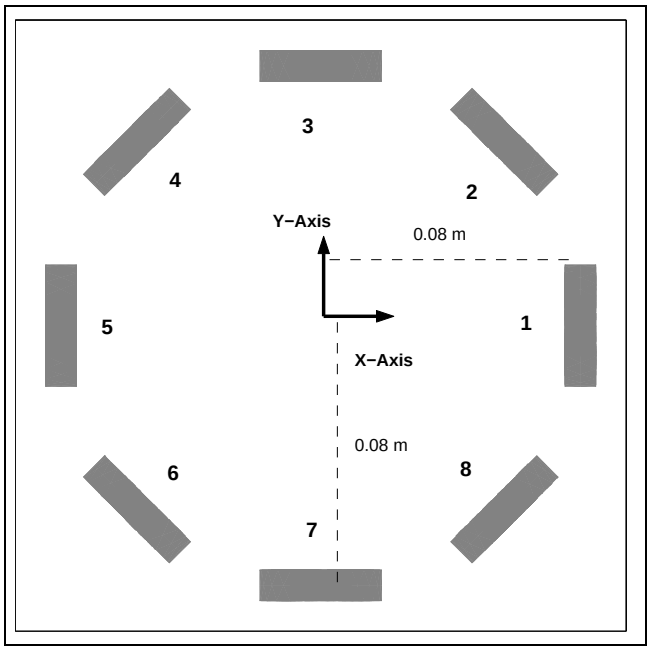

Figure 3.1: Excitation and sensing coils, view from the top

3.3 Whitney finite elements

Edge finite element has its origin from a work by Whitney [173] in differential forms in algebraic topology. Nedlec [107], [108] is the first scientist to extend the edge finite elements in three dimensional. Since then edge finite elements have been used in various electromagnetic problems. Eddy current and magnetostatic problems are among many other electromagnetic problems that are benefited from the advancement of edge FEM [12], [48], [18], [129], [166], [167] [130], [91], [90], [74]. In [1], [2] edge elements are used for an integral formulation for computational electromagnetics.

Edge finite element is a member of family of vector finite elements. Whitney elements are from three forms including, *0-form* defined for a scalar potential ϕ bases for first order nodal FEM, *1-form* defined for the edges and a vector potential $\boldsymbol{u}$ and it is the base for the edges FEM and *2-form* defined for vector field $\boldsymbol{u}$ and it is the base for the

facet elements.

In a general any Whitney form associated with p-simplex $i_0, i_1, i_2, ..., i_p$ is [30]

$$w_{i_0,...,i_p} = p! \sum_{j=1}^{p} (-1)^j \phi_{ij} d^0 \phi_{i_0} ..... \wedge d^0 \phi_{ij-1} \wedge d^0 \phi_{ij+1} \wedge ... \wedge d^0 \phi_{ip} \qquad (3.16)$$

where ϕ_i is a piecewise linear function that has value 1 in node i and zero in other nodes of the element and d^0 is the exterior derivation. The value of a variable x can be defined by $x = \sum_i \phi_i(x) x_i$ with x_i value of x in node i and $\sum_i \phi_i(x) = 1$. The operator d^1 is for *grad* ϕ for *0-form* and d^2 is for *curl* $\boldsymbol{u}$ for *1-form* and d^3 is for *div* $\boldsymbol{u}$ for *2-form*. Based on equation (3.16) the lowest order is the form of degree zero defined in nodes. We have $w_i = \phi_i$, which has value 1 at node i and zero in any other nodes. The function w_i is continuous across facets. If i and j are nodes for an edge, the *1-form* belonging to this edge is $\boldsymbol{w}_{ij} = \phi_i \nabla \phi_j - \phi_j \nabla \phi_i$. Tangential component of $\boldsymbol{w}_{ij}$ is 1 along edge between nodes i, j and zero along any other edges. Tangential component of the vector field $\boldsymbol{w}_{ij}$ is continuous across facets. If i, j, k are nodes belonging to a face, the *2-form* belonging to the facet elements is $\boldsymbol{w}_{ijk} = \phi_i \nabla \phi_j \wedge \phi_k + \phi_j \nabla \phi_k \wedge s\phi_i + \phi_k \nabla \phi_i \wedge s\phi_j$. The normal component of the vector field $\boldsymbol{w}_{ijk}$ is continuous across facets.

Conformity of the Whitney forms is an interesting property of them. The conformity of Whitney elements is *grad* $w^0 \subset \boldsymbol{w}^1$ and *curl* $\boldsymbol{w}^1 \subset \boldsymbol{w}^2$ and *div* $\boldsymbol{w}^2 \subset w^3$, here w^3 is for scalar fields and has the same properties as *0-form*.

In this thesis we are working with nodal FEM based *0-form* and edge FEM based on *1-form*. Properties of nodal FEM that make them interesting for the scalar field computations are very well known, we use nodal FEM for the forward problem of ERT and ECT (scalar fields) next chapters. We also use an edge finite element technique for vector field computation in eddy current and magnetostatic problems.

Edge FEM has some promising advantages compared with the more conventional

nodal FEM for vector field computations. In edge FEM a vector field is represented using a basis of vector valued functions. Nodal FEM was used for the vector fields in electromagnetics. Although nodal FEM is easy and straightforward and its outcome accurate, several serious problems have been identified when the ordinary nodal-based finite elements were employed to compute vector electric or magnetic fields, most notably

- Long computation time
- Large memory requirements
- Lack of adequate gauge conditions for vector magneto-static analysis
- Satisfaction of the appropriate boundary conditions at material and conducting interfaces
- Difficulty in treating the conducting and dielectric edges and corners due to the field singularities associated with these structures
- Occurrence of non-physical or so-called spurious solutions, especially in waveguide and scattering problems, etc.

A very important advantage of edge FEM in computational electromagnetics is their superiority in imposing physically necessary continuity properties for inter-elements, and not imposing any additional continuity. For eddy current and magnetostatic problems we developed edge FEM based on a formulation involving edge finite element modelling of the magnetic vector potential $\boldsymbol{A}$ [12]. The tangential component of $\boldsymbol{A}$ is continuous between two neighboring elements, which satisfies tangential continuity of the electric fields. The magnetic flux density is curl of magnetic vector potential,

continuity of tangential component of magnetic vector potential ensures the normal continuity of magnetic flux density. Continuity of normal component of the magnetic flux density and tangential component of electric fields are two physical continuity and are satisfied by edge finite element formulation.

3.4 Forward problem

The electromagnetic field in the eddy current problem can be described either in terms of a field, a potential or a combination of both. One can use different combinations of these quantities as state variables [12]. Although different formulations would produce the same answers in exact arithmetic, they may differ in accuracy when implemented numerically and the implementation will differ in complexity and computational cost. We have implemented two of the most popular edge FEM formulation in forward modelling. We use a formulation based on magnetic vector potential $\boldsymbol{A}$ and an electric scalar potential V [12]. We have also implemented a method based on the $\boldsymbol{A}$,$\boldsymbol{A}$ formulation [73].

3.4.1 $\boldsymbol{A},\boldsymbol{A}-V$ formulation

First order tetrahedral edge finite elements are employed to model the magnetic vector and the first order nodal tetrahedral elements electric scalar potential. We have developed a more general eddy current software for time harmonic eddy current modelling. For the field quantities we have $\boldsymbol{E} = -i\omega(\boldsymbol{A} + \nabla V)$ (the time derivative for electric potential is used to ensure the symmetry of linear system of equations) and $\boldsymbol{B} = \nabla \times \boldsymbol{A}$.

Let us consider the quasi-static electromagnetic fields governed by

$$\nabla \times (\nu \nabla \times \boldsymbol{A}) + i\omega\xi(\boldsymbol{A} + \nabla V) = \mathrm{J}_{\boldsymbol{s}}. \tag{3.17}$$

$$i\omega\nabla \cdot (\xi(\boldsymbol{A} + \nabla V)) = 0 \tag{3.18}$$

where $\xi = \sigma + i\omega\varepsilon$ and σ , ε are the electric conductivity and permittivity and $\nu = 1/\mu$. The boundary conditions of $\boldsymbol{A} \times \boldsymbol{n} = 0$ on Γ, the surface of the whole simulation domain and $\boldsymbol{n} \cdot (-i\omega\xi\boldsymbol{A} - i\omega\xi\nabla V) = 0$ on Γ_e, the surface of the eddy current region.

Far field boundary conditions of normal component of magnetic field density zero are set. In edge FEM the degree of freedom is the tangential components of the vector field.

The linear system of equations can be solved using the Incomplete Conjugate Gradient (ICCG) method [97],[75]. The electric vector potential $\boldsymbol{T}_s$ is defined in the coil region to represent the current in the excitation coil. Here $\nabla \times \boldsymbol{T}_s = \boldsymbol{J}_s$ and using this formulation guarantees a divergence free current source for the right hand side of equation (3.17) and improves the convergence of the linear solver. For simple coil shapes we are using some analytical formulation for the computation of $\boldsymbol{T}_s$ [12], and there is no need to mesh the coil itself. For complicated coil shapes the boundary value problem $\nabla \times (\frac{1}{\sigma}\nabla \times \boldsymbol{T}_s) = 0$ is solved with suitable boundary conditions in the coil region. More detailed study of the current source modelling will be presented later in this section.

Finite element discretization of (3.17) ,(3.18) using edge basis functions yields

$$\int_{\Omega} (\nabla \times \boldsymbol{N} \frac{1}{\mu} \cdot \nabla \times \boldsymbol{A}) dx^3 + \int_{\Omega_e} (i\omega\xi \boldsymbol{N} \cdot (\boldsymbol{A} + \nabla V)) dx^3 = \int_{\Omega_c} (\nabla \times \boldsymbol{N} \cdot \boldsymbol{T_s}) dx^3 \tag{3.19}$$

and

$$\int_{\Omega_e} (i\omega\xi \nabla\phi \cdot (\boldsymbol{A} + \nabla V)) dx^3 = 0. \tag{3.20}$$

where $\boldsymbol{N}$ is any linear combination of edge basis functions, $\boldsymbol{N}_{ij} = \phi_i \nabla\phi_j - \phi_j \nabla\phi_i$, ϕ is standard nodal basis, Ω is the entire region, Ω_e the eddy current region, and Ω_c the current source region. $\nabla \times \boldsymbol{N}$ and ∇L are constant in each elements so the integration is simple within an element. For those terms including $\boldsymbol{N}$ we calculate the volume integrals by Gaussian quadratures method [179]. The Gaussian quadratures provide the flexibility of choosing not only the weighting coefficients but also the locations where the functions are evaluated. We use five Gaussian points to evaluate the integrals in eachtetrahedral element.

The induced voltages (V_m) in sensing coils are calculated using

$$V_m = -i\omega \int_{\Omega_c} (\boldsymbol{A} \cdot J_0) dx^3 \tag{3.21}$$

where $_0$ is a virtual unitary current passing through the coil.

To see the result of the forward solver, consider a cylindrical object with diameter 0.14 m and length 0.14 m placed in the centre of the coil ring and has conductivity 0.8 Sm^{-1}. Figures 3.2, 3.3 show the real part of the magnetic flux intensity in plane z=0 and in 3D and figures 3.4 and 3.5 shows the real part of the eddy current when the excitation coil is carrying $1Am^{-2}$ current at frequency 150kHz and placed at (0,-0.08)

m in two and three dimensions. The conductive object is modelled as a cylindrical object with diameter 0.14 m and length 0.14 m placed in the centre of coil ring (0,0) with conductivity $0.8Sm^{-1}$. As discussed in the next section, the shape of the eddy currents inside of the conductive background affect the sensitivity map.

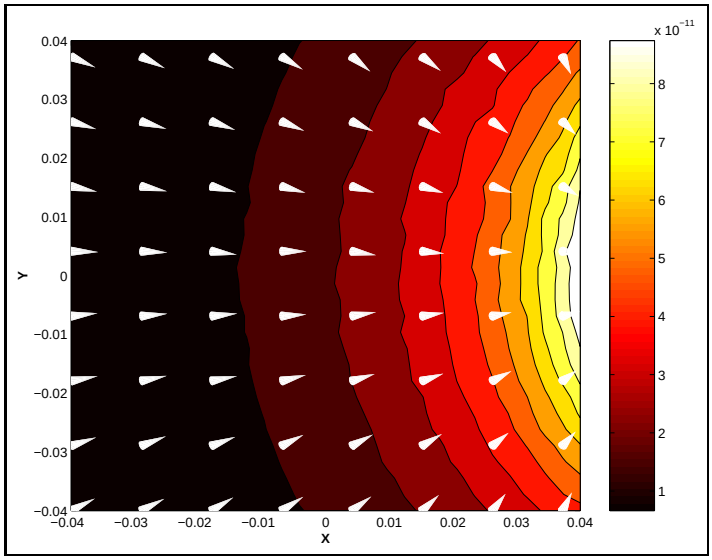

Figure 3.2: The real part of the magnetic flux intensity (B in Tesla) for the electric current of $1Am^{-2}$ in the coil

Figure 3.6 shows the magnetic field intensity when we insert a cylindrical object with radius 0.03 m with relative permeability of 1000 centred at (0,0.025)m.

3.4.2 $\boldsymbol{A}, \boldsymbol{A}$ formulation

In the "$\boldsymbol{A}, \boldsymbol{A}$" formulation using edge FEM [73], [12], $\boldsymbol{A}$ in a conductive region includes the gradient of the electric scalar potential, and Maxwell's equation reduce to the vector Helmholtz equations. Conformity results of Whitney forms means that gradient of the form of degree of 0 is a subset of the form of degree of 1 (edge finite element). This property enable us to use [73] a formulation based on magnetic vector potential

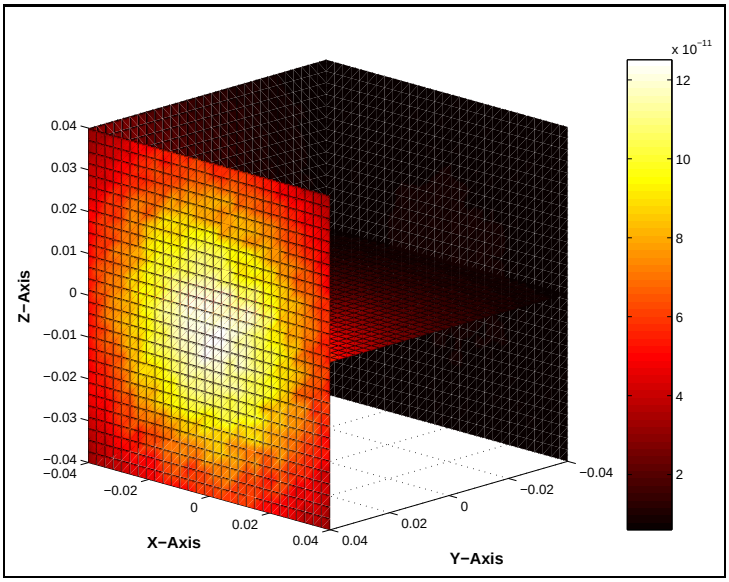

Figure 3.3: The real part of the magnetic flux intensity (B in Tesla) for the electric current of $1Am^{-2}$ in the coil in 3D

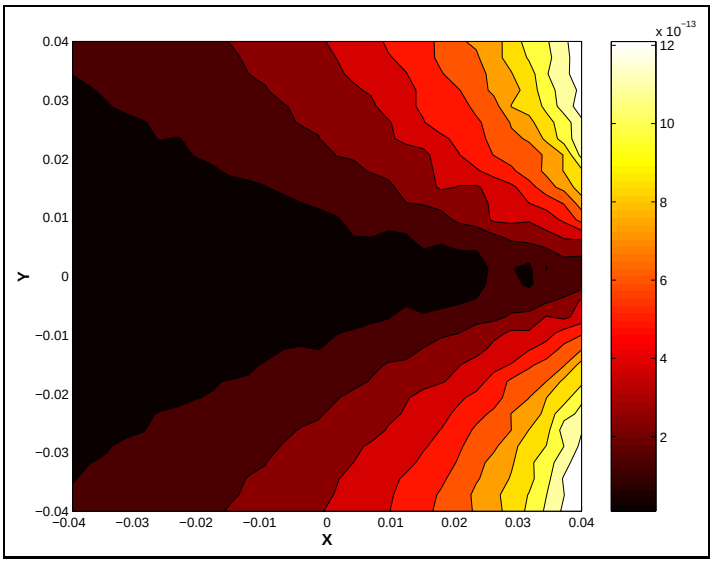

Figure 3.4: The real part of the eddy current intensity (in Am^{-2}) for an electric current density of $1Am^{-2}$ in the coil

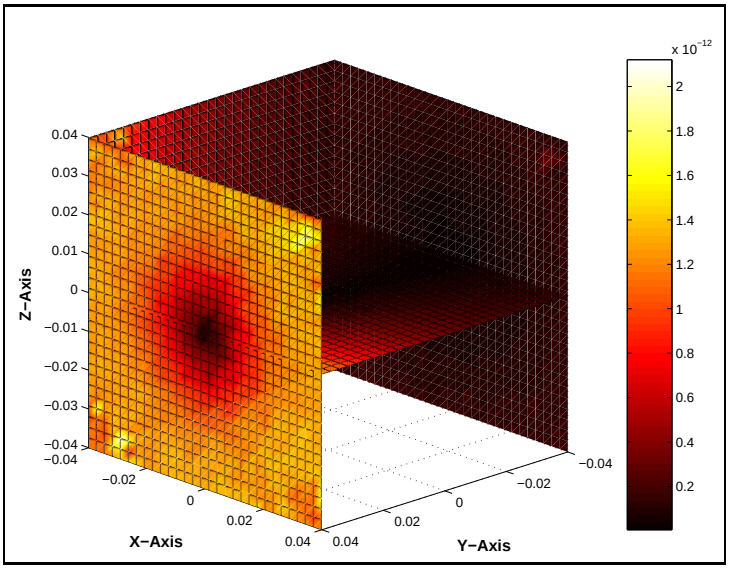

Figure 3.5: The real part of the eddy current intensity (in Am^{-2}) for an electric current density of $1Am^{-2}$ in the coil

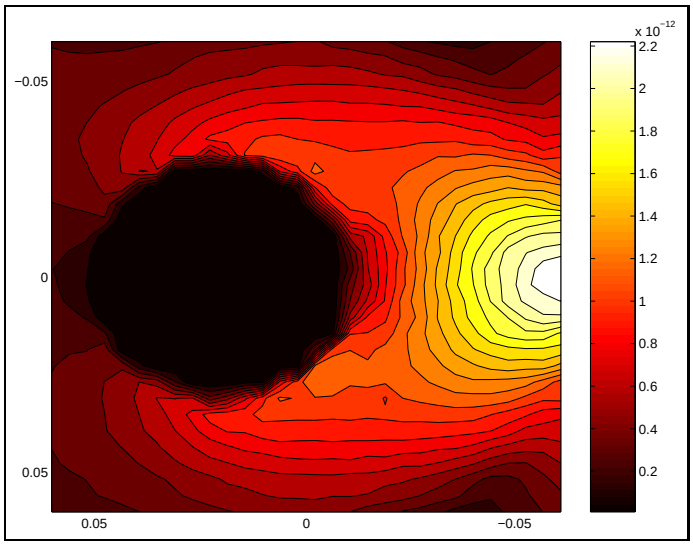

Figure 3.6: The real part of the magnetic field intensity (B in Tesla) for the electric current of $1Am^{-2}$ in the coil and inserting a cylinder with relative permeability of 1000

$\boldsymbol{A}$, which can be written

$$\nabla \times \left(\tfrac{1}{\mu}\nabla \times \boldsymbol{A}\right) + i\omega\sigma\boldsymbol{A} = J_s. \tag{3.22}$$

The finite element discretization of 3.22 with edge element basis functions yields

$$\int_{\Omega} (\nabla \times \boldsymbol{N}\frac{1}{\mu} \cdot \nabla \times \boldsymbol{A})dx^3 + \int_{\Omega_e} (i\omega\sigma\boldsymbol{N} \cdot \boldsymbol{A})dx^3 = \int_{\Omega_c} (\boldsymbol{N} \cdot \mathrm{J}_{\boldsymbol{s}})dx^3 \tag{3.23}$$

where $\boldsymbol{N}$ is any linear combination of edge basis functions, Ω is the entire region, Ω_e the eddy current region, in which $\sigma > 0$, and Ω_c the current source region, again $\boldsymbol{T}_s$ is used to model the current source.

A set of experimental data was collected from the 8 coils MIT system, where the conductive object was a copper bar (a cylinder with radius 0.019 m and length 0.20 m) placed in center of the object space. The normalized induced voltages (all data were normalized with respect to measurement number 1, which is coil 1 excited and coil number 2 is measured) for simulation using our edge FEM software as well as the experimental results are shown in figure 3.7. There is a relatively large difference between measurement of coil 8 and coil 2 when coil 1 is excited in measurement data, we belive this could be because of a mismatch in position of the coils number 2 or 8. In [146] the forward problem for both magnetostatic and the eddy current has been validated against experimental data as well as a commercial package called MAFIA. The number of elements in the edge FEM for this simulation was 86400, simulated at a frequency 5kHz. Image reconstruction for a single copper bar in different positions has been done earlier in [146].

Figure 3.8 shows the the imaginary part magnetic flux intensity in plane z=0 when the excitation coil is carrying $1Am^{-2}$ current at frequency 5kHz and placed at (0,-0.08) m is shown below. For the conductive object here we assumed a cylindrical object

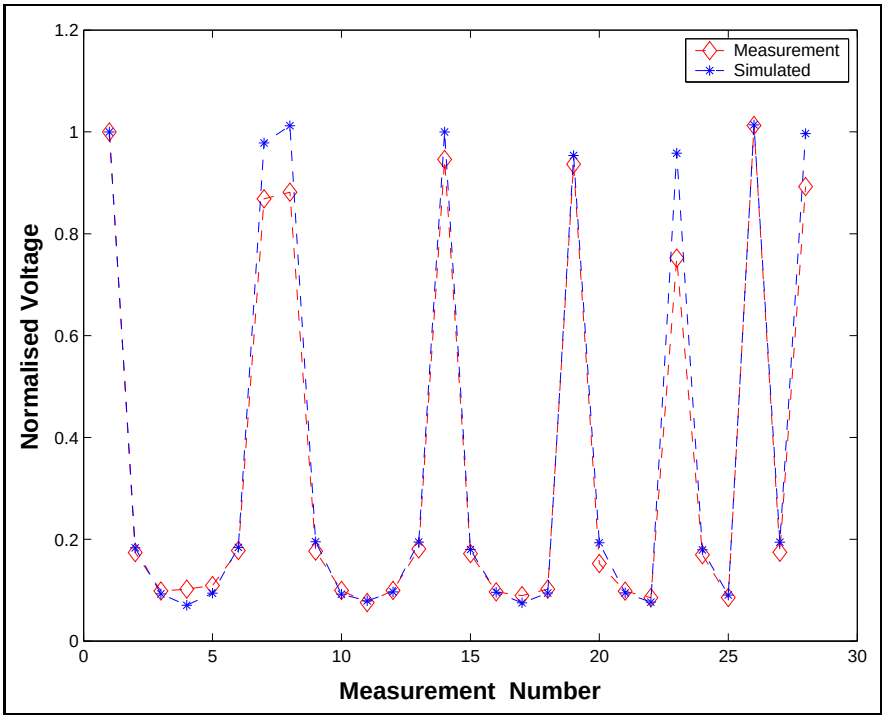

Figure 3.7: Imaginary part of the measurement voltage for a copper bar (conductivity $5.8 \times 10^7 Sm^{-1}$) with diameter 0.038 m and length 0.20 m centered at (0,0). The voltages are normalized with respect to measurement of coil 2 when coil 1 is excited for both simulation and measurement data.

with diameter 0.038 m and length 0.2 m placed in the centre of coil ring (0,0) and has conductivity $5.8 \times 10^7 Sm^{-1}$. Figure 3.9 show the real part of the magnetic flux intensity. Figure 3.10 shows the imaginary part of the eddy current.

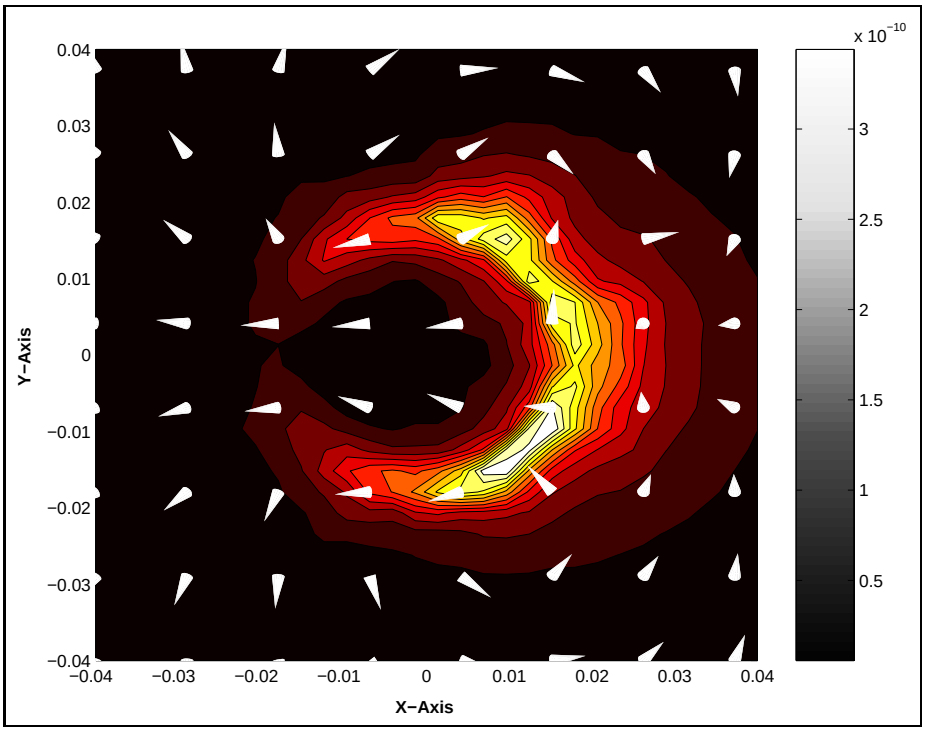

Figure 3.8: The imaginary part magnetic flux intensity (B in Tesla) for the electric current of $1Am^{-2}$ in the coil (with copper bar)

3.4.3 Current source modelling (right hand side)

Special attentions are needed to formulate the excitation current in edge element modelling of the eddy current and magnetostatic problems [129]. Current density needs to be defined in a way that the normal continuity of the current density are satisfied between two elements. Here we explain various methods for the current source modelling and then deal with the main field modelling. In edge element the current source needs to be defined along the edges and also be able to model a divergence free cur-

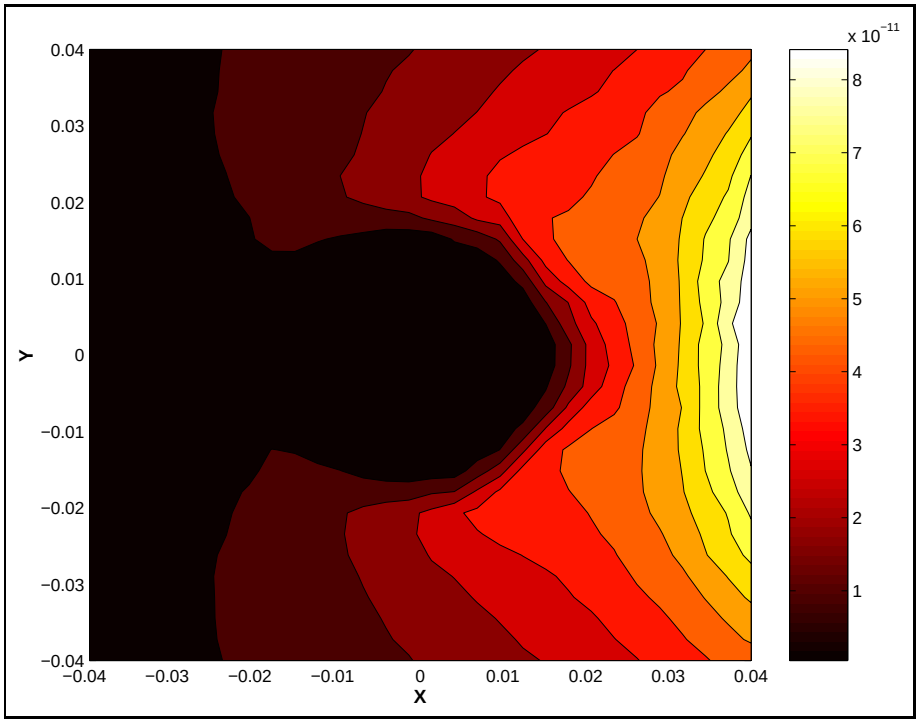

Figure 3.9: The real part magnetic flux intensity (B in Tesla) for the electric current of $1Am^{-2}$ in the coil (with copper bar)

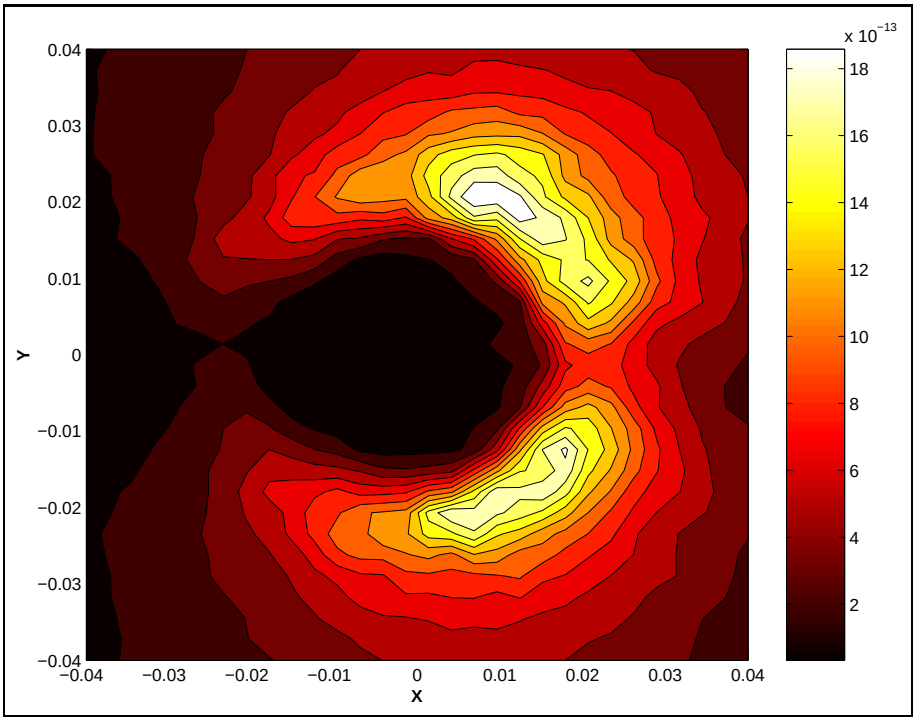

Figure 3.10: The imaginary part of the eddy current (in Am^{-2}) for the electric current of $1Am^{-2}$ in the coil (with copper bar)

rent desnsity, otherwise the linear system of equations arising from edge FEM does not converge [129]. In the cases in which the current distribution is not known in advance, a boundary value problem is set up either in terms of electric scalar potential or electric vector potential. In such cases we have

$$\nabla \cdot J_s = 0 \tag{3.24}$$

Electric Scalar potential

In this method the electric scalar potential is used for computing the current density. Obviously the nodal based FEM is used for interpolation of the electric scalar potential.

It is possible to solve the above equation using electric scalar potential.

We can say

$$\nabla(\sigma \cdot \nabla V) = 0 \tag{3.25}$$

here σ is the conductivity of the coil region and V is the electric scalar potential in coil region. We use a Neumann or Dirichlet boundary condition, respectively for voltage or current source. In this case after computation of V by nodal FEM. We have

$$J_s = \sigma \boldsymbol{E}_s \tag{3.26}$$

Then we have in each point

$$\boldsymbol{J}_s = \sigma(\nabla\phi)V \tag{3.27}$$

where ϕ is the nodal shape function and V is calculated potential of the nodes.

We may want to use this J_s on the right hand side (R.H.S) but the numerical experiments show that the convergence behavior of the solution of the system of equations of the magnetostatic fields of the edge elements of magnetic vector potential formulation is better when we use we use T_s as a source term, in which $\nabla \times \boldsymbol{T}_s = J_s$. Substituting J_s to $\boldsymbol{T}_s$ we have to solve

$$\int_{\Omega_c} (\nabla \times \boldsymbol{N}) \cdot (\nabla \times \boldsymbol{T}_s) dx^3 = \int_{\Omega_c} (\nabla \times \boldsymbol{N}) \cdot J_s dx^3 \tag{3.28}$$

where Ω_c is a simply connected region containing the coils and J_s is the imposed current density.

Analytical model for a simple coil shape

It is possible to analytically calculate the current distribution J_s or more likely the current vector potential distribution $\boldsymbol{T}_s$ analytically in some specific types of coils. For example, for a cylindrical coil around the z-axis with the center at the origin of a cylindrical coordinate system, having an inner radius r_i, outer radius r_0, height h and carrying a current density $\boldsymbol{J} = J_1 \boldsymbol{e}_\theta$, the following function $\boldsymbol{T} = T_1 \boldsymbol{e}_z$ is appropriate (e_θ and e_z are the unit vectors in azimuthal and axial directions, respectively)

$$\boldsymbol{T}_s = \begin{cases} 0 & when \quad |z| > \frac{h}{2} \quad or \quad r > r_0 \\ J_1(r_0 - r_i) & when \quad |z| < \frac{h}{2} \quad and \quad r < r_i \\ J_1(r_0 - r) & when \quad |z| < \frac{h}{2} \quad and \quad r_i < r < r_0 \end{cases}$$

with this definition of the current density, we will have a current source where $\nabla \cdot J_s = 0$ is exactly satisfied analytically. As with all numerical integration over elements, we have some errors compared to an analytical formulation.

Method based on calculation of $\boldsymbol{T}_s$ by edge FEM

This method uses the computation of $\boldsymbol{T}_s$ in current from

$$\nabla \times (\frac{1}{\sigma} \nabla \times \boldsymbol{T}_s) = 0 \tag{3.29}$$

here the boundary condition can be calculated using

$$\oint_{C_i} \boldsymbol{T}_s \cdot \boldsymbol{dl} = \int_{\Gamma_i} J_s \cdot \boldsymbol{n} dx^2 \tag{3.30}$$

for any closed path C_i in a fundamental set of loops in the graph with Γ_i being a surface bounded by the curve C_i. Figure 3.11 shows a mesh of the coil and figure 3.12 shows the electric current density in the coil.

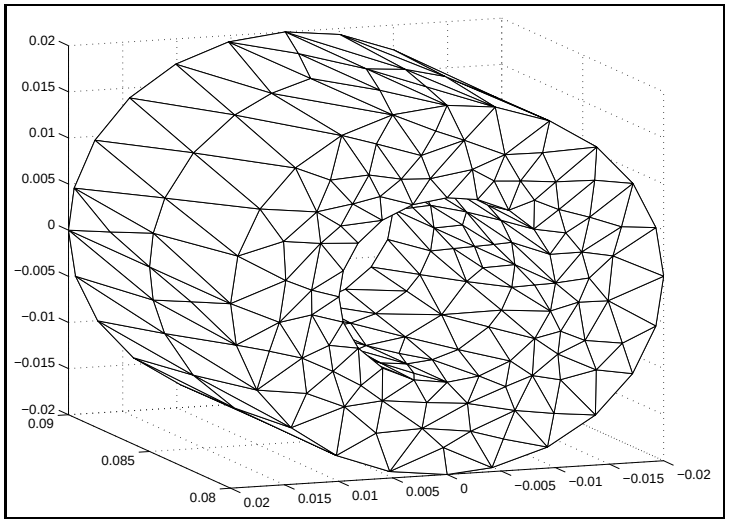

Figure 3.11: Coil mesh

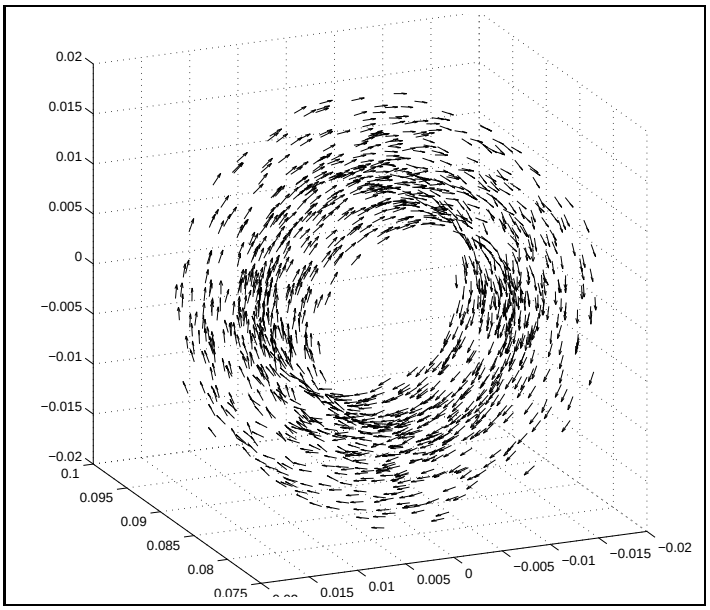

Figure 3.12: Calculated current source

Method for computation of $\boldsymbol{T}_s$: element by element by facet current

In this method we have to calculate the current passing from each facet and then calculate the $\boldsymbol{T}_s$ by

$$\oint_{C_i} \boldsymbol{T}_s \cdot \boldsymbol{dl} = \int_{\Gamma_i} J_s \cdot \boldsymbol{n} dx^2 \tag{3.31}$$

for any closed path C_i in a fundamental set of loops in the graph with Γ_i being a surface bounded by the curve C_i . Obviously this method is useful when we know the current density distribution.

Method using Line Integration

First, the volume of the current source is approximated by multiple lines.

In the cross section of the source, the lines are located at the points of numerical integration of 2D. The total current is shared by the weighting factor of 2D numerical

integration.

Second, in the flowing direction, the lines are approximated by the chains of small straight sticks. The numerical line integration is evaluated in an element only, not across the boundary.

The term of $\int(\boldsymbol{N}\cdot J_s dx^3)$ is calculated by the three numerical line integration, two in the cross section and one in the flowing direction. We know the current continuity is guaranteed in this formulation. This formulation is also independent on mesh division.

3.5 Sensitivity analysis

The gradient is derived from the solution to two forward problems: an ordinary and an "adjoint" problem. In contrast, a finite difference computation of the gradient requires the solution of multiple forward problems, one for each unknown parameter used in modelling the perturbed region. The general formulation is equation (3.15) and we use this equation for our forward problem formulations in this thesis. The general form of the sensitivity formula is

$$S = \frac{\partial V_{ij}}{\partial \sigma_k} = -\frac{1}{I_i I_j}\int_{\Omega_{ek}} (\boldsymbol{E}_i \cdot \boldsymbol{E}_j) dx^3 \tag{3.32}$$

Equation (3.32) gives the sensitivity of the induced voltage in pairs of coils labelled as $i,\ j$ with respect to an element and Ω_{ek} is the volume of element number k and I_i and I_j are excitation current for coils. Here $\boldsymbol{E}_i$ and $\boldsymbol{E}_j$ are the electric field intensity resulting from the forward solution when coil i and j are excited respectively.

3.5.1 Sensitivity for $\boldsymbol{A}, \boldsymbol{A}-V$ formulation

With the $\boldsymbol{A}, \boldsymbol{A}-V$ formulation and using edge FEM, the sensitivity to a change in the conductivity of the conducting region can be calculated using an adjoint field method as derived in this chapter and discussed in [42], [70], [69] where the integral becomes the inner product of $\boldsymbol{E}$ fields and the Jacobian can be calculated by performing this integration for a chosen basis for the conductivity perturbation $\delta\sigma$. Using the shape function of edge elements $\boldsymbol{N}_e$ and nodal elements of ϕ_e, the electric field $\boldsymbol{E}$ inside each element can be expressed as follows

$$\boldsymbol{E} = \boldsymbol{N}_e \boldsymbol{A}_e + \nabla\phi_e V_e \tag{3.33}$$

where $\boldsymbol{A}_e$ are defined along the edges, and V_e is calculated electric potential for the nodes. Then the sensitivity term for each element is as follows

$$S = \frac{\partial V_{ij}}{\partial \sigma_k} = -\frac{\omega^2}{I_i I_j} \int_{\Omega_{ek}} (\boldsymbol{A}_e^i \boldsymbol{N}_e + V_e^i \nabla\phi_e) \cdot (\boldsymbol{N}_e \boldsymbol{A}_e^j + \nabla\nabla\phi_e V_e^j)^T dx^3 \tag{3.34}$$

In the edge FEM software implemented here, one can calculate $\boldsymbol{A}$ in all elements by (3.33) where $\boldsymbol{N}_e$ is a matrix of shape functions for all elements and $\boldsymbol{A}_e$ is a vector of the solution of the forward problem. One can use equation (3.34) simply for the region Ω_f that includes more than one finite element. Then the computation of the Jacobian matrix is a matrix vector multiplication for each measurement. In the software package developed for this study, one can define all components of the Jacobian matrix for the anisotropic material properties. The forward problem and the sensitivity formula is based on a general complex admittivity, but for the inverse problem, we are concentrating in conductivity imaging. However extension of the inverse formulation to a complex admittivity problem is trivial.

The sensitivity plot changes with the background conductivity [143]. For example, if a conductive object is introduced into the space the sensitivity in the surface layers of the object increases due to the circulation of the eddy current. The sensitivity also depends on the geometrical configuration of the sensing and exciting coils. For example using a single frequency and fixed shape of the conductive object, for high conductivity the higher eddy current density region is very small and regions close to the boundary of the object have higher sensitivity. When the conductivity decreases the area of high sensitivity spreads toward the centre of the object. Finally, when the conductivity goes to zero the more sensitive area is no longer effected by the conductive background shape and it is only effected by the geometrical configuration of the sensing and exciting coils.

Figure 3.13 shows the sensitivity map for two opposite coils, two coils are placed in $(0, 0.08)m$ and $(0, -0.08)m$ and the background is a homogeneous cylindrical object with conductivity $0.8Sm^{-1}$ and length and diameter of 0.14 m placed in the centre of the coil ring. Figure 3.14 shows a 3D sensitivity map. Figure 3.15 shows the sensitivity map for two coils in 90 degree, and figure 3.16 is the sensitivity map between coil 5 and coils (8,1,2) as a gradiameter.

3.5.2 Sensitivity for $\boldsymbol{A}, \boldsymbol{A}$ formulation

With the $\boldsymbol{A}, \boldsymbol{A}$ formulation and using the edge FEM, the sensitivity to a change in the conductivity of the conducting area can be calculated using the dot product of the electric fields [83], given $\boldsymbol{E} = -i\omega\boldsymbol{A}$ where the integral becomes the inner product of the $\boldsymbol{E}$ fields and the Jacobian can be calculated by performing this integration for a chosen basis for the conductivity perturbation $\delta\sigma$. Using the shape function with edge

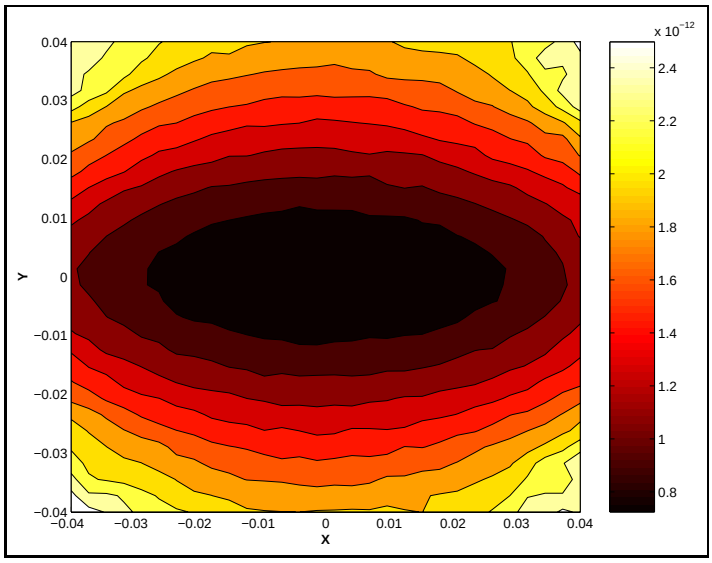

Figure 3.13: Sensitivity plot for two opposite coils for unit current density in excitation coil, the sensitivity values are in VmS^{-1}

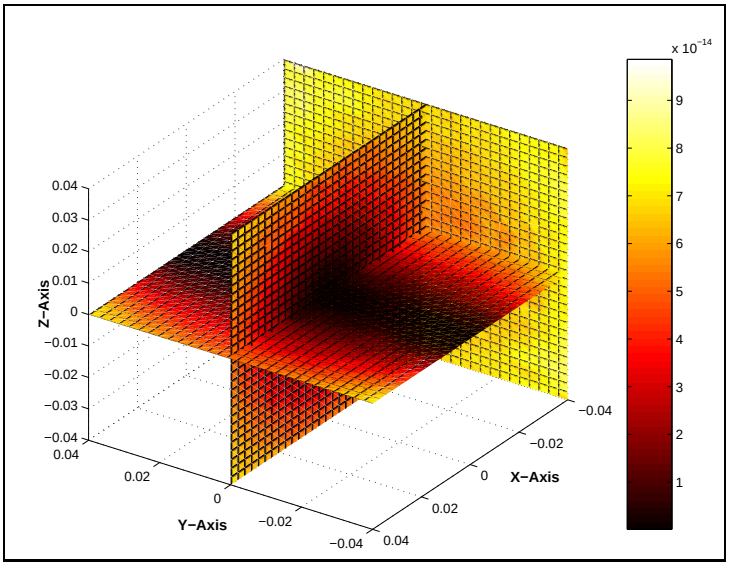

Figure 3.14: Sensitivity plot for two opposite coils in 3D for unit current density in excitation coil, the sensitivity values are in VmS^{-1}

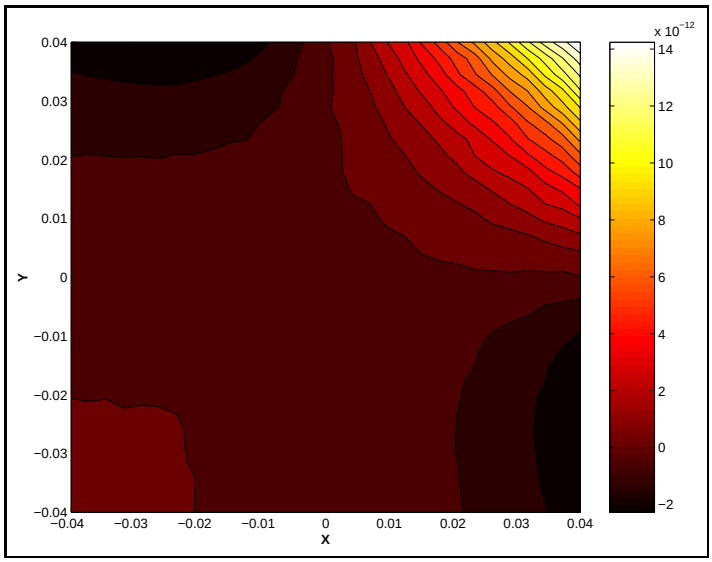

Figure 3.15: Sensitivity plot for two coils at 90 degrees for unit current density in excitation coil, the sensitivity values are in VmS^{-1}

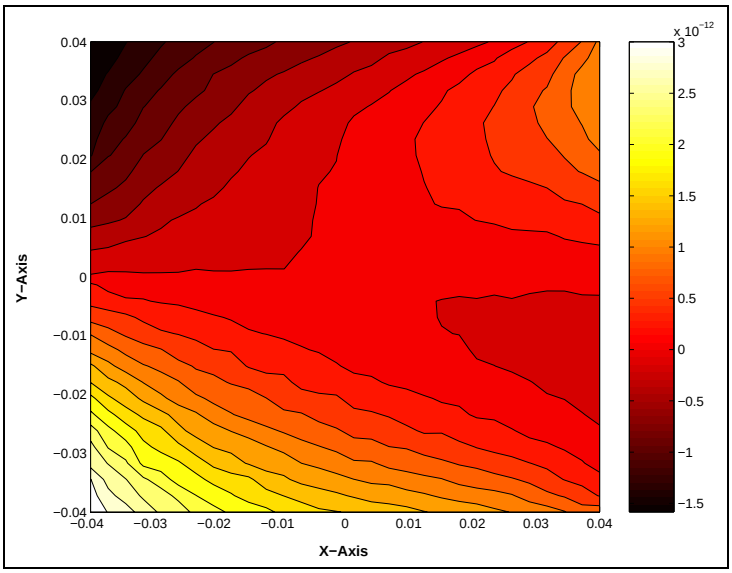

Figure 3.16: Sensitivity plot for gradiameter for unit current density in excitation coil, the sensitivity values are in VmS^{-1}

elements $\boldsymbol{N}_e$, the potential $\boldsymbol{A}$ inside each element

$$\boldsymbol{A} = \boldsymbol{N}_e \cdot \boldsymbol{A}_e \tag{3.35}$$

where $\boldsymbol{A}_e$ are defined along edges. The sensitivity term for each element is

$$S = \frac{\partial V_{ij}}{\partial \sigma_k} = -\frac{\omega^2}{I_i I_j} \boldsymbol{A}_e^i \left(\int_{\Omega_{ek}} (\boldsymbol{N}_e \cdot \boldsymbol{N}_e^T) dx^3 \right) (\boldsymbol{A}_e^j)^T \tag{3.36}$$

The sensitivity calculated in (3.34) or (3.36) is a complex number $S = S_r + iS_i$ and S_r, S_i which are real and imaginary parts of the sensitivity term. These terms represent the change in V_r, V_i, i.e. real and imaginary part of the measurement voltage $V = V_r + iV_i$. Some industrial MIT measurement systems [11] measure the amplitude of the induced voltage $|V|$. The sensitivity term with respect to the amplitude then is calculated as follow

$$S_{amp} = \frac{V_r S_r + V_i S_i}{|V|} \tag{3.37}$$

Some medical MIT measurement systems [78] measure the phase . The sensitivity term with respect to the phase is calculated as follows

$$S_{phase} = \frac{V_r S_i - V_i S_r}{|V|^2}. \tag{3.38}$$

The sensitivity plot changes with the background conductivity [143]. For example, if a conductive object is introduced into the space the sensitivity in the surface layers of the object increases due to the circulation of the eddy current. The sensitivity also depends on the geometrical configuration of the sensing and exciting coils. For example using a single frequency and fixed shape of the conductive object, for high conductivity the higher eddy current density region is very small and regions close to

the boundary of the object have higher sensitivity. When the conductivity decreases the area of high sensitivity spreads toward the centre of the object. Finally, when the conductivity goes to zero the more sensitive area is no longer effected by the conductive background shape and it is only effected by the geometrical configuration of the sensing and exciting coils.

Figure 3.17 shows the sensitivity map for two opposite coils, two coils are placed in $(0, 0.08)$ m and $(0, -0.08)$ m and the background is a homogenous cylindrical object with conductivity $5.8 \times 10^7 Sm^{-1}$ and length and diameter of 0.038 m placed in centre of coil ring. Figure 3.18 shows the sensitivity map for two coils with 90 degree, two coils are centred at $(0, 0.08)$ m and $(0.08, 0)$ m and the background is a homogenous cylindrical object with conductivity $5.8 \times 10^7 Sm^{-1}$ and length and diameter of 0.038 m placed in centre of coil ring.

3.5.3 Jacobian matrix

The Jacobian matrix is assembled in a way that each row of it is the calculated sensitivity term for an element for all measurements. Figure 3.19 shows the distribution of the singular values of the real and imaginary part of the Jacobian matrix. In a noise and error free situation it is possible to reconstruct an image with up to 28 parameters. In real data and with measurement errors according to the Discrete Picard criteria some of the small singular values may not be able to contribute to the image reconstruction. It is worth noticing that some of these small singular values may represent important and desirable part of the images which may not be reconstructed due to noise and error in the measurement.

To illustrate the degree of ill conditioning in the problem the singular values are plotted

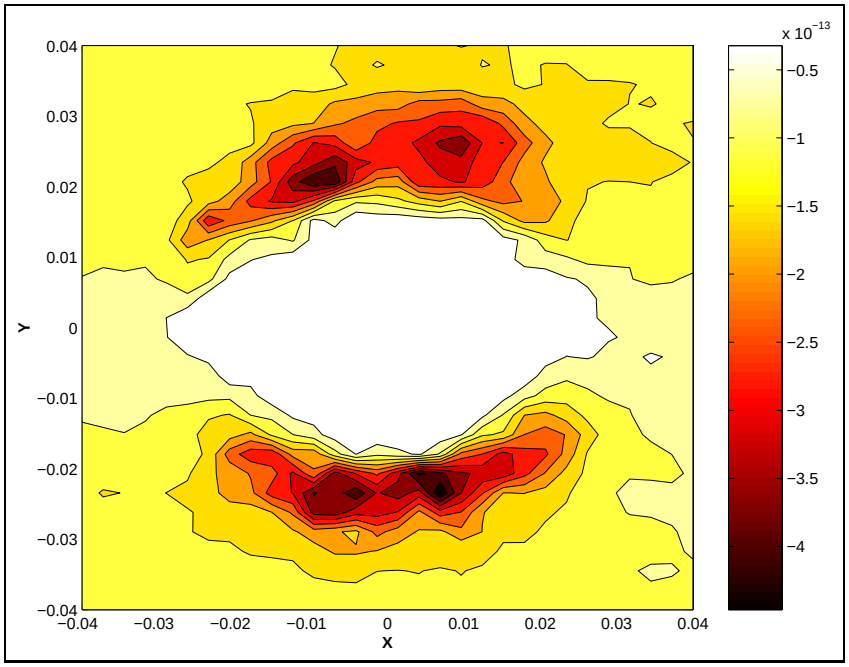

Figure 3.17: Sensitivity plot for two opposite coils for the imaginary part of the induced voltage for unit current density in excitation coil, the sensitivity values are in VmS^{-1}

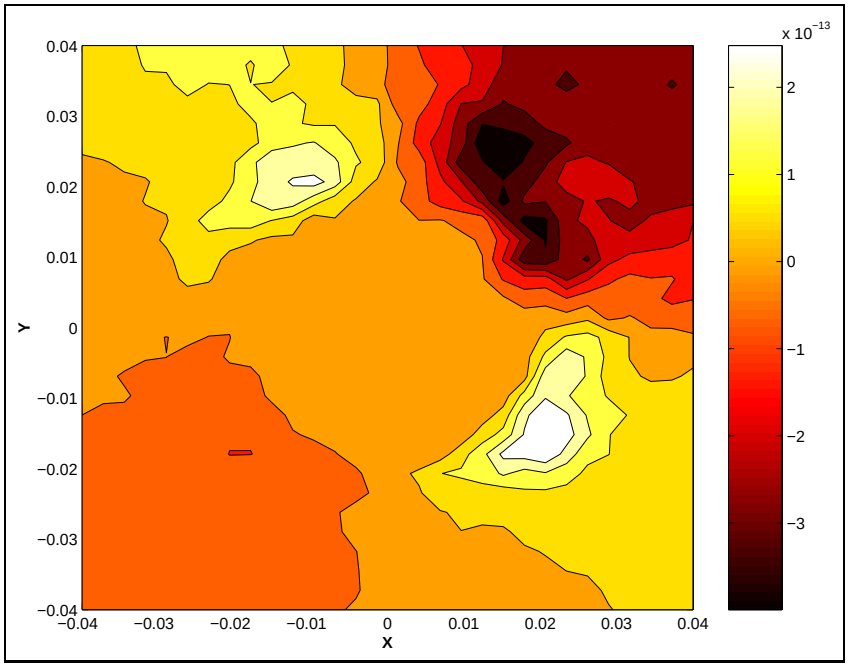

Figure 3.18: Sensitivity plot (imaginary part of the induced voltage) with for two coils at 90 degrees for unit current density in excitation coil, the sensitivity values are in VmS^{-1}

on the log scale (figure 3.19). The roughly linear decay of the first 28 singular values shows that the problem is ill-posed. Here the background conductivity is the cylinder C1 with homogeneous conductivity of 4 Sm^{-1} and frequency is 1MHz. In medical MIT the in-phase component, of the received signal contains are used to reconstruct conductivity of the tissue [163]. The quality of imaging depends on the precision with which real part can be measured. In figure 3.19 one can see that using the imaginary part of receiving signal (with this particular conductivity and frequency) the inverse problem is actually better posed than using the real part. In practical terms measuring the imaginary part (detecting a very small signal due to the conductive object is a very large primary signal) is very difficult task for medical MIT application.

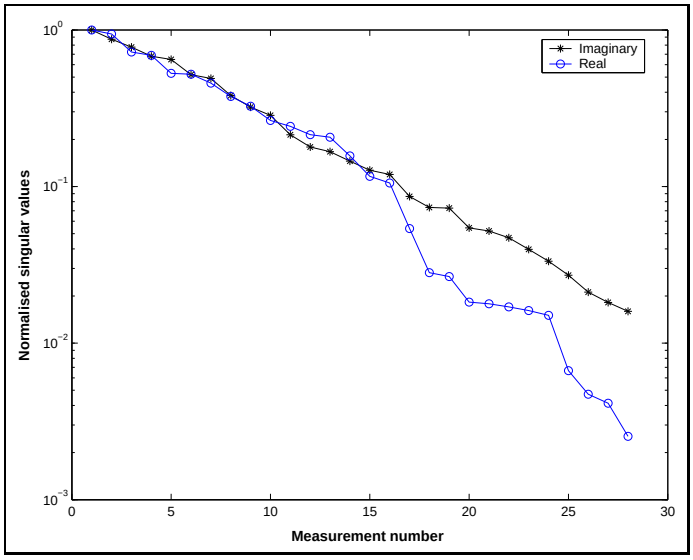

Figure 3.19: Singular values of the Jacobian matrix ($\boldsymbol{J}$) for the real and imaginary part of the measurement voltages on a logarithmic base (background is C1 with conductivity 4 Sm^{-1} and frequency 1 MHz).

Figure 3.20 shows the sensitivity map for background C1 with conductivity 5.8×10^7 Sm^{-1} and frequency 5 kHz. This figure shows that using real part or imaginary part to reconstruct conductivity is more ill-posed that the problem of figure 3.19, but the

ill-posedness of the real part and imaginary part data is similar.

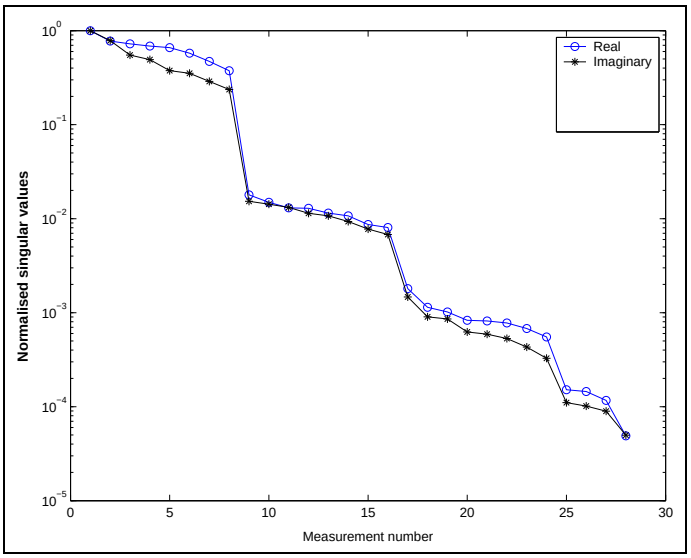

Figure 3.20: Singular values of the Jacobian matrix (***J***) for the real and imaginary part of the measurement voltages on a logarithmic base (background is C1 with conductivity $5.8 \times 10^7\ Sm^{-1}$ and frequency 5 kHz).

3.6 Inverse problem

The image reconstruction is to find the distribution of electrical conductivity σ within the region of interest using the knowledge of all 28 induced voltage measurements. This can be done using iterative schemes based on optimization methods. We implemented an optimization algorithm that finds a distribution for σ to minimize equation

$$\| V_m - F(\sigma) \|^2 + R(\sigma) \tag{3.39}$$

where $R(\sigma)$ is the penalty term and can be implemented in discrete form using a regularization matrix. Where the descent direction of σ can be found using the Tikhonov

Gauss-Newton method

$$\delta\boldsymbol{\sigma}_{n+1} = \left(\boldsymbol{J}_n^T\boldsymbol{J}_n + \alpha^2\boldsymbol{R}^T\boldsymbol{R}\right)^{-1}\boldsymbol{J}_n^T\left(\left(\boldsymbol{V}_m - \boldsymbol{F}\left(\boldsymbol{\sigma}_n\right)\right) - \alpha^2\boldsymbol{R}^T\boldsymbol{R}\boldsymbol{\sigma}_n\right) \tag{3.40}$$

For $n = 1$ this is a linear reconstruction algorithm. Here $\boldsymbol{J}_n$ is the Jacobian calculated with the conductivity $\boldsymbol{\sigma}_n$, $\boldsymbol{V}_m$ is the vector of voltage measurements and the forward solution $\boldsymbol{F}\left(\boldsymbol{\sigma}_n\right)$ is the predicted voltage from the forward model with conductivity σ_n. The matrix $\boldsymbol{R}$ is a regularization matrix which penalizes extreme changes in conductivity removing the instability in the reconstruction, at the cost of producing artificially smooth images. Here $\boldsymbol{R}$ is a matrix, typically a difference operator between neighboring voxels. We take $\boldsymbol{R}$ as first order Laplacian operator in discrete form approximated by finite difference. Here $\boldsymbol{R}(i,j) = -1$ for $i \neq j$ when two elements are neighbors (sharing at least one node) and $\boldsymbol{R}(i,i) = -\Sigma_j\boldsymbol{R}(i,j),\ i \neq j$.

This effect can be seen in figure 3.21 where the eigenvalues have been clustered when the Tikhonov regularization matrix is applied to formulate a smoothness assumption to the conductivity map.

The other type of regularization is total variation (TV) regularization. Using TV regularization one can improve the reconstruction of blocky images and sharp edges [17]. A more practical study of TV will be given in chapter 6, here we mention the implementation of TV regularization in our 3D tetrahedral mesh for completeness. TV regularization matrix can be implemented as follows. Let the area of each facet i between two voxels be $q_i, i = 1,2,..,I$. The k-th row of the matrix $\boldsymbol{S} \in \mathbb{R}^{I\times P}$ (here I is number of facets and P is number of tetrahedral elements) is chosen to be $\boldsymbol{S}_k = [0,...0,1,...,-1,0,...,0]$, where 1 and -1 occur in the columns related to the elements with common facet k. Each row of $\boldsymbol{S}_k$ then weighted with area q_k of the facet k, where $\boldsymbol{T}V = \boldsymbol{S}^T\boldsymbol{Q}\boldsymbol{S}$ is the total variation regularization matrix and $\boldsymbol{Q}$ is a diagonal

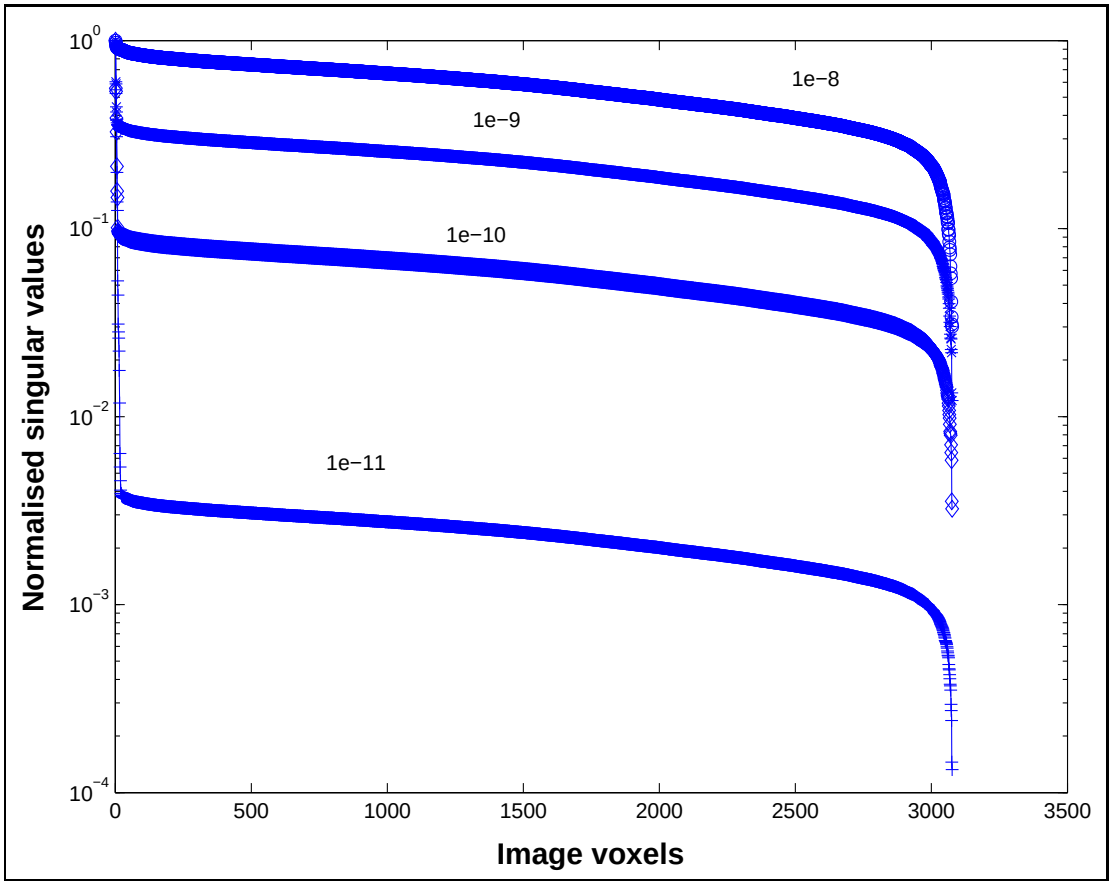

Figure 3.21: Singular value distribution for $\boldsymbol{J}^T\boldsymbol{J} + \alpha^2\boldsymbol{R}^T\boldsymbol{R}$ for cylinder C1 for different regularization parameters (different values for α^2)

matrix with $\boldsymbol{Q}(k,k) = q_k$.

As an iterative reconstruction algorithm, the regularized Gauss-Newton method starts with an initial conductivity distribution $\boldsymbol{\sigma}_0$. The forward problem is solved and the predicted voltages compared with the calculated voltages from the forward model. The conductivity is then updated using (3.40). The process is repeated until the predicted voltages from the FEM agree with the calculated voltages from the finite element model to measurement precision. In the non-linear steps, the Jacobian matrix is also updated in each step.

3.6.1 Low conductivity contrast

In order to evaluate the quantitative reconstruction we considered a simple inverse problem example. In this example the MIT system works in frequency 0.1 MHz and the true and reconstructed conductivity can be seen in figure 3.22 for noise free data. The number of unknowns are smaller than number of independent measurements, so as expected the inverse solver can reconstruct all 20 values with a reasonable accuracy with exact data. When we add two percent noise the reconstruction results are shown in figure 3.23.

In all remaining reconstruction examples with low contrast conductivity the frequency is 1 MHz, the relative permeability is 1, the relative permittivity is 100, and the measurement data is the simulated real part of the induced voltage. In all cases an additional Gaussian noise of 2 percent was added to the simulated data. The simulated data was generated using a fine mesh of 208000 tetrahedral elements.

Figure 3.24 shows a simple example, reconstruction of a spherical background with conductivity $1Sm^{-1}$ and a spherical inclusion with conductivity $2Sm^{-1}$. In all MIT im-

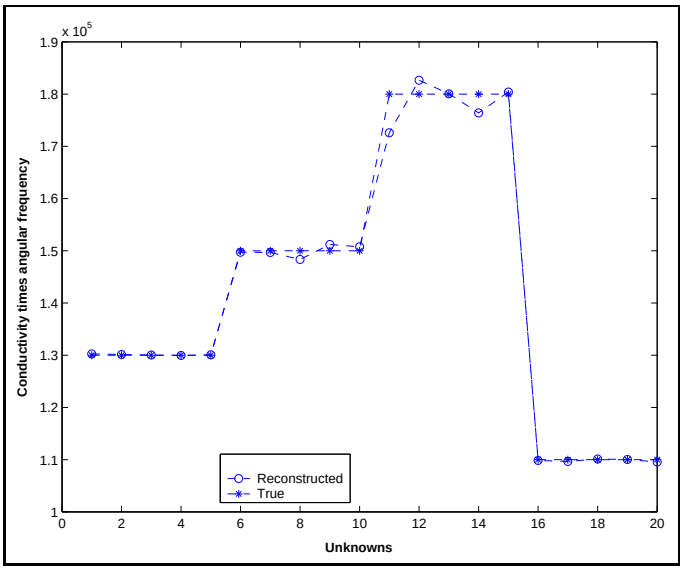

Figure 3.22: Reconstruction of 20 unknowns using noise free data

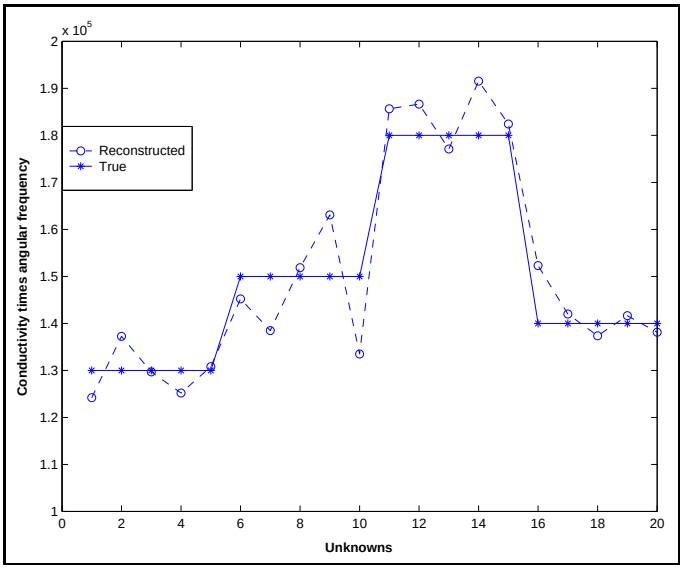

Figure 3.23: Reconstruction of 20 unknowns using with 2 percent noise

ages presented in this chapter we omit the colorbar as we did not recover the absolute conductivity values.

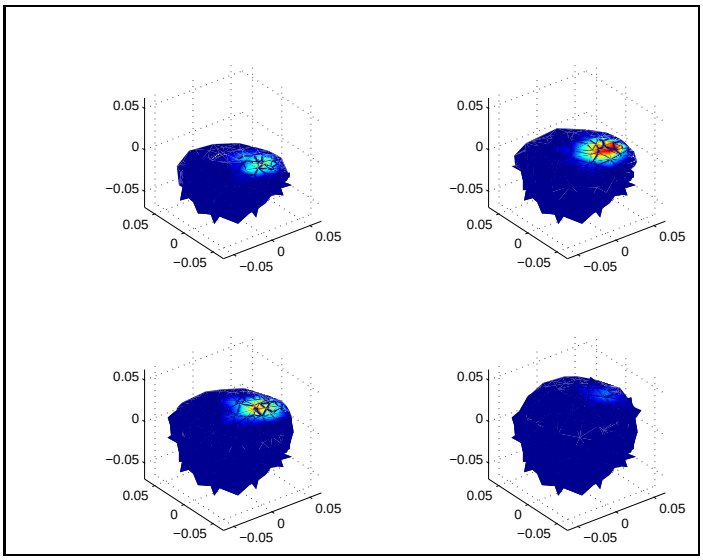

Figure 3.24: Reconstruction of one inclusion in a spherical background in different Z level

Figure 3.25 shows a conductivity distribution of a ring shape. The background has conductivity $1Sm^{-1}$ and the ring has conductivity $5.8Sm^{-1}$. We added 1 percent Gaussian noise to the simulation data generated by the phantom of figure 3.25. The reconstructed image is shown in figure 3.26. The convergence plot of the nonlinear inverse solver and the voltage differences is shown in figure 3.27. The reduction of the voltage differences during the iteration down to the noise level is shown in figure 3.28. The maximum value of the reconstructed conductivity of figure 3.26 is $5.6Sm^{-1}$ which is not exactly the expected value, because of the presence of noise. The mesh for the inverse problem had 80600 elements and the region of interest for imaging in the cylindrical background includes 3760 elements.

Figure 3.29 shows a conductivity distribution with background conductivity $0.8Sm^{-1}$ and four cylindrical inclusions with conductivity $4Sm^{-1}$. The reconstructed image in

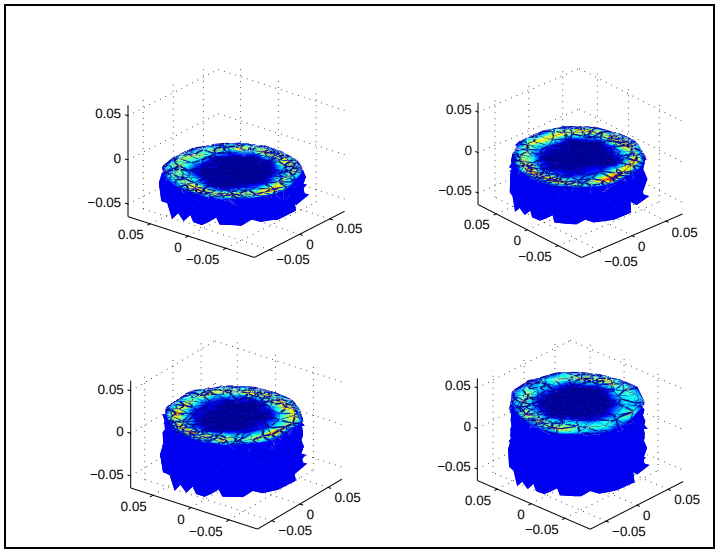
0.05
0
−0.05
0.05
0
−0.05
0.05
0
−0.05

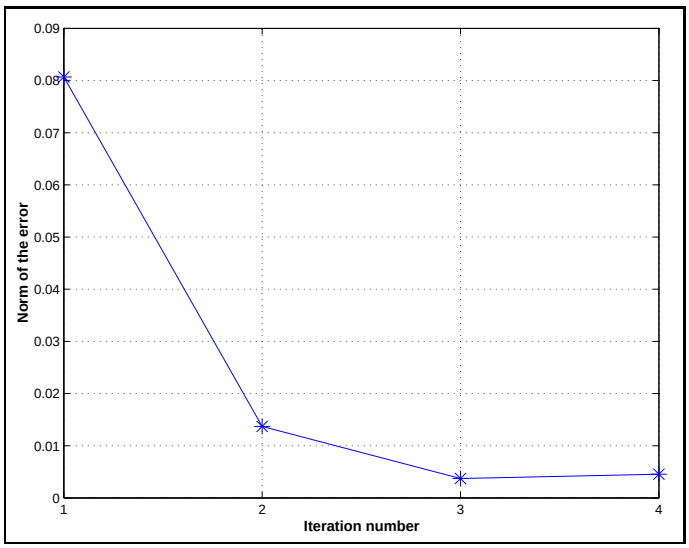

Figure 3.27: Convergence plot, shows the norm of the differences between measured and simulated voltages. Measurement and simulated voltages are normalized with respect to simulated voltage of the free space.

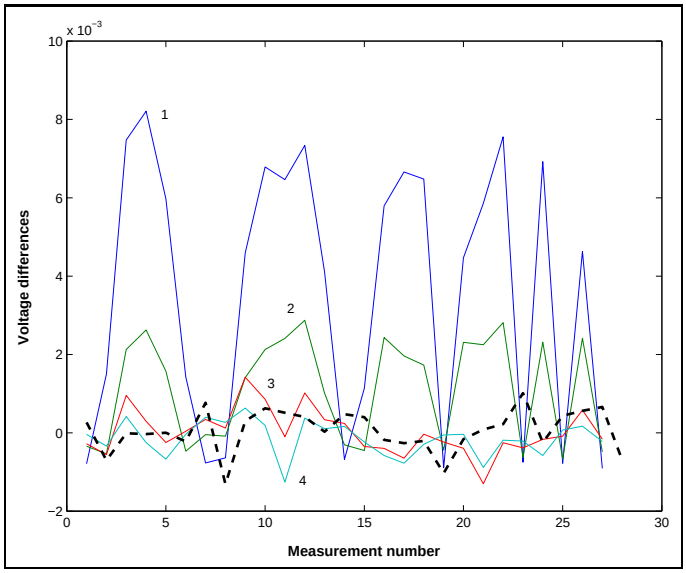

Figure 3.28: Voltage differences (normalized) for 28 measurements for 4 iterations, dashed line shows the added noise

figure 3.30 was performed with 5 iteration steps.

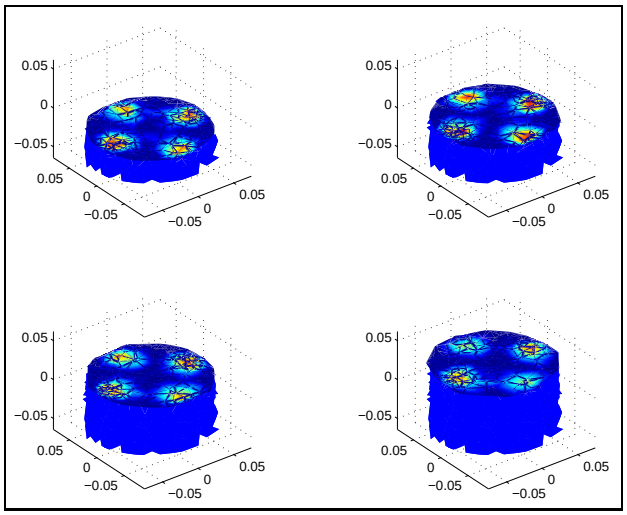

Figure 3.29: True conductivity distribution for four inclusions in different Z level

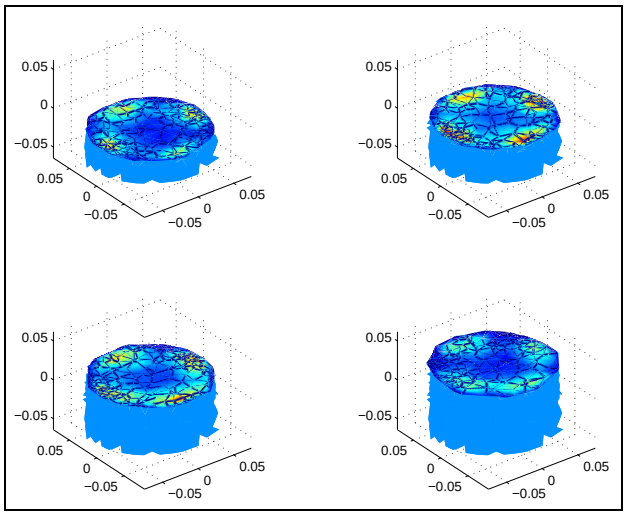

Figure 3.30: Reconstruction of the conductivity distribution of figure 3.29 in different Z levels

Importantly it was not possible to reconstruct an annular object, meaning inserting a conductive cylinder placed at centre of figure 3.25 and with diameter 0.03 m with conductivity of $10Sm^{-1}$. The reconstructed image is more or less is the same as figure 3.26, which means we could not detect the central object. The initial guess was the

homogeneous conductivity of $1Sm^{-1}$ and the external ring was reconstructed in few iterations, and central region's conductivity remains as an initial guess. The sensitivity map here for a ring is shown in figure 3.31 showing very small sensitivity value in the central region, this could be one reason for the failure to detect a central object within an annular object.

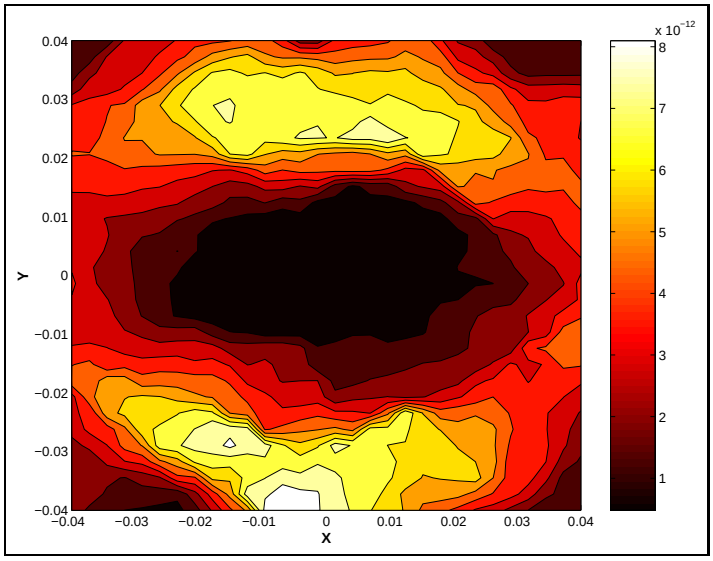

Figure 3.31: The sensitivity map for two opposite coils from the background conductivity distribution of figure 3.25

To further show the dependence of the shape of the sensitivity map to the background we insert four cylinders with diameter 0.04 m and length 0.14 m placed at (0.05,0) m, (-0.05,0) m, (0,0.05) m, (0,-0.05) m and conductivity of $4Sm^{-1}$ to the previous homogeneous cylinder (0.14 m diameter and 0.14 m length and conductivity $0.8Sm^{-1}$ and the centre in (0,0)). Figure 3.29 shows the conductivity background including four higher conductive objects. The change in the sensitivity map can be seen in figure 3.33. This shows that the sensitivity map changes with the conductivity background, as the distribution of eddy currents changes with the background. Figure 3.32 shows the real part of the eddy current for the conductivity background of figure 3.29 when

the excitation is coil 1. After a few iterations 4 objects in corners were reconstructed, the sensitivity value given the position of 4 corner has a higher value in centre, so the central object could be reconstructed in this example.

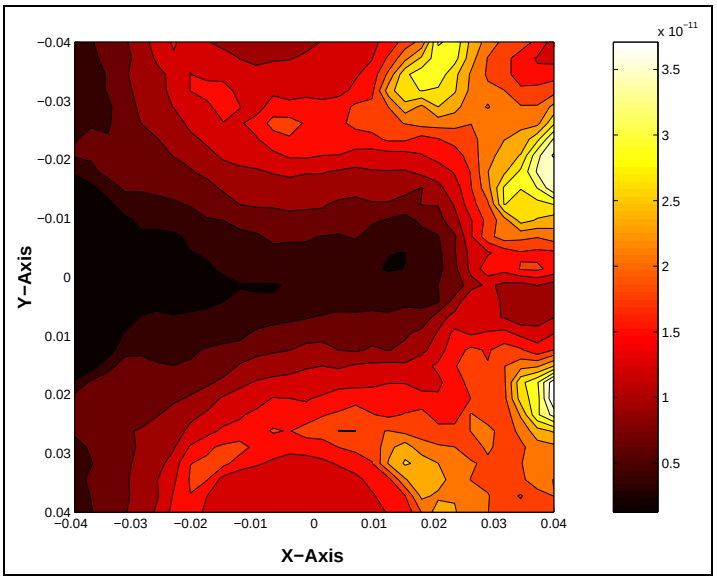

Figure 3.32: The real part of eddy current for coil 1 with conductivity distribution of figure 3.29

Figure 3.29 shows a conductivity distribution with background conductivity $0.8Sm^{-1}$ and five cylindrical inclusions including one in the centre with conductivity $4Sm^{-1}$. The reconstructed image in figure 3.30 was performed with 7 iteration steps. As we have seen from the sensitivity plot of figure 3.17, detecting an object in the centre is more complicated because the sensitivity is very low in the centre of a conductive background. But in this particular example four higher conductive objects in the corners cause an improvement of the sensitivity map of the centre as shown in figure 3.33. So that the trace of the inclusion in the centre can be seen in the reconstructed image of figure 3.35. But in general it is hard to detect the inclusion(s) located inside a conductive background as the sensitivity analysis shows a smaller sensitivity in the central region of the conductive background for all coil combinations.

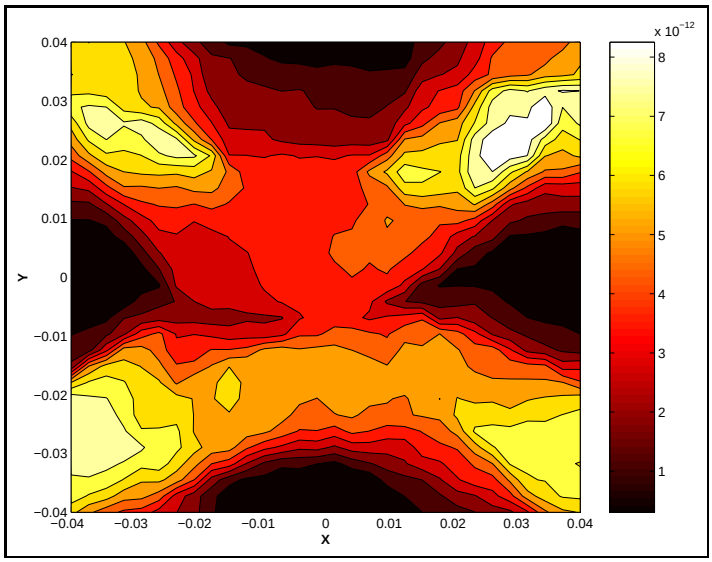

Figure 3.33: The sensitivity map for two opposite coils from the background conductivity distribution of figure 3.29

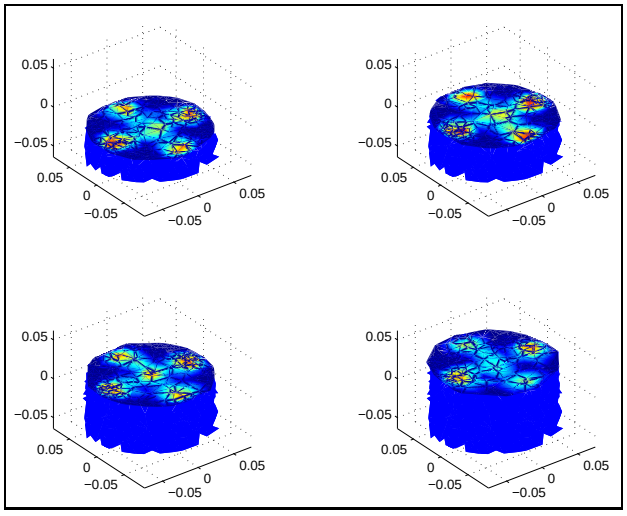

Figure 3.34: True conductivity distribution for five inclusions in different Z levels

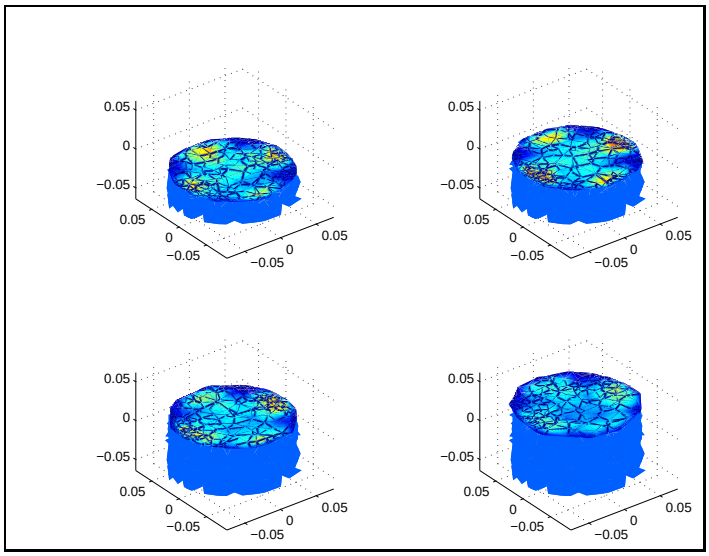

Figure 3.35: Reconstruction of the conductivity distribution of figure 3.34 in different Z levels

3.6.2 High contrast examples

Figure 3.36 shows a test problem, molten steel flow (with conductivity $2.1 \times 10^6 Sm^{-1}$) with a cross shape inside of a refractory nozzle with an inside diameter 0.14 m and length 0.14 m with conductivity $0\,Sm^{-1}$. The simulation data (28 measurement of the amplitude of the measurement voltages) has been generated using the distribution of figure 3.36 and the forward model with 315607 elements. Gaussian noise with a level of two percent of the mean value of the measurement voltages was added to the simulated measurement data. For image reconstruction we used a different mesh which has a total number of elements of 86400 and the number of the voxels in the region of interest for the imaging (the cylinder) are 3800. The initial guess for the image reconstruction was the cylinder full of molten steel. The reconstructed image is shown in figure 3.37. Figure 3.38 shows the norm of the differences between the measured and simulated voltages. The norm of error in figure 3.38 is a normalized value, and described by $\|(\boldsymbol{V}_m - \boldsymbol{F}(\boldsymbol{\sigma}))/\boldsymbol{V}_0\|$, where $\boldsymbol{V}_0$ is measurements voltage of

the free space.

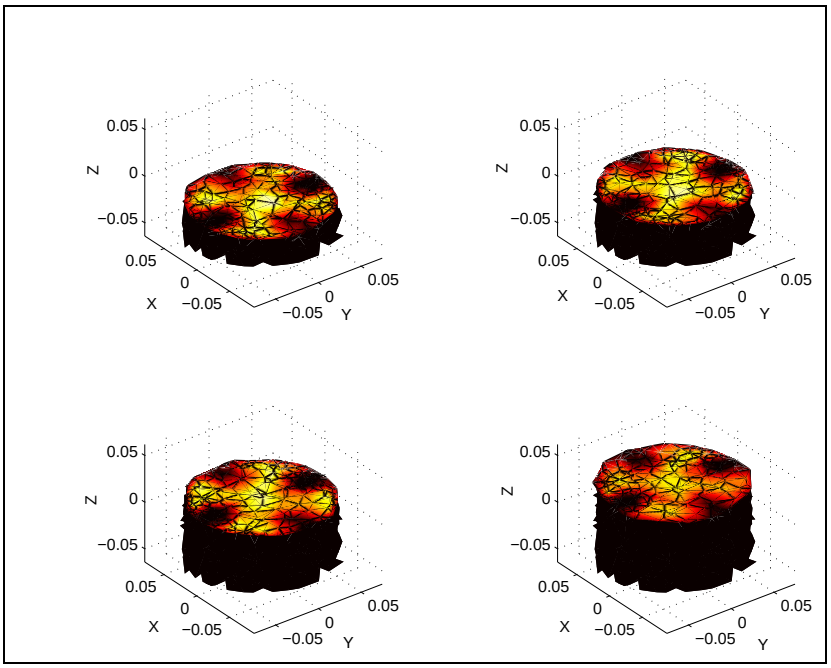

Figure 3.36: True steel flow in different Z levels

After 10 iterations the quality of the reconstructed image and the norm of the mismatch error did not improve significantly, as the difference between measured and simulated voltages are smaller than the noise. With smaller conductivity contrast such as medical MIT [100], the number of iterations to generate suitable image is less. One step could provide a satisfactory image for low contrast conductivity imaging of medical MIT. The next example is the reconstruction of three metal bars (with conductivity $2.1 \times 10^6 Sm^{-1}$) shown in figure 3.39, the reconstruction of these three bars can be seen in figure 3.40, using 6 nonlinear iterations. Again an additional 2 percent Gaussian noise was added to the simulation data, and the reconstruction results. Reconstruction of the shape of the metal flow and location of metal bars are good, but the reconstruction of the absolute conductivity values are not satisfactory. Further study is needed to improve the quantitative images. It is worth noticing that in reconstructed results as

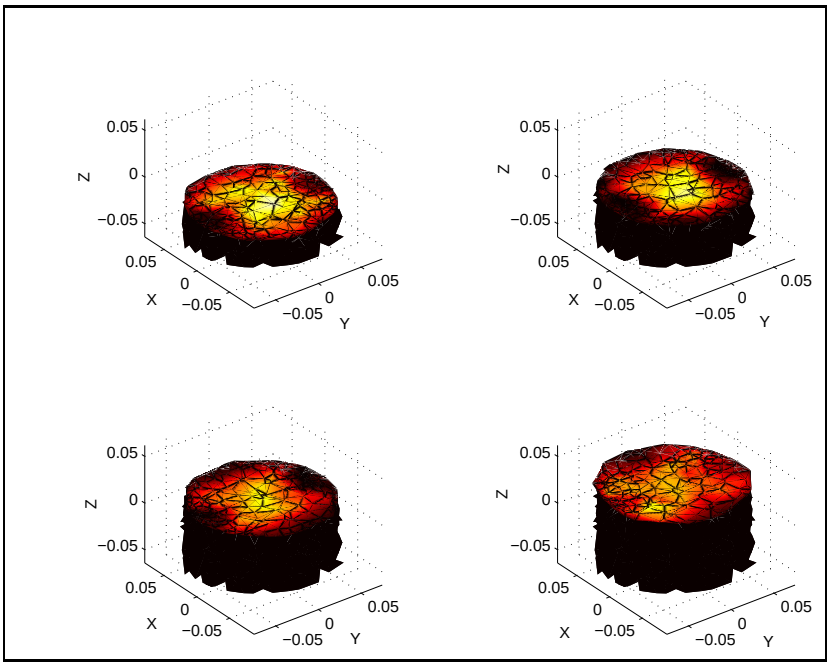

Figure 3.37: Reconstructed steel flow in different Z levels

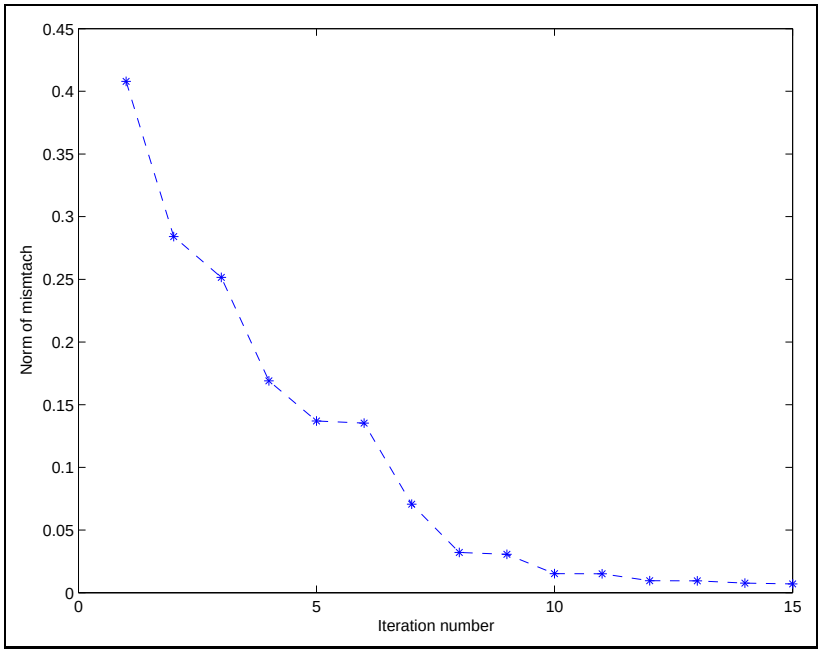

Figure 3.38: Norm of the error between the measured and simulated voltages (all voltages are normalized to the induced voltage from the free space)

expected the quality of the images on planes in the area of coils are much better than the planes further away, because the sensitivity reduces when we move away from the coil.

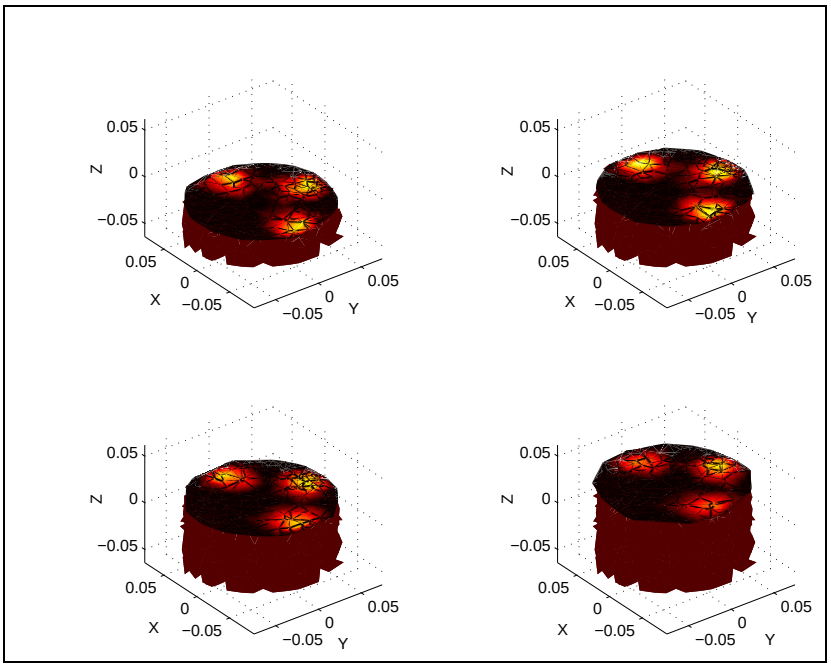

Figure 3.39: Three metal bars in different Z levels

3.6.3 Experimental results

Figure 3.41 shows a block diagram of the hardware for an MIT system, which consists of a sensor array, data acquisition unit and host computer. A new MIT system was designed and fabricated in Prof. A. J. Peyton's group in Lancaster University. The data acquisition unit houses the electronics required to sequence the a.c. excitation field, and acquire the secondary field values from the detector coils. The host computer controls the measurement process and implements the image reconstruction algorithm, which is the concern of this chapter. The system used in this study was developed in order to investigate the flow of liquid steel during continuous casting. Here the sensor

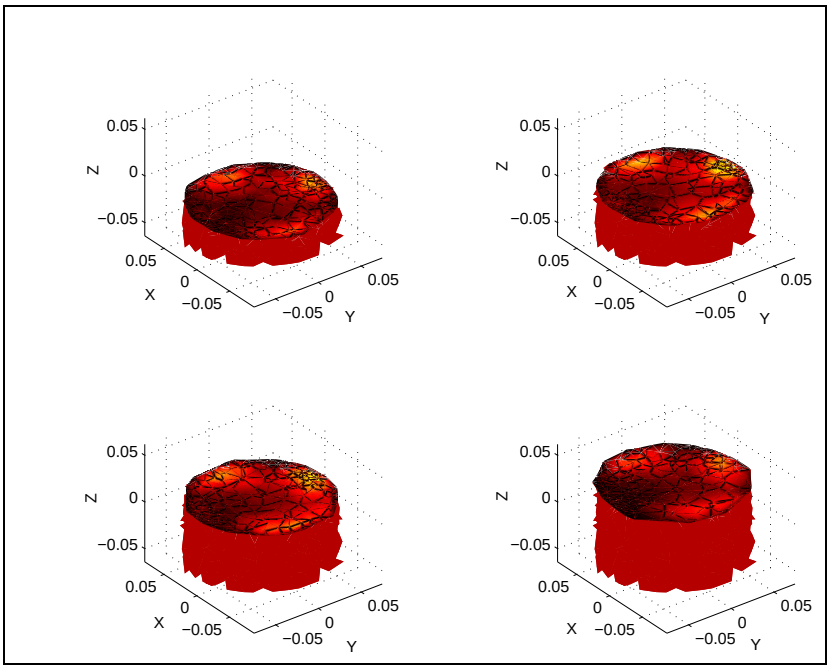

Figure 3.40: Reconstruction of three metal bars in different Z levels

array consisted of 8 coils as shown in figure 3.42, which were used both for excitation and detection. The geometrical information of the new MIT system is similar to the simulation model presented in figure 3.1. Each coil has 45 turns and with a 0.05 m outer and 0.04 m inner diameter and a length of 0.01 m. The coils are placed in a circular ring and the distance between two opposite coil was 0.16 m. The applied current was a 5 kHz sine wave.

The experimental results are shown for one, two, three and four metal bars inside of the region of interest. Figures 3.43 show a copper rod in centre with diameter 9 mm. This is about the minimum size can be detected by the current experimental system in a region of interest with diameter 160 mm. Figure 3.44 shows reconstruction of a copper and an aluminum rod diameter 12.5 mm each. Figure 3.45 shows the reconstruction of three copper bars with diameter 19 mm each. Figure 3.46 show the reconstruction of three copper bar, diameter 19mm each and an aluminum bar diameter 12.5 mm.

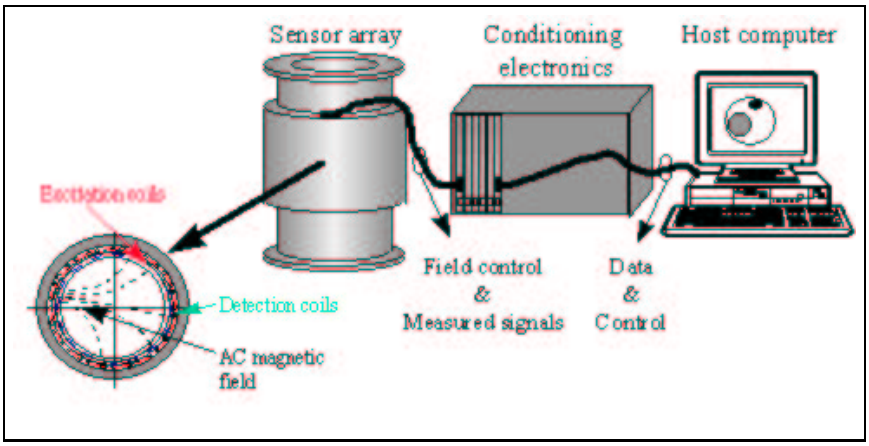

Figure 3.41: Block diagram of a the experimental MIT system (this image is from Prof. A.J. Peyton)

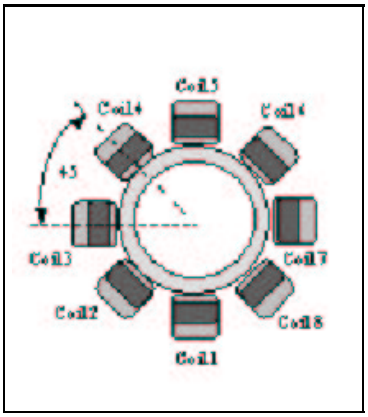

Figure 3.42: Coil arrangement in a MIT sensor array used in this study (this image is from Prof. A.J. Peyton)

Figure 3.47 shows reconstruction of a rectangular metal object in centre and dimension of $80mm \times 50mm$ cross section. Figure 3.48 shows reconstruction of a quarter of a cylinder (diameter 180 mm) of aluminum. Figure 3.49 shows reconstruction of copper tube, which is laminated with thin copper sheets.

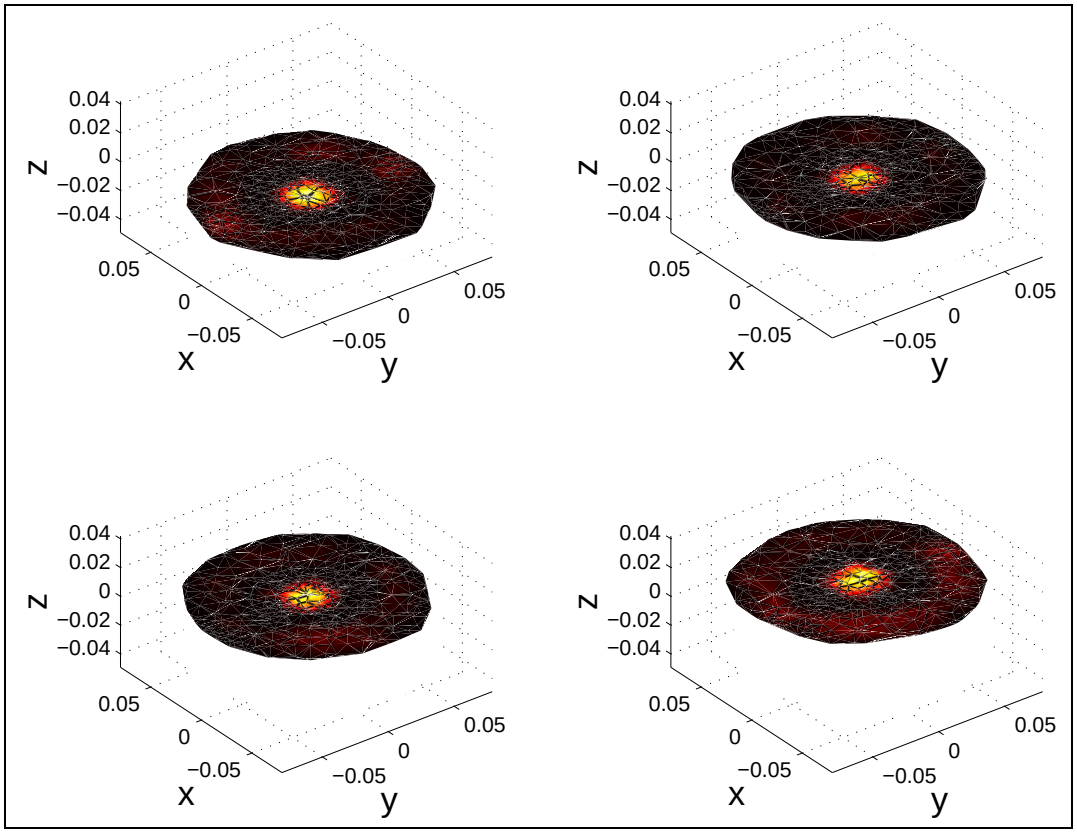

Figure 3.43: Reconstruction of one metal bars, a copper rod at centre with diameter 9mm in different Z level

Using Mayavi [128] for the visualization can improve the data presentation in 3D MIT. Here we present some examples of showing the MIT images using Mayavi. A Matlab function written by Borsic [14] to convert the image data generated from Matlab to a Visualization ToolKit (VTK) file used by Mayavi has been used here. In figure 3.50 reconstruction of a rectangular shape object is shown. An isosurface plot of the electrical conductivity from the rectangular shape object is shown in figure 3.51.

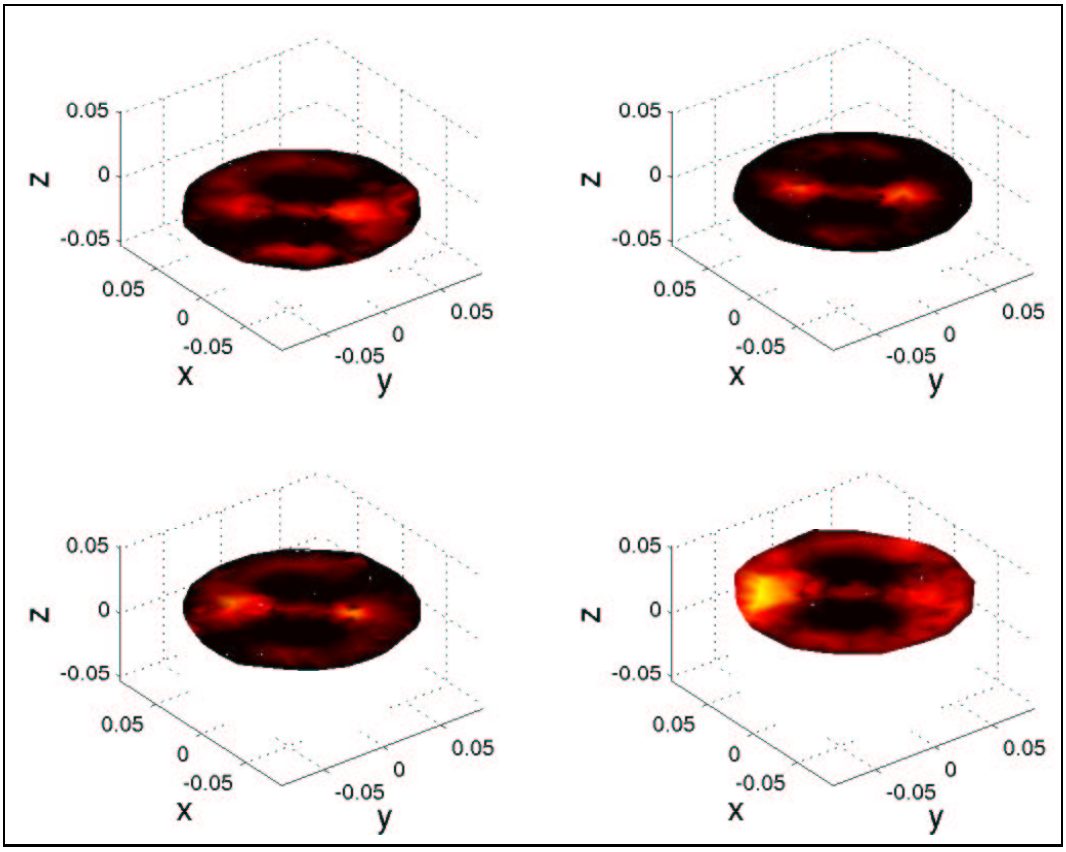

Figure 3.44: Reconstruction of two metal bars, a copper and aluminum bar with the same size in different Z level

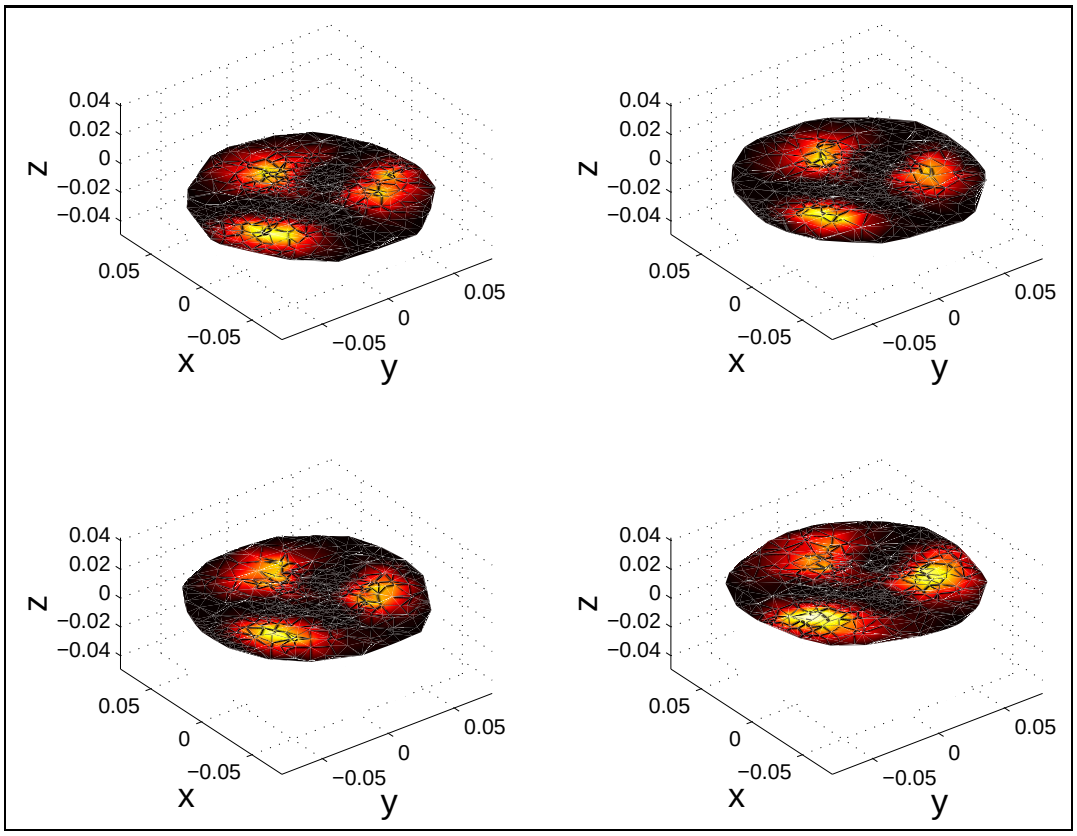

Figure 3.45: Reconstruction of three metal bars, three copper rods with the same size in different Z level

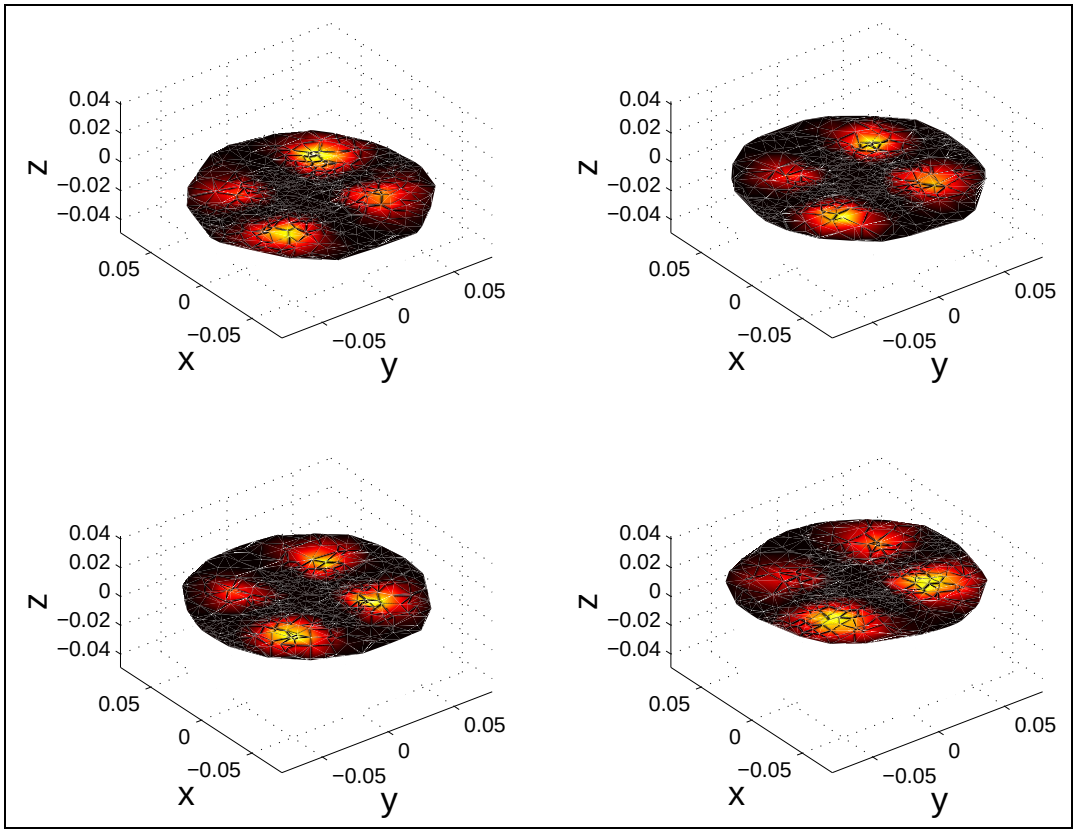

Figure 3.46: three copper rods and one aluminum rod in different Z level

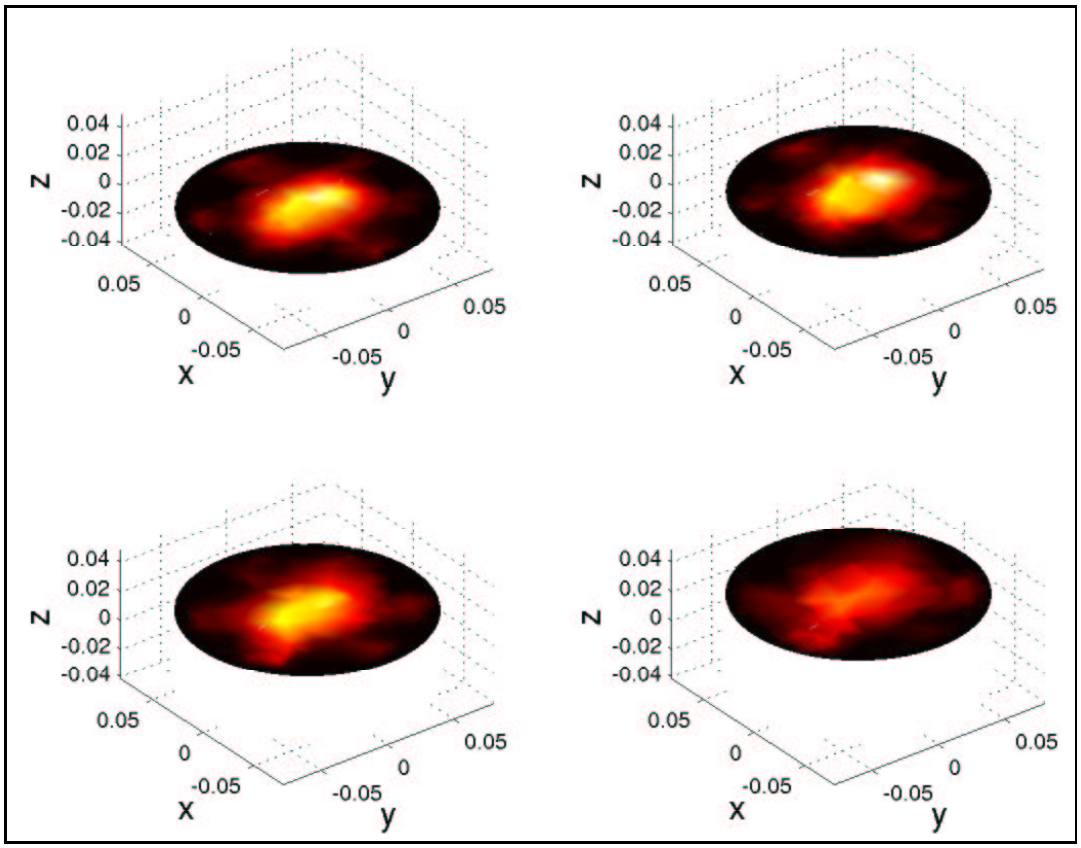

Figure 3.47: Reconstruction of a rectangular object in centre in different Z level

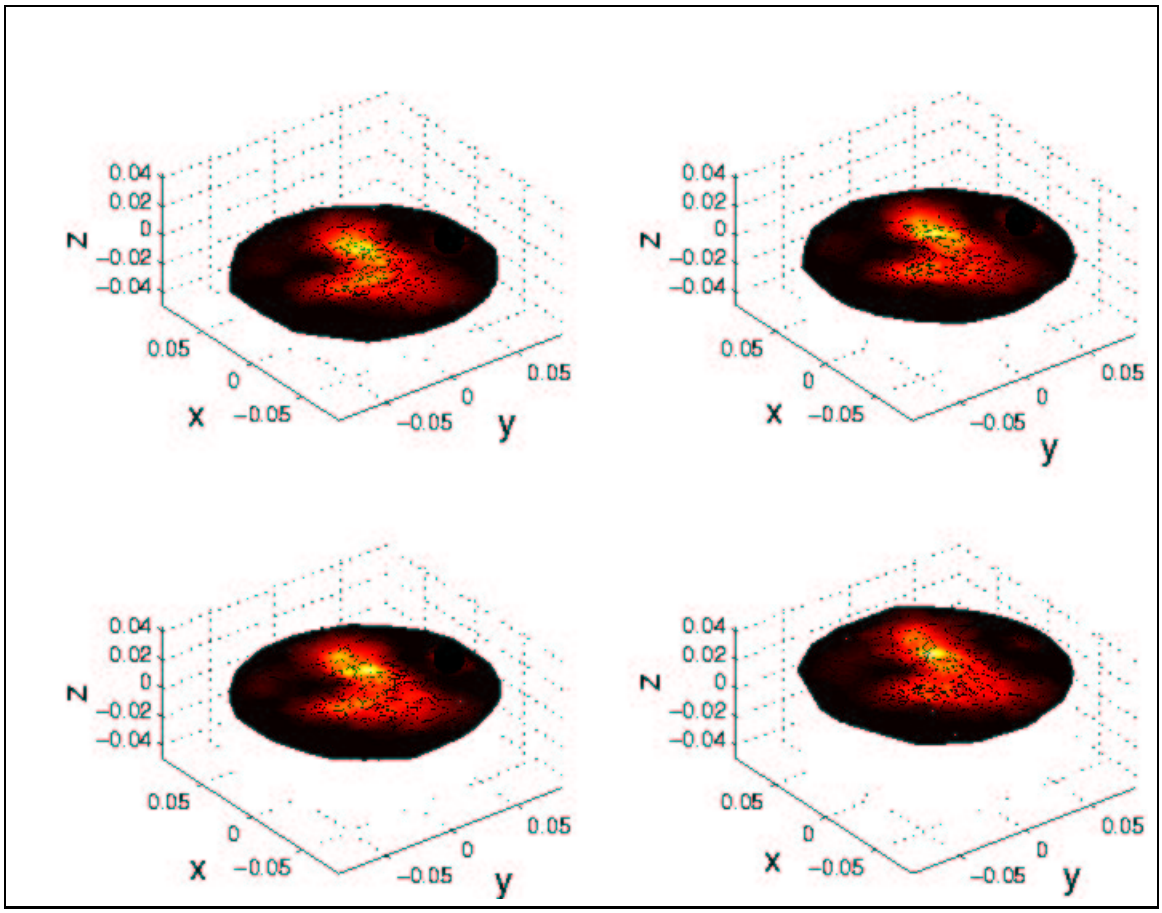

Figure 3.48: Reconstruction of a quarter of a metallic cylinder in different Z levels

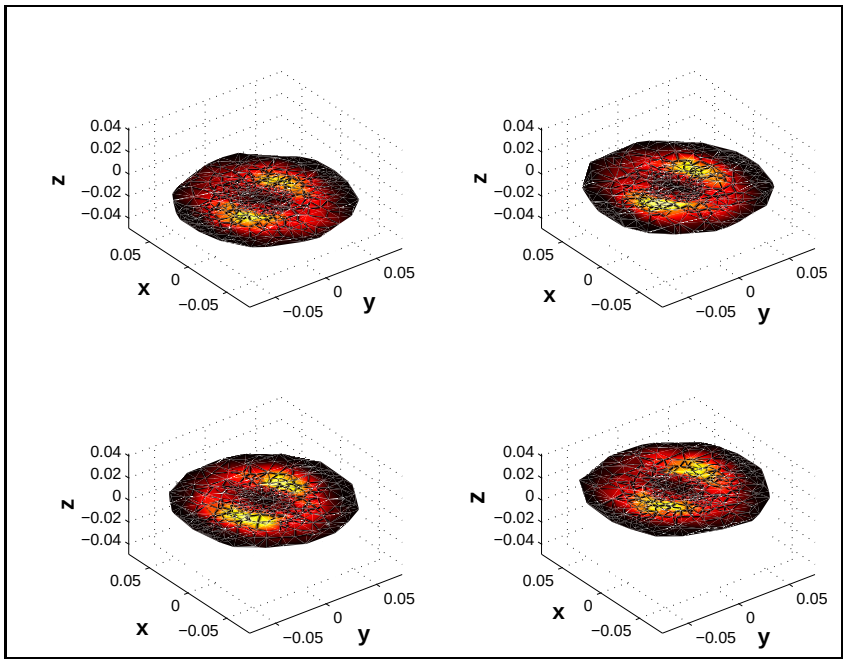

Figure 3.49: Reconstruction for a tube shape copper in different Z levels

Figure 3.52 shows 3D shape of four metal bars also presented in figure 3.46.

3.7 Applications of MIT

MIT has potential applications in fields such as medical imaging, nondestructive testing, environmental cleaning, geophysics. If there is a contrast or change in PEP of an object to be imaged, MIT potentially can be used as a static or dynamic imaging tool. In an ideal case with perfect accuracy and enough speed, MIT is able to image the PEP contrasts in static mode. It can image online changes in PEP in dynamical mode. In reality the measurements are noisy and also there are numerical errors in simulated data generated by forward models. These errors impose a limitation in resolution and contrast of the image. The limited speed of the measurement system and the simulation tools may limit the speed of MIT for online imaging. If the sensitivity of the measurement system is very low for part of the object, we may not be able to

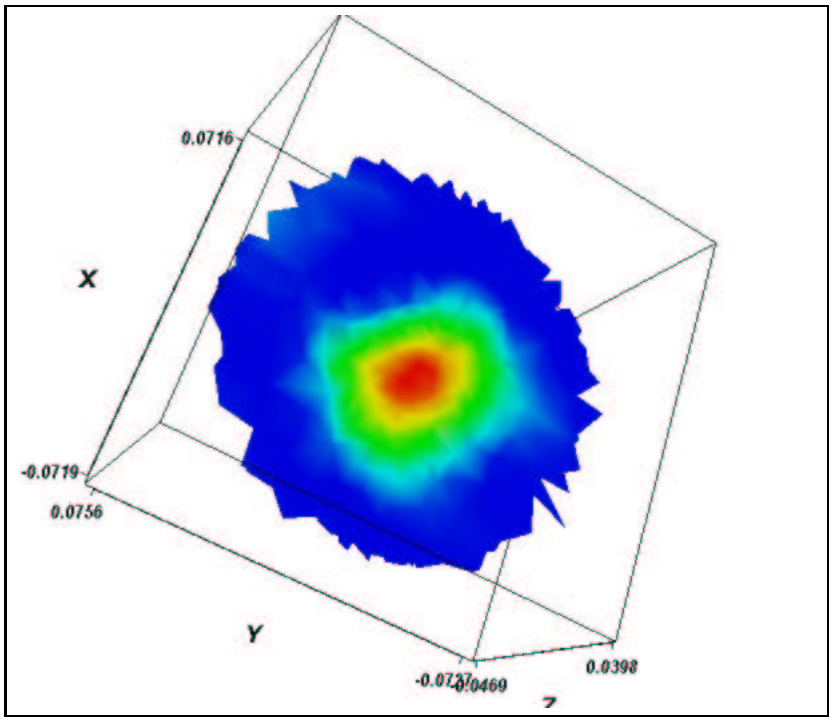

Figure 3.50: Rectangular metal object

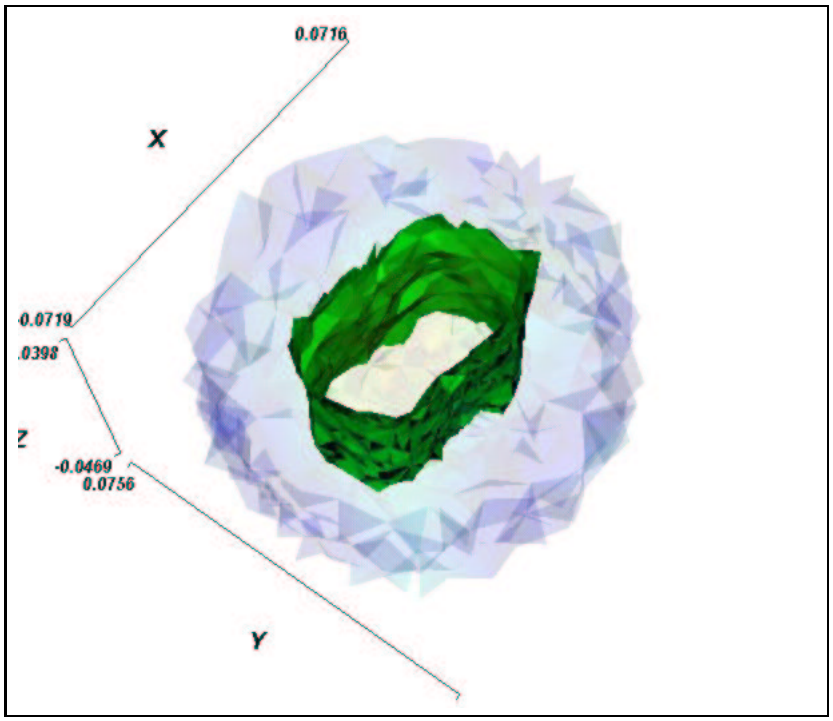

Figure 3.51: Rectangular metal object, isosurface for electrical conductivity

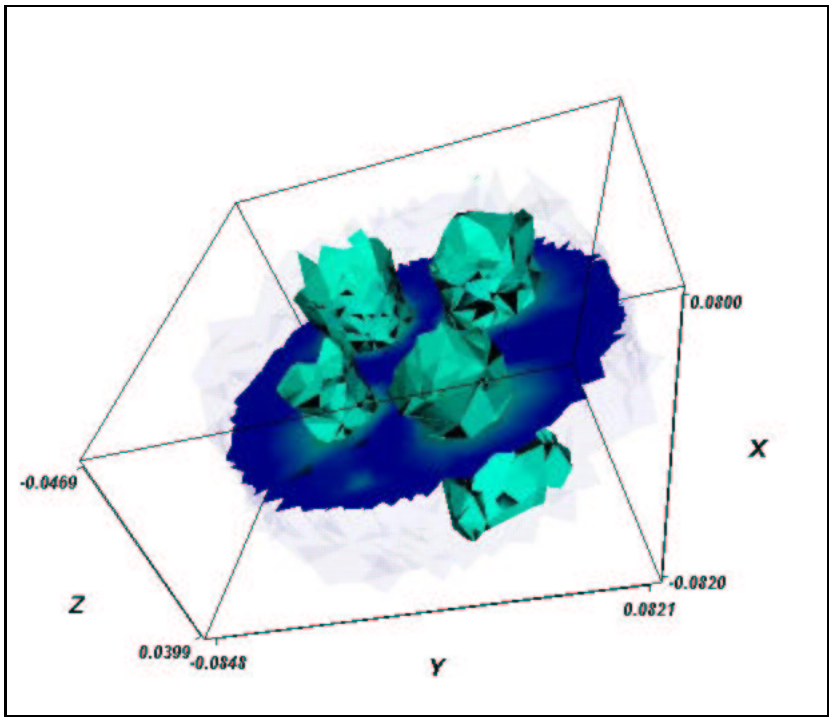

Figure 3.52: Four metal bars of figure 3.46

image those regions. This acceptable sensitivity is bounded also by the accuracy of the measurement system, accuracy of the simulation models and reconstruction techniques. The feasibility study of MIT for each application plays a vital role in success of each MIT project. The implemented software in this thesis enables us to have a synthetic analysis of the MIT system, also one may use it for feasibility studies for different applications.

3.7.1 Industrial Process

There is increasing interest in using PEP images in monitoring of the industrial processes. ERT and ECT attracts many process engineers to collaborate with scientists to develop those techniques for the process monitoring purposes. MIT is potentially a good alternative and sometimes the only option for process monitoring as it has the

advantage of being contact less. In EIT when an insulating object surrounds a conductive object, this makes it impossible to image the conducive object. Molten steel flow visualization [11] is an interesting application of MIT in continuous casting in the steel industry. Identification of the solidification of the metal object during the casting [117] is also a potential MIT application, that have been studied previously. Tomographic condition monitoring of Taphole operation is also an ongoing project in industrial application of MIT. MIT can be used in many other industrial applications. In this thesis we contribute on improving some image and shape reconstruction techniques that enable MIT to be used for the multi-phase material monitoring. Specifically we concentrated on imaging of the molten steel flow.

An interesting application of MIT with high contrast conductivity imaging is the molten metal flow visualization in continuous casting of steel. Continuous casting, see figure 3.53, is a key process by which molten steel is formed into semi-finished billets, blooms and slabs. Liquid steel from basic oxygen steelmaking (BOS) or electric arc furnace (EAF) processes and subsequent secondary steelmaking, is transferred from a ladle, via a refractory shroud, into the tundish. The tundish acts as a reservoir, both for liquid steel delivery and removal of oxide inclusions. A stopper rod or sliding gate liquid (not shown) is used to control the steel flow rate into the mould through a submerged entry nozzle (SEN). The SEN distributes the steel within the mould, shrouds the liquid steel from the surrounding environment, and reduces air entrainment thus preventing re-oxidation, and maintaining steel cleanliness.

Primary solidification takes place in the water-cooled copper mould and casting powder is used on the surface to protect against re-oxidation and serve as a lubricant in the passage of the strand through the mould. Exiting the mould, the strand consists of a solid outer shell surrounding a liquid core. This is continuously withdrawn through a

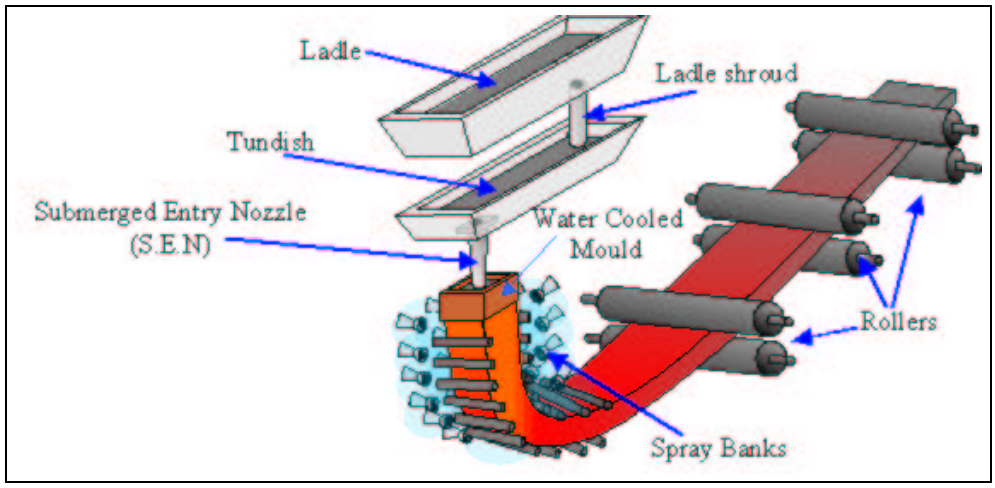

Figure 3.53: Overview of the continuous casting process (this image is from Prof. A.J. Peyton)

series of supporting rolls and banks of water sprays where further uniform cooling and solidification take place. The resulting cooled and solidified strand is finally divided by cutting torches into pieces as required for removal and further processing. Figure 3.54 shows a photograph of the process with the SEN labelled.

At present, the metal level in the mould, which is maintained by automatic flow control, is usually measured using electromagnetic or radioisotope metal level sensors in the mould. Several possible flow regimes could exist within an SEN as shown in figure 3.55, examples of which are bubbly flow (argon bubbles with the stream) figure 3.55(a), central stream with a half filled nozzle figure 3.55(b) and annular flow (a stream with a central gap) figure 3.55(c). Other flow regimes are possible and transitions from one flow mode to the other can occur during casting depending on the flow rate of steel and gas for the given casting conditions. Therefore, an on-line flow visualization approach, based on a rugged and inherently safe sensor, would be highly desirable. Knowledge of the flow regime in the SEN would enable improved control of conditions in this area of the caster.

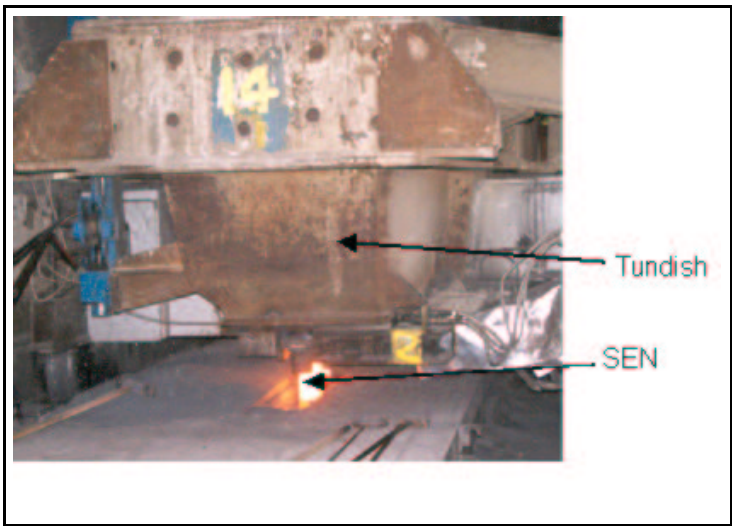

Figure 3.54: Photography of the continuous casting process showing the SEN and tundish (courtesy Corus plc.)

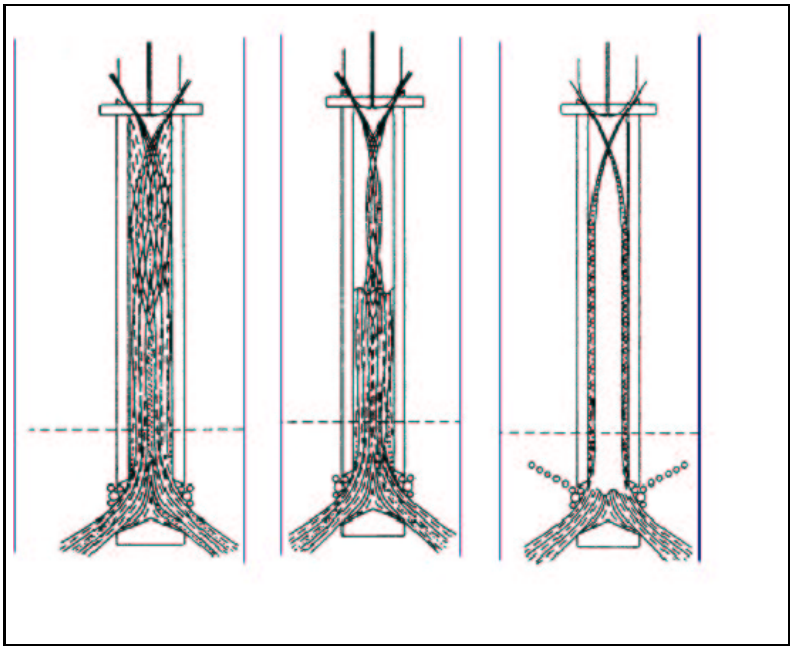

Figure 3.55: Examples of flow regimes of molten steel from left to right, Bubbly, Centred and Annular (this image is from Prof. A. J. Peyton)

3.7.2 Non Destructive Testing

In eddy current testing [153] technique a time-varying current flowing in an exciting coil induces eddy currents in a specimen under testing. The eddy currents field depends on the spatial distribution of the resistivity and magnetic permeability and is detected by a suitable number of magnetic sensors. Information concerning the spatial distribution of the resistivity is then retrieved by inversion of the measured data. In this frame, the problem of reconstructing 3D volumetric anomalies in conductors is presently receiving considerable attention. The problem is very difficult from a theoretical, experimental and computational point of view. From the theoretical point of view, the actual information that can be retrieved from experimental data should be assessed, for a given experimental noise level. Eddy current testing (it has the same basis as MIT) is very well known in Non Destructive Testing (NDT) where the eddy current method is used for crack detection in metallic objects. Although it called eddy current testing but in fact it can be categorized as an MIT system too, as it images indeed the conductivity distribution. The forward and inverse problems are the same as MIT. Most eddy current instrument (and probes) are dedicated to a particular application, such as the detection of cracks, inspection of tubes, metal sorting, or determination of coating thickness or conductivity. From point of view of this thesis we consider the eddy current testing as a PEP imaging system similar to MIT technique, as it can be a multiple (coil/coil) or single coil measurement, where the objective is to map the shape and position of the cracks. This thesis contributes in forward modelling, inverse solution and the sensitivity analysis of eddy current testing system.

3.7.3 Medical Applications

In medical applications the non-invasive measurement of the impedance of biological tissue can yield data of diagnostic relevance. For example a change in impedance can give an indication of the healing process of wounds and of skin irritations. The traditional way is to apply the current directly to the tissue and measure the voltage with electrodes. This leads to stray capacitances between the electrodes as well as between the ground and the patient especially at frequencies above 500kHz. If the patient has acute pain it is not always possible to touch the skin, so a non-contact method must be used. In some applications (e.g. impedance measurement in the brain) impedance can hardly be measured with surface electrodes. Such a sensor could be an instrument, which is moved around on the skin of a patient, in order to detect areas with impedances that deviate from normal. The non-contact measurement is based on the idea that a time varying magnetic field induces eddy currents in the conductive tissue. These eddy currents will create a field by themselves and a change in the signal can be detected. This change is expected to be very small, so a high resolution of the measuring system is necessary [141]. Electrical bio-impedance measurement (EBIM) is an important physiological measurement technique that gives information on tissue characteristics. The coil-coil method is a non-invasive, contact free method for the EBIM. In contrast to the conventional techniques which are applying electric current and measuring the voltages using electrodes, the coil-coil method measures impedance using pairs of coils.

There are some advantages of this contact-less system compared with electrode systems. First that we do not need to attach electrodes, which is an advantage for intensive care patients and patients with damaged skin. Secondly the number of measurements can be increased by mechanical moving of the coils which is not feasible with an

adhesive electrodes system. Thirdly, injected current cannot generate high current density in a volume surrounded by a less conductive region, so it is practically impossible to obtain detail information on the parts inside of such a region (screening effect). Coil-coil EBIM aims to estimate the electrical conductivity of biological tissue from external measurements [78]. This technique appears especially attractive for the monitoring of pathologies in the brain, which are correlated with local fluid shifts, for example oedema, haemorrhage's or epileptic events [157],[142]. In applications like cryosurgery monitoring [127] where we are looking for relatively larger changes in the conductivity (normal tissue compared with freezing tissue), in particular in cryosurgery monitoring of the head where the screening effect makes the task difficult for conventional bio-impedance measurement we suggest the coil-coil system may be advantageous. MIT in medical applications are working in higher frequency and the contrast are low for the conductivity compared to the industrial applications. The forward model, sensitivity analysis and the image reconstruction technique developed for this thesis are perfectly usable for MIT in medical applications.

3.8 Discussion

In MIT the image is the distribution of the electric conductivity based on detecting the induced current caused by a time varying magnetic source. Basically the magnetic source is a coil carrying sine wave current outside of the conductive volume. The direct measurement of the eddy currents is not so easy, but one can measure the effect of eddy currents by their magnetic field results in the induced voltage on external sensing coils. The measurement process can be described by a general eddy current problem. There is not an analytical solution to the eddy current problem in all cases.

In this thesis an edge FEM software has been developed to numerically simulate the forward problem of MIT. A sensitivity formula has been derived that calculates the changes in induced voltages due to the small change in conductivity of a region. The computer program includes an edge FEM code for the general eddy current problem, computation of the Jacobian matrix, nonlinear Gauss-Newton method, generating the regularization matrix and visualization functions have been implemented in Matlab. The forward problem and the Jacobian computation can work for the anisotropic material distribution, but the image reconstruction presented in this chapter is for isotropic material distribution. In this chapter we presented a nonlinear image reconstruction method using a regularized Gauss-Newton scheme for MIT, which uses the forward solver, sensitivity formula and regularization method to reconstruct the conductivity profiles in a stable manner. The image reconstruction method has been tested successfully for various MIT examples with conductivity range of medical and industrial applications. In general the conductivity times frequency is a decisive factor for the nonlinearity of the inverse problem in MIT, so just low contrast conductivity contrast may not be enough to use a linear reconstruction method. As the frequency increases, the electrical interference between two inclusions located close to each other increases, which cause the change in sensitivity plot and consequently the nonlinearity. A large number of iterations are needed for the high contrast conductivity problem.

Chapter 4

MAGNETOSTATIC PERMEABILITY TOMOGRAPHY

Magnetostatic permeability tomography (MPT) is an imaging modality, part of a larger family of magnetically coupled electromagnetic imaging techniques similar to MIT [58]. MPT attempts to reconstruct the permeability distribution of an object using magnetostatic measurement data. The data for image reconstruction are external magnetic field measurements on the surface of the object due to an applied magnetostatic field. Given the normal and tangential components of the magnetic field in the surface the internal isotropic permeability distributions can be uniquely defined [151]. In the previous chapter we presented a simplifying model for the excitation and sensing coils so they could approximately reflect the measurement of normal and tangential components of the magnetic field. The magnetostatic fields are applied to the object. The primary magnetic field can be generated using permanent magnet or an electromagnet such as solenoid. The resulting magnetic field can be detected using a magnetometer, or for alternating magnetic field a detection coil. In this thesis we apply an alternating

electric current to the excitation coil(s) and measure the induced voltages in sensing coils. With our explanation of a simple coil model in previous chapter, the coil-coil (throughout this thesis) measurement gives similar information to the data from tangential and normal components of the magnetic field. There are potential applications for MPT with magnetostatic fields in material inspection. For example structural materials in reinforced concrete, often made of steel, are sometimes damaged due to ingress of corrosive solutions. This damage changes the magnetic permeability. An MPT system can give information about the steel bars inside of the concrete as well as reconstructing their number, shape and position. In [50], [126] an inductive scanner has been used to recover the conductivity and permeability of steel bars within a concrete structure. In this thesis we focus on tomographic notion of a magnetostatic imaging system using the forward solution and Jacobian matrix, which can be described as a phenomenological method. Non-phenomenological methods as described in [81](techniques that ignore the underlying physical process of the forward problem) also can be used for the inverse problem of MPT; as an example the simple linear superposition used in [50]. We present a numerical method to solve the reconstruction problem in three dimensional. There have been some previous studies to reconstruct permeability distributions using magnetostatic data in two dimesions. In [88], [89] MPT reconstruction has been studied for two dimensions, Wexler's method [172] has been used to reconstruct the permeability distribution. As for other similar problems Wexler's method used for MPT shows very slow convergence and requires several hundred solutions of the forward problem, which makes the technique computationally very expensive especially in three-dimensions. A regularized one step permeability reconstruction for simple geometry used with an analytical forward problem has been presented in [28]. Given the fact that the inverse problem in MPT is a nonlinear

problem and there is not an analytical solution for the general form of the magnetostatic forward problem, the method proposed in [28] can not be used in general. In this chapter a regularized Gauss-Newton method based on a finite element model is used. It incorporates *a priori* information in the regularization, the method is nonlinear and the convergence of the method is known to be good for similar inverse problems [121]. The method has been widely used for a similar inverse problem in EIT (see for example [121]). Edge FEM has been used to solve the magnetostatic problem formulated using the magnetic vector potential [12]. For the calculation of the Jacobian matrix an efficient adjoint field method has been used. We show the results of 3D permeability reconstruction for a numerically simulated MPT system.

4.1 Simulated MPT system

The simulated MPT system here is assumed to have 8 coils, which are used for applying and detecting the magnetostatic fields. The coils have 0.04 m inner and 0.05 m outer diameter and 0.02 m length. The coils are arranged in a circular ring surrounding the object to be imaged. In this example the distance between centre of two coils in opposite sides is 0.160 m, centre of coils ring is at (0,0,0). Coil arrangement of figure 3.1 has been used here for MPT modelling. The system could have a magnetic shield but in this chapter the far field boundary condition $\boldsymbol{B}_n = 0$ is applied to the model and a magnetic shield has not been considered, $\boldsymbol{B}_n$ is the normal component of the magnetic flux intensity. The frequency of the applied current is 16kHz, and for simplicity we use a $1(Am^{-2})$ current applied to the excitation coil. The region of interest for the permeability imaging is a cylinder with radius 0.07 m, length 0.10 m centred at (0,0,0) and has a relative permeability of 3 (we call it C1). Each coil is excited in turn and the

induced voltages are measured in the remaining coils.

4.2 Forward problem of MPT

The forward problem is to predict the measurement data given the permeability distributions, and given the applied current pattern and geometrical data. The interior magnetic fields are needed for the efficient computation of the Jacobian matrix, which will be described in next section. The magnetostatic field can be modelled either by a scalar field (for example by magnetic scalar potential) or vector field (for example by magnetic vector potential). The magnetostatic field have been formulated using edge FEM for the magnetic vector potential ($\boldsymbol{A}$) [18] here. Edge FEM has the advantage of satisfying normal continuity of the magnetic field, so it handles multiple connected materials and jumps in permeability. Given $\boldsymbol{B} = \nabla \times \boldsymbol{A}$ then

$$\nabla \times (\nu \nabla \times \boldsymbol{A}) = \mathrm{J}_{\boldsymbol{s}} \tag{4.1}$$

where $\nu = 1/\mu$, this is the same as the eddy current problem with conductivity zero. The finite element discretization of (4.1) the governing equations using edge element basis functions is

$$\int_{\Omega} (\nabla \times \boldsymbol{N}\nu \cdot \nabla \times \boldsymbol{A}) dv = \int_{\Omega_c} (\boldsymbol{N} \cdot \mathrm{J}_{\boldsymbol{s}}) dx^3 \tag{4.2}$$

where $\boldsymbol{N}$ is any linear combination of edge basis functions, Ω is the entire region and Ω_c is the current source region. In order to improve the convergence of the edge FEM we use an electric vector potential $\boldsymbol{T}_s$ to represent the current in excitation coil in which $\nabla \times \boldsymbol{T}_s = \boldsymbol{J}_s$, described in previous chapter [129]. Incomplete Cholesky conjugate gradient (ICCG) has been successfully used to solve the linear system of

equations (4.2), arising from the edge FEM forward model without applying any gauge conditions.

4.2.1 Induced Voltages

In figure 4.1 the normalized induced voltage for coils $2, 3, \ldots, 8$ when coil 1 is excited is shown, the object (cylinder C1) is symmetric with respect to the coils 2,3,..,8 and the voltages are normalized with respect to the induced voltage in coil 2. A maximum error in computation (about 1.5 percent) is the difference between voltages of coils 2 and 8 as they are closest to the excitation coil (The coils 2,8 are in the same position with respect to coil 1 so ideally the calculated voltage for them must be the same). The permeable object (relative permeability of 3) is the cylinder C1 and the rest of space has relative permeability 1.

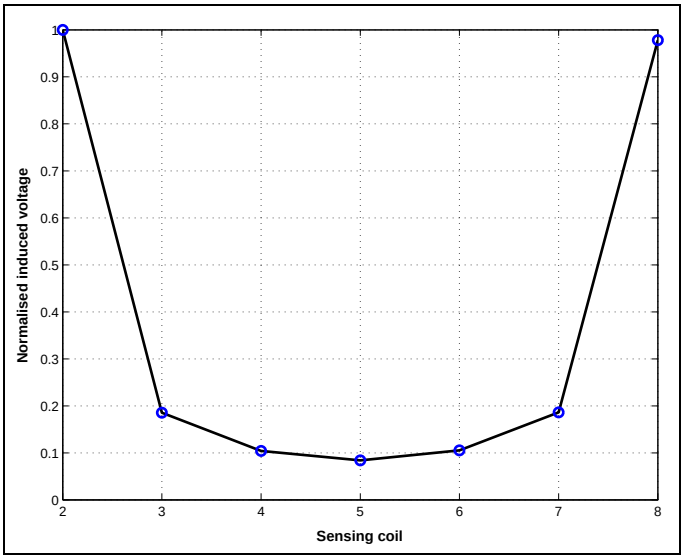

Figure 4.1: Normalized induced voltage in coil 2-8 when the coil 1 is excited

With 69804 elements we tested the accuracy of the simulated voltage measurement with respect to the stopping criteria for the ICCG for the calculation of the magnetic vector potential. Figure 4.2 shows the error in the calculated voltage of coil 1 when

coil 3 is excited. Figure 4.3 shows the error in the calculated voltage in coil 1 when coil 1 is excited. We choose 10^{-8} for the stopping criteria since the accuracy of the calculated voltages do not improve beyond that. Here we chose a given mesh density and solved the forward problem with different residual level, the smaller resudual level was chosen as more accurate.

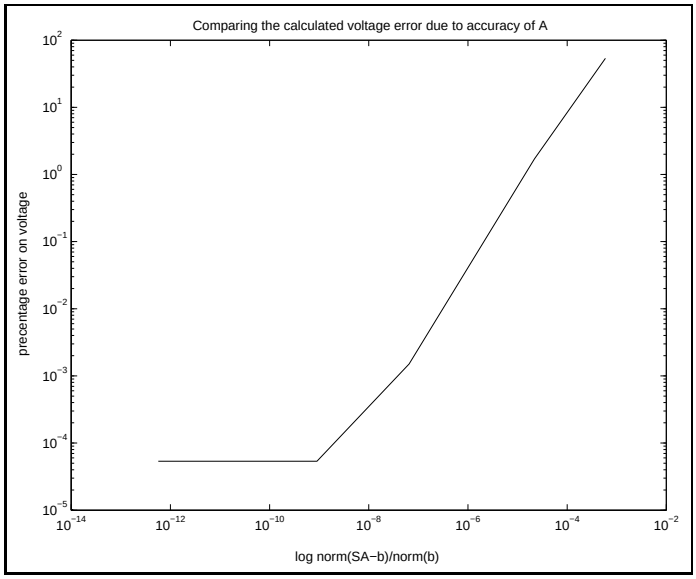

Figure 4.2: Error in induced voltage in coil 1 when coil 3 is excited with respect to the error norm for stopping ICCG

4.3 Sensitivity analysis

There are a number of ways to model the excitation and measurement coils. As in any imaging system the sensors must be modelled. Rather than modelling individual turns of copper wire, we will use a simplified model of a coil as a surface (topologically at least) as an open ended cylinder. When used as an excitation coil this surface carries a tangential current J_s. This is equivalent to a surface that is perfectly conducting in one direction (angular for a cylinder) and an insulator in another (axial) direction, with

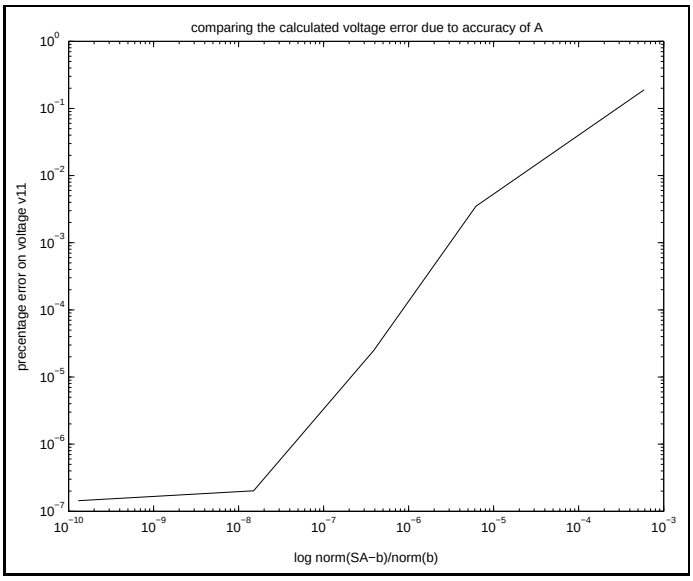

Figure 4.3: Error in induced voltage in coil 1 when coil 1 is excited with respect to the error norm for stopping ICCG

each loop fed by a perfect current source. The excitation coil is modelled to give an accurate tangential $\boldsymbol{H}$. With a similar argument the measured induced voltage in the exciting coil is the same as the measurement of the normal component of the magnetic field. There might be an external magnetic screen (shielding) which means that the normal component of $\boldsymbol{B}$ vanishes. In this study we assume a far field boundary condition, and where there is no shielding one would nevertheless need to apply far field boundary conditions to Maxwell's equations. The general form of the sensitivity analysis for Maxwell's equation, which has been studied in [42] and discussed further in the last chapter can be applied here. The sensitivity to the change in permeability, equation (3.6), of a region is proportional to an integral over the volume of the perturbing region of the inner product of the magnetic field $\boldsymbol{H}$ from sensing and exciting coil [42], [69]. In [83] a more ideal model of the coils is considered to represent the measurement of the tangential $\boldsymbol{H}$ (for exciting coils) and normal $\boldsymbol{B}$ (as sensing coil) in the surfaces. In [83] a sensitivity formula has been derived for the general electro-

magnetic problem of MIT. A more detailed description is also given in the previous chapter. A numerical form of the sensitivity formula using a magnetic vector potential formulation of the forward problem for MPT is implemented. Using the matrix of edge elements $\boldsymbol{N}_e$ in each element ($\boldsymbol{N}_e$ is the shape function in each element), the magnetic field $\boldsymbol{B}$ inside each element can be expressed as follows

$$\boldsymbol{B} = (\nabla \times \boldsymbol{N}_e) \cdot \boldsymbol{A}_e \tag{4.3}$$

where $\boldsymbol{A}_e$ are defined along edges and are the solution of the forward problem. The sensitivity term for each element is expressed as follows based on the general form of equation(3.5) (term H is for the sensitivity with respect to permeability)

$$\frac{\partial V_{ij}}{\partial \mu_k} = \frac{i\omega}{I_i I_j \mu_0 \mu_k^2} \boldsymbol{A}_e^i \left(\int_{\Omega_{ek}} (\nabla \times \boldsymbol{N}_e) \cdot (\nabla \times \boldsymbol{N}_e)^T dx^3 \right) (\boldsymbol{A}_e^j)^T \tag{4.4}$$

Equation (4.4) gives us the sensitivity of the voltage induced in coil i when coil j is excited with respect to μ_k relative permeability of element k. Here μ_0 is the permeability of free space, Ω_{ek} is the volume of element number k and I_j and I_i are excitation current for coils. For first order edge basis functions the curl of the basis function is constant in each element so the integral in equation (4.4) is a constant and easy to calculate in each element. In figure 4.4 one can see a plot of the sensitivity when the excitation and sensing coils are coaxial (Coil 1 and 5) and are placed in two opposite sides of the object, two coils are centred at $(0.08, 0, 0)m$ and $(-0.08, 0, 0)m$, and the background is the cylinder (C1). Figure 4.4 shows that the sensitivity is higher in the centre and also near to the coils, and figure 4.5 shows a three dimensional sensitivity map. Figure 4.6 is the sensitivity map for coils 1 and 3, two coils in 90 degrees. Figure 4.7 shows the sensitivity plot of coil 5 as an excitation coil and coils 8,1,2 are as

a gradiameter. The voltage of the gradiameter is $V_1 + V_2 - V_8$, where V_1 and V_2 and V_8 are voltages in coils 1, 2 and 8 respectively. All these sensitivity values are for a current density of $1Am^{-2}$.

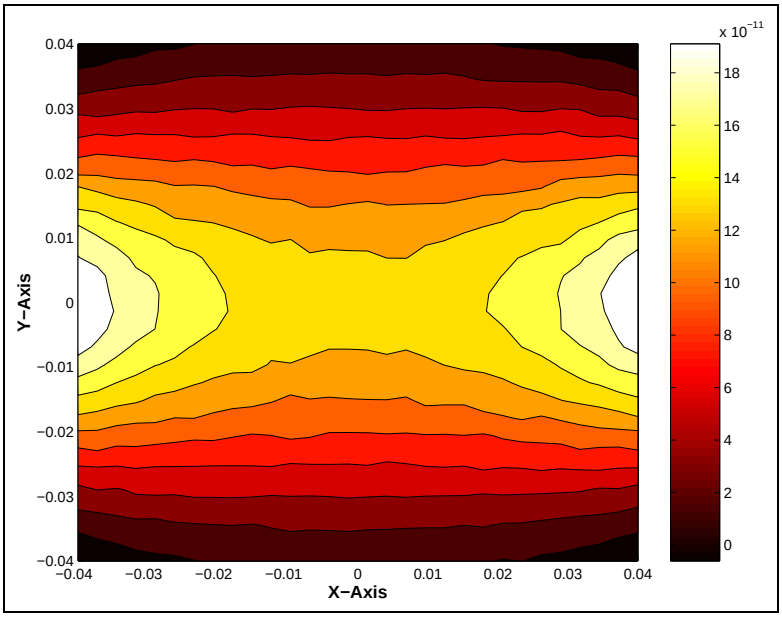

Figure 4.4: Sensitivity plot for coils 1,5 as excitation and sensing coils in plane Z=0, the sensitivity value is in volt/(unit change in relative permeability)

Each row of the Jacobian matrix is a sensitivity of one of the measured voltages to a small change in each voxel's permeability value. In figure 4.8 one can see the singular values of the Jacobian matrix for the cylinder C1. The linear decay on a logarithmic scale shows that the inverse problem is severely ill-posed. In this study we use 28 mutual inductance measurement.

4.4 Image reconstruction

Image reconstruction in MPT is an inverse medium problem. The regularized Gauss-Newton method has been used for the image reconstruction for electrical imaging

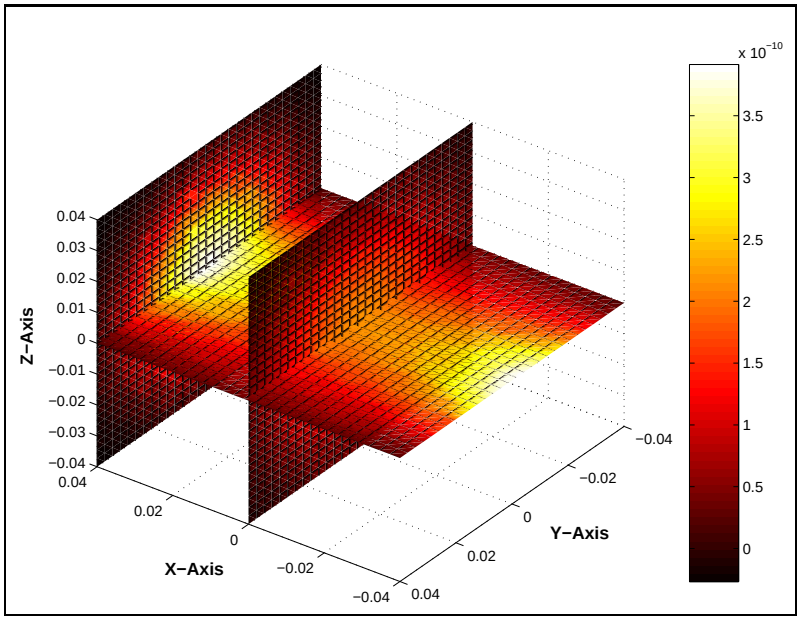

Figure 4.5: Sensitivity plot for coils 1,5 as excitation and sensing coils in three dimensional, the sensitivity value is in volt/(unit change in relative permeability)

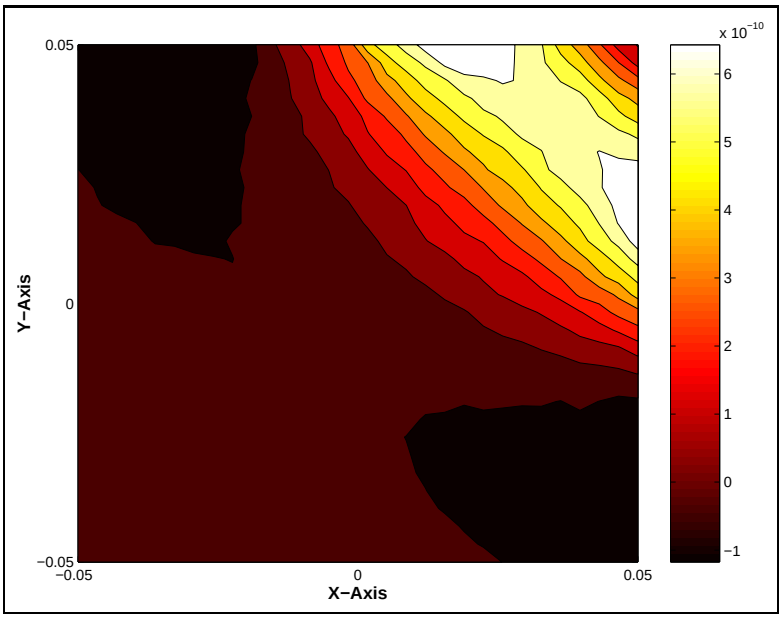

Figure 4.6: Sensitivity plot for coils 1,3 as excitation and sensing coils in plane Z=0, the sensitivity value is in volt/(unit change in relative permeability)

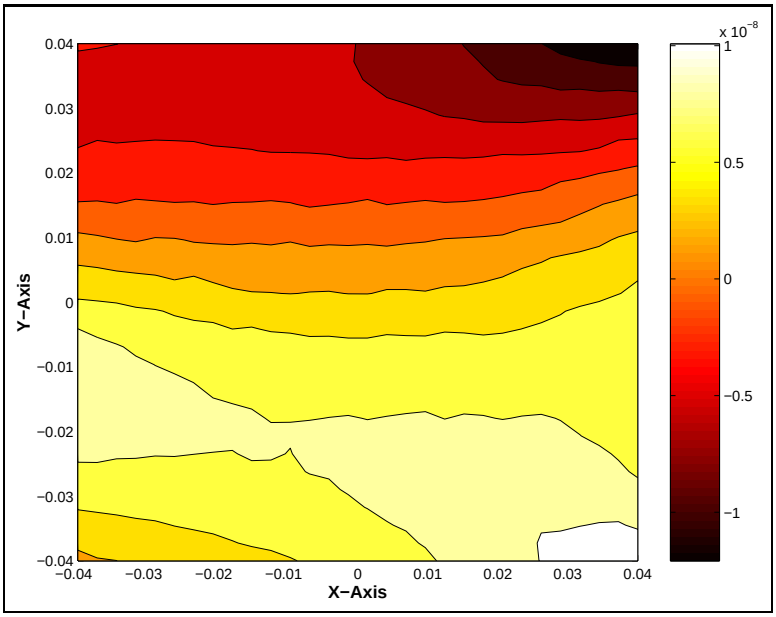

Figure 4.7: Sensitivity plot for coils 8,1,2 as a gradiameter, and coil 5 is an excitation coil in plane Z=0, the sensitivity value is in volt/(unit change in relative permeability)

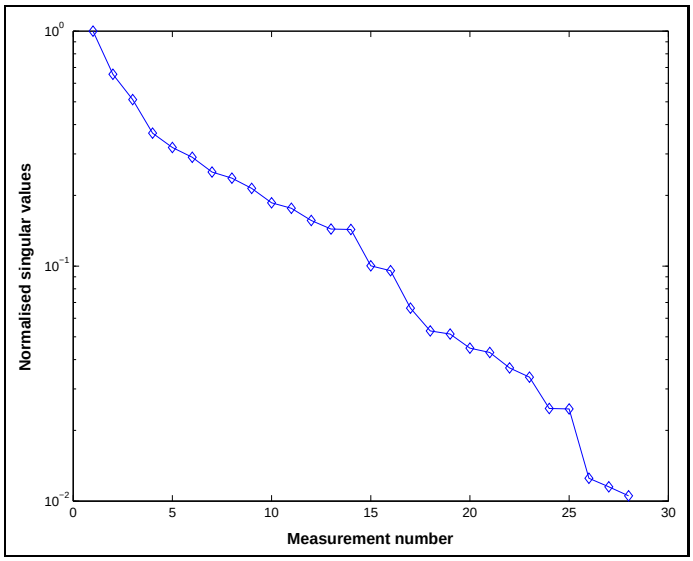

Figure 4.8: Plot of the singular values for 28 independent measurement (normalized to the 1st and largest singular value)

[120], [121], [147]. In [147] a regularized and one step Gauss-Newton method has been applied to the electrical conductivity imaging of MIT. In this chapter a general nonlinear regularized Gauss-Newton scheme is applied to an interesting and new imaging method, magnetostatic permeability tomography. The forward solution provides a good understanding of the measurement process and the Jacobian matrix provides partial knowledge of the inverse solution. The regularized Gauss-Newton scheme provides a direction to improve the solution from a given point. The regularization methods enable us to include some prior knowledge of the measurement noise as well as prior knowledge of the permeability distribution, so the ill-posed inverse problem can be stabilized.

The algorithm starts with an initial permeability distribution. The forward problem is solved and the predicted voltages compared with the calculated voltages from the forward model. The permeability is then updated using the Jacobian matrix. The process is repeated until the measurement data agree with the calculated voltages from the finite element model up to the measurement precision. The Jacobian matrix needs to be updated in each step, as the sensitivity map changes with change on background permeability.

Reformulation of the inverse problem to include prior information is known as regularization. A natural assumption will be that $\|\boldsymbol{R}\mu\|$ is not too large, which can mean the permeability is small, or slowly changing or smooth. Where $\boldsymbol{R}$ is the Laplacian smoothing regularization matrix used for MIT. We solve this minimization problem by regularized Gauss-Newton, described in equation (3.40), which is a compromise between the error of the mismatches between the measurement ($\boldsymbol{V}_m$) and the predicted voltages and the deviation from the prior information. Here α regularization parameter was chosen as 10^{-7}.

For the first test, we inserted two bars with relative permeability of 4 into the cylinder C1 as a test phantom (see figure 4.9.a). Figure 4.9.b shows the reconstructed image from the test phantom of figure 4.9.a. Figure 4.9 is cross section of a 3D image in different Z levels.

In the second test, four high permeability bars were inserted with relative permeability of 50 as shown in figure 4.10.a. Figure 4.10.b shows the reconstruction of this test phantom, the nonlinear reconstruction steps have been applied. The convergence plot which shows the norm of the differences between measured and simulated voltages depicted in figure 4.11. In both cases in order to avoid a so called “inverse crime” two different meshes were used, for generating simulated measurement data and for the forward solver and 2 percent Gaussian noise (2 percent of the mean value of the measurement voltages) was added to the data.

4.4.1 Remarks and summary

The image in the lower contrast case (figure 4.9) is more affected by the noise in the data as the changes on the voltages are small. For the higher permeability contrast case (figure 4.10) the measurement signals are higher, so if the objective is to recover shape and location of the high contrast inclusions the resulting images are better than the low contrast case in terms of spatial resolution. The maximum permeability values in reconstructed image in figure 4.9 is 3.89 and in figure 4.10 is 26.67. Although the spatial resolution of the reconstructed image in the case of high contrast permeability is good, the quantitative values of the permeability are not accurate. Reconstruction of the absolute value of the permeability in higher contrast is a more complicated task. Three major reasons for this are: the smoothing assumption of the Tikhonov regularization, the underdetermined nature of the problem, and the effect of measurement

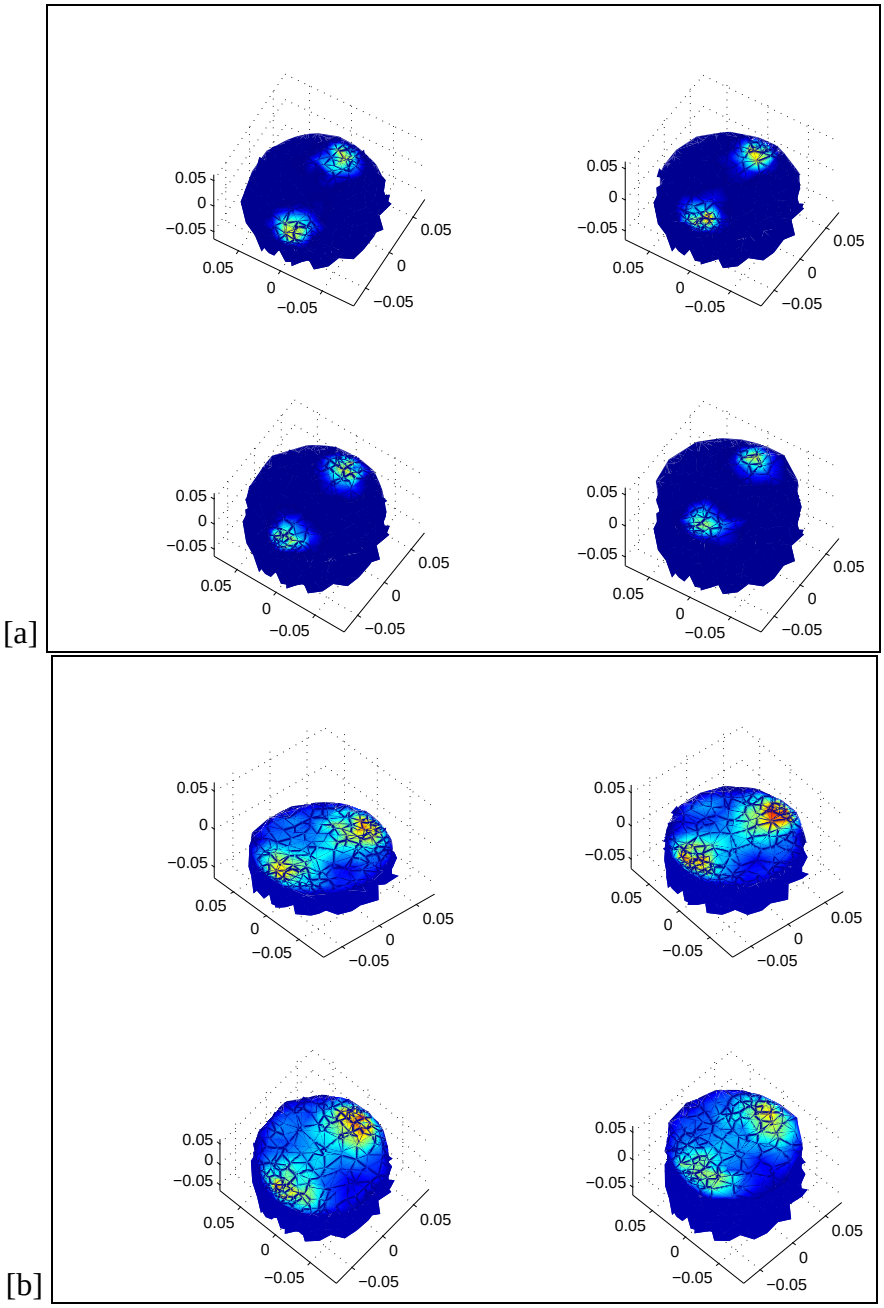

Figure 4.9: Reconstruction of the test phantom in (a) can be seen in (b), the image is for different Z levels of cylinder C1.

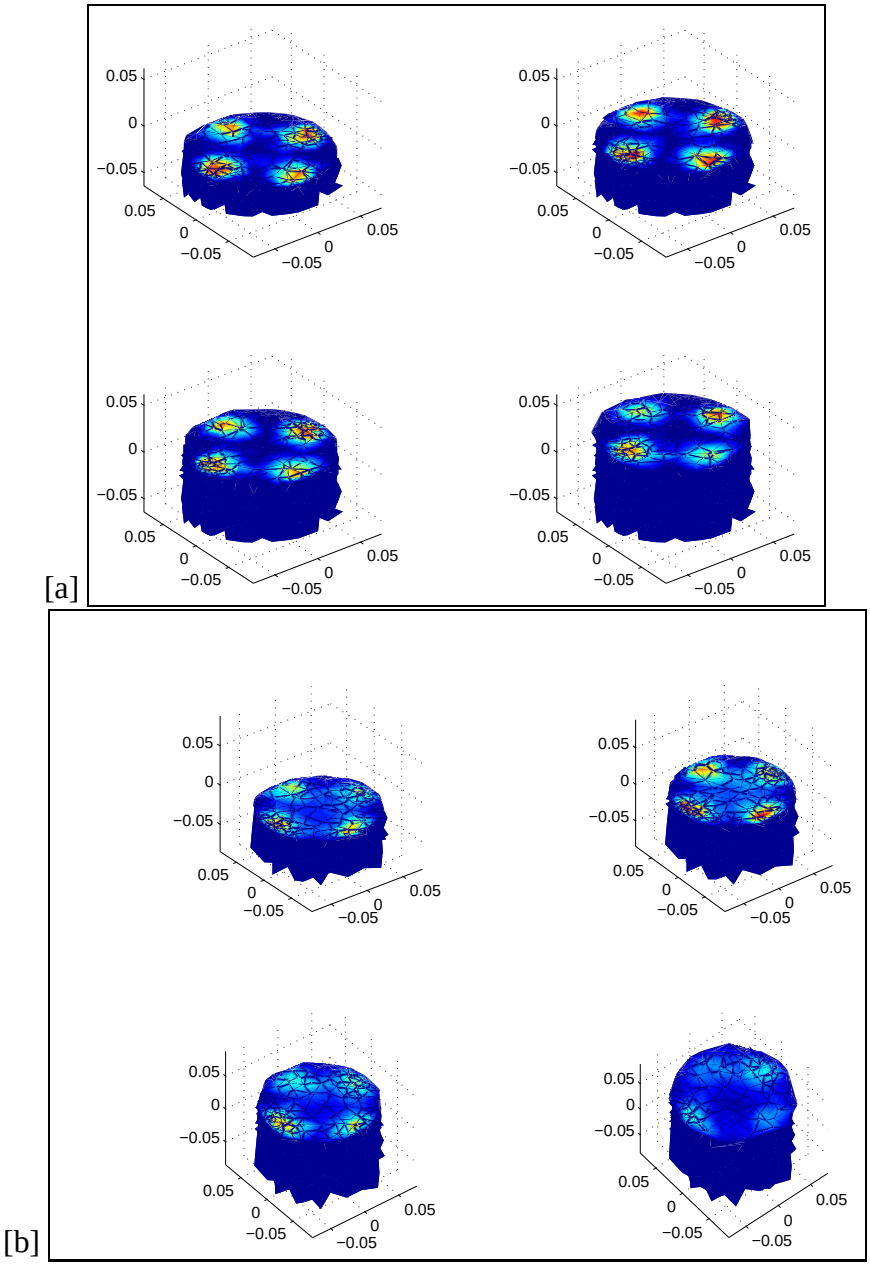

Figure 4.10: Reconstruction of the test phantom in (a) can be seen in (b), the image is for different Z levels of cylinder C1.

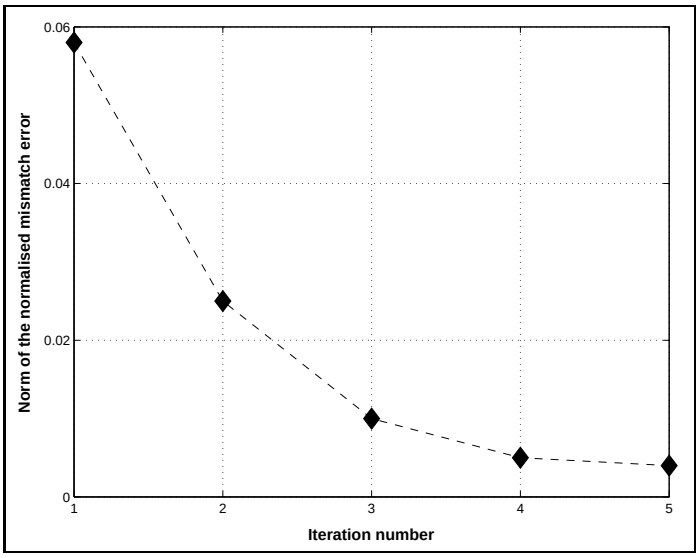

Figure 4.11: Norm of the error between measured and simulated voltage (Voltages are normalized to the voltage of free space)

noise to the reconstructed quantitative values of the image (because of the saturation explained below). Quantitative accuracy of the image can be improved by additional constrains or *a priori* knowledge, or different regularization schemes such as total variation regularization [31]. A method has been introduced in [35] to use *a priori* information of location of inclusions and solving the inverse problem for the reduced number of unknowns (here the value of permeability in entire region is the unknown, for example for the image of figure 4.10 we have one background and four inclusions, so there are 5 unknowns to be recovered). Shape reconstruction methods can be used for two phase material reconstruction (for example monotonicity based shape reconstruction of Tamburrino and Rubinacci [155]), for a given low and high value of the permeability values. The third reason depends on the measurement accuracy. For high contrast, the sensitivity plot has saturation property, which means if we perturb a region and increase the permeability of the region, the resulting changes to the measurement voltages are linear with permeability changes, as we increase the perme-

ability to the higher values the changes in the induced level out (see figure 4.12). This explains why it is hard to find the absolute permeability distribution in higher contrast case with noisy data.

Figure 4.12 shows the change on induced voltages (for all 28 measurements), when the relative permeability of an spherical object (Radius 0.02 m and centered at (0.03,0,0) m), when the background is a cylinder C1. One can see that the voltages are changing linearly and saturation occurs for higher permeability changes. For this perturbation test in order to avoid the discretization error we used a high mesh density (208000 elements). As the voltage differences between two high contrast inclusions are very small, this difference will often be overshadowed by noise.

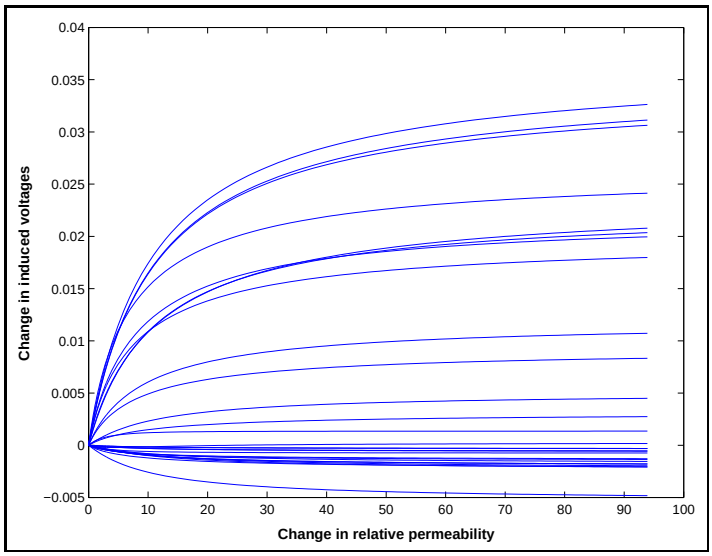

Figure 4.12: Change in induced voltages (normalized to the voltage for free space) due to perturbation of permeability of a spherical object. Note the validity of a linear approximation for small changes and saturation for high changes

In figure 4.12 one region has been perturbed, and if we consider perturbation of more than one region (especially perturbation objects closed to each other) we can see the lack of superposition and the interferences between perturbed fields and perhaps more

complicated pattern of the change in the measurement voltages. In the test example of figure 4.10 the high permeability inclusions are far from each other and the spatial resolution of the reconstructed image is good. If two high permeability inclusions are close to each other, so that their magnetic field interfere, the spatial resolution of the image will be degraded. Further studies are needed for high contrast permeability imaging especially when the absolute value of the permeability is required.

4.5 Discussion

This chapter introduced a 3D magnetostatic permeability tomography (MPT) system. Knowing the tangential component of the applied field and normal component of the measured field uniquely defines the permeability distributions for all possible excitations [151]. In practise, a finite set of external excitation and sensing coils (or the magnetic field sensors) can be used for the measurement configuration and so a finite amount of information can be extracted from those limited data. Like other boundary value inverse problems, inverse MPT problem is an ill-posed nonlinear problem, so regularization is needed for a stable solution. We presented a numerical method to solve the reconstruction problem in three dimensions using a regularized Gauss-Newton scheme. The forward problem has been solved using edge FEM and an efficient technique has been employed to calculate the Jacobian matrix. The permeability of the object is assumed to be linear and isotropic. The reconstruction results for permeability was presented using synthetically generated data with additive noise. Reconstruction results presented for high and low contrast permeability imaging. In the case of low contrast a linear step is used to recover the permeability distribution. In the higher contrast case, the linear property does not hold and a nonlinear reconstruc-

tion must be applied. Further study is needed to solve the inverse problem of high contrast permeability, both in terms of regularization and quantitative accuracy of the reconstructed images.

Chapter 5

FORWARD PROBLEM IN ERT

Electrical resistance tomography (ERT) seeks to image the conductivity from external measurements of the potential using multiple field patterns of low frequency as a result of the excitation at the external boundary. In ERT dielectric effects and magnetic fields are considered to be negligible. A promising application of ERT is medical imaging, where currents of low intensity are used in order to image electrical properties of the human body. ERT has been tested to detect epileptic seizures (see [13]), functional brain activity triggered by external stimuli (see [122]) and internal cortical hemorrhage (see [34]), conditions which all cause local and temporal conductivity changes in brain tissue. Linearization techniques are widely used and require the repeated solution of a linear forward problem. To account correctly for the presence of electrodes and contact impedances, the so-called complete electrode model (CEM) is applied [150],[123]. Implementing a standard FEM for this particular forward problem yields a linear system that is symmetric and positive definite and solvable via the conjugate gradient (CG) method. However, preconditioners are essential for efficient convergence. Preconditioners based on incomplete factorization methods are com-

monly used but their performance depends on user-tuned parameters. To avoid this deficiency, we apply a black-box algebraic multigrid, using both standard commercial and freely available software. The suggested solution scheme dramatically reduces the time cost of solving the forward problem. Numerical results are presented using an anatomically detailed model of the human head. We do not restrict ourselves to a particular application. Rather, we focus attention, broadly, on media with conductivity distributions with coefficients that are generally anisotropic and/or discontinuous. In this chapter the main objective is to improve the speed of the forward ERT solvers by applying an algebraic multigrid method as a preconditioner for CG.

5.1 Forward modelling of ERT

The forward problem in ERT is to predict the voltage on the sensing electrodes given applied current to the exciting electrodes. The main part of an ERT measurement system is shown in figure 6.1. The electric current applied to the excitation electrodes and the potential between electrodes are measured using phase sensitive detection and a differential amplifier.

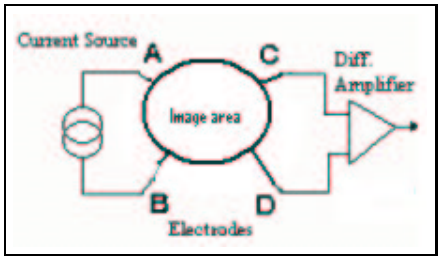

Figure 5.1: An electrical impedance measurement used in ERT

Let $\Omega \subset \mathbb{R}^3$ be a Lipschitz domain with C^2-continuous boundary Γ, to which L electrodes are attached. In the absence of interior sources or charges, the low-frequency,

time-harmonic Maxwell's equations reduce to a genera;ized Laplace equation, i.e. the elliptic partial differential equation,

$$\nabla \cdot (\hat{\sigma} \nabla u) = 0 \quad \text{in} \quad \Omega. \tag{5.1}$$

Here u is the scalar electrical potential and $\hat{\sigma}$ is a symmetric and positive definite tensor of electrical conductivity coefficients. The equation (5.1) is solved in conjunction with the set of boundary conditions prescribed by the so-called complete electrode model. A theoretical study of the model can be found in [150] and details of finite element implementations and numerical considerations are given in [159] and [121]. Specifically, the boundary current density satisfies,

$$\int_{e_l} \hat{\sigma} \nabla u \cdot \hat{n} = I_l \quad \text{on} \quad \Gamma_1, \tag{5.2}$$

$$\hat{\sigma} \nabla u \cdot \hat{n} = 0 \quad \text{on} \quad \Gamma_2, \tag{5.3}$$

whilst for the boundary electric potential measurements, the relation,

$$u + z_l \hat{\sigma} \nabla u \cdot \hat{n} = V_l \quad \text{on} \quad \Gamma_1, \tag{5.4}$$

is valid. Here, I_l denotes the current on the surface of the lth electrode, e_l, V_l is the electric potential measured by e_l, z_l is the associated contact impedance and $\hat{n}$ is the outward-pointing unit normal vector. In addition, $\Gamma_1 \subset \Gamma$ denotes the union of the pieces of the boundary situated underneath the electrodes and $\Gamma_2 = \Gamma \setminus \Gamma_1$ is the remainder of the surface. The model is known (see [150]) to have a unique solution up to an additive constant. Hence, one can apply a reference condition for the potential by grounding one of the boundary electrodes, yielding the Dirichlet boundary condition

$$u = 0 \Big|_{\Gamma_G} \quad \Gamma_G \subset \Gamma_1. \tag{5.5}$$

Alteratively, (5.5) can be applied to a randomly selected node in the model. Applying the charge conservation theorem, we also impose,

$$\sum_{l=1}^{L} I_l = 0. \tag{5.6}$$

5.2 Discrete problem

To solve (5.1) together with (5.2)–(5.4) numerically, the domain is partitioned into k tetrahedra with a total of n vertices. The conductivity coefficients are each approximated by a piecewise constant function on that mesh. Given a standard nodal basis (Whitney "0-form") $\{\phi_i\}_{i=1}^{n}$ for the set of piecewise linear functions, a potential is sought in the form,

$$u_h = \sum_{i=1}^{n} u_i \phi_i. \tag{5.7}$$

Multiplying (5.1) by an arbitrary test function v, which is sufficiently smooth, and integrating over Ω gives,

$$\int_{\Omega} v \nabla \cdot (\hat{\sigma} \nabla u_h)\, dx^3 = 0 \qquad \text{in } \Omega. \tag{5.8}$$

Integrating by parts yields,

$$\int_{\Omega} \hat{\sigma} \nabla u_h \cdot \nabla v\, dx^3 = \int_{\Gamma_1} \hat{\sigma} \nabla u_h \cdot \hat{n} v\, dx^2 + \int_{\Gamma_2} \hat{\sigma} \nabla u_h \cdot \hat{n} v\, dx^2,$$

so that imposing (5.3) and (5.4) on u_h gives,

$$\int_{\Omega} \hat{\sigma} \nabla u_h \cdot \nabla v\, dx^3 = \sum_{l=1}^{L} \int_{e_l} \frac{1}{z_l} (V_l - u_h)\, v\, dx^2. \tag{5.9}$$

Substituting for u_h from (5.7) in (5.9) gives,

$$\begin{aligned} \sum_{i=1}^{n} \left\{ \left(\int_{\Omega} \hat{\sigma} \nabla \phi_i \cdot \nabla v\, dx^3 + \sum_{l=1}^{L} \int_{e_l} \frac{1}{z_l} \phi_i v\, dx^2 \right) \right\} u_i \\ - \sum_{l=1}^{L} \left(\int_{e_l} \frac{1}{z_l} v\, dx^2 \right) V_l = 0, \end{aligned} \tag{5.10}$$

so that setting $v = \phi_j$, $j = 1:n$, yields n algebraic equations. Imposing the remaining boundary condition (5.2) on u_h and applying (5.4) yields an additional L algebraic equations,

$$I_l = \frac{1}{z_l} V_l |e_l| - \sum_{i=1}^{n} \Big(\int_{e_l} \frac{1}{z_l} \phi_i \, dx^2 \Big) u_i, \qquad l = 1:L, \tag{5.11}$$

where, here, $|e_l|$ denotes the area of the lth electrode. Hence, assembling $\boldsymbol{K}_M \in \mathbb{R}^{n\times n}$, $\boldsymbol{K}_Z \in \mathbb{R}^{n\times n}$, $\boldsymbol{K}_V \in \mathbb{R}^{n\times L}$ and $\boldsymbol{K}_D \in \mathbb{R}^{L\times L}$, via,

$$\begin{aligned}
\boldsymbol{K}_M(i,j) &= \int_\Omega \hat{\sigma} \nabla\phi_i \cdot \nabla\phi_j \, dx^3 \qquad i,j = 1:n, \\
\boldsymbol{K}_Z(i,j) &= \sum_{l=1}^{L} \int_{e_l} \frac{1}{z_l} \phi_i \phi_j \, dx^2 \qquad i,j = 1:n, \\
\boldsymbol{K}_V(i,l) &= -\int_{e_l} \frac{1}{z_l} \phi_i \, dx^2 \qquad i = 1:n, l = 1:L, \\
\boldsymbol{K}_D(s,l) &= \begin{cases} \frac{1}{z_l}|e_l| & s = l \\ 0 & s \neq l \end{cases}, \qquad s,l = 1:L,
\end{aligned}$$

leads to the matrix equation,

$$\begin{pmatrix} \boldsymbol{K}_M + \boldsymbol{K}_Z & \boldsymbol{K}_V \\ \boldsymbol{K}_V^T & \boldsymbol{K}_D \end{pmatrix} \begin{pmatrix} \boldsymbol{u} \\ \boldsymbol{v} \end{pmatrix} = \begin{pmatrix} \boldsymbol{0} \\ \boldsymbol{I} \end{pmatrix}, \tag{5.12}$$

where $\boldsymbol{u}(i) = u_i$, $\boldsymbol{v}(l) = V_l$ and $\boldsymbol{I}(l) = I_l$, for $i = 1:n$, $l = 1:L$.

5.3 Linear system of equations

The main focus here will be in efficiently solving linear system of equations arising from the FEM with CEM. In EIDORS-3D preconditioned conjugate gradient was used with incomplete Cholesky (IC) factorization as preconditioner. In [65] a geometric multigrid (GMG) is considered as an alternative solver for a forward problem in EIT without CEM. Whilst using GMG to solve such problems on simple geometries is

straight-forward, this is not so for complicated domains (such as the human head, see [52], [9]) with discontinuous and/or anisotropic coefficients. In particular, it requires the generation of a hierarchy of finite element meshes which can be vastly expensive and time-consuming.

AMG (see [137], [138], [154]) is a highly attractive plug-in solver for 3D problems posed on irregular domains. Popularized by Ruge and Stüben in the 1980s, the approach is derived from traditional multigrid principles (see [21]), but, crucially, does not require the user to supply geometric information associated with a hierarchy of finite element meshes. Convergence theory is largely based on heuristic arguments and limited to the class of so-called M-matrices. An SPD matrix $\boldsymbol{K} \in \mathbb{R}^{n\times n}$ is an M-matrix if $\boldsymbol{K}(i,i) > 0, i = 1:n$, and $\boldsymbol{K}(i,j) \leq 0, i, j = 1:n, i \neq j$.

However, the resulting scheme has optimal work complexity and provided that basic criteria are satisfied, it can be applied as a black-box preconditioner, i.e. without tuning parameters.

The performance of an AMG method as a preconditioner for CG solver has been compared with more traditional IC preconditioner. The speed of the forward solvers are improving substantially by using this AMG scheme. To understand the concept of AMG first we describe the geometrical multigrid method.

5.3.1 AMG preconditioned conjugate gradient

In contrast to GMG, AMG do not need FE meshes with hierarchical grids. AMG still has the most advantages of GMG. AMG is an optimal solver with optimal time and memory complexity, which is especially suited for sparse linear system of equations with large condition number. In dealing with a complex geometry such as human

brain, the coarsest grid in GMG is too large to be solved efficiently by a direct solver. Instead of different grid level, AMG uses the finest grid and produces all system matrices and right hand sides related to coarser levels numerically. This is called set up stage for AMG. In this chapter we are using a ready to use AMG scheme provided by FEMLAB [46]. Here is a brief description of a V-Cycle of AMG as a base for the method. We skip many details i.e., set up stage of AMG. A V-cycle of AMG can be expressed as follows

Data: Linear system of equations

Result: An approximation solution of the equations

Relax ν_1 times on the fine grid $\boldsymbol{K}_2\boldsymbol{x}_2 = \boldsymbol{f}_2$ (for example using Gauss-Seidel forward) ;

Calculate the defect $\boldsymbol{r}_2 = \boldsymbol{K}_2\boldsymbol{x}_2 - \boldsymbol{f}_2$;

Project the defect $\boldsymbol{r}_1$ onto the coarse grid $\boldsymbol{r}_1 = \boldsymbol{I}_1^2\boldsymbol{r}_1$;

Solve the coarse grid problem $\boldsymbol{K}_1\boldsymbol{v}_1 = \boldsymbol{f}_1$;

Project the coarse grid correction $\boldsymbol{v}_1$ onto fine grid $\boldsymbol{v}_2 = \boldsymbol{I}_2^1\boldsymbol{v}_1$;

Update $\boldsymbol{x}_2$ by $\boldsymbol{v}_2$, $\boldsymbol{x}_2^{\text{new}} = \boldsymbol{x}_2 - \boldsymbol{v}_2$;

Relax ν_2 times on the fine grid $\boldsymbol{K}_2\boldsymbol{x}_2 = \boldsymbol{f}_2$. (for example using Gauss-Seidel backward) ;

Algorithm 4: A V-cycle for AMG

Here we are not using AMG as an iterative solver, it is used as a preconditioner for PCG . It is essential to use Gauss-Seidel forward in pre-smoothing and Gauss-seidel backward in post-smoothing step to obtain symmetric preconditioner, so it can be used for PCG.

In [104] and [72], similar forward problems with simple Neumann boundary conditions are studied. The first work reports on the efficiency of AMG as a solver for a

finite difference discretization, which does yield an M-matrix. The system matrix for the forward problem in the complete electrode model, to be discussed below, has a slightly different structure. This is the first time that AMG has been investigated as a solution methodology for it. Our numerical experience reveals that AMG can be applied effectively as a black-box preconditioner for the original system matrix despite the presence of positive off-diagonal entries which violate the M-matrix property.

M-Matrix property for CEM

Attention must be paid to the efficiency of the solution of (5.12) since it must be solved for a number of right-hand sides, corresponding to different current patterns. For brevity, we write the system (5.12) as $\boldsymbol{K}\boldsymbol{x} = \boldsymbol{f}$. Note that since the problem is well-posed (see [150]), $\boldsymbol{K}$ is symmetric positive definite (SPD). We employ CG as a solver and use a single V-cycle of AMG as a preconditioner. Since the contact impedances and the averaged conductivity coefficients are positive, it follows immediately from the above definitions and the definition of the standard linear basis functions (e.g. see [33]) that,

- $\boldsymbol{K}_M(i,i) > 0, \boldsymbol{K}_Z(i,i) > 0$, for $i = 1:n$,
- $\boldsymbol{K}_D(l,l) > 0$ for $l = 1:L$,
- $\boldsymbol{K}_Z(i,j) \geq 0$ for $i, j = 1:n$,
- $\boldsymbol{K}_V(i,l) \leq 0$ for $i = 1:n, j = 1:L$.

All these properties have consequences for AMG. Note that since $L << n$, $\boldsymbol{K}_V$ and $\boldsymbol{K}_D$ represent only a few rows and columns of the whole coefficient matrix. The success of any multigrid preconditioner is thus determined by the properties of $\boldsymbol{K}_M + \boldsymbol{K}_Z$.

Here, $\boldsymbol{K}_Z$ and $\boldsymbol{K}_M$ contribute positive off-diagonal entries to K, violating the M-matrix property.

However, $\boldsymbol{K}_Z$ is extremely sparse if the number of electrodes is small. In practice, the number of significant positive off-diagonal entries contributed by $\boldsymbol{K}_Z$ is small. Here we examine the use AMG as a preconditioner for CEM model of forward ERT problem.

5.4 Numerical results

5.4.1 Cylinder test example

In ERT applications, the *time cost* of solving the forward problem is the main topic in this section. To illustrate the real benefits of using the suggested solution scheme, we present numerical results using an optimized commercial code. All the experiments in this sections were performed on a unix machine in Matlab using FEMLAB (see [46]) and its integrated AMG software. For CG, we use a zero initial guess and terminate the iteration when the residual error 10^{-8}.

To test the performance of the preconditioner with respect to mesh size, with fixed conductivity distribution, we repeat the experiment on the cylinder. The cylinder has a length of 3 cm and diameter of 2 cm. Anisotropic conductivity of $\hat{\sigma} = \texttt{diag(1,2,3)}$ is assigned for all three cylinders (with different node numbers). Iteration counts and solve times (in elapsed seconds) for unpreconditioned CG are listed in Table 5.1. Results with AMG preconditioning are given in Table 5.2.

Here, ‘set-up’ refers to the initial process of assembling the components of AMG. It is performed once, outside the CG iteration, so the total time cost in Table 5.2 is the sum of the last two columns.

Table 5.1: Unpreconditioned CG, cylinder example

n	iter	solve time
1,060	178	0.21
10,441	344	5.08
93,209	724	149.90

Table 5.2: CG-AMG iteration, cylinder example

n	iter	set-up time	solve time
1,060	10	0.03	0.11
10,441	14	0.31	1.98
93,209	14	20.60	13.60

Table 5.3: CG-IC iteration, cylinder example, $n = 93,209$

ε	iter	fac. time	solve time
10^{-1}	396	3.3	196.75
10^{-2}	97	262.4	67.70
10^{-3}	41	5,617.0	42.30

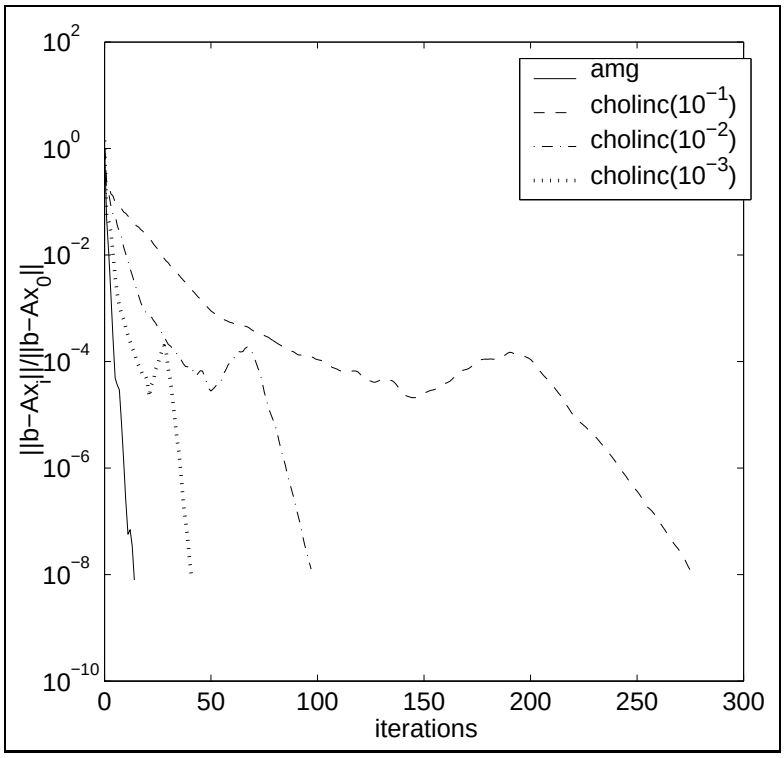

Figure 5.2: Convergence of CG with AMG and IC preconditioning.

In Table 5.3 we list, for a fixed problem size, iteration counts for CG iteration with IC preconditioning. Here, ε denotes the drop tolerance parameter. The results illustrate the fact that better convergence is obtained by allowing more fill-in. However, factorization time increases unacceptably. A disadvantage for non-specialists is that ε needs to be tuned to the problem at hand. One does not know, a-priori which value of ε will yield the quickest solution time. In this example, doing no preconditioning at all is actually faster than performing the factorization.

Convergence rates of both preconditioning schemes are compared in figure 5.2. Note that in the AMG experiment, no parameters are tuned. It is applied as a black-box. The key observations are that the time cost grows linearly with respect to the problem size and the convergence rate is optimal.

5.4.2 Example of the head model

In this section we examine the efficiency of the proposed preconditioning scheme for a challenging real-life application, involving a complicated geometry. Specifically, we are interested in the use of ERT for monitoring cryosurgery (see [114]), a technique that uses freezing to destroy tumorous tissues. We focus on the human head which contains tissues with highly discontinuous conductivity coefficients. The head mesh and the electrode models were generated by Nick Polydorides earlier in [122].

In this simulation, we are interested in evaluating changes in voltage measurements induced by the introduction of a spherical ice ball, (representing frozen tissue) into the brain (see [127], [114].) We solve the complete electrode forward problem on two finite element meshes, labelled M1 and M2. The first has 9,063 nodes and 44,304 elements (also used in [122]) and the finest one has 59,372 nodes and 327,015 elements. To begin, we solve the problem with the conductivity coefficients prescribed in Table 5.4. Next, we introduce into the domain, an ice ball with conductivity $10^{-5}\,Sm^{-1}$, and diameter $15\,mm$. We label these models, on meshes M1 and M2, MP1 and MP2 respectively. In all the experiments, a total of sixteen electrodes are used and an opposite current pattern of $1\,mA$ is applied. The arrangement of the surface electrodes is shown in figure 8.2.a and the ice ball is centered at the point $(100, 100, 100)$. A cross section of the conductivity map is shown in figure 8.2.b, the plot was produced by MayaVi [128].

Table 5.5 summarizes the performance of CG with IC preconditioning for the forward problems constructed on both meshes, with and without ice. Again, the choice of the drop tolerance ε for the factorization plays a key role in the time cost of each solution. Note however, that since for each forward problem one needs to solve the same lin-

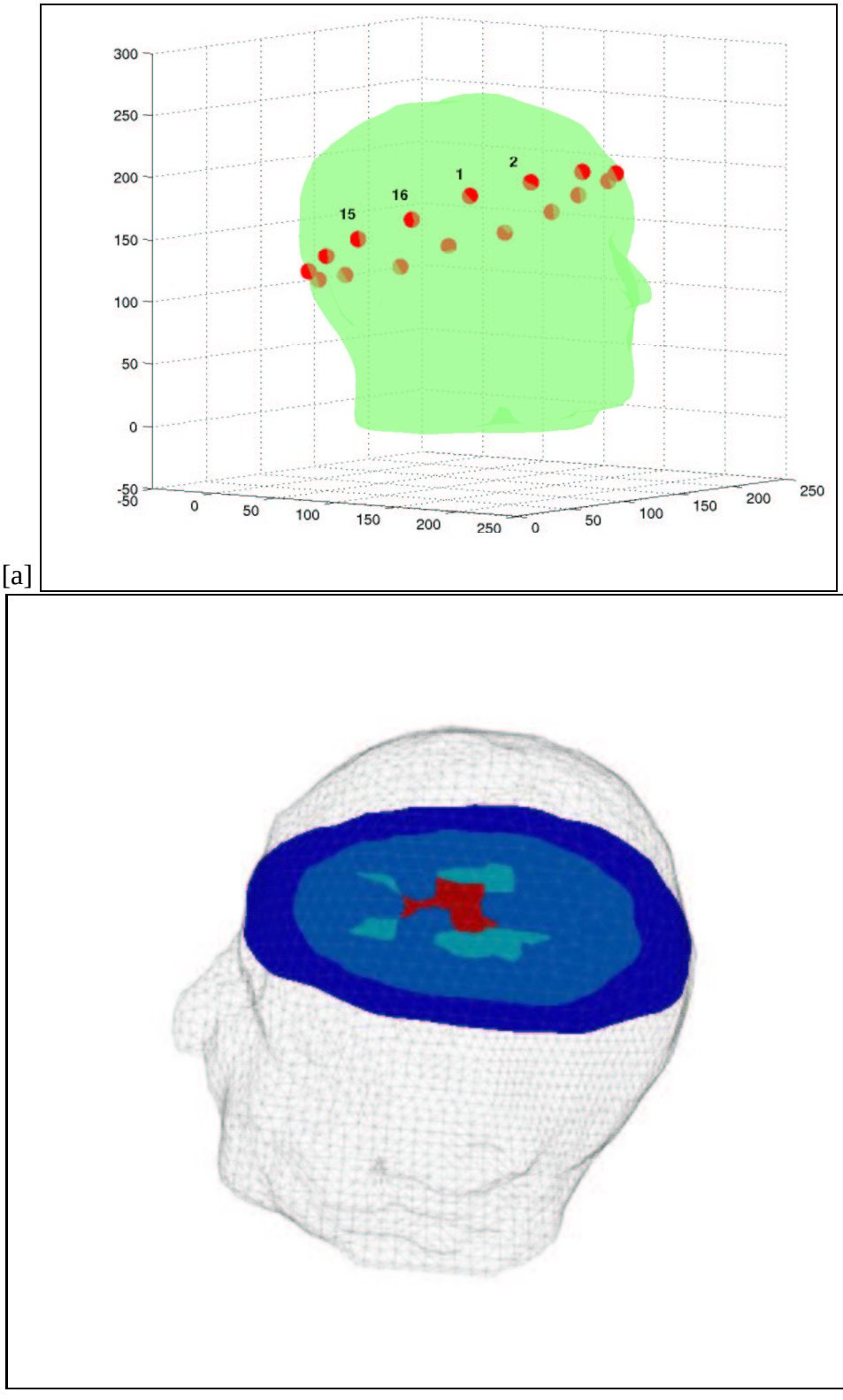

Figure 5.3: Arrangement of 16 surface electrodes, numbered anti-clockwise (a) and a cross section of conductivity map of the brain (b)

Table 5.4: Conductivity coefficients for the head model in Sm^{-1}

Tissue	Conductivity
scalp	0.172
skull	0.067
csf	1.540
gray matter	0.345
brain	0.150

ear system of equations with several right hand sides (different current patterns), this complicates the choice of ε. The results presented below are averaged over fifteen different right-hand sides. Overall, the choice $\varepsilon = 10^{-3}$ proved most efficient. However, the optimal choice is hard to ascertain and depends on each individual problem.

Table 5.6 shows the performance of CG with AMG preconditioning for the same experiments. Comparing the time costs of the two approaches, we see that the CG-AMG method is significantly faster.

Table 5.5: CG-IC iteration, drop tolerance $\varepsilon = 10^{-3}$

	iter	fac. time	solve time
M1	849	12.21	45.31
MP1	851	12.04	45.62
M2	2,856	430.25	1,305.68
MP2	3,100	420.91	1,411.32

Finally, we increase the size of the ice ball from zero to a maximum volume of $1cm^3$, in twelve steps, and evaluate the measurement voltage during the freezing process. In this case we use mesh M2. In the first step the initial guess for the CG iteration to solve the forward problem is set to zero. In each of the subsequent eleven steps we use the solution of the forward problem from the previous step as an initial guess. This

Table 5.6: CG-AMG iteration

	iter	set-up time	solve time
M1	16	0.36	1.81
MP1	18	0.36	2.01
M2	20	6.06	12.90
MP2	21	6.06	13.46

also helps to reduce the time cost of the total solve. The time needed to solve the first forward problem (one current pattern) is 19.26 sec. The average time for each of the eleven remaining forward problems is only 8.36 sec.

Figure 5.5 shows the electric potential distribution when electric current is applied between two electrodes. Figure 5.6 shows the electric current density when two opposite electrodes are excited. The FE mesh is also shown in figure 5.4.

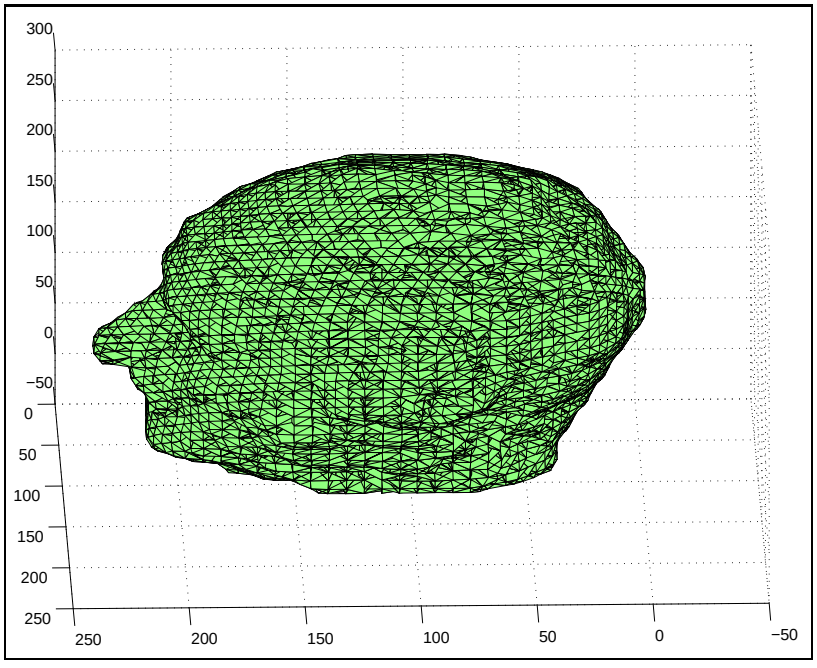

Figure 5.4: Mesh of the head

Figure 5.7 shows that the voltage difference between electrodes 1 and 8 (see figure

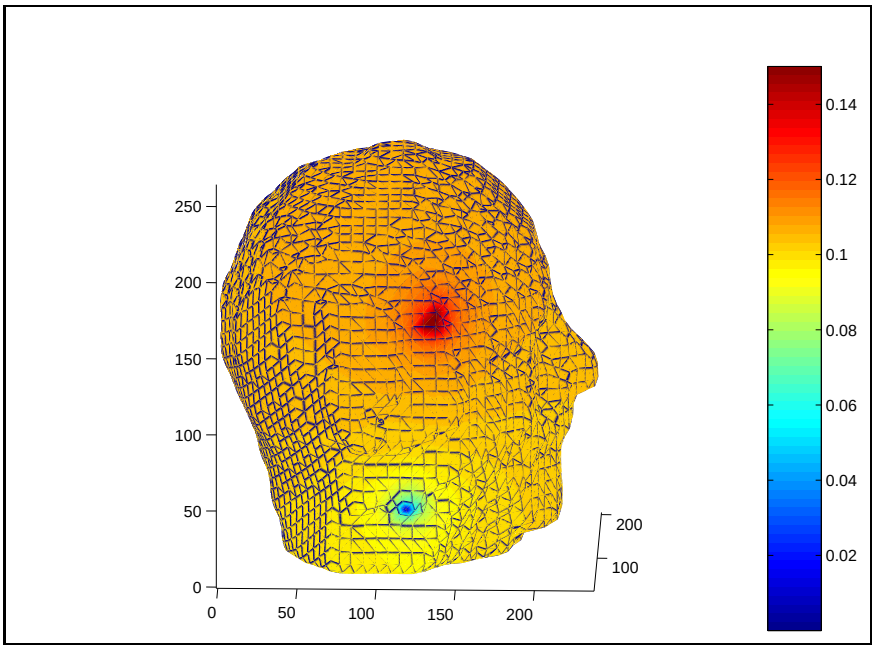

Figure 5.5: The electric potential distribution (in mv) on the surface for the head model with two electrodes excited

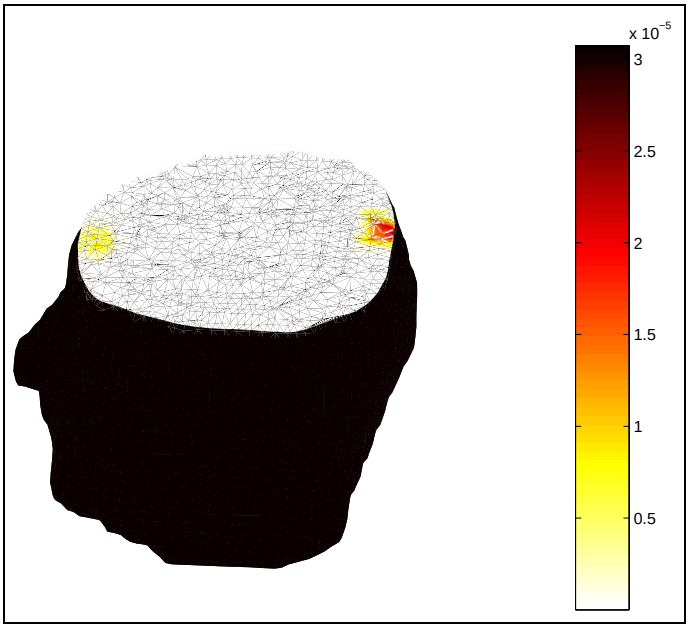

Figure 5.6: Current density when two opposite electrodes are excited

8.2) when the current source and sink electrodes are numbers 3 and 10. The voltage difference increases almost linearly with the volume of the ice ball. A similar observation has been reported in [127]. The measurement voltages for the other electrodes exhibit the same behavior.

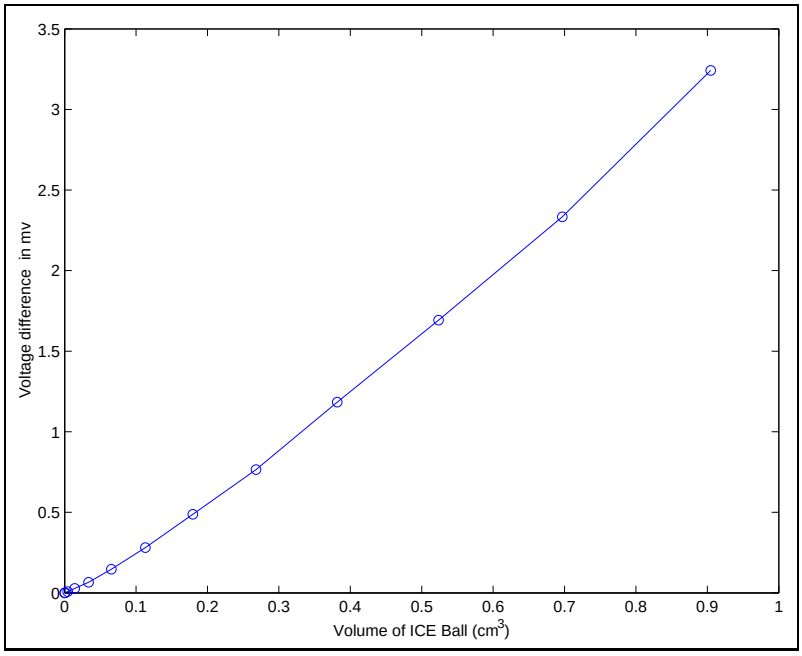

Figure 5.7: Voltage differences with respect to volume of the ice ball, the voltage difference between electrodes 1 and 8 when the current is applie to electrodes 3 and 10

Figure 5.8 shows the saturation of the voltage measurement when we change the conductivity of a region.

5.5 Discussion

We have described the application of AMG as a black-box preconditioner for the complete electrode model, a forward problem arising in ERT applications. With further

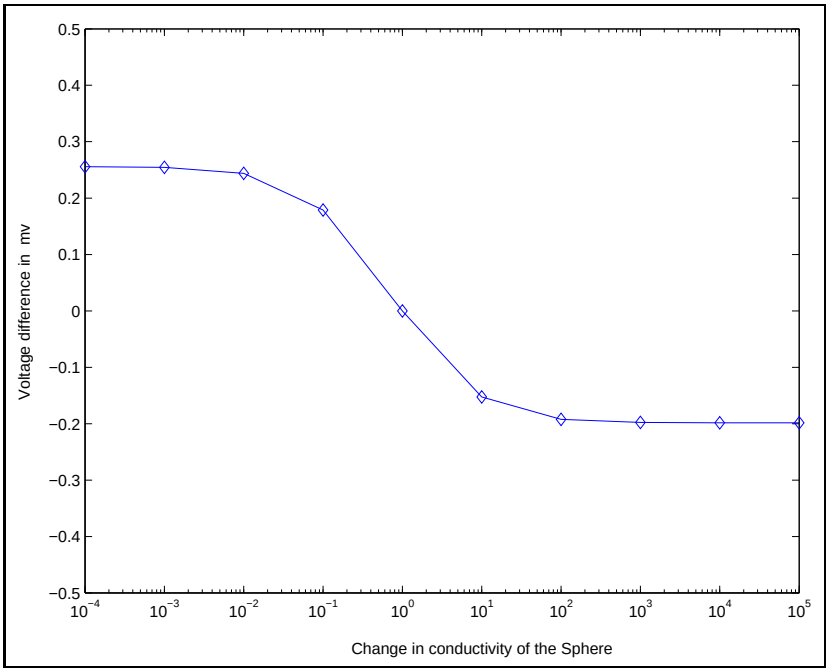

Figure 5.8: Voltage differences with respect to volume of the ice ball, the voltage difference between electrodes 1 and 8 when the current is applie to electrodes 3 and 10, shows a satuaration type curve

study the AMG scheme can be used for complex condutivity in EIT and the eddy currernt problem in MIT. Numerical results illustrate that with this preconditioning scheme, the convergence of CG is independent of the mesh size and highly robust with respect to jumps in conductivity coefficients. Further, it offers significant advantages over traditional incomplete factorization methods. Work complexity is optimal with respect to the problem size and no parameters require tuning. As a case study we considered the feasibility of using ERT for cryosurgery monitoring. The use of AMG as a preconditioner for the forward problem leads to a significant decrease in the time cost of solving the image reconstruction problem. Our numerical experience shows if $\boldsymbol{K}_Z$ includes very large positive numbers(for example contact impedance smaller than 10^{-6} for homogeneous conductivity of 1) the AMG preconditioned CG will not converge, the same problem will occur with IC preconditioned CG. This is not only because of the violation of the M-Matrix but also the poor condition number of the system of equations. Physically when the contact impedance is very small, it is better to change the formulation to point electrode model, and AMG works very well for a point electrode model as it has been reported earlier [148]. For an acceptable (practical) range for the contact impedance value number of iteration of AMG preconditioned CG is almost steady. One of the most challenging problems in brain EIT is to solve the large forward problem. Our CG-AMG did improve the speed of the forward solvers. Application of parallel computing in CG-AMG would be the next step to further improve also speed of the forward solvers.

Chapter 6

ELECTRICAL CAPACITANCE TOMOGRAPHY

Electrical capacitance tomography (ECT) attempts to image the permittivity distribution of an object by measuring the electrical capacitances between sets of electrodes placed around its periphery. Image reconstruction in ECT is a nonlinear and ill-posed inverse problem. Various regularized linear image reconstruction methods have been used for ECT. The linear reconstruction techniques are fast and are able to create satisfactory images for low contrast permittivity distributions. The saturation property of the inverse problem in ECT for higher contrast permittivity distribution means that linear reconstructions techniques are unable to create suitable images. In this thesis, we tackle the problem of nonlinearity, and we use regularization techniques to overcome the ill-posedness. We apply smoothing Tikhonov type regularization for low contrast and total variation regularization when there are jumps in permittivity. We have implemented a regularized Gauss-Newton scheme for nonlinear image reconstruction. The forward problem has been solved in each iteration using FEM and the Jacobian

matrix is recalculated using an efficient method based on the adjoint field method. The results from experimental ECT data demonstrate an advantage of total variation (TV) regularization for sharp edges, and improvement on the image quality using nonlinear reconstruction method.

Potential applications include monitoring of oil and gas mixtures in oil pipe lines and flow measurement in pneumatic conveying [44], [43], [3]. Assuming an electrostatic approximation, valid for the range of frequency used in practise, the problem is equivalent to the inverse conductivity problem of Calderón [27]. Landweber's linear iteration, "linear back projection", regularized one step reconstruction method have been applied to the reconstruction of images from experimental ECT data, [175], [176], [93]. In [24], [68] the authors studied the nonlinear inverse problem for simulated ECT data. In [165] an adaptive method has been used to calculate the regularization parameter in regularized Gauss-Newton reconstruction, which claims to improve the edge detection in ECT images compared with using one regularization parameter in all iteration steps. The regularization parameter has been studied using the L-curve method in [54] for regularized Gauss-Newton and simulated ECT data. For two phase materials, shape reconstruction techniques such as monotonicity shape reconstruction [156], level set method [39], [31] and linear sampling methods [26] have some advantages over the image reconstruction methods, as the prior assumption of two phase permittivity can be included effectively.

Most commonly used nonlinear image reconstruction techniques for electrical imaging [120] are based on repeated linearization and nonlinear iterative steps. In this thesis we show experimental results as well as some numerical results for a new ECT program (in Matlab) which has been developed for nonlinear ECT reconstruction. For mesh generation we use a QMG [102] mesh generator adapted for ECT sensor geom-

etry in previously released EIDORS ECT [14].

We demonstrate the application of TV regularization to reconstruct sharp edges and the jumps in permittivity using both simulation and experimental data.

6.1 ECT system

A typical ECT sensor [177] comprises an array of conducting plate electrodes, mounted on the outside of a non-conducting pipe, surrounded by an electrical shield (figure 6.1.a). Figure 6.1.b shows an experimental ECT system [124] that has been used for part of the experimental data on this chapter. For metal walled vessels, the sensor must be mounted internally, using the metal wall as the electrical shield. Additional components include radial and axial guard electrodes, to improve the quality of the measurements and hence images. It is not necessary for the electrodes to make physical contact with the specimen, so ECT can be used on conveyor-lines, or externally mounted to plastic piping to reduce the risk of contamination.

6.2 Forward problem

The forward problem in ECT is the problem of calculating the capacitance matrix from given geometrical information of the sensor array and applied potential, as well as the guessed permittivity distribution of the cross section. Practical ECT systems are designed to reduce the external coupling between the electrodes. Many different ECT protocols are possible, depending on which combination of groups of electrodes are used. In a simple and commonly used protocol, each of the drive electrodes in turn is set to some fixed potential, the others set to zero, while the total charge is measured

[a]

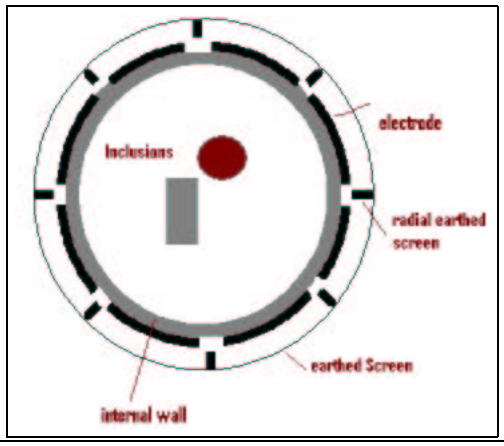

[b]

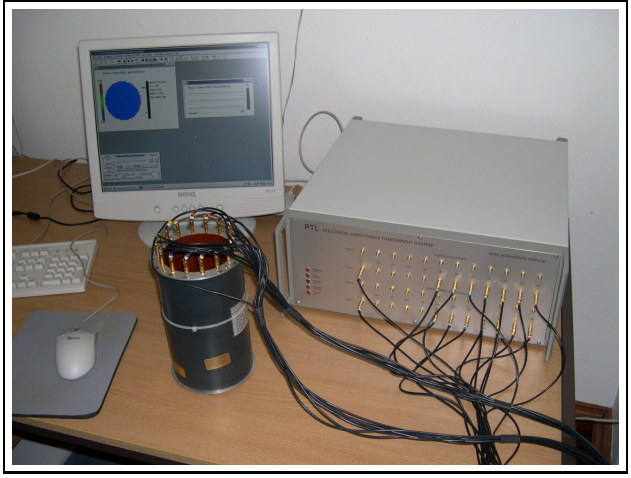

Figure 6.1: (a): Cross section through sensor showing electrodes and screen, (b): The PTL (Process Tomography Limited, Wilmslow, www.tomography.com) ECT system showing sensor, ECT system and host computer

on each of remaining electrodes (those electrodes are set to zero potential). There is a cylindrical screen around the electrode array set to zero potential, and a radial guard is placed in the gap between the electrodes. The shields are used to reduce the exterior capacitance coupling between the electrodes. For the mathematical model we use assumes the electrostatic approximation, $\nabla \times E = 0$, effectively ignoring wave propagation. We take $E = -\nabla u$ and in the absence of internal charges

$$\nabla \cdot (\varepsilon \nabla u) = 0 \ \ in \ \ \Omega \tag{6.1}$$

where Ω is the whole region of the modelling, u is electric potential, ε is dielectric permittivity. With the boundary condition

$$u = V_l \qquad \text{on } e_l \tag{6.2}$$

where e_l is the $l-$th electrode, held at the potential V_l, usually attached on the surface of an insulator. V_l is the potential for an excitation electrode and zero for sensing electrodes. In addition shields are set to zero volt [54]. The electric charge on the $l-$th electrode is given by

$$Q_l = \int_{e_l} \varepsilon \frac{\partial u}{\partial \mathbf{n}} dx^2 \tag{6.3}$$

where $\mathbf{n}$ is the inward normal on the $l-$th electrode, the capacitance is then $C_l = Q_l V_l$. We represent the permittivity as a piecewise constant function using FEM (first order triangular elements). In this study electrodes are relatively long and translationally invariant objects and a two dimensional model agrees well with measured data [69]. With finite element discretization of the boundary value problem we have a linear system of equations $\boldsymbol{Kx} = \boldsymbol{f}$, where the matrix $\boldsymbol{K}$ is the discrete representation of the

operator $\nabla \cdot \varepsilon \nabla$ and the vector $\boldsymbol{f}$ is the boundary condition term and $\boldsymbol{x}$ here is the electric potential in all nodes. This linear system of equations can be solved efficiently by using the Preconditioned Conjugate Gradient (PCG) method [122]. The forward problem in 2D ECT is not a large scale forward model, but our numerical experience shows the same kind of the advantages for CG method with AMG preconditioner compared to the CG with incomplete Cholesky as preconditioner, which may be helpful for 3D ECT forward modelling.

6.2.1 Some results of the forward solver

In figure 6.2.a one can see a typical mesh for an ECT system, and the electric potential distribution (shown in figure 6.2.b) when electrode 1 is set to +1 volt and the other electrodes set to zero. The numbering is used to identify electrodes, the electrodes numbered anticlockwise, starting at the electrode near to "3 o'clock" position (see figure 6.1.a). The ECT system considered in this chapter, in common with many experimental systems, has only 8 electrodes.

The vectors of the electric field are shown in 6.2.c (electrode 1 is set to +1 volt and others set to zero). The number of triangular elements used in forward model is 6400, and the number of elements in the region of interest for imaging is 725. In experimental ECT systems the capacitance data are normalized using calibration [174]. The normalized capacitance is $\lambda = \frac{C_{\text{meas}} - C_{\text{air}}}{C_{\text{high}} - C_{\text{air}}}$, where C_{air} is the capacitance measurement for the empty pipe and C_{high} is the capacitance measurement when the pipe is full of a material with high permittivity. C_{meas} is the absolute capacitance measurement.

Figure 6.3 shows the experimental data collected from a test example versus the results from the forward solver. In the test example we have a plastic rod (permittivity 1.8)

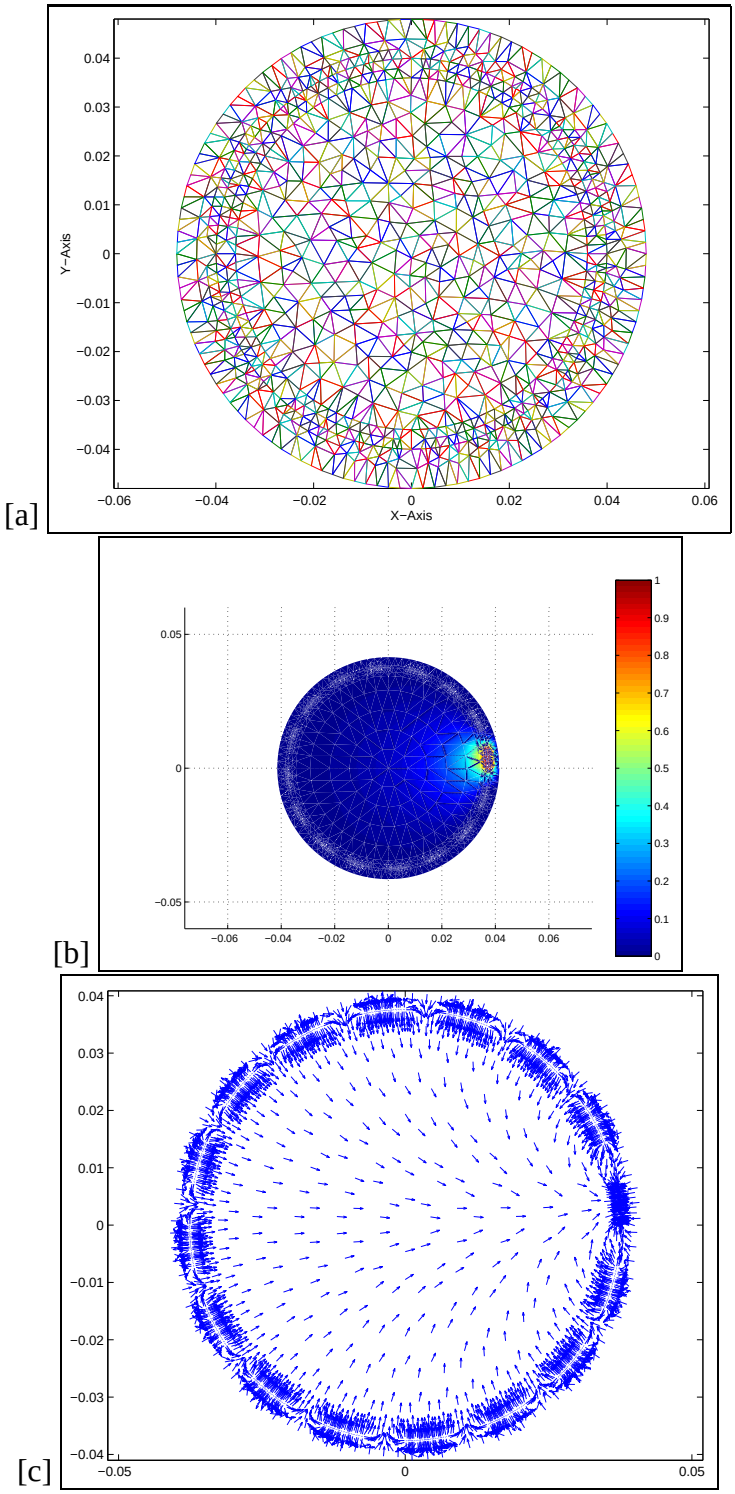

Figure 6.2: (a): Typical ECT mesh, (b): Electric potential distribution and (c): Electric field vector (for a 16 electrodes ECT)

close to wall and the measured data and simulated ones show good agreement.

Figure 6.4 shows the error between measured and simulated capacitance in figure 6.3.

Figure 6.5 shows another experimental test data collected from a test example verses the results from the forward solver. In the test example we have a plastic ring (permittivity 1.8) and the measured data and simulated ones shows a good agreement.

Figure 6.6 shows the percentage of the error between measured and simulated capacitance model in figure 6.5.

6.2.2 Discussion on boundary condition

A different boundary condition has been proposed for ECT by [165], [24]. The authors applied the Dirichlet boundary condition to the electrodes and a homogeneous Neumann boundary condition applied to the gap between the electrodes.

The charge measured on the $l-th$ electrode Q_l is a combination of Q_l^{int}, Q_l^{ext}

$$Q_l^{ext} = \int_{e_l} \varepsilon \frac{\partial u^{ext}}{\partial \mathbf{n}} dx^2 \tag{6.4}$$

and

$$Q_l^{int} = \int_{e_l} \varepsilon \frac{\partial u^{int}}{\partial \mathbf{n}} dx^2 \tag{6.5}$$

where u^{int}, u^{ext} are on the interior and exterior surface of the electrode. So this is a result of coupling both through the interior and exterior of the sensor. As the gap between electrodes are very small we make the simplifying assumption that permittivity changes inside of the sensor have negligible electric field exterior to the sensor. Indeed this is one design goal of the sensor system. To decouple the interior and exterior

[a]

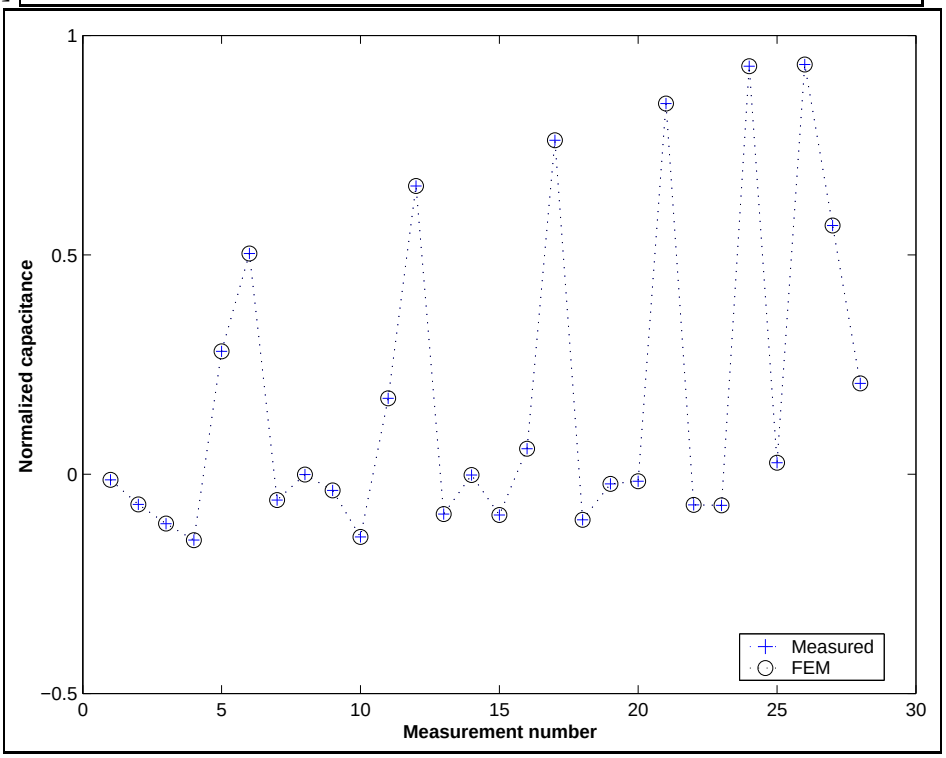

[b]

Figure 6.3: Experimental data collected from test example of (a) versus the FEM results

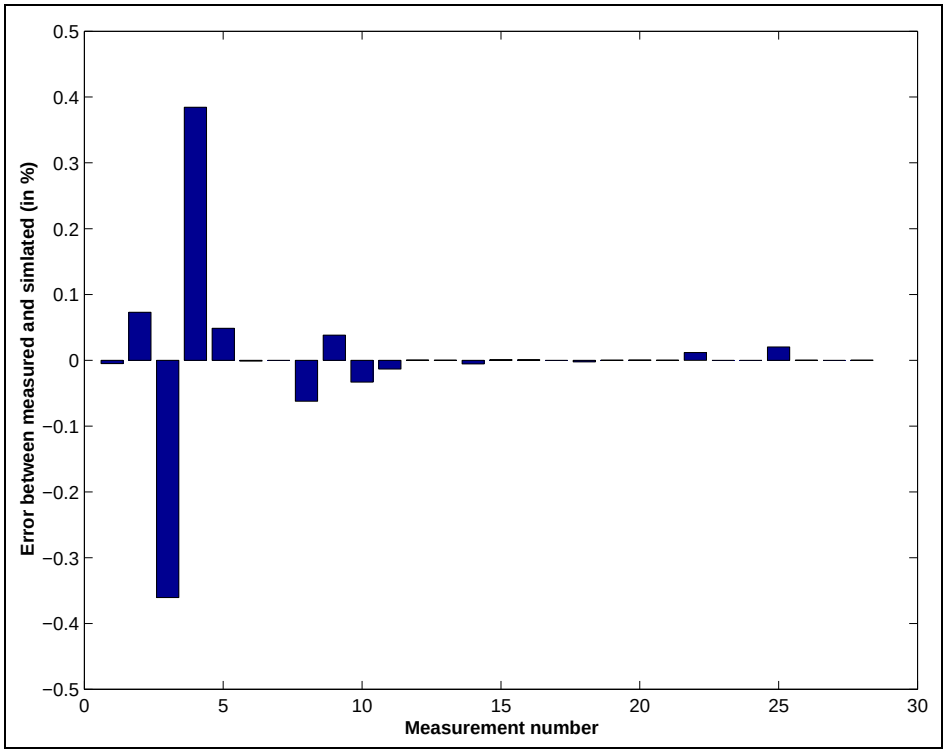

Figure 6.4: Percentage error between measured and simulated capacitance for the model of figure 6.3

[a]

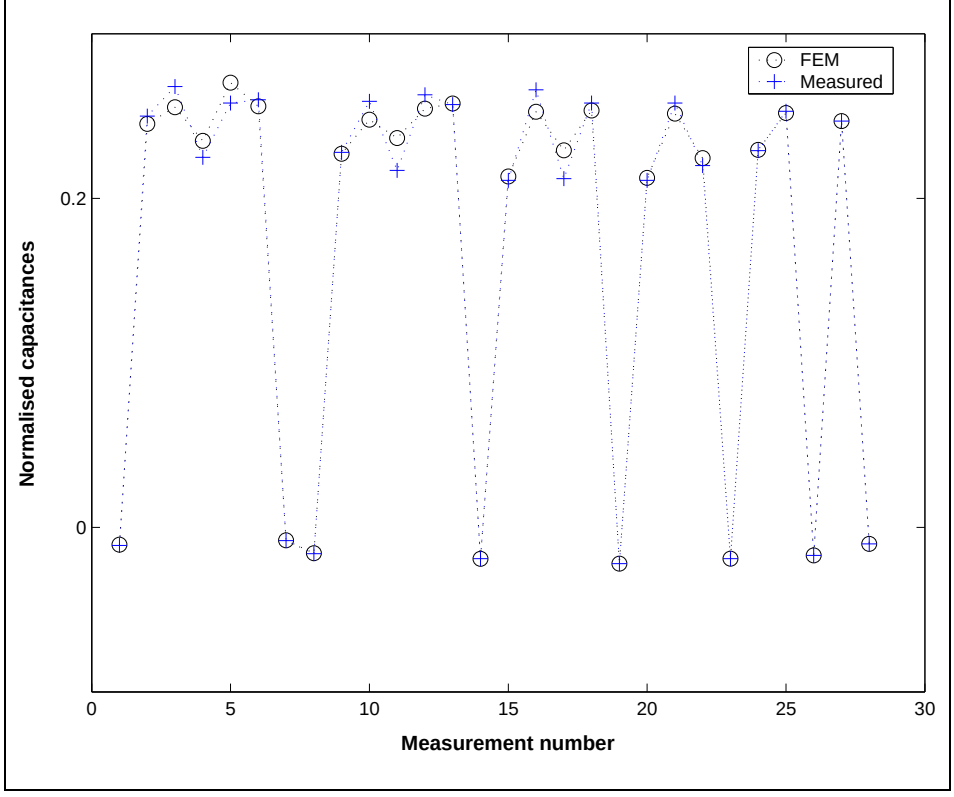

[b]

Figure 6.5: Experimental data collected from test example of (a) versus the FEM results

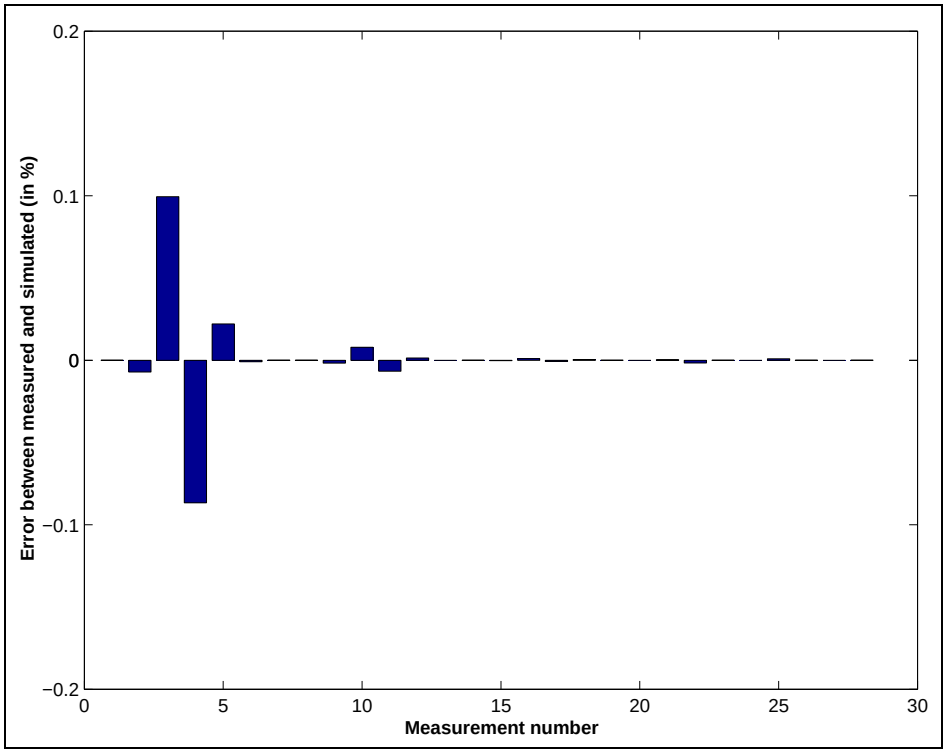

Figure 6.6: Percentage error between measured and simulated capacitances for the model of figure 6.5

fields we could assume a zero Neumann condition in the gaps between electrodes as [165], [24]. This means that Q_l^{int} is independent of ε inside the sensor, and can be found by calibrating the sensor using materials of known permittivity in the interior. The inverse problem of finding ε inside the sensor volume is now the classical problem of EIT, where the "conductivity" coefficient is to be determined from pairs of current and voltages data at the boundary of a domain. This is a more ideal assumption than the real ECT shielding.

6.3 Sensitivity analysis

We calculate the Fréchet derivative of the measured capacitance on the electrodes with respect to a perturbation in the permittivity. For our purposes we perform a simple perturbation calculation ignoring higher order terms. This can simply be extended to a formal proof using operator series [27], but here we give a simple derivation for completeness. Using Green's identity or for the less smooth potentials the weak form of $\nabla \cdot \varepsilon \nabla u = 0$, for any w

$$\int_\Omega \varepsilon \nabla u \cdot \nabla w dx^3 = \int_{\partial\Omega} w \varepsilon \frac{\partial u}{\partial n} dx^2. \tag{6.6}$$

Here dx^3 and dx^2 are volume and surface measures. In particular for $w = u$ we have the power conservation formula

$$\int_\Omega \varepsilon |\nabla u|^2 dx^3 = \int_{\partial\Omega} u \varepsilon \frac{\partial u}{\partial n} dx^2 = \sum_{l=1}^{L} \int_{e_l} V_l \varepsilon \frac{\partial u}{\partial n} dx^2 \tag{6.7}$$

hence

$$\int_\Omega \varepsilon |\nabla u|^2 dx^3 = \sum_{l=1}^{L} V_l Q_l. \tag{6.8}$$

This simply states that the power input is stored in the domain Ω. We now take perturbations $\varepsilon \to \varepsilon + \delta\varepsilon$, $u \to u + \delta u$, $Q_l \to Q_l + \delta Q_l$, Q_l here is collected charge in electrode l and $1 \leqslant l \leqslant L$ and L is the number of the electrodes, with the voltage in each electrode V_l held constant. Ignoring second order terms gives

$$\int_\Omega \delta\varepsilon |\nabla u|^2 \, dx^3 + 2\int_\Omega \varepsilon \nabla u \cdot \nabla \delta u \, dx^3 + O(\| \delta\varepsilon \|^2) = \sum_{l=1}^{L} \delta Q_l V_l. \tag{6.9}$$

Using this and equation (6.6) with $w = \delta u$ we get

$$\int_\Omega \delta\varepsilon |\nabla u|^2 \, dx^3 + 2\int_{\partial\Omega} \delta u \varepsilon \frac{\partial u}{\partial n} dx^2 + O(\| \delta\varepsilon \|^2) = \sum_{l=1}^{L} \delta Q_l V_l \tag{6.10}$$

In the boundary in the electrode position $\delta u = 0$ and in gap between the electrode we have $\frac{\partial u}{\partial \mathbf{n}} = 0$, so we can simplify the equation and have the desired result

$$\sum_{l=1}^{L} \delta Q_l V_l = \int_\Omega \delta\varepsilon |\nabla u|^2 \, dx^3 + O(\| \delta\varepsilon \|^2) \tag{6.11}$$

This gives only the total change in power, to get the change in charge on a particular electrode e when a voltage is driven in some or all of the other electrodes. This type of perturbation or linearized calculation will be familiar from the other linear inverse problems, for example in EIT [121], [84]. To get the change in Q on electrode e_i when e_j is driven, we consider potential u_i when e_i is driven and u_j when e_j is driven. Applying 6.11 to $u_i \pm u_j$ and subtracting gives

$$\delta Q_{ij} = \frac{1}{V_j} \int_\Omega \delta\varepsilon \nabla u_i \cdot \nabla u_j \, dx^3 + O(\| \delta\varepsilon \|^2) \tag{6.12}$$

where Ω is the perturbed region. Here ∇u_i and ∇u_j can be calculated by the solution of the forward problem when electrodes i and j are excited.

This sensitivity formula results in an efficient method for assembly of the Jacobian matrix. It confers a particular advantage when u is calculated using the FEM as the integral of gradients over elements is also calculated in the assembly of the system matrix K. To calculate the Jacobian matrix one must choose a discretization of the permittivity. We take the permittivity to be piecewise constant on triangular elements, in which case the sensitivity of measurement (i, j) to a change in triangle T_k is simply $S_d(T_k)\nabla u_i \cdot \nabla u_j$, as S_d is the area of the triangle. Figure 6.7 shows sensitivity plot between electrodes 1-3, 1-4 and 1-5 for an empty tank.

6.4 Inverse problem

In general the inverse problem in ECT is to reconstruct the permittivity distribution in the interior given the capacitance data from exterior electrodes. This is an ill-posed and nonlinear problem, and therefore hard to solve with noisy measurement data and error in simulation of the forward model. An *a priori* knowledge of the permittivity distributions may help to give an acceptable approximation solution. Prior knowledge is also a key to choosing the reconstruction scheme as there is no stable method to solve the inverse problem. One needs also consider the intended use of an ECT image when choosing the reconstruction method. For example sometimes an indication of the location of an object inside of the pipe is enough, in other case, it is important to create an accurate image of the shape of anomalies, and in some applications the absolute value of the permittivity distribution is required. In this section we study the linear and nonlinear inverse problem for ECT. Two main regularization techniques, Tikhonov type and Total Variations (TV) are also briefly discussed here. The major difference between the two regularization methods is that the TV does not smooth

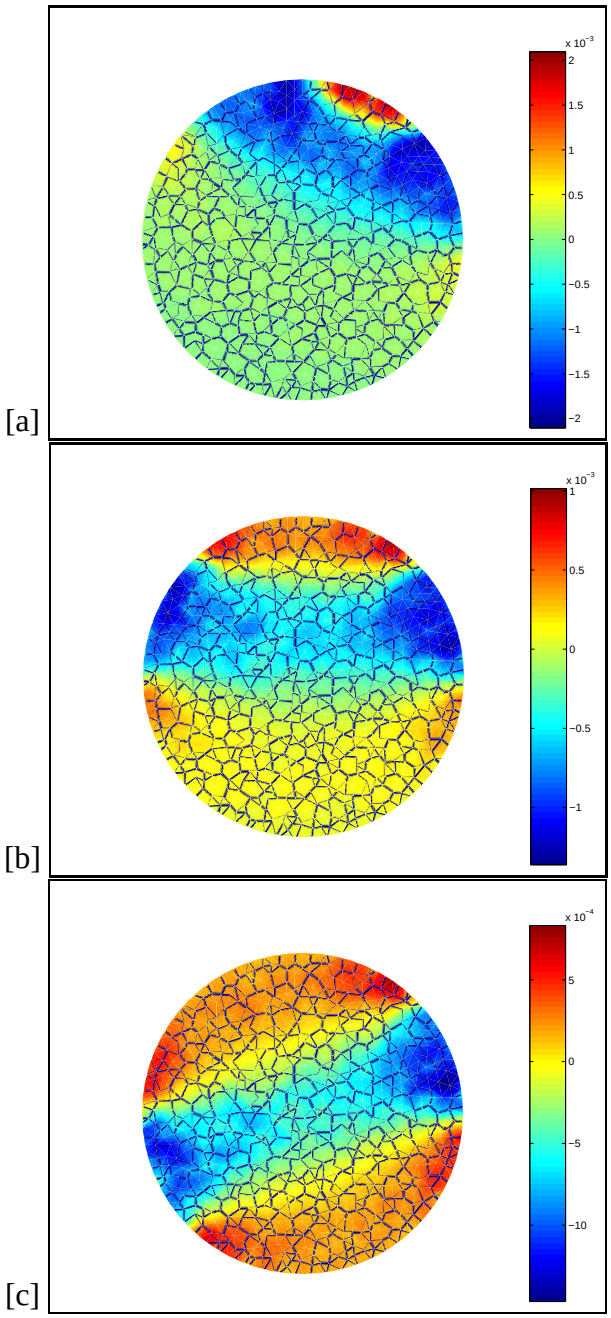

Figure 6.7: Sensitivity map between electrodes: (a): 1-3, (b): 1-4 and (c): 1-5, for the free space background

jump-discontinuities so that can improve the reconstruction of sharp edges and jumps dicontinuity in permittivity. It worth mentioning that the linear iterative methods, such as Krylov subspace methods [122] and Landweber [176] have an intrinsic regularization property.

6.4.1 Linear methods and regularization

When the linearity assumption fails consequently the linear reconstruction will not be able to produce accurate image.

In general the inverse problem in ECT is to reconstruct the permittivity map of the interior given the capacitance data from exterior electrodes. This is an ill posed and nonlinear problem, and hard to solve with noisy measurement data and errors in simulation of the forward model. The prior knowledge of the permittivity distributions may help to solve the problem to an acceptable approximation solution. Prior knowledge is also a key to choosing the reconstruction scheme as there is no a unique and reliable method to solve the inverse problem. The questions to be answered by an ECT image also determines which method must be used. For example sometimes an indication of where about an object inside of the pipe is enough, in other cases it is important to create an accurate image of the shape of anomalies and sometimes the absolute value of the permittivity distribution is required. In this section we study two major categories of the inverse problem in ECT, linear and nonlinear. Two main regularization techniques, Tikhonov type and total variation also subject of a brief discussion here. The major difference between the two regularization methods is that the total variation does not smooth jump-discontinuities. A common choice for the regularization matrix $\boldsymbol{R}$ is a discrete approximation to the Laplace operator, in which case the penalty term

is

$$R(\varepsilon) = \int_{\Omega_{in}} |\nabla \varepsilon(x)|^2 dx \tag{6.13}$$

Ω_{in} is the interior region and not includes the wall area. If the element number t_m has at least one vertex in common with elements $t_1, t_2, \ldots t_i$ and $i \neq m$ then $\boldsymbol{R}(t_m, t_{j=1:i}) = -1$ and $\boldsymbol{R}(t_m, t_m) = \sum_{j,j\neq m}(\boldsymbol{R}(t_m, t_j))$.

Figure 6.8 shows the reconstructed image from a plastic ring and a plastic rod (permittivity 1.8 for both ring and rod) in centre using one step Tikhonov regularization. As we decrease the regularization parameter the feature of the real object is more clear in the reconstructed image.

Total variation regularization

Although Tikhonov type regularization provides a good method to reconstruct smooth parameters both in terms of contrast and shape, it fails to reconstruct the sharp edges and absolute values for high contrast. TV regularization is a suitable method for both sharp edges and high contrast. Using TV regularization to reconstruct the sharp edges has been discussed in [15], [16] for EIT. The recovery of sharp edges in ECT using TV regularization is identical and just as important as EIT. In others word the TV functional is used to encourage blocky images as regularized solution. The TV functional of a continuum

$$TV(\varepsilon) = \int_{\Omega_{in}} |\nabla \varepsilon(x)| dx \tag{6.14}$$

Ω_{in} is the interior region and not includes the wall area. Here we choose to use minimum total variation method presented in [160]. Let the length of each edge *i* between

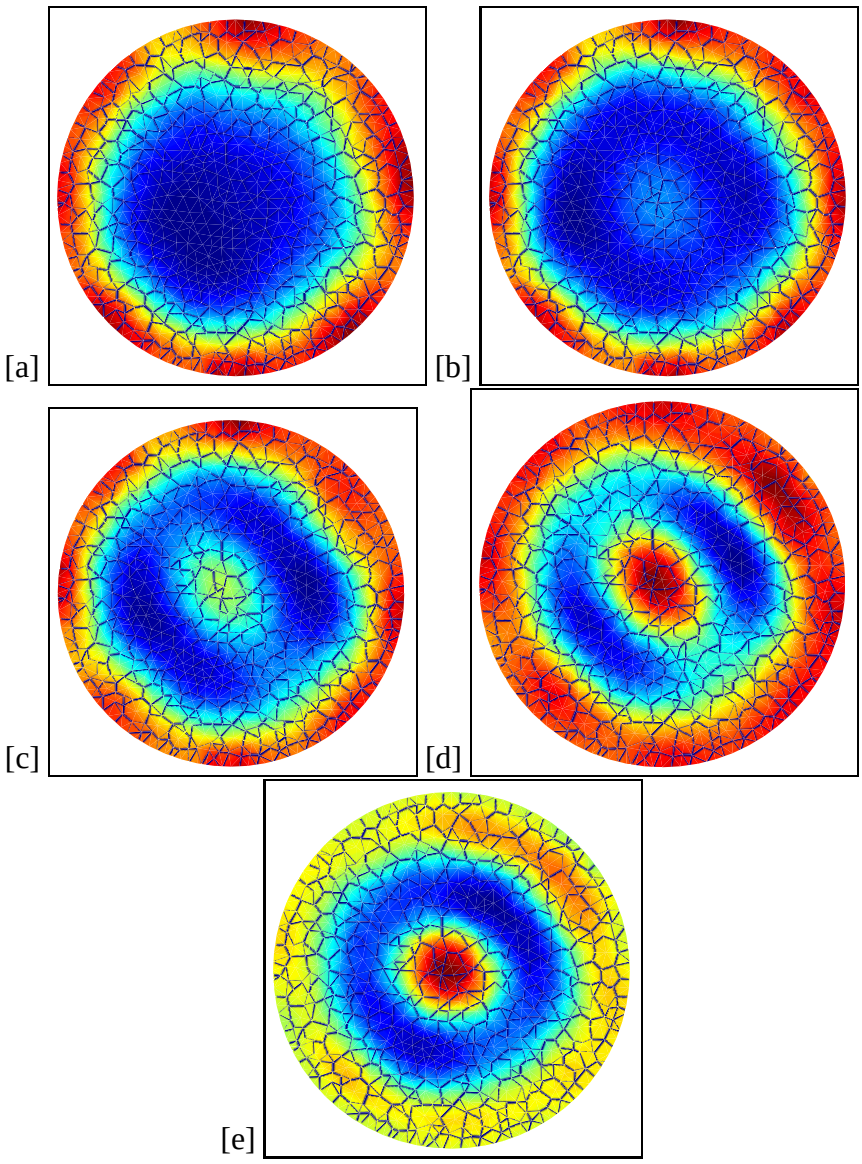

Figure 6.8: Reconstructed image when α is (a): $10^{-2}, (b) : 10^{-3}, (c) : 10^{-4}, (d) : 10^{-5}$, the target includes a ring and a rod at the centre of the ring with permittivity value of 1.6

two pixels be $d_i, i = 1,2,..,I$. The k-th row of the matrix $\boldsymbol{S} \in \mathbb{R}^{I \times P}$ (here I is number of edges and P is number of elements) is chosen to be $\boldsymbol{S}_k = [0,...0,1,...,-1,0,...,0]$, where 1 and -1 occur in the columns related to the triangle with common edge k. Each row of $\boldsymbol{S}_k$ has been weighted with length d_k of the edge k, where $\boldsymbol{T}V = S^T DS$ is the regularization matrix and D is a diagonal matrix with $D(k,k) = d_k$. The term $\| \boldsymbol{TV\varepsilon} \|$ gives an approximation to the total variation of the distribution ε [37].

6.4.2 Nonlinear inverse problem

In some ECT applications the permittivity changes are high, for example a mixture of oil and water. In this high contrast ECT problem, the linear method fails to solve the inverse problem properly. The predicted values using linearization (Jacobian matrix) has an error with respect to the perturbation and solving the forward problem. In order to show the nonlinearity of the capacitance changes with respect to the change in permittivity, we choose a circular object with 10 percent of the image area in centre of the pipe and perturbed its permittivity. Figure 6.9 shows the nonlinearity in terms of scaling. The lack of superposition is also an aspect of nonlinearity that makes it difficult to separate two objects near to each other using linear reconstruction. It is also clear that the saturation exhibited in this plot shows that the reconstruction of higher contrast permittivity for absolute values of permittivity is very difficult as the differences in measured capacitances are very small.

The sensitivity map changes as the background permittivity changes. Figure 6.10.b shows the sensitivity map between two opposite electrodes when the background is a permittivity distribution of figure 6.10.a, which includes an object with permittivity 8. This sensitivity map differs from the sensitivity map shown in figure 6.7.c for the free space.

[a]

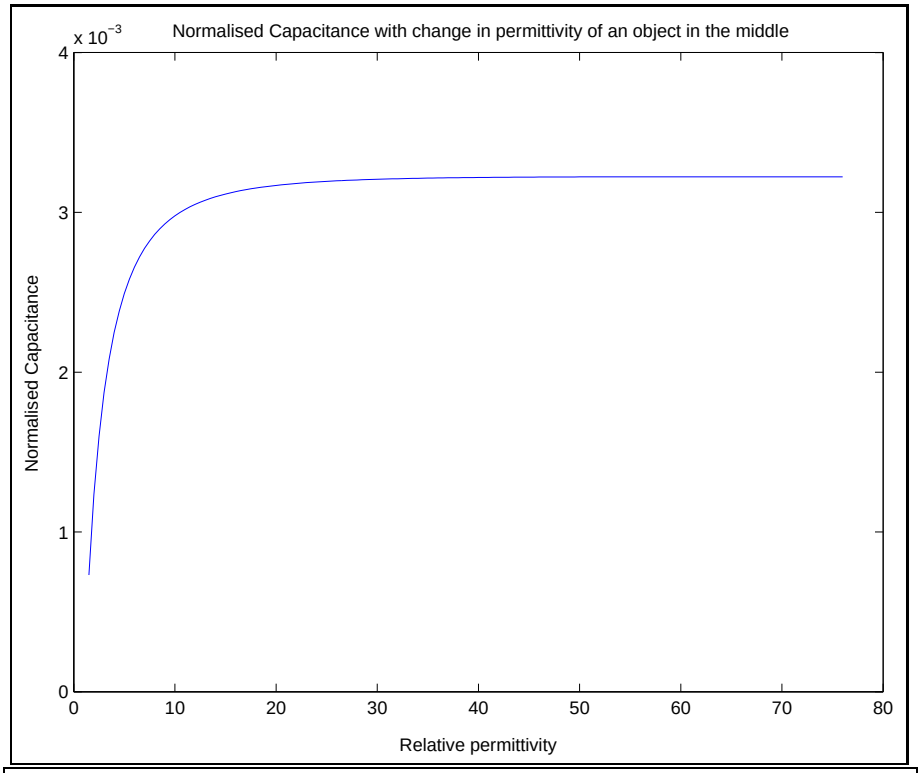

[b]

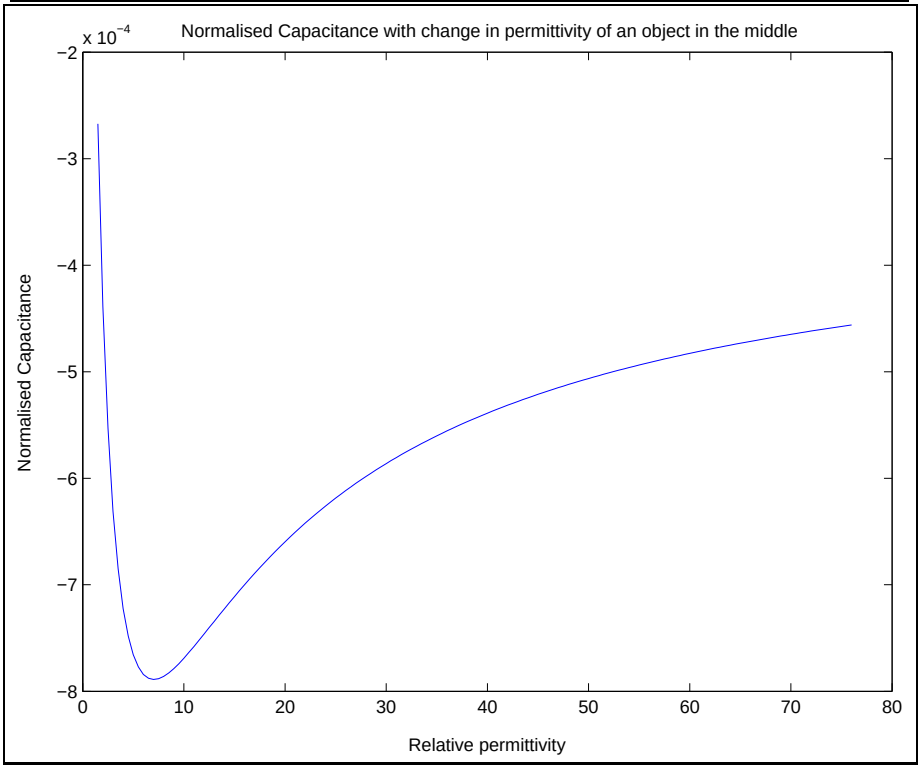

Figure 6.9: Capacitance measurement between electrodes (a): 1-3 and (b): 1-5 for perturbation of an inclusion

[a] 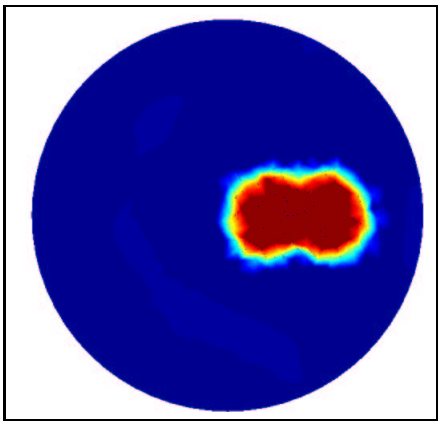 [b] 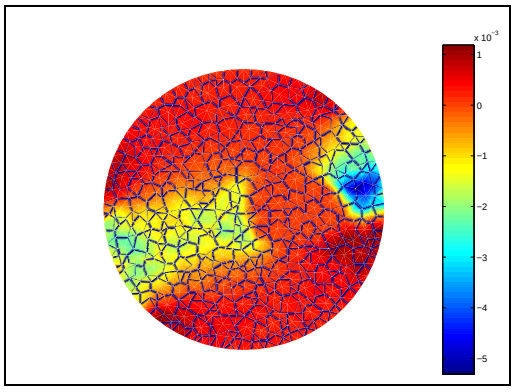

Figure 6.10: (a): Including an object with permittivity 8 to the free space background and (b): Sensitivity plot for the background is permittivity distribution in (a)

Figure 6.11.b also shows the change in sensitivity map between two opposite electrodes when the background is the permittivity distribution of figure 6.11.a, which includes a rod with permittivity 2.

[a] 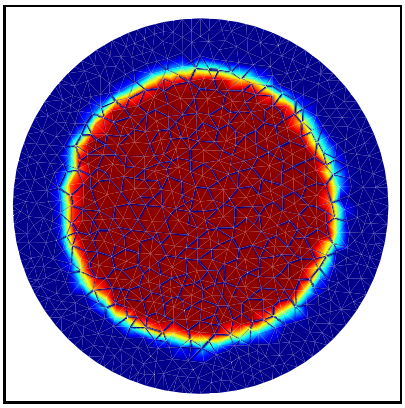 [b] 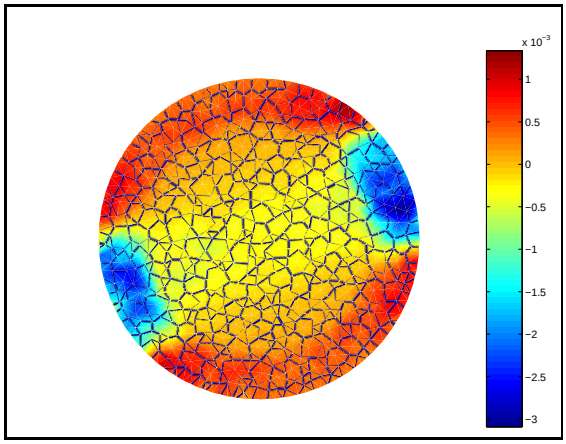

Figure 6.11: (a): Rod with permittivity 2 inserted in centre and (b): Sensitivity plot for the background permittivity distribution of (a)

High permittivity inclusions change the pattern of the electrostatic field between two electrodes. The change of the field pattern changes the sensitivity map. Change of the sensitivity map with the background permittivity distribution maks the requirement to update the sensitivity map (Jacobian matrix) in image reconstruction using non-linear

iterative method. The ill-posed inverse permittivity problem is very sensitive to any source of error (in model or in measurement data) that includes the error in computed Jacobian matrix.

6.5 Results

We solve the regularized inverse problem using an iterative method. Starting with an initial guess (permittivity of free space 1) the update formula in nonlinear iteration, described in equation (3.40), TV and Tikhonov regularization are also compared in some examples.

In order to validate the reconstruction software we have applied it to previously published experimental data by [175]. Figure 6.12 shows the reconstruction of the plastic rod in the centre, plastic rod near to the wall and two plastic rods and a plastic ring. Figure 8.9 is the reconstructed image of a plastic rod inside a ring of plastic which was also from the data published in [175].

Figure 6.13 shows the image reconstruction using synthetic (noise free) data generated by test model of figure 6.13.a. In figure 6.13.b one can see the image reconstruction using Tikhonov regularization method. Figure 6.13.c shows the image reconstruction for the same model when TV was used for the regularization. This example shows that TV regularization can help to improve the reconstruction of the absolute value of the permittivity. Tikhonov regularization is not suitable to reconstruct the absolute permittivity values of high contrasts. In this example regularized nonlinear iterative steps has been used, we stop the iterations when there was no more improvement in the convergence of the nonlinear solver for both cases.

Figure 6.14 shows reconstruction of real experimental data using nonlinear steps, wa-

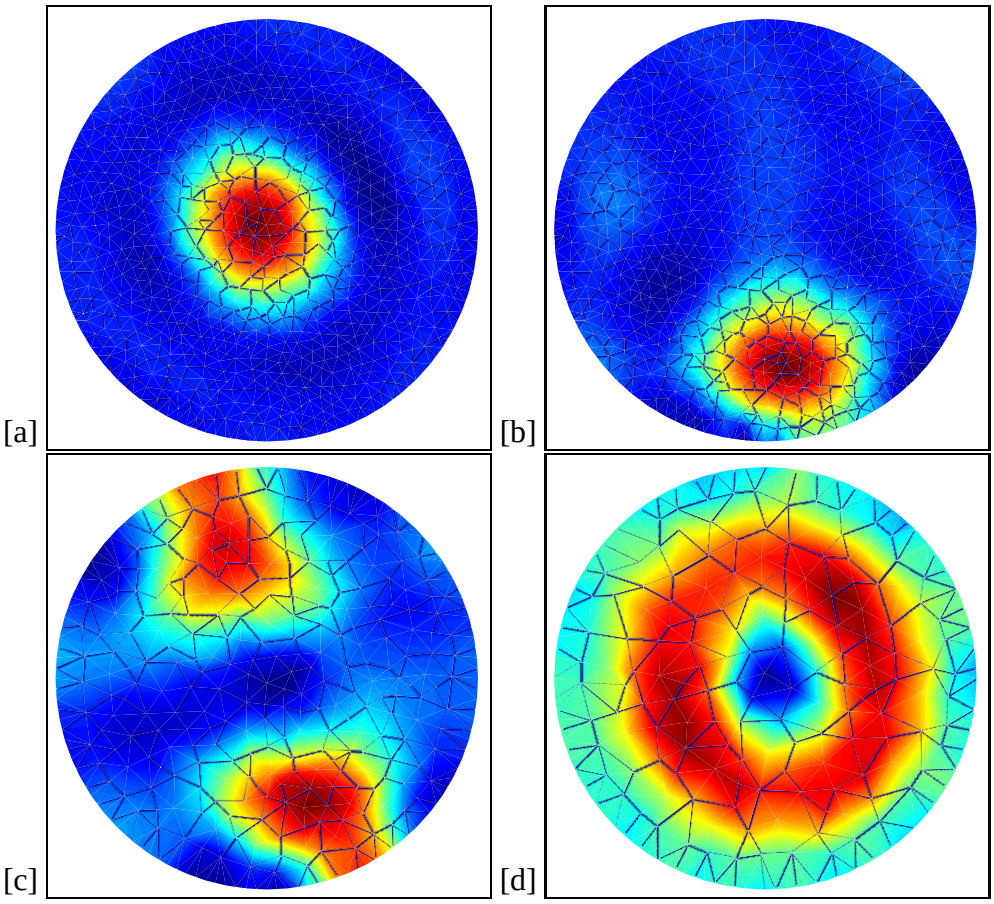

Figure 6.12: Reconstruction of plastic bar(s) and ring using regularized linear steps, permittivity 1.8 for plastic, figure (a) is a rod in centre, (b) a rod close to wall, (c) two rods close to wall and (d) a ring

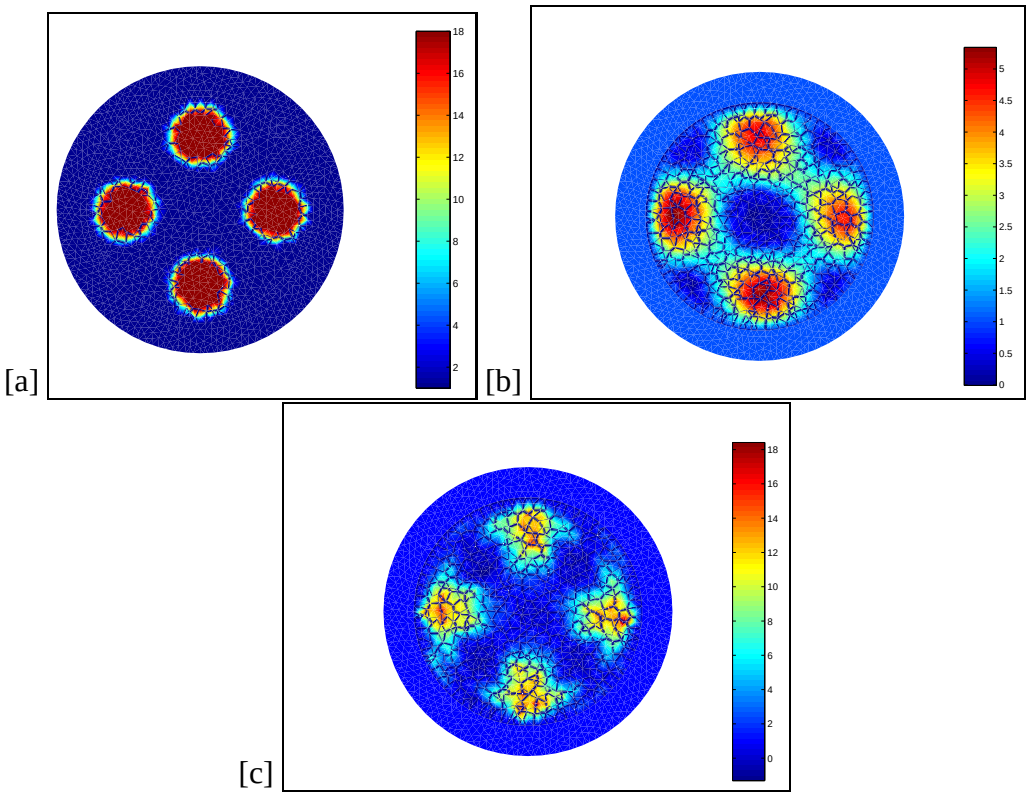

Figure 6.13: Results of reconstruction of simulated data (a): True model, (b): Image reconstruction using Tikhonov regularization and (c): TV regularization with noise free data.

ter (permittivity 80) inside of the glass tube (permittivity 3.5), here we used TV for the regularization with 16 iterative steps, the maximum value of the permittivity in this image is 9 and one can see the higher permittivity region (water) in the image in the centre but finding absolute value of the permittivity is rather complicated task as the changes in the measured capacitances are in the saturation part of typical sensitivity curve shown in figure 6.9. In experimental data (because of noise and saturation) it is hard to find the absolute value of high permittivity inclusions.

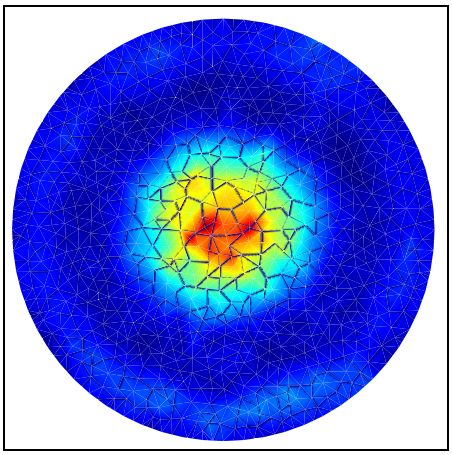

Figure 6.14: Reconstruction of water inside of a glass tube

In figure 6.15 the reconstruction of tube with 20 percent filled with glass (horizontal) , shows a model from reconstruction of a horizontal flow.

The experimental test in figure 6.16 is 4 plastic rods (permittivity 1.8) that has been reconstructed using nonlinear reconstruction steps and Tikhonov regularization and the reduction of the cost functional by the iteration steps has been shown in figure 6.16. The norm of the cost function and observation of the image quality during iteration shows an improvement in image quality, for successive iterations.

Figure 6.17 shows the reconstruction of wood objects with square cross section. Using TV regularization and nonlinear iterative steps the sharp edges of the square can be

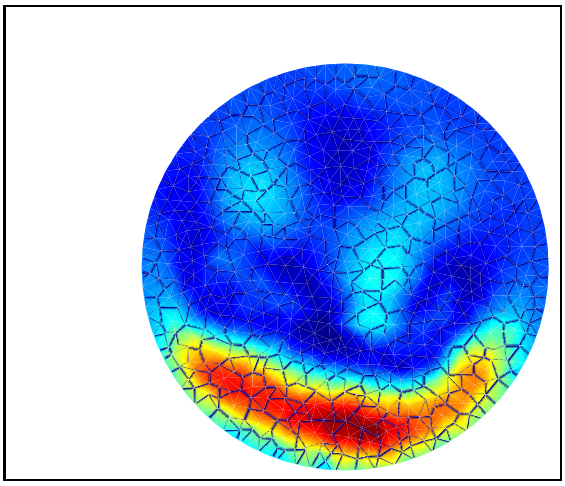

Figure 6.15: Reconstruction of tube, 20 percent of the area filled with glass

seen in reconstructed images. Figure 6.17.b (TV) preserve the edges of the square object better than figure 6.17.a (Tikhonov) For two square objects figure 6.17.c it is harder to recover all the sharp edges, as expected with so few measurements.

Figure 6.18 shows the reconstruction of wooden objects with some thresholds. In this figure it can be seen that the sharp edges can be recovered better by using TV regularization.

Figure 6.19 shows an experimental ECT test, with three plastic cylinders (permittivity 1.8) with water (permittivity 80). This is a high contrast problem with multiple objects, which is heavily nonlinear. The quality of the image improves with nonlinear iterations.

By contrast figure 6.20 shows the reconstructed images of a plastic object with cross shape. TV and Tikhonov regularization were used to reconstruct these images.

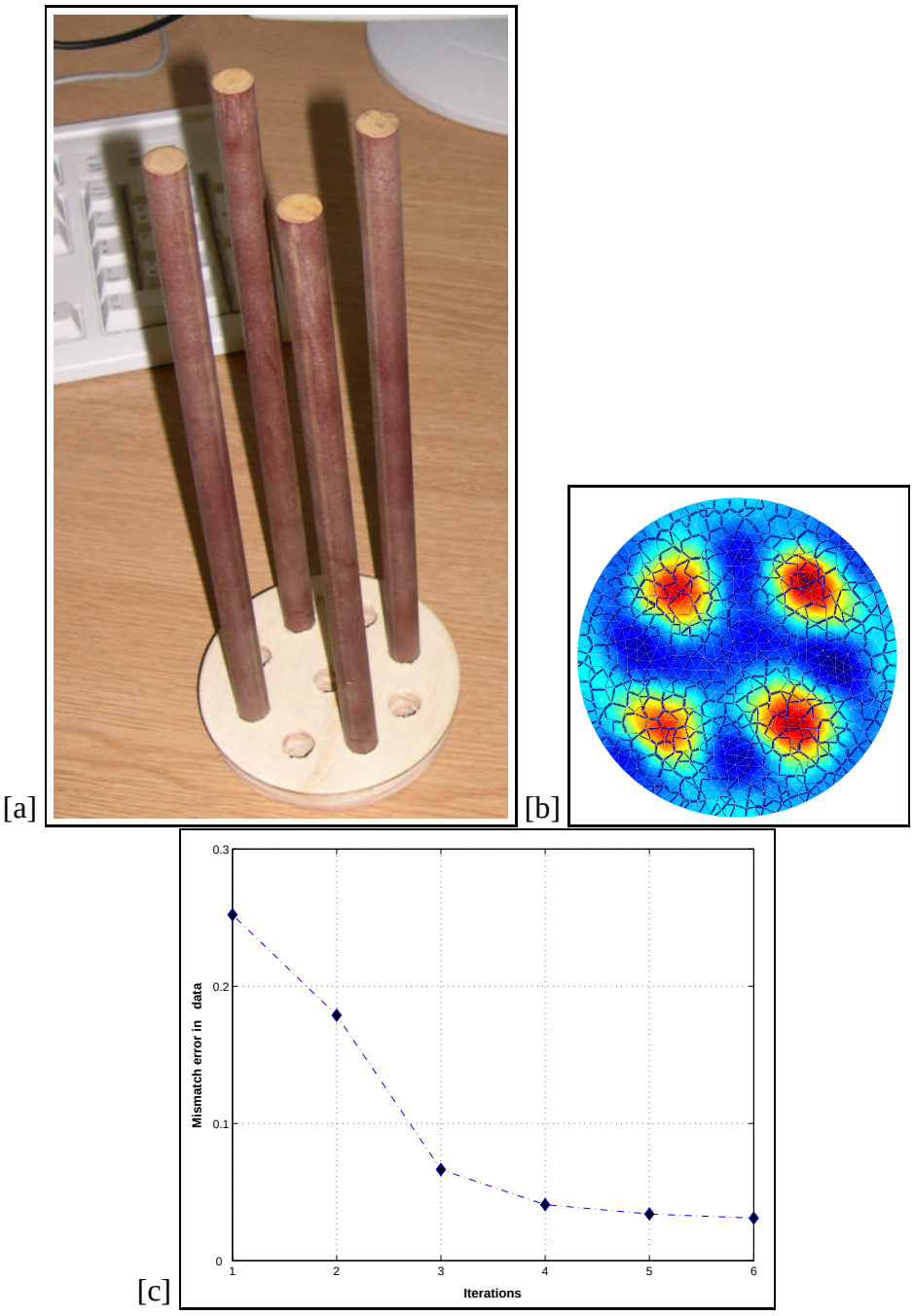

Figure 6.16: Reconstruction of 4 plastic rods shown in (a): from experimental data shown in (b), and reduction in cost function shown in (c)

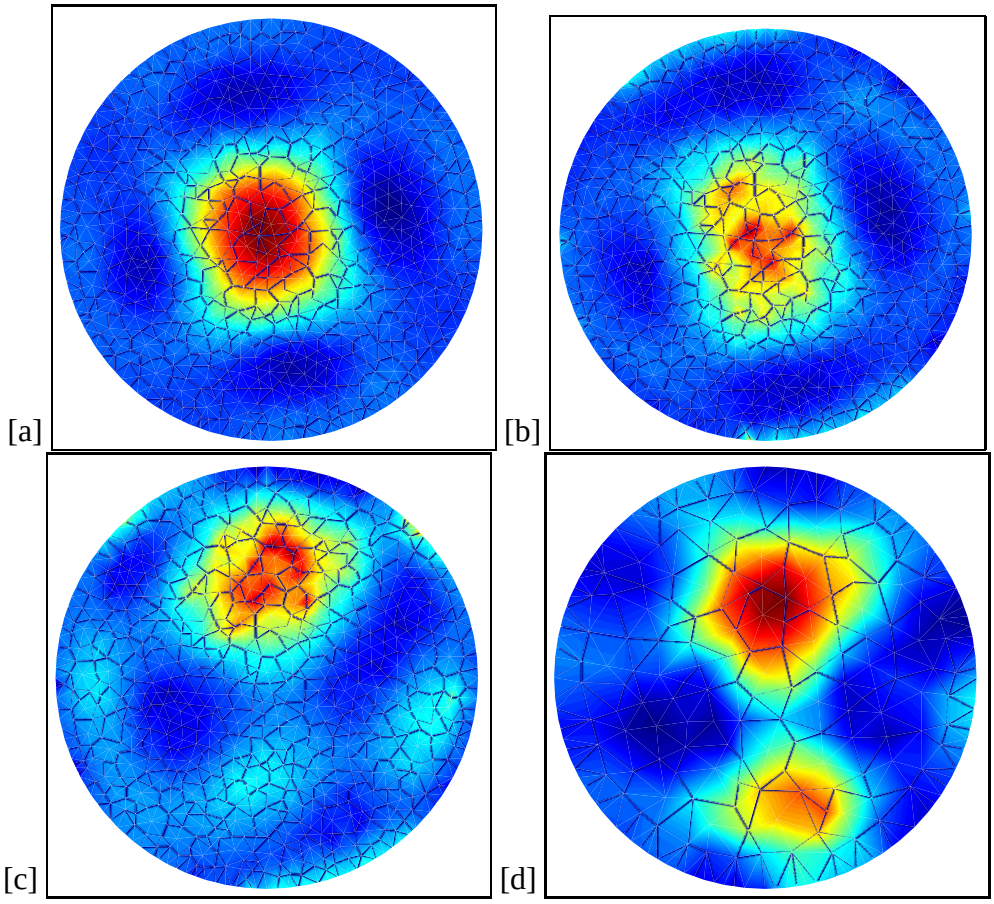

Figure 6.17: Reconstruction of wood with square cross section (permittivity 2), using TV and Tikhonov regularization. (a) Tikhonov regularization of the square object in centre, (b) TV regularization of the square object in centre, (c) TV regularization of square object close to the wall and (d) Tikhonov regularization of two square objects

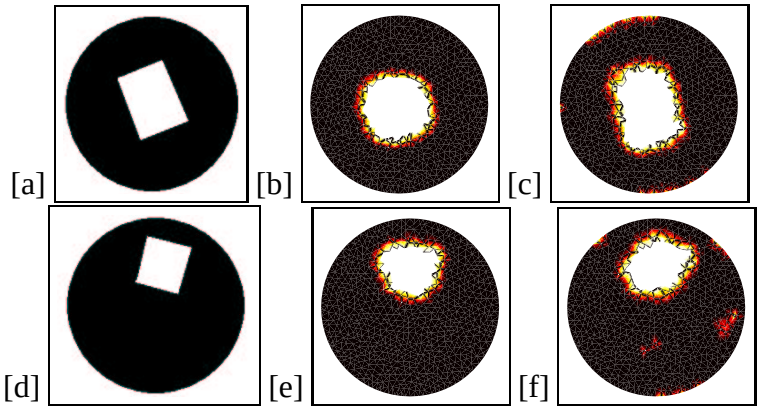

Figure 6.18: Reconstruction of wooden object with square cross section (permittivity 2), using TV and Tikhonov regularization. (a) True object in centre, (b) Tikhonov reconstruction, (c) TV reconstruction, (d) True object, (e) Tikhonv regularization and (f) TV regularization

6.6 Discussion

We studied nonlinear image reconstruction algorithm for 2D ECT. Numerical simulations show the saturation and the failure of superposition aspects of nonlinearity of the inverse ECT problem. Linear reconstruction methods are able to tackle the ill-posedness using a regularization matrix or iterations (linear iterations), but are not suitable for nonlinear problems. For two phase problems one should use shape reconstruction methods, which we study in next chapters. Absolute permittivity reconstruction for high contrast materials was better recovered by using total variation regularization. Total variation improves the separation between inclusions and the shape of each inclusion. The noise in measurement data makes the low contrast images more blurred than high contrast images. Presence of the noise makes it hard to recover the absolute permittivity values for high contrast because of saturation. The high contrast permittivity objects can interfere with each other (this can be seen as a blurring in high contrast images especially when the objects are close to each other, and a linear

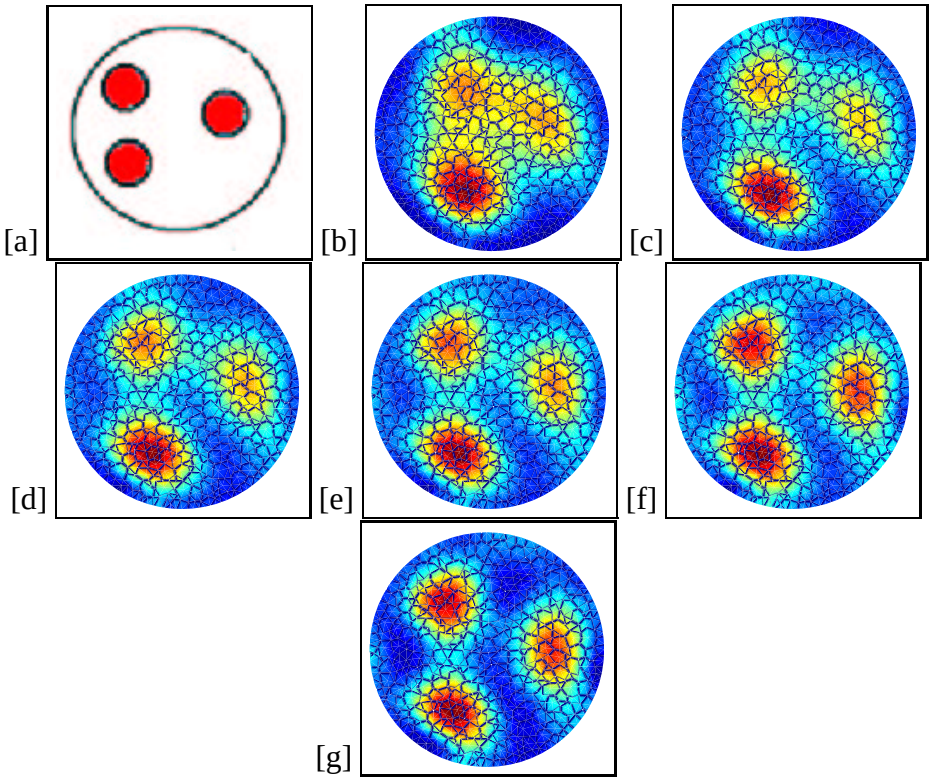

Figure 6.19: Improvement of the image quality using nonlinear steps: (a) Real phantom, (b): Step 1, (c): Step 2, (d): Step 3, (e): Step 4, (f): Step 8 and (g): Step 12. Thanks to Bastian Mahr and colleagues from Institute of Process Engineering at university of Hannover in Germany for the experimental ECT data for this test

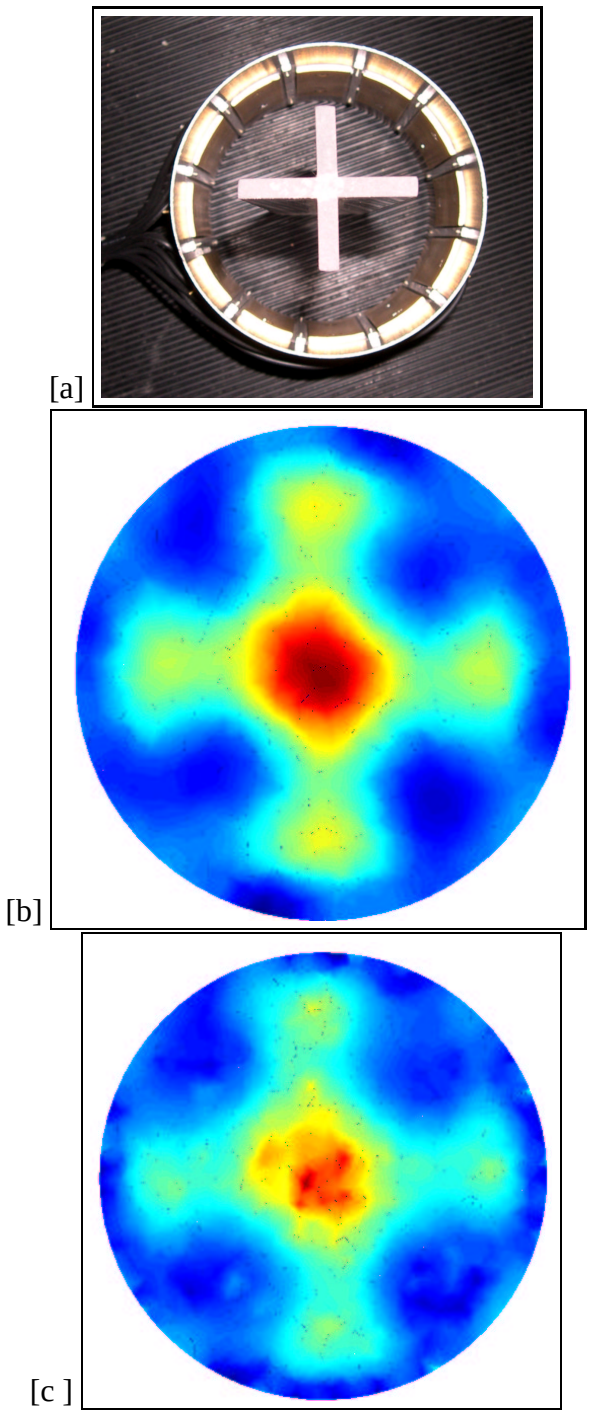

Figure 6.20: Reconstruction of a cross shape plastic object in from experimental data using TV and Tikhonov regularization, The experimental data was collected by PTL, (a) A cross shape inclusion, (b) Tikhonov reconstruction, and (c) TV reconstruction

method is used). For better separation of high contrast objects a nonlinear method is necessary. In this chapter the proposed method was tested against experimental data from three different sources, Hannover University in Germany, Industrial Process Tomography at UMIST and PTL in Manchester UK.

Chapter 7

MONOTONICITY METHOD

The monotonicity method was introduced to the shape reconstruction of ERT by Tamburrino and Rubinacci [155]. The non-iterative inversion method of Tamburrino and Rubinacci provides a low computational cost reconstruction method for tomography data from two component mixtures, such as oil and air (in ECT). In this chapter we study a shape reconstruction method for two phase materials using the monotonicity property. In ERT and ECT the resistance and capacitance matrices are monotone. In MIT a second order moment extracted from multifrequency transimpedance data has the monotonicity property [134], [135] , [136]. The reconstruction method uses the monotonicity property of the data as a test applied to each pixel. The criterion, however, only gives a partial classification by an excluding and an including test [7]. In this chapter we study the monotonicity properties and the inversion algorithm for two phase materials.

7.1 Electrical resistance tomography

The ERT data is a set of the measurements of the DC resistances between pairs of electrodes in contact with the conductor under investigation. In ERT the measurement can be interperrated to Dirichlet to Neumann map. Dirichlet to Neumann has some major properties. It is self adjoint, positive definite, uniquely defines the internal conductivity map and it is monotone [155]. We use the monotonicity property to build a shape reconstruction algorithm. We further concluded that the numerical model including complete electrode model (CEM) of ERT is monotone as well [156].

The relation between electrodes currents and voltages is given by a matrix multiplication $\boldsymbol{V} = \mathtt{R}I$, where $\mathtt{R}$ is the resistance matrix, an $(L \times L)$ symmetric matrix, $\boldsymbol{V}$ and $\boldsymbol{I}$ are the columns vectors of electrodes voltages and currents, respectively (assuming that one electrode is grounded, number of electrodes here $(L+1)$. In most ERT systems (except ACT1... ACT4 at RPI and OXBAT 2 3 at Oxford Brooks) the diagonal arrays of the resistance matrix are not measured, in such cases our proposed method can not be used. The main property of the resistance matrix, from the perspective of the inversion method, is the monotonicity, for all x we have

$$\eta_1(\boldsymbol{x}) \geq \eta_2(\boldsymbol{x}) \quad \forall \boldsymbol{x} \quad \text{in } \Omega_c \Rightarrow \mathtt{R}_1 \geq \mathtt{R}_2 \tag{7.1}$$

where Ω_C is the conductive domain, $\mathtt{R}_k$ is the resistance matrix associated to the conductivity $1/\eta_k$ (η_k is the resistivity of the material).

For two phases problem, (7.1) can be recast as

$$D_\beta \subseteq D_\alpha \subseteq \Omega_c \Rightarrow \mathtt{R}_\alpha \geq \mathtt{R}_\beta \tag{7.2}$$

where D_γ is the region including conductivity level γ and $\mathtt{R}_\gamma$, for $\gamma \in \{\alpha, \beta\}$ is the

resistance matrix related to a resistivity η_γ defined as

$$\eta_\gamma(\boldsymbol{x}) = \begin{cases} \eta_i \ \forall \boldsymbol{x} \in D_\gamma \\ \eta_b \ \forall \boldsymbol{x} \in \Omega_c / D_\gamma \end{cases},$$

η_b is the resistivity of the first phase that we call the background phase, and $\eta_i > \eta_b$ is the resistivity of the second phase that we call inclusion or anomalous phase. We stress that the monotonicity (7.1) and (7.2) hold for the actual resistance matrix and for the numerically computed resistance matrix.

7.2 Electrical capacitance tomography

As is well known, for linear problems, the capacitance matrix $\boldsymbol{C}$ relates the electrodes charges and voltages. Specifically, we have $\boldsymbol{Q} = \boldsymbol{C}\boldsymbol{V}$, where $\boldsymbol{V}$ and $\boldsymbol{Q}$ are the columns vectors of electrodes voltages and charges, respectively. In a system having $(L+1)$ electrodes (one electrode is grounded) $\boldsymbol{V}$ and $\boldsymbol{Q}$ have L components and $\boldsymbol{C}$ is a $(L \times L)$ symmetric and positive definite matrix. Typical measurements protocols directly provide the elements of $\boldsymbol{C}$.

The operator mapping the dielectric permittivity into the capacitance matrix satisfies the following monotonicity property:

$$\varepsilon_1(\boldsymbol{x}) \geq \varepsilon_2(\boldsymbol{x}) \ \ \forall \boldsymbol{x} \in \Omega_d \Rightarrow \boldsymbol{C}_1 \geq \boldsymbol{C}_2 \tag{7.3}$$

where Ω_d is the region of interest for dielectric imaging, $\boldsymbol{C}_k$ is the capacitance matrix associated to the permittivity ε_k. For the two phase problem, (7.3) can be recast as

$$D_\beta \subseteq D_\alpha \subseteq \Omega_d \Rightarrow \boldsymbol{C}_\alpha \geq \boldsymbol{C}_\beta \tag{7.4}$$

where $\boldsymbol{C}_\gamma$, for $\gamma \in \{\alpha, \beta\}$, is the capacitance matrix related to a permittivity ε_γ defined as

$$\varepsilon_\gamma(\boldsymbol{x}) = \begin{cases} \varepsilon_i, \ \forall \boldsymbol{x} \in D_\gamma \\ \varepsilon_b, \ \forall \boldsymbol{x} \in \Omega_d \backslash D_\gamma \end{cases} \tag{7.5}$$

Here ε_b is the permittivity of the first phase that we call the background phase, and $\varepsilon_i > \varepsilon_b$ is the permittivity of the second phase that we call the inclusion phase (notice that if $\varepsilon_i < \varepsilon_b$ then the r.h.s. of (7.4) is given by $\boldsymbol{C}_\beta \geq \boldsymbol{C}_\alpha$). We notice that (7.4) follows directly from (7.3). The proof of (7.3) can be found in [155] with reference to another elliptic problem: the steady ohmic conduction. We highlight that the monotonicity given by (7.3) relies on the ellipticity of the governing partial differential equation.

7.3 Magnetic induction tomography

The goal of MIT is the reconstruction of the resistivity of a conductor through eddy current induced by a set of coils. Specifically, we assume as data the change of the coil impedance due to the induced eddy currents. The mathematical model (in terms of magnetic vector potential A) is given by

$$\nabla \times \left(\frac{1}{\mu} \nabla \times A \right) + i\omega\sigma A = J_s \tag{7.6}$$

together with suitable interface and regularity (at infinity) conditions. Here, μ is the magnetic permeability, ω is angular frequency, σ is the electrical conductivity, J_s is the current flowing in the excitation coil. It is possible to show that [155],[156]

$$Re\left\{ \boldsymbol{Z}_0(i\omega) - \boldsymbol{Z}_\eta(i\omega) \right\} = \omega^2 \boldsymbol{P}_\eta^{(2)} + o\left(\omega^4\right), \ \omega \to 0 \tag{7.7}$$

where *Re* is for real part of a complex number, ω is the angular frequency, $Z_0(i\omega)$ is the impedance matrix when the conductor is not present and $\boldsymbol{Z}_\eta(i\omega)$ is the impedance matrix when a conductor of resistivity η is present. The main property of the second order moment is its monotonicity [155],[156]

$$\eta_1(\boldsymbol{x}) \geq \eta_2(\boldsymbol{x}) \; ; \; \forall \boldsymbol{x} \; ; \text{ in } \Omega_e \Rightarrow \boldsymbol{P}_1^{(2)} \geq \boldsymbol{P}_2^{(2)} \tag{7.8}$$

where $\boldsymbol{P}_k^{(2)}$ is the second order moment associated to the conductivity $1/\eta_k$.

For two phases problem, (7.8) can be recast as

$$D_\beta \subseteq D_\alpha \subseteq \Omega_e \Rightarrow \boldsymbol{P}_\alpha^{(2)} \geq \boldsymbol{P}_\beta^{(2)} \tag{7.9}$$

where Ω_e is the eddy current region, $\boldsymbol{P}_\gamma^{(2)}$, for $\gamma \in \{\alpha, \beta\}$ is the second order moment related to a resistivity η_γ defined as

$$\eta_\gamma(\boldsymbol{x}) = \begin{cases} \eta_i \; \forall \boldsymbol{x} \in D_\gamma \\ \eta_b \; \forall \boldsymbol{x} \in \Omega_e / D_\gamma \end{cases} . \tag{7.10}$$

The monotonicity (7.8) and (7.9) has been proved for a numerical model [134], however, it is possible to show that they hold also for the actual second order moment. The monotonicity satisfied in MIT involves $\boldsymbol{P}^{(2)}$ whereas we measure the impedance matrix $\delta\boldsymbol{Z}(i\omega)$ at the angular frequencies $\omega_1, \ldots, \omega_v$. Therefore, we need a preliminary step to apply the non-iterative inversion method aimed to extract $\boldsymbol{P}^{(2)}$ from the measured data. A detailed description of this calculation can be seen in [156], [134], [135], [136]. The author's contribution in monotonicty MIT is the derivation of the second moment term for edge FEM formulation of MIT.

Using edge FEM used to solve the forward model of equation (7.6). The linear system of equations is $(\boldsymbol{K}_r + i\boldsymbol{\omega}K_i)\boldsymbol{a} = \boldsymbol{b}$, where $\boldsymbol{K} = \boldsymbol{K}_r + i\omega\boldsymbol{K}_i$ is the system matrix and $\boldsymbol{a}$ is

the solution of edge element and $\boldsymbol{b}$ is the right hand side (multiple right hand side for all excitations). The transimpedance can be expressed as $\delta\boldsymbol{Z}(i\omega) = i\boldsymbol{b}^T\boldsymbol{K}^{-1}\boldsymbol{b}$. Here we approximate $\boldsymbol{K}^{-1}$

$$\begin{aligned}\boldsymbol{K}^{-1} = (\boldsymbol{K}_r + i\omega\boldsymbol{K}_i)^{-1} &= (\boldsymbol{I} + i\omega\boldsymbol{K}_r^{-1}\boldsymbol{K}_i)\boldsymbol{K}_r^{-1} \\ &= \sum_{m=0}^{\infty}(-i\omega\boldsymbol{K}_r^{-1}\boldsymbol{K}_i)^m\boldsymbol{K}_r^{-1} \\ &= \boldsymbol{K}_r^{-1} - i\omega\boldsymbol{K}_r^{-1}\boldsymbol{K}_i\boldsymbol{K}_r^{-1}\end{aligned} \tag{7.11}$$

Assuming resistivity of coil is zero (or subtracted from total impedance), $\delta\boldsymbol{Z}(i\omega) = i\boldsymbol{b}^T(\boldsymbol{K}_r^{-1} + i\omega\boldsymbol{K}_r^{-1}\boldsymbol{K}_i\boldsymbol{K}_r^{-1})\boldsymbol{b}$ and resistivity term is $Re\{\delta\boldsymbol{Z}(i\omega)\} = -\boldsymbol{b}^T(\boldsymbol{K}_r^{-1}\boldsymbol{K}_i\boldsymbol{K}_r^{-1})\boldsymbol{b}$. Here $\boldsymbol{a}_r = \boldsymbol{K}_r^{-1}\boldsymbol{b}$ is the solution of the magnetostatic problem (for all excitations). The real part can be written $Re\{\delta\boldsymbol{Z}(i\omega)\} = -\boldsymbol{a}_r^T K_i\boldsymbol{a}_r$. With expansion of the resistive part we have

$$Re\{-\delta\boldsymbol{Z}(i\omega)\} = \omega^2\boldsymbol{P}^{(2)} + \omega^4\boldsymbol{P}^{(4)} + o\left(\omega^6\right) \quad \text{for } \omega \to 0. \tag{7.12}$$

Therefore, to extract $\boldsymbol{P}^{(2)}$ from the data, we neglect the terms of order six and higher, and we compute $\boldsymbol{P}^{(2)}$, the estimate of $\boldsymbol{P}^{(2)}$, by minimizing

$$\Psi_{ij}(\boldsymbol{p}_2, \boldsymbol{p}_4) = \sum_k \omega_k^{-np}\left[(-Re\{\delta\boldsymbol{Z}(i\omega_k)\})_{ij} - \boldsymbol{p}_2\omega_k^2 - \boldsymbol{p}_4\omega_k^4\right]^2 \tag{7.13}$$

we set $\left(\boldsymbol{P}^{(2)}\right)_{ij} = \boldsymbol{p}_{2,ij}$, $\left(\boldsymbol{P}^{(4)}\right)_{ij} = \boldsymbol{p}_{4,ij}$, where $(\boldsymbol{p}_{2,ij}, \boldsymbol{p}_{4,ij})$ minimizes $\Psi_{ij}(\boldsymbol{p}_2, \boldsymbol{p}_4)$. In equation (7.12) $\delta Z(i\omega)$ is the measured (therefore noisy) impedance variation matrix and the term ω_k^{-np} is used to properly weight the data collected at different frequencies. np is usually a small integer. We found that in equation (7.12) it is possible

to neglect the term of order six and higher as the electromagnetic field penetrates inside the conductor, as usually is the case to image the interior part of the material. After from this preprocessing required to extract $\tilde{\boldsymbol{P}}^{(2)}$ from the available data, we can use the non-iterative inversion algorithm by replacing the resistance matrix with its second order moment equivalent.

7.4 Inversion algorithm

The inversion method presented here for two-phase problems is a quantitative non-iterative inversion method requiring the solution of a number of direct problems growing as $O(N)$, where N is the number of voxels used to dicretize the unknown. In the following we briefly summarize the inversion method with reference to the ERT. This inversion method can be applied to ECT and MIT without major modification, since ECT and MIT satisfy a monotonicity property that is formally identical to (7.1), (see (7.3) and (7.8)).

The inversion method is based on the following property of the unknown-data mapping

$$D_\beta \subseteq D_\alpha \subseteq \Omega_c \Rightarrow \mathtt{R}_\alpha - \mathtt{R}_\beta \text{ is a positive semi - definite matrix} \tag{7.14}$$

Reversing (7.14) we obtain the proposition at the basis of the inversion method

$$\mathtt{R}_\alpha - \mathtt{R}_\beta \text{ not a positive semi - definite matrix} \Rightarrow D_\beta \not\subseteq D_\alpha. \tag{7.15}$$

Proposition (7.15) is a criterion allowing us to exclude the possibility that D_β is contained in D_α by using the knowledge of the resistance matrices $\mathtt{R}_\alpha$ and $\mathtt{R}_\beta$. Notice

that (7.15) does not exclude that D_α and D_β are overlapped, i.e. does not exclude the case $D_\beta \cap D_\alpha \neq \emptyset$ where $\emptyset$ is the void set. Let us initially assume that the measured resistance matrix $\tilde{\mathtt{R}}$ is noise free ($\tilde{\mathtt{R}}$ corresponds to the anomaly in V), that the conductive domain Ω_c is divided into N "small" non-overlapped parts $\Omega_1,\ldots,\Omega_N$ and that the anomalous region V is the union of some Ω_k's. The proposition (7.15) leads in a rather natural way to the inversion method. In fact, to understand if a given Ω_k is part of V , we need to compute the largest positive and the smallest negative eigenvalues of the matrix $\tilde{\mathtt{R}} - \mathtt{R}_k$, where $\mathtt{R}_k$ is the resistance matrix corresponding to an anomalous region in Ω_k. If the product of these two eigenvalues is negative, then $\tilde{\mathtt{R}} - \mathtt{R}_k$ is not a positive semi-definite matrix and, therefore, from (7.15) applied to $\tilde{\mathtt{R}}$ and $\mathtt{R}_k$ it follows that $\Omega_k \subset V$. Since Ω_k is either contained in V or external to V (we are assuming that V is union of some Ω_k's), it follows that Ω_k cannot be included in V. It is worth noting that the criterion (7.15) is a sufficient condition to exclude Ω_k from V. Therefore, the reconstruction $\tilde{V}$ obtained as the union of those Ω_k such that $\tilde{\mathtt{R}} - \mathtt{R}_k$ is positive semi-definite includes V, i.e. $V \subseteq \tilde{V}$. Here we briefly explain two tests to find Ω_{ext} and Ω_{int} to identify the inclusion. The true anomaly V is a subset of the anomaly calculated from the exclusion test and the anomaly calculated by the inclusion test is a subset of the true anomaly.

7.4.1 Exclusion test

To determine Ω_{ext} which means finding pixels certainly not part of the inclusion. For each Ω_k, find the eigenvalues, $\lambda_{k,j}$, of $\tilde{\mathtt{R}} - \mathtt{R}_k$, and calculate the sign index s_k,

$$s_k = \frac{\sum_j \lambda_{k,j}}{\sum_j |\lambda_{k,j}|} \tag{7.16}$$

The estimate of Ω_{ext} is then composed of all Ω_k such that $s_k = 1$. Now in practise, noise in $\mathcal{R}$ means that the small eigenvalues may change sign, hence the test is modified either by eliminating eigenvalues close to zero, $\lambda_{k,j} \to 0$ if $|\lambda_{k,j}| < \varepsilon$, or by relaxing the test condition $s_k \geq 1 - \varepsilon$. The latter approach was used here with the value of ε chosen by minimizing $||\tilde{\mathrm{R}} - \mathrm{R}_{\Omega_{\text{ext}},\varepsilon}||_2^2$.

7.4.2 Inclusion test

To determine Ω_{int}, means finding pixels definitely in inclusion. For each Ω_k in Ω_{ext}, find the eigenvalues, $\lambda_{k,j}$, of $\mathrm{R}_{\Omega Ext-k} - \tilde{\mathrm{R}}$, and the sign index t_k,

$$t_k = \frac{\sum_j \lambda_{k,j}}{\sum_j |\lambda_{k,j}|} \tag{7.17}$$

The estimate of Ω_{int} is then composed of all Ω_k such that $t_k < 1$. Again in practise the modified tests have, $\lambda_{k,j} \to 0$ if $|\lambda_{k,j}| < \varepsilon$, or the relaxed condition $t_k \leq 1 - \varepsilon$. As with the exterior test, the choice of ε, in the latter condition, is made by minimizing $||\tilde{\mathrm{R}} - \mathrm{R}_{\Omega\text{ext}-k,\varepsilon}||_2^2$.

7.5 Results for ECT and ERT

Many examples of shape reconstruction for 2D ERT (with point electrode model) have been presented in [155]. We have presented some more examples in 2D, 3D ERT with complete electrode model and ECT in [156] and [7]. Here we present some more sample shape reconstruction examples.

Figure 7.1 shows the reconstruction of true object in 2D ERT with the result of including and excluding tests. Figure 7.2 shows the reconstruction of true object in 2D

ECT with the result of excluding and including tests. ERT system has 32 electrodes. In 2D ERT examples, the background conductivity is 1 Sm^{-1} and the inclusion has conductivity 2 Sm^{-1} and relative permittivity of the background in ECT is 1 and the inclusion has relative permittivity of 3. Figure 7.3 shows 3D ERT reconstruction of true object with the result of excluding and including test. The ERT system here includes 32 electrodes. The background conductivity is 1 Sm^{-1} and the inclusion has conductivity 2 Sm^{-1}.

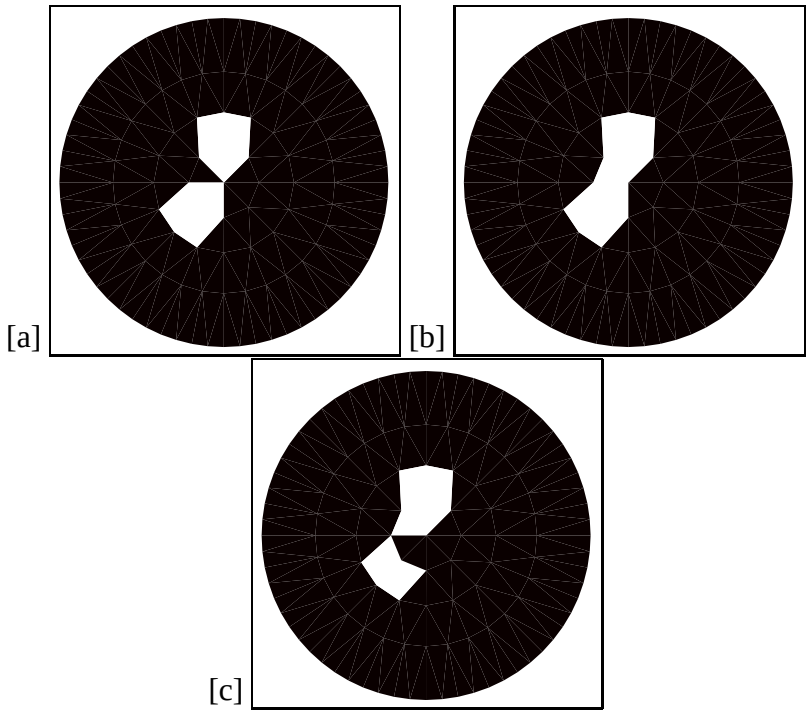

Figure 7.1: Example of 2D ECT, (a): True shape, (b): Excluding test and (c): Including test

7.6 Discussion

The monotonicity underlying resistance, capacitance potentially offers a fast, stable, non-iterative and non-linear reconstruction algorithm for two-phase mixtures. In this

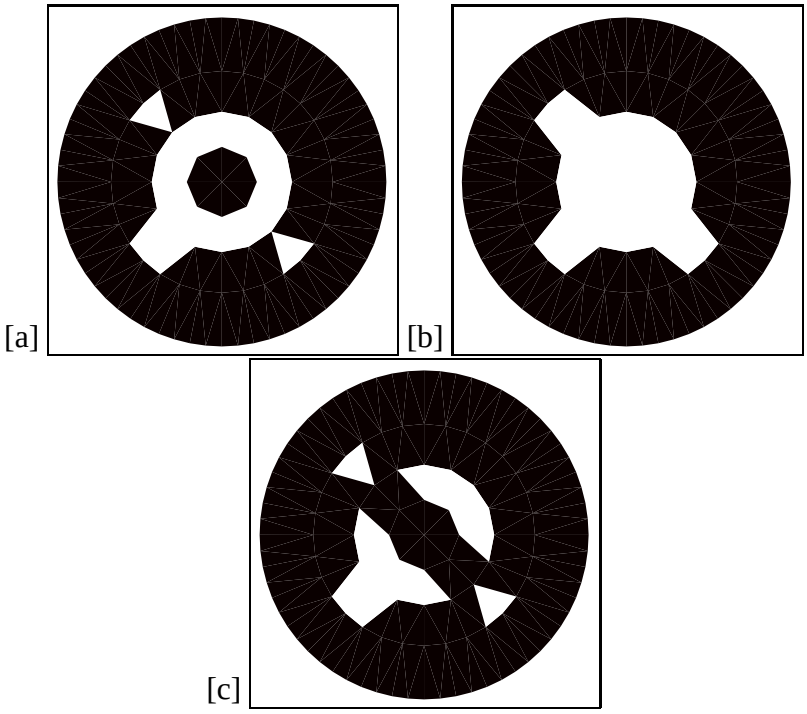

Figure 7.2: Example of 2D ERT, (a): True shape, (b): Excluding and (c): Including

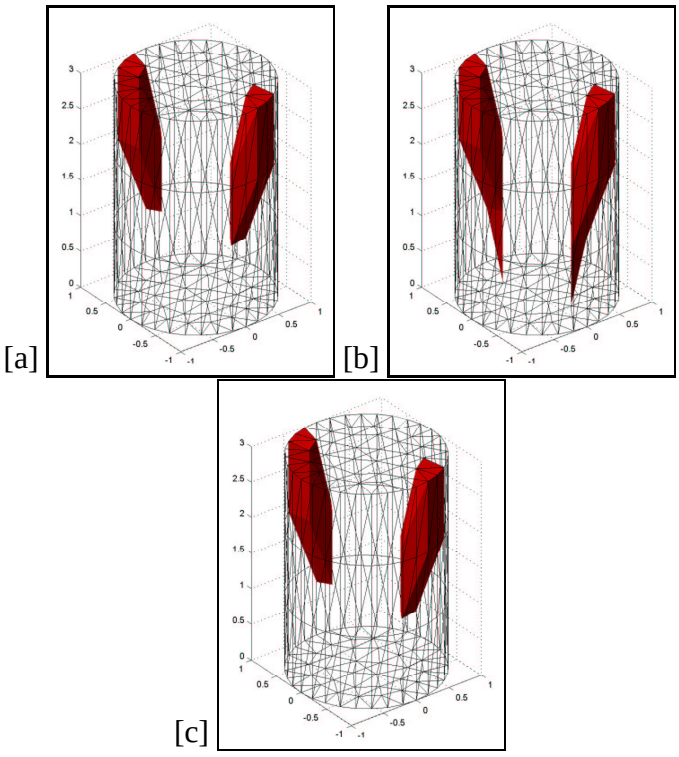

Figure 7.3: Example of 3D ERT, (a): True shape, (b): Excluding and (c): Including

reconstruction technique there is no need for any assumptions of the smoothness of material properties; it is only required that (obviously) the material properties of the two phases are different. More work needs to be done in applying the method to experimental data. In MIT the second order moment of the impedance matrix has the monotonicity property. The second order moment can be extracted from multifrequency measurement of transimpedance of MIT. Preliminary work has been done in MIT [156], further work is needed to apply the monotonicity of multifrequency data to MIT. The numerical study shows that the real object is a subset of the reconstructed shape from the including test and the excluding test is an inclusion that is a subset of the true object. Therefore there will be few pixels that can not be identified by this algorithm. We have implemented a Bayes-Monotonicity [7] approach in which these undecided pixels are analyzed by a binary Monte Carlo Marko Chain (MCMC). The result of such a scheme is a probability distribution of an uncertain pixel being part of the inclusion. It is worth noticing that the test matrices $\mathbb{R}_1, \ldots, \mathbb{R}_N$, where N is the number of pixels in the inverse problem can be pre-computed and easily stored since they are $L \times L$ symmetric matrices, where $L+1$ is the number of electrodes that, generally does not exceed a few dozen. In addition, the computational cost of calculating the largest and smallest eigenvalues of $\tilde{\mathbb{R}} - \mathbb{R}_k$ is moderate. The method is non-iterative in the sense that we can decide if Ω_k is part of V independently from Ω_i for $i \neq k$.

Chapter 8

NARROWBAND LEVEL SET METHOD

The level set method was introduced by Osher and Setain for modelling of front propagations [112]. The method has many applications including fluid mechanics, optimal design, image processing and inverse problems. There have been some initial studies in using various types of level set techniques for shape reconstruction in electrical and electromagnetic imaging (see for example [39, 139, 85]). The level set method is well-suited for the shape reconstruction application since it is able to easily accommodate topological changes of the boundaries. The shapes are given as the zero level set of a higher dimensional function. If we change this higher dimensional function (called the 'level set function'), for example by adding an update, we move the shapes accordingly. In particular, topological changes are performed automatically this way.

A new shape reconstruction method for electrical resistance and capacitance tomography is presented using a narrowband level set formulation. In this shape reconstruction approach, the conductivity (or permittivity) values of the inhomogeneous background

and the obstacles are assumed to be (approximately) known, but the number, sizes, shapes, and locations of these obstacles have to be recovered from the data. A key point in this shape identification technique is to represent geometrical boundaries of the obstacles by using a level set function. This representation of the shapes has the advantage that the level set function automatically handles the splitting or merging of the objects during the reconstruction. Another key point of the algorithm is to solve the inverse problem of the interfaces between two materials using a narrow-band method, which not only decreases the number of unknowns and therefore the computational cost of the inversion, but also tends to improve the condition number of the discrete inverse problem compared to pixel (voxel) based image reconstruction. Level set shape reconstruction results shown in this thesis are some of the first ones using experimental data of impedance tomography. The experimental results also show some improvements in image quality compared with the pixel based image reconstruction. The proposed technique is applied to 2D resistance and capacitance tomography for both simulated and experimental data. In addition, a full 3D inversion is performed on simulated 3D resistance tomography data.

8.1 Sensitivity formula

The forward problems of ERT and ECT have been discussed in previous chapters. A derivation of the sensitivity formula for ERT can be seen in [120]. For ECT we derived an efficient sensitivity formula in chapter 6. We use the linearized sensitivity of the measurement to a change in permittivity for ECT and to the change in electric conductivity in ERT. This type of perturbation calculation, which mathematically amounts to calculating the Fréchet derivative of the measurement data with respect to

permittivity and conductivity, is standard in a broad class of inverse problems (see for example [84]). A treatment of this linearization for full Maxwell's equations can be found for example in [150]. At each point in the domain the calculated sensitivity is essentially proportional to the inner product of two electric field vectors $\boldsymbol{E}_i \cdot \boldsymbol{E}_j$ at the given location. In particular, we have for ERT

$$\frac{dV_{ij}}{d\sigma}\delta\sigma = \int_{\Omega} \delta\sigma \boldsymbol{E}_i \cdot \boldsymbol{E}_j \, dx^3 \tag{8.1}$$

and for ECT

$$\frac{dV_{ij}}{d\varepsilon}\delta\varepsilon = -\int_{\Omega} \delta\varepsilon \boldsymbol{E}_i \cdot \boldsymbol{E}_j \, dx^3. \tag{8.2}$$

Here, Ω is the perturbed region and $\boldsymbol{E}_i$ and $\boldsymbol{E}_j$ are the calculated electric fields of the forward problem when electrodes i and j are excited. This sensitivity formula results in an efficient method for the assembly of the Jacobian matrix. In the FEM model introduced in the previous section, we have $\boldsymbol{E} = -\nabla u$.

8.2 Inverse interface problem using level set

Compared to the more typical pixel (voxel) based reconstruction schemes, the shape reconstruction approach has the advantage that the prior information about the high contrast of the inclusions is incorporated explicitly in the modelling of the problem. With this technique, a more accurate reconstruction of the high contrast objects can be achieved than is possible with the more traditional reconstruction schemes. This is because most regularization schemes for the traditional methods, which are necessary for stabilizing the inversion, have the side-effect of artificially smoothing the reconstructed images. Therefore, these schemes are not well-suited for reconstructing high contrast objects with sharp boundaries.

In order to arrive at a robust and efficient shape-based inversion method, a powerful technique needs to be incorporated for computationally modelling the moving shapes. We have chosen to use the level set technique [85, 112] to describe the changing shapes, since this method is able to easily model topological changes of the boundaries. In this technique, the shapes which define the boundaries, are represented by the zero level set of a level set function Ψ. Let's consider γ as electrical conductivity in ERT or dielectric permittivity in ECT. If D is the inclusion with conductivity or permittivity γ_{int} embedded in a background with conductivity (or permittivity) γ_{ext}, the boundary of the inclusion, which is also an interface between two materials, is given by the zero level set

$$\partial D := \{r : \Psi(r) = 0\} \tag{8.3}$$

where the image parameter at each point r is

$$\gamma(r) = \begin{cases} \gamma_{int} & \{r : \Psi(r) < 0\} \\ \gamma_{ext} & \{r : \Psi(r) > 0\} \end{cases} \tag{8.4}$$

If we change this level set function for example by adding an update, we move the shapes accordingly. This relation is used in the level set technique when constructing updates to a given level set function such that the shapes are deformed in a way which reduces a given cost function.

In general, one possibility for moving the shapes in order to solve our shape reconstruction problem is to introduce a shape evolution of the level set function which is described by a Hamilton-Jacobi equation

$$\frac{\partial \Psi}{\partial t} + \alpha(t)|\nabla \Psi| = 0. \tag{8.5}$$

Here $\alpha(t)$ is a velocity function of evolving contours in their outward normal direction, which is usually chosen to point into the gradient direction of the cost functional in each time step of the evolution. This approach leads to a steepest descent flow for the inversion.

However, the following approach is slightly different. We want to combine well-known and very efficient optimization techniques (based on the Gauss-Newton approach) with our newly developed shape based inversion approach. Using optimization strategies for the shape inversion as an alternative to a shape evolution approach was already suggested in the early paper by Santosa [139]. In order to mathematically derive this new optimization scheme for our situation, we will denote the mapping which assigns to a given level set function Ψ_D the corresponding parameter distribution γ by $\gamma = \Phi(\Psi_D)$.

The parameter distribution γ has the same meaning as in the traditional Gauss-Newton inversion scheme. The only difference is that in the shape based situation it is considered as having only two values, namely an inside value and an 'outside' value. This assumption can be generalized by allowing these inside and outside values to be smoothly varying functions, separated by the interface. We will not consider this extension here. However, in our new approach it will only be an intermediate parameter, linking the data finally to the new basic unknown of the inverse problem, namely the level set function Ψ_D.

Having defined this mapping Φ, we can replace now the iterated parameter γ_n by $\gamma_n = \Phi(\Psi_{D^n}) = \Phi(\Psi^n)$. Instead of the forward mapping $F(\gamma)$ we need to consider now in the new Gauss-Newton type approach the combined mapping

$$G(\Psi) = F(\Phi(\Psi)).$$

If we perturb the latest best guess for the level set function Ψ by some small correction $\delta\Psi$, the linearized response in the data will be

$$G^{'}[\Psi]\delta\Psi = F^{'}[\Phi(\Psi)]\Phi^{'}[\Psi]\delta\Psi \tag{8.6}$$

according to the chain rule. In [139] Santosa has shown that the linearized infinitesimal response in the parameter due to a perturbation in the level set function can be formally described as

$$\Phi^{'}[\Psi]\delta\Psi = -(\gamma_{int} - \gamma_{ext})\frac{\delta\Psi}{|\nabla\Psi|}\delta_{\partial D} \tag{8.7}$$

where $\delta_{\partial D}$ is the Dirac delta function concentrated on the boundary of the latest best guess for the shape D. The singular nature of the Dirac delta function which is involved in this expression causes some mathematical complications when directly applying this expression to the Gauss-Newton update. Instead we use

$$\delta_{\partial D}(x) \approx C_\rho \chi_\rho(x)$$

where χ_ρ is the indicator function of a small narrowband of half-width ρ centred at ∂D, and C_ρ is the corresponding normalization factor. With this approximation, we get

$$\Phi^{'}[\Psi]\delta\Psi \approx -(\gamma_{int} - \gamma_{ext})\frac{\delta\Psi}{|\nabla\Psi|}C_\rho\chi_\rho(x). \tag{8.8}$$

It is convenient to further approximate $|\nabla\Psi| \approx c_1$ with some constant c_1, which usually is justified if we rescale our level set function after each step, or even recalculate it as a signed-distance function repeatedly. We finally arrive at

$$\Phi^{'}[\Psi]\delta\Psi \approx a\chi_\rho(x)\delta\Psi \tag{8.9}$$

with the constant

$$a = -\frac{\gamma_{int} - \gamma_{ext}}{c_1}C_\rho.$$

We denote the discretized form of $\Phi'[\Psi]$ by $\boldsymbol{K}$, and the Jacobian of $\boldsymbol{G}$ by $\boldsymbol{B}$. Then, the new Gauss-Newton update is

$$\boldsymbol{\Psi}_{n+1} = \boldsymbol{\Psi}_n + \lambda_n \left(\boldsymbol{B}_n^T \boldsymbol{B}_n + \alpha^2 \boldsymbol{R}^T \boldsymbol{R}\right)^{-1} \boldsymbol{B}_n^T \left(\boldsymbol{A}_d - \boldsymbol{G}\left(\boldsymbol{\Psi}_n\right)\right) \tag{8.10}$$

with

$$\boldsymbol{B} = \boldsymbol{J}\boldsymbol{K}, \qquad \boldsymbol{B}^T = \boldsymbol{K}^T \boldsymbol{J}^T, \qquad \boldsymbol{B}^T \boldsymbol{B} = \boldsymbol{K}^T \boldsymbol{J}^T \boldsymbol{J}\boldsymbol{K}. \tag{8.11}$$

Notice that (8.11) implies that $\boldsymbol{B}^T \boldsymbol{B}$ can be restricted to be defined only on the narrow-band, since both $\boldsymbol{K}$ and $\boldsymbol{K}^T$ contain discretized versions of $\chi_\rho(x)$, $\boldsymbol{A}_d$ is measurement data, α is the regularization parameter and λ_n is the stpe-size parameter.

There are two parameters to be tuned in this level set formulation. The optimal choice of these two parameters depends on the mesh density, the conductivity (or permittivity) contrast and the initial guess. The relaxation parameter λ has mainly the meaning of a step-size parameter: it essentially determines the magnitude of changes in the shape in a given update. The effect of the regularization parameter α depends on the choice of the regularization operator $\boldsymbol{R}$. Using for $\boldsymbol{R}$ the identity, this regularization parameter has a positive effect on the stability of the inversion without increasing too much the smoothness of the reconstructions. When using a Laplacian for $\boldsymbol{R}$ instead, the effect will be a smoothing of the updates over the domain. The larger we choose α, the smoother the update will be. Here the optimal choice of the parameter α will depend on several factors, for example on the complexity of the correct shape of each inclusion (which is a-priori unknown), the spatial position of the different inclusions with respect to each other and with respect to the electrodes, and on the initial guess. If α is chosen to be too large, it is more difficult for the scheme to split objects in order to perform a topological change. This means, resolution may suffer when α is chosen too large, and the scheme might have difficulties detecting smaller objects

which are at a certain distance from inclusions with a more dominant effect on the data. In our numerical experiments presented here, we are mainly using the identity for L during the level set based inversion. We will indicate in the following discussion which regularization parameter α was chosen in the presented situations.

The numerical implementation:

Number of elements: N , Number of measurements: M , Number of Nodes: P The inclusion is D and the boundary of inclusion is ∂D

- $N \times 1$ vector containing the value of the level set function $\mathbf{\Psi}$ which has the same format as the real conductivity. We assign this in center of each element. So we have $\boldsymbol{\gamma}_k$ as a conductivity (permittivity) and $\mathbf{\Psi}^k$ for $k = 1, 2, ..., N$. Where $\boldsymbol{\gamma}_k = \boldsymbol{\gamma}_{\text{int}}$ and $\mathbf{\Psi}^k < 0$ for inclusion and $\boldsymbol{\gamma}_k = \boldsymbol{\gamma}_{ext}$ and $\mathbf{\Psi}^k > 0$ for back ground. For example $\mathbf{\Psi}^k = -dist(\partial D)$.

  We start with an initial guess for the shape function like:

  $\mathbf{\Psi}^k = (X - X_0)^2 + (Y - Y_0)^2 + (Z - Z_0)^2 - \rho^2$ level set function and (X_0, Y_0, Z_0) are cartesian coordinate of the center and ρ is radius of the sphere.

- Search for zero level set $\mathbf{\Psi}^k = 0$, for each element $k = 1, 2, ..., N$ compare sign of $\mathbf{\Psi}^k$ with sign of the nearest neighbors. If $\mathbf{\Psi}^k$ changes sign use it as an interface.

- Narrowband function, we need a $N \times 1$ vector indication narrow bands, those who are in narrowband get 1 and the others 0.

- A $N \times M$ matrix for updating the $\delta\mathbf{\Psi}$ level set. we calculate the update with equation (8.11).

- Update for level set function and relaxation:

  $\mathbf{\Psi}_{\text{new}} = \mathbf{\Psi}_{\text{old}} + \lambda\delta\mathbf{\Psi}$

- Optionally smooth the level set function.
- Calculate $\boldsymbol{\gamma}_{\text{new}} = \boldsymbol{\gamma}_{\text{int}}$ when $\boldsymbol{\Psi} < 0$ and $\boldsymbol{\gamma}_{\text{new}} = \boldsymbol{\gamma}_{\text{ext}}$ when $myvec\Psi > 0$.

The pixel or voxel based image reconstruction results in this section are all based on the standard regularized Gauss-Newton method using Tikhonov regularization as described in [84].

8.3 Results

The pixel or voxel based image reconstruction results in this section are all based on the generalized regularized Gauss-Newton method using Tikhonov regularization as described in previous chapters.

8.3.1 Simulation 2D ERT

The first numerical example is a simple but representative example of a 2D cross section of a pipe, which may be used in industrial process tomography. We use an opposite current pattern for this application. In figure 8.2 the reconstruction of inclusions with conductivity of 8 Sm^{-1} embedded in a background with conductivity 1 Sm^{-1} is shown. The data was generated synthetically using our forward model, and Gaussian noise with S.D. of 1 percent of the largest measurement was added to these simulated measurement data.

Figure 8.1.a shows a mesh for 12 electrodes system. We apply electric potential 1 volt to the electrode number 4 and the rest of the electrodes are grounded. Figure 8.1.b shows the electric potential distribution.

In order to avoid the so called inverse crime, we used different meshes, namely a

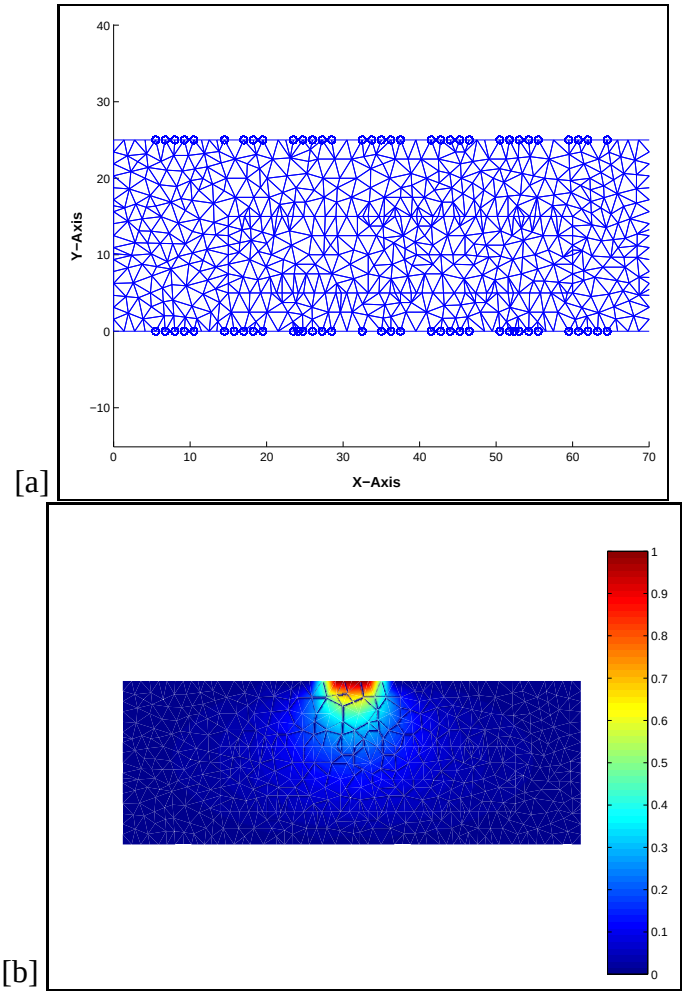

Figure 8.1: (a): Mesh for 12 electrodes system (This mesh was provided by Dr Frank Podd) and (b): Electric potential distribution when electrode number 4 is excited

triangular mesh for the FEM model for calculating the simulated data, and a uniform grid mesh (a 100 by 100 grid) during the level set reconstruction. The level set method was able to identify the position and a relatively accurate shape of the inclusion. Figure 8.3 shows the evolution of the norm of the residuals during the shape reconstruction process.

In the next example we attempt to reconstruct two objects which are located relatively close to each other. It is interesting to see that two objects could be clearly separated in the level set based reconstruction. The inclusions have a conductivity of 25 Sm^{-1} and the background medium has a conductivity value of 1 Sm^{-1}. With a standard regularized pixel based solution it is hard to separate these two objects. The initial guess was a circle in the far right of the pipe. With a choice of the regularization parameter to be $\alpha = 10^{-3}$, we were able to reconstruct after 120 iterations one of the disc shaped inclusions (on the left hand side), but it takes many more iterations to also reconstruct the second one. When we choose the regularization parameter to be smaller, namely $\alpha = 10^{-6}$, we successfully reconstruct after 48 iterations the two objects as shown in figure 8.4.

For alternative approaches and examples for level set reconstructions in the literature (mainly applied to simulated data) see [85], [31] and [139]. A 3D level set reconstruction for ERT has been presented in [25].

8.3.2 Reconstruction in 3D ERT

Figure 8.5 shows the electrode arrangement for a 32 electrodes ERT system. There are two planes of 16 electrodes. The adjacent current pattern has been used for excitation. To solve the forward problem we use a finite element scheme with 9568 tetrahedral

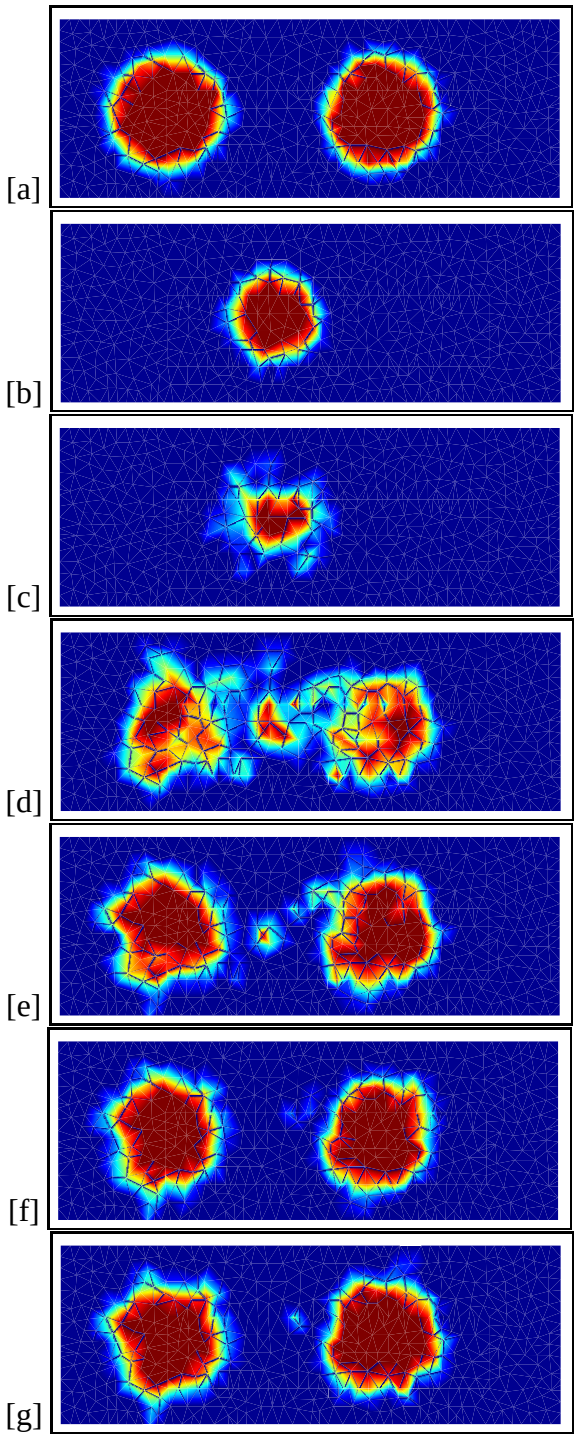

Figure 8.2: True image and the evolution of the shape during the level set reconstruction

[Convergence]

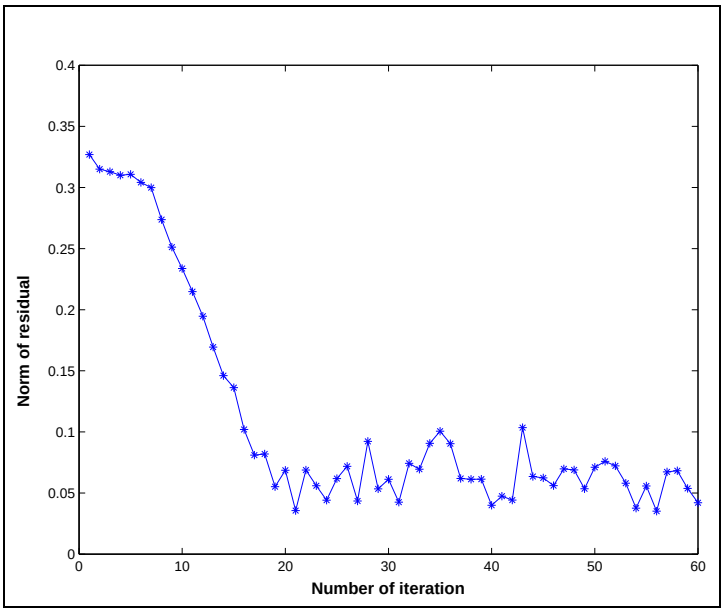

Figure 8.3: Evolution of the norm of the residuals during the shape reconstruction.

[True object]

[Initial guess]

[Step 48]

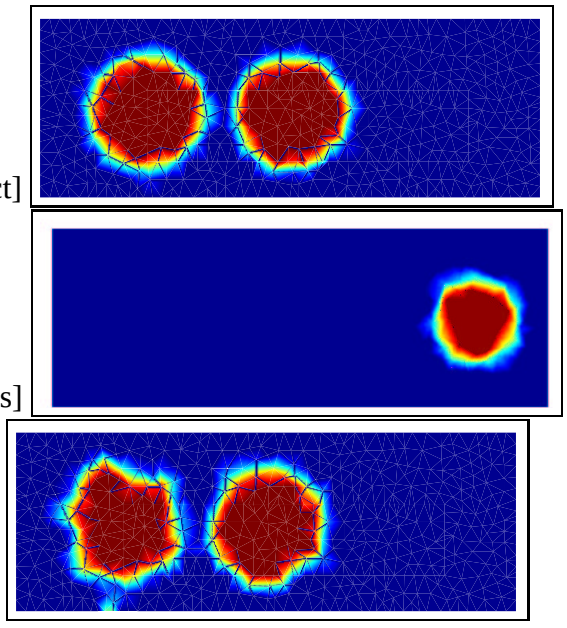

Figure 8.4: True image and level set solution for two objects close to each other

elements.

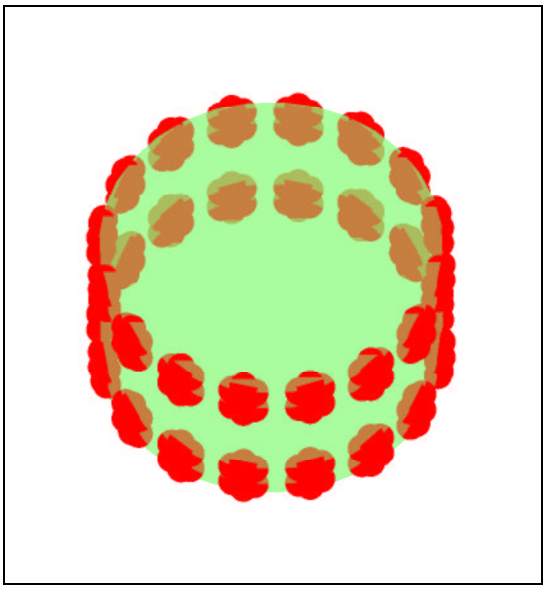

Figure 8.5: Electrodes in 3D ERT

The figures 8.6, 8.7, 8.8 show the true shapes and the reconstructed shapes for different 3D ERT examples. In all these examples the background has a conductivity of 1 Sm^{-1} and the inclusions have a conductivity value of 20 Sm^{-1}.

[True] 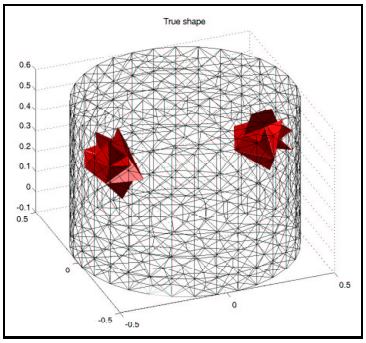

[Reconstructed] 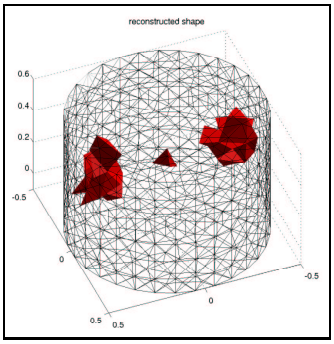

Figure 8.6: True image and level set solution for two inclusions

[True] 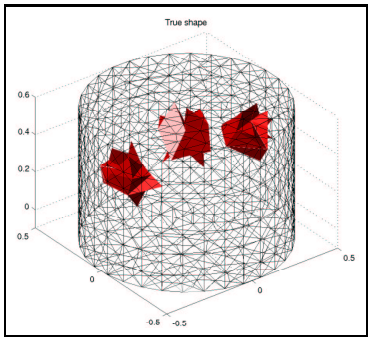

[Reconstructed] 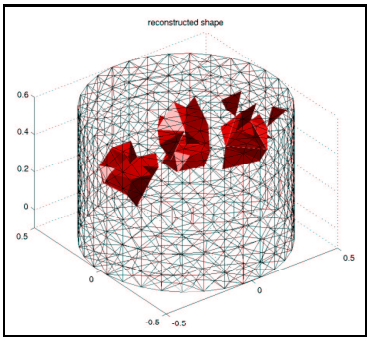

Figure 8.7: True image and level set solution for three inclusions

[True] 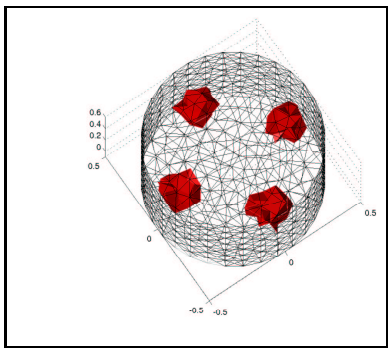
[Reconstructed] 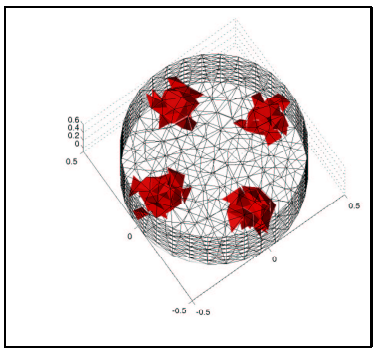

Figure 8.8: True image and level set solution for four inclusions

8.3.3 Experimental ERT results

Figure 8.9 shows reconstructions from experimental data for different examples using both the level set based shape reconstruction scheme and a standard Gauss-Newton pixel-based reconstruction scheme [84]. Three plastic rods were used the largest one with diameter 6.17 cm (we call it r1) the second one with diameter 5.14 cm (we call it r2) and the third one with diameter 4.18 cm (we call it r3). The first example shows three circular rods, in figure 8.9.a, r3 is in top left, r1 in far right and r2 close to r1. The second example shows three different circular objects which are all well separated from each other, in 8.9.b r3 is on the top, r1 in the right and r2 in the left. The third example shows three circular objects of which two are close to each other and near to some electrodes, in figure 8.9.c, r1 is in the bottom right, r2 and r1 are in the top left. Finally, the fourth example shows two circular objects, figure 8.9.d is the same as 8.9.b with r2 removed. The measurement data consisted of 104 voltage measurements from adjacent current pattern and from a 16 electrodes ERT system with a diameter of 30 cm of electrode ring. The number of iterations used for pixel-based reconstruction was 4, and the number of iterations for the level set method was 24, 15, 27, 15 for these four test examples, respectively. The initial guess was a circle centered at (0,0) and with diameter of 6 cm.

Figures 8.10 and 8.11 show the improvement in condition number and reduction in the size of the inverse problem by using the level set method.

8.3.4 Experimental ECT results

Figure 8.12 shows reconstructions for some situations with ECT data which have been used already earlier for a different reconstruction method in [176]. To evaluate the

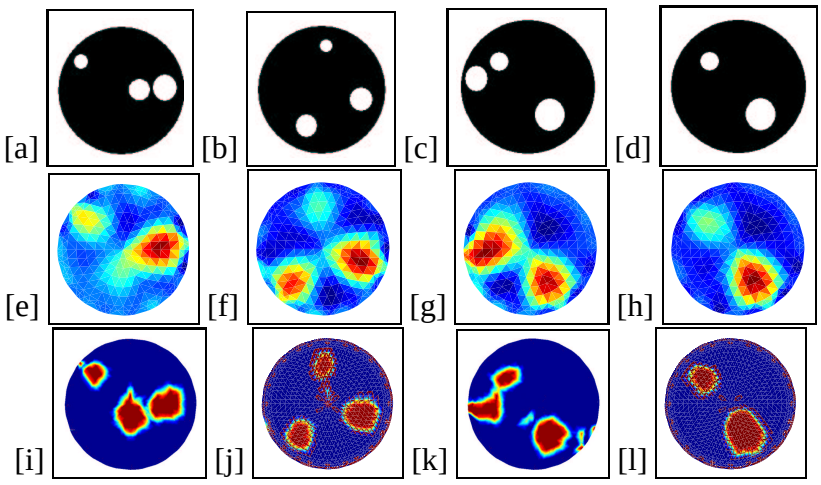

Figure 8.9: Level set reconstructed for ERT experimental data. The top row shows the real object, the center row the pixel based reconstruction, and the bottom row the shape based reconstruction using level sets.

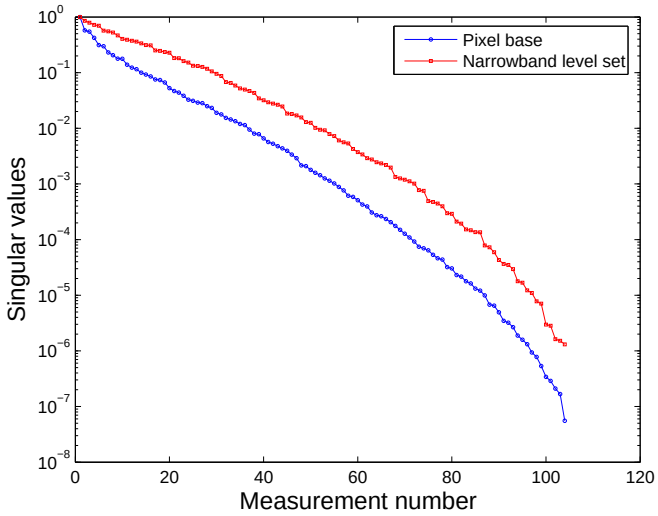

Figure 8.10: Improving the condition of the inverse problem

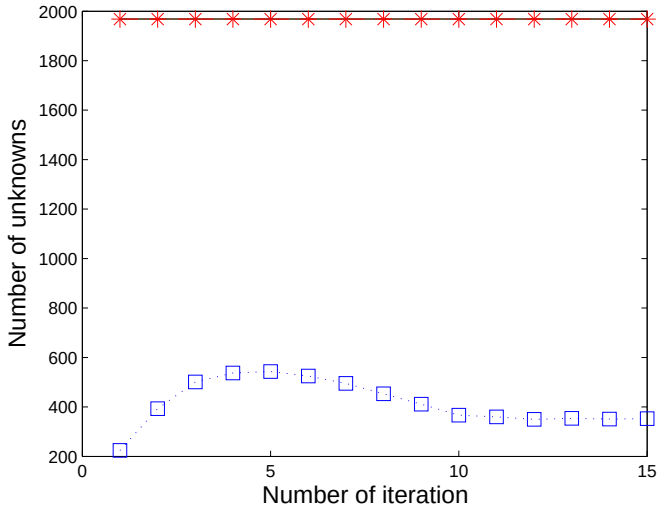

Figure 8.11: Reduction in size of an inverse problem, square for level set and star for pixeled based imaging

level set and pixel based algorithms, the experimental data was used from an 8 electrode sensor 84 mm in diameter. The measurement electrodes are 10 cm long (third direction) and are mounted symmetrically on the outside of an insulating pipe, and 28 measurement data are used the image and shape reconstruction. In the first example, a ring of Perspex with a circular object (Perspex 26 mm in diameter) in the centre is considered. In the second example two circular objects (Perspex 32 mm in diameter each) considered. The third example considers a single ring of Perspex with a circle in centre (air with diameter 26mm), and the fourth example one circular object (Perspex 32 mm in diameter) near the wall. All these inclusions are Perspex objects with relative permittivity of 1.8, and the background is free space with relative permittivity of 1. The number of iterations for the pixel-based reconstruction was 3 in all cases, and the number of iterations for the level set method was 25, 48, 16, 17, respectively.

Figure 8.13 shows an evolution of the shape of the inclusion from the initial guess

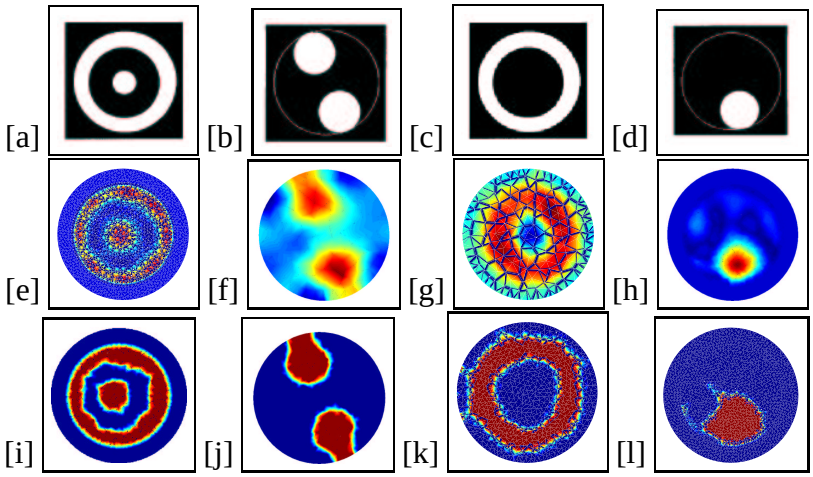

Figure 8.12: Level set reconstruction in ECT imaging from experimental data. The region of interest is the interior of the pipe. The top row shows the real object, the center row is the pixel based reconstructions, and the bottom row is the level set based shape reconstructions

during 17 iterations.

8.4 Discussion

In this chapter we studied some efficient computational algorithms for large scale inverse problems in ERT and ECT. Inversion of the large scale Jacobian matrix is computationally expensive both in time and memory as the Jacobian matrix is a full matrix. A narrowband level set method has been studied in this chapter to reconstruct the interfaces between two conductive regions. The size of the effective inverse problem to be solved decreases, and the problem becomes better posed. In situations where the unknown objects can be represented by shapes with a high contrast to the background, shape based identification is much better adapted to the problem than a pixel based reconstruction scheme. A pixel based scheme can be used in order to find a good ini-

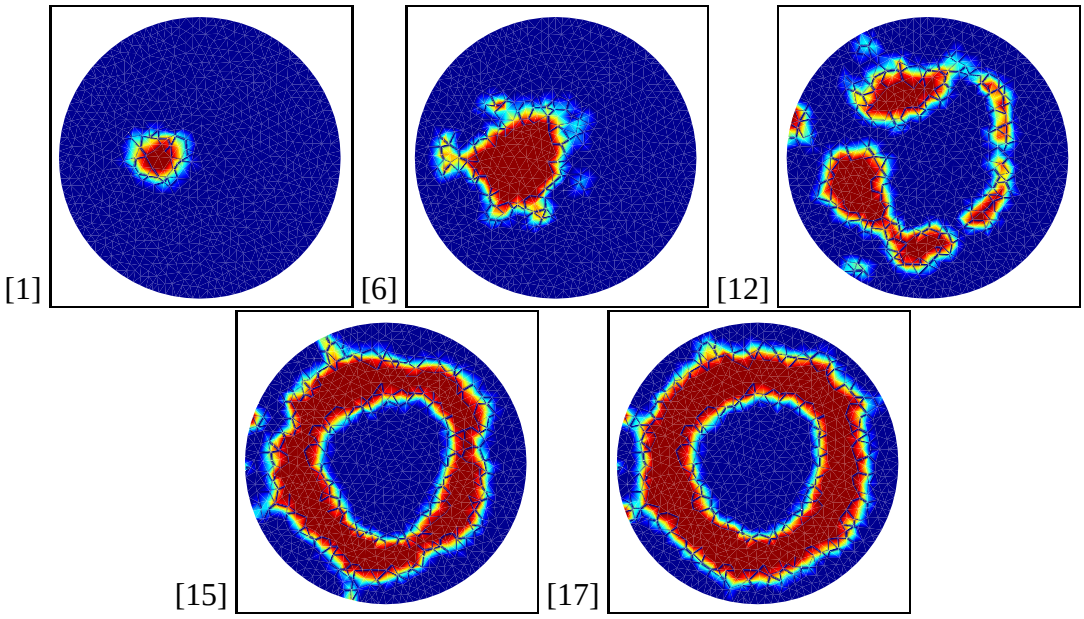

Figure 8.13: Evolution of level set for example 3 of figure 8.12

tial guess for the shape evolution. However, when continuing a pixel based inversion for more than a few iterations, the convergence to the high contrast obstacles becomes very slow due to the smoothing effect of most regularization schemes. When a shape based inversion scheme is used instead, convergence is extremely fast and gives very good results.

The performance of our shape based inversion scheme in practical situations has been demonstrated by presenting shape reconstructions from real experimental ECT and ERT data. The improvements of this method compared to more traditional pixel-based reconstructions are indicated by the presented results. Separating two objects which are close to each other is typically a hard task in pixel-based EIT imaging. Here, our scheme was able to successfully separate two nearby objects from each other using the level set based method. Moreover, we have shown that the level set formulation can recover objects with a high contrast to the background, which is another difficulty in more traditional pixel-based inversion schemes.

An interesting side-effect of our specific scheme is the restriction of the basic operators to be defined only on the narrow band around the most recent best guess. This reduces the dimension and the complexity of the operators significantly. In particular, the condition number of the corresponding Jacobian tends to be much better than in the corresponding pixel-based inversion scheme, simply because the sizes of the involved matrices are smaller. Moreover, most operations on these smaller-sized matrices can be performed more rapidly than in a full Gauss-Newton inversion. Therefore, the individual update is less expensive than in the pixel based inversion scheme. That makes the technique in particular attractive for large scale inversion problems. Finally we have found that, with a suitable choice of the step size (for example using a line-search technique), the total number of iterations can be reduced as well.

Chapter 9

CONCLUSION AND FUTURE WORKS

Imaging is the science of building 2D or 3D reconstructions from exterior measurements. The applications include medical and industrial tomography, geomagnetic prospecting, ground penetrating radar, industrial non-invasive testing and many others. Computational imaging algorithms involve the solution of large-scale inverse problems, in the form of constrained or unconstrained optimization problems. Due to the similarities in the underlying mathematical formulations of the problems, one can design algorithms which can be combined to solve large classes of application problems.

Many imaging problems belong to the general class of inverse problem, whose solutions are extremely sensitive to data errors (and rounding errors in the computations). An approximated solution to these problems can be computed by incorporating a priori information about the desired solution into the reconstruction model. This information can be defined explicitly, e.g., by requiring the solution to satisfy given constraints or

to lie in a given subspace, or the information can be implicit, e.g., by requiring that the solution satisfies certain smoothness conditions. The algorithms that incorporate these requirements into the solution process are called *regularization algorithms*, and they usually take the form of a linear or nonlinear optimization algorithm that involves a combination of a "goodness-of-fit" (such as the residual norm) and a "quality measure" (such as a semi-norm) of the solution. In this thesis various types of electrical impedance and magnetic induction tomography systems were studied both in terms of the forward simulation and the inverse problem.

Applications of the nonlinear inverse solver in ERT, ECT, MIT, MPT have been the main subject of this thesis. Large scale inverse problems have been studied including efficient calculation of the Jacobian matrix and improving the speed of the forward solver. Three-dimensional EIT is more practical as a result of our AMG scheme that has improved the computational cost by reducing the computational time for the forward solvers. AMG was applied to the large scale forward problem of brain EIT with complete electrode model.

Applications of shape and image reconstruction methods have been studied for the above mentioned imaging techniques. A narrowband level set method was applied to the experimental EIT data. The large scale inverse problem in three-dimensional EIT has been solved successfully by a narrowband level set method. The computational time for the inversion decreases compared to more traditional pixel (voxel) based method, as we are dealing with the interfaces rather than all pixels. The results of experimental tests shows that our new narrowband technique can produce more accurate images, especially separation of two nearby objects, than the conventional Tikhonov regularized pixel based method. The experimental data for test in level set for EIT was collected from data released in EIDORS-2D by Dr Marko Vauhkonen and

colleagues [158].

Some extension of Tamburrino's monotonicity method have been studied for two phase materials. For MIT multifrequency data are required for this technique. The method is considered as a fast nonlinear and non-iterative method. Further works are required to apply the technique to the experimental data and optimization of the technique for real time online application.

It is always essential for an image or shape reconstruction technique to be applied to the experimental data. In most cases in this thesis proposed inverse solvers were tested successfully against experimental data. A nonlinear image reconstruction scheme was applied to the ECT inverse problem using experimental data for the first time. Experimental MIT reconstruction using an FE based inverse solver were among the first results and the level set method was applied to the experimental ECT and ERT data for the first time.

Improvements have been made in ECT images, as a result of applying a regularized nonlinear method. Applying TV regularization in ECT can improve the edge detection for sharp edges. We were able to reconstruct square and cross shaped objects and high contrast objects from experimental ECT data. The ECT experimental data were collected from various ECT systems, from Dr W. Yang's group in industrial process tomography at UMIST, from B. Mahr from Hannover University in Germany and from the company PTL in UK.

In MIT the edge FEM has been implemented as a powerful computational tool to simulate the forward problem. An efficient sensitivity formula based on the adjoint field method was derived . It has been demonstrated that the sensitivity maps are changing with the background conductivity. Then the requirement of a nonlinear solver seemed essential to further progress in MIT. As a result of this study, nonlinear inverse solvers

were designed for the MIT problem and the results are presented for both medical and industrial range of applications. The experimental results presented in this thesis are based on independent test data generated by a newly developed MIT system by Prof. A.J. Peyton and colleagues and demonstrate the feasibility of newly developed FE based inverse solvers. This thesis introduces three-dimensional MPT based on a simulated model and some reconstruction results are given.

9.1 Future works

Many interesting projects and studies can be done as a continuation of this thesis, some of them related to the applications and the measurement strategies and some of them in modelling and mathematics. Here we give some examples.

9.1.1 Modelling and algorithms

This thesis focused on the development the bases for the modular imaging algorithms based on the finite element method (FEM), with specific applications in electrical impedance tomography and magnetic induction tomography. Prototype algorithms have been implemented in Matlab. While FEM models are advantageous for their ability to describe complex structures in two and three dimensions, they also require more skills from the user and programmer, and hence they are currently not a standard part of general inverse problem software. However, the design of a modular inverse solver software makes the stage set for the use of modular FEM models in a general regularization framework.

We suggest by having modular inverse solvers we can attempt an adaptive choice of reconstruction algorithm or regularization schemes. We know that each reconstruction

method is able to detect some information regarding the main object, so it could be an idea to have a main management software to make a decision each time to choose a reconstruction algorithm. To make it clear, we use a simple example. If we do not know if the material distribution is two phase or not, we may first use a pixel based reconstruction to recover the material distribution. By analyzing the information acquired from this step we may be able to deduce that the material was two phase, and then extract better information by using a shape based method.

FEM models, are frequently used as "building blocks" in the solution of many engineering problems, and they also make a suitable basis for computational imaging problems, e.g., in sound and vibration reconstruction problems or electrical impedance tomography problems. In this thesis we dealt with isotropic and linear materials. Part of the computer programs including the forward solvers and the Jacobian matrices have been developed in a way that can handle anisotropic materials. More studies are needed to solve the inverse problem of anisotropic and nonlinear materials especially in MIT.

In most of these tomographic techniques, the qualitative information of the image has been improved. For example we have improved sharp edges using TV in 2D ECT and we have improved separations between objects by employing the level set method. The quantitative accuracy still is a challenging problem both experimentally (due to some saturation properties we have shown) and mathematically.

The nonlinear inverse problem can be solved using regularized linear iterative steps: there are research opportunities in the solution of linear system of equations arising in each nonlinear step. One can further explore efficient ways of regularization and especially choice of the regularization parameter. Computational imaging in two and, in particular, three dimensions involve the processing of large amounts of data, and

must be performed with algorithms suited for such large-scale problems. Hence there is a growing interest in iterative algorithms that only involve matrix-vector multiplications and thus avoid the high computational complexity of classical factorization algorithms. Another advantage of the iterative methods is that they only require the operation of the "forward model" on the iteration vectors, and they are matrix-free in the sense that they only require access to a computational module that produces the result of applying the forward operator to a vector. Hence the forward operator is not restricted to be a (sparse) matrix – it can be a sophisticated model that involves, say, the solution of a partial differential equation. It is precisely these features and advantages of iterative methods that make them well suited for designing modular regularization algorithms which, in principle, can make use of any forward operator, as long as it is available as a computational module.

Application of the level set method and AMG for complex conductivity can be an interesting future study. One needs to study further surface based (curve based) regularization schemes when using the level set method. Application of AMG in curl-curl operator of magnetostatic and eddy current forward problem will be a very helpful tool to speed up the forward solvers.

One could study simultaneous reconstruction of permeability and complex conductivity using MIT data. Similar to the optical tomography (recovering absorption and scattering coefficient) [4] some normalization are required to stabilize the inverse problem here.

We suggest an adaptive frequency method for MIT. Depending on the conductivity distribution, each excitation coil will have different frequency. We choose these frequencies in a way that produces the best distinguishability and makes resulting inverse problem better posed. Assume a linear situation and linear image reconstruction. The

background conductivity is given $\boldsymbol{\sigma}_0$. Given an MIT system with N coils, the measurement voltage $\boldsymbol{V}_m(\boldsymbol{\sigma}_{true}, \boldsymbol{\omega})$ and simulated voltages $\boldsymbol{F}(\boldsymbol{\sigma}_0, \boldsymbol{\omega})$ are $N \times N$ matrices. k-th row of the matrix belongs to the excitation coil k with frequency ω_k. We choose $\boldsymbol{\omega} = \omega_1, \omega_2, ...\omega_N$ ($\omega_L < \boldsymbol{\omega} < \omega_H$ in which ω_L and ω_H are lowest and highest frequency by measurement system), in a way that minimizes the condition number of $\boldsymbol{J}(\boldsymbol{\sigma}_0, \boldsymbol{\omega})$, in the same time maximizes $\| \boldsymbol{V}_m - \boldsymbol{F} \|^2$. In proposed algorithm, first the image will be reconstructed by a single frequency data, which gives an estimated conductivity distribution $\boldsymbol{\sigma}_1$. Then we maximize $\| \boldsymbol{F}(\boldsymbol{\sigma}_1, \omega) - \boldsymbol{F}(\sigma_0, \omega) \|^2$, to find the best frequencies. Then the measurement data will be created by these optimum frequencies. Next the image will be reconstructed by this optimum data. By maximizing the differences between measurement and simulated data one can reduce the effect of the noise on data and consequently on reconstructed images. Reducing the condition number of the Jacobian matrix makes the inverse problem better posed, so that more singular values can contribute in image reconstruction and more accurate details can be recovered.

9.1.2 Some applications

The computational modules developed in this project have a general interest in inverse problems; however, we also had some specific applications in mind within the areas of industrial and medical electromagnetic imaging. Molten Steel flow visualization is a potential application that is commercially important and we expect to be feasible. Two phase techniques developed in this thesis are well suited for recovering the flow regime using MIT data. Steel solidification monitoring is another area of interest and can be approximated to a two phase material problem. Eddy current NDT is a similar problem, it is two phase, so that the notion of regularization and two phase materials

can be used in NDT crack detection.

As an example of large scale inverse and forward problem in EIT, brain tomography could be an interesting problem. Our large scale techniques namely AMG and the level set method can be used here. We applied AMG to the EIT forward problem of brain imaging. We also applied level set method to some 3D test examples, it can be further studied for brain tomography.

There are many potential applications for an MPT system, including the application mentioned in this thesis (detecting steel bars inside concrete). Magnetic permeability mapping can produce an indication of stress in metal objects, the notion of MPT and inverse permeability problem could improve the stress sensing. Study of the nonlinear materials will be particularly interesting here, where we deal with magnetic curves, saturation and nonlinear materials.

Techniques developed in this thesis are general, many of them could be used when there are limited angle tomography data. Many NDT devices or bio-impedance devices could benefit of using notion of the inverse problem or tomography. In many applications increasing the number of measurements from one to few measurements (for example 20 measurements from an 8 electrodes EIT) does not make the measurement system terribly complicated. But this multiple measurement data together with a smart pattern recognition scheme could produce valuable results. In some cases a tomography system can be used just for the proof of the concept and acquiring the pattern recognition idea, then the tomographic system can be replaced by a decision making chip that triggers an alarm with more accuracy based on an understanding of the material distribution map.

Dehydration of liquids in human body is an issue for example for soldiers fighting in deserts. Using electrical impedance techniques one could relate the level of liquids

in human body to a conductivity measure. Our proposal for that would be a set of MIT measurements with possible assembling the sensors inside the clothes (by smart textile technology) and using a pattern recognition method to set an alarm. It might be possible to assemble the sensor in some surfaces near to the body a subsurface conductivity study will be interesting here.

We have studied use of EIT for monitoring freezing tissues in cryosurgery, however we suggest MIT may be a suitable technique for this application. The large changes in conductivity, permittivity and perhaps permeability of the freezed tissues make it possible to be detected by MIT. MIT also have a potential to map the temperature during hyperthermia.

Appendix A

SELECTED PUBLICATIONS

The following is a list of papers appeared or accepted for publication by the author relevant to this work.

- M Soleimani, CE Powell and N Polydorides, *Improving the Forward Solver for the Complete Electrode Model in EIT using Algebraic Multigrid*, Vol. 24 issue 5, pp. 577-583, May 2005.
- M Soleimani, WRB Lionheart, *Image reconstruction in three-dimensional magnetostatic permeability tomography*, IEEE Transactions on Magnetics, Vol. 41, issue 4, pages 1274-1279, April 2005
- M Soleimani, WRB Lionheart, O Dorn, *Level set reconstruction of conductivity and permittivity from boundary electrical measurements using experimental data*, Inverse Problems in Science and Engineering (in press 2005)
- M. Soleimani, WRB Lionheart, *A nonlinear image reconstruction in electrical capacitance tomography using experimental data*, Meas. Science and Tech. (2005)

- M. Soleimani , *Numerical modelling and analysis of the forward and inverse problems in electrical capacitance tomography*, to appear in International Journal for Information Systems Sciences, (2005).

- M Soleimani, A Movafeghi, M H Kargarnovin and H Soltanian-Zadeh, *Hardware design and reconstruction results of SUT-1 EIT system,* The International Journal of Scientific Research (IJSR) vol. 15 2005

- M.Soleimani, A. Movafeghi, *A Shape Reconstruction Method for Electrical Resistance Tomography for Two Phase Materials,* The International Journal of Scientific Research (IJSR) vol.15 2005

- M. Soleimani, W.R.B Lionheart, A. J. Peyton, X. Ma C. Ktistis and W. Yin , *Linear and nonlinear image reconstruction applied to experimental data of various types of magnetic induction tomography*, 6th Conference on Biomedical Applications of Electrical Impedance Tomography, London, UK, June 2005.

- M.Soleimani, A.Movafeghi , *Electrical permittivity shape identification using electrical capacitance tomography data and level set formulation,* In proc. MVIP 2005

- RG Aykroyd, M Soleimani and WRB Lionheart, *Full shape reconstruction from partial ERT monotonicity information using a Bayes-MCMC approach*, Proc. 4th World Congress on Industrial Process Tomography, Aizu, Japan, 2005.

- RM West, M Soleimani, RG Aykroyd, and WRB Lionheart, *MCMC algorithm acceleration using a hybrid linearised/non-linear forward problem strategy applied to the Bayesian analysis of 3D ERT data,* Proc. 4th World Congress on Industrial Process Tomography, Aizu, Japan, 2005.

- M Soleimani, WRB Lionheart, AJ Peyton, X Ma , *"Inverse finite element method applied to magnetic inductance tomography experimental data*, Proc. 4th World Congress on Industrial Process Tomography, Aizu, Japan, 2005.

- Manuchehr Soleimani, William R B Lionheart, Malcolm Byars, John Pendleton, *Nonlinear image reconstruction in ECT base on a validated forward model*, Proc. 4th World Congress on Industrial Process Tomography, Aizu, Japan, 2005.

- M. Soleimani, R.G. Aykroyd, S.Freear, W.R.B. Lionheart, and F Podd, *Multimodal data fusion for enhanced imaging applied to 3D ERT with Ultrasound time of flight data* , Proc. 4th World Congress on Industrial Process tomography, Aizu, Japan, 2005.

- M Soleimani, WRB Lionheart, *Magnetostatic permeability tomography in material inspection*, In Proc., 7th Biennial ASME Conference Engineering Systems Design and Analysis, ESDA 04 (ISBN: 0-7918-3741-6).

- M Soleimani, WRB Lionheart, A J Peyton, X Ma, *Molten metal flow visualization using mutual inductance tomography*, In Proc., 7th Biennial ASME Conference Engineering Systems Design and Analysis, ESDA 04 (ISBN: 0-7918-3741-6).

- M Soleimani, WRB Lionheart, Oliver Dorn, *Reconstruction of shape of inclusions in electrical resistance capacitance tomography using level set method*, In Proc. XII. International Conference On Electrical Bio-Impedance V. Electrical Impedance Tomography, Gdansk, Poland, 2004 (ISBN: 8391768163).

- M Soleimani, Juan Felipe P. J. Abascal, WRB Lionheart, *Simultaneous Recon-*

struction of the Boundary Shape and Conductivity in 3D Electrical Impedance Tomography, In Proc. XII. International Conference On Electrical Bio-Impedance V. Electrical Impedance Tomography, Gdansk, Poland, 2004 (ISBN: 8391768163).

- M Soleimani, WRB Lionheart, *Feasibility study of 3D permeability reconstruction using magnetostatic permeability tomography,* In Proc. XII. International Conference On Electrical Bio-Impedance V. Electrical Impedance Tomography, Gdansk, Poland, 2004 (ISBN: 8391768163).

- M Soleimani, WRB Lionheart, *Improvement of electrical capacitance tomography imaging using total variation regularization,* In Proc. XII. International Conference On Electrical Bio-Impedance V. Electrical Impedance Tomography, Gdansk, Poland, 2004 (ISBN: 8391768163).

- M Soleimani, *Forward problem in MR-EIT using edge finite element* , In Proc. XII. International Conference On Electrical Bio-Impedance V. Electrical Impedance Tomography, Gdansk, Poland, 2004 (ISBN: 8391768163).

- A Movafeghi, A R Nateghi, M Soleimani, Mohammad H. Kargarnovin and Hamid Soltanianzadeh, *Image reconstruction algorithms for SUT-1 EIT System,* In Proc. XII. International Conference On Electrical Bio-Impedance V. Electrical Impedance Tomography, Gdansk, Poland, 2004 (ISBN: 8391768163).

- M Soleimani, WRB Lionheart, *Image reconstruction in magnetic induction tomography using a regularized Gauss Newton method,* In Proc. XII. International Conference On Electrical Bio-Impedance V. Electrical Impedance Tomography, Gdansk, Poland, 2004 (ISBN: 8391768163).

- M Soleimani, RG Aykroyd, RM West, S Meng, WRB Lionheart and N Poly-

dorides, *Bayes-MCMC reconstruction from 3D EIT data using a combined linear and non-linear forward problem solution strategy,* In Proc. XII. International Conference On Electrical Bio-Impedance V. Electrical Impedance Tomography, Gdansk, Poland, 2004 (ISBN: 8391768163).

- RG Aykroyd, M Soleimani and WRB Lionheart, *Bayes-MCMC reconstruction from ERT data with prior constraints from resistance matrix monotonicity,* Proc. of 3rd International Symposium on Process Tomography in Poland (ISBN: 8372831386).

- M Soleimani , WRB Lionheart, *Level Set Method for Shape Reconstruction in Electrical Resistance Tomography,* Presented for new frontiers in computational mathematics Jan 2004 Manchester UK

- M Soleimani, William R B Lionheart, Claudia H Riedel and Olaf Dssel, *Forward Problem in 3D Magnetic Induction Tomography (MIT),* In Proc. 3rd World Congress on Industrial Process Tomography, The Rockies, Alberta, Canada Tuesday 2nd - Friday 5th September 2003 (ISBN: 08531 62409).

- M Soleimani, W R B Lionheart, A J Peyton, X Ma, *Image Reconstruction in 3D Magnetic Induction Tomography Using a FEM Forward Model,* In Proc. 3rd World Congress on Industrial Process Tomography, The Rockies, Alberta, Canada Tuesday 2nd - Friday 5th September 2003 (ISBN: 08531 62409)

- A Tamburrino, G Rubinacci, M Soleimani, WRB Lionheart, *A Noniterative Inversion Method for Electrical Resistance, Capacitance and Inductance Tomography for Two Phase Materials,* In Proc. 3rd World Congress on Industrial Process Tomography, The Rockies, Alberta, Canada Tuesday 2nd - Friday 5th September 2003 (ISBN: 08531 62409).

- M Soleimani, R Sadleir, K Jersey-Willuhn, *Simultaneous Reconstruction of the Boundary Shape and Conductivity in 2D Electrical Impedance Tomography,* In Proc. 3rd World Congress on Industrial Process tomography,The Rockies, Alberta, Canada ,Tuesday 2nd - Friday 5th September 2003 (ISBN: 08531 62409).

- W R B Lionheart, M Soleimani, A J Peyton, *Sensitivity Analysis in 3D Magnetic Induction Tomography (MIT),* In Proc. 3rd World Congress on Industrial Process Tomography, , The Rockies, Alberta, Canada Tuesday 2nd - Friday 5th September 2003 (ISBN: 08531 62409).

- M Soleimani, WRB Lionheart, *Recent progress in image reconstruction of magnetic induction tomography for monitoring of the molten metal*, ON-LINE MEASUREMENTS FOR QUALITY IN THE METALS INDUSTRIES, 7-8 October 2003 London

- A J Peyton, S D Dickinson, W R B Lionheart, M soleimani, and WDN Pritchard, *Electromagnetic imaging and tomography - a review of recent advances*, ON-LINE MEASUREMENTS FOR QUALITY IN THE METALS INDUSTRIES, 7-8 October 2003 London

- M Soleimani, Catherine Elizabeth Powell, *Black-box Algebraic Multigrid for the 3D Forward Problem Arising in Electrical Impedance Tomography,* Presented and abstract published in Proc. 4th Conference on Biomedical Applications of Electrical Impedance Tomography, Apr. 2003.

- M Soleimani, *Image Reconstruction in magnetic induction tomography,* Report submitted for UMIST Graduate office 2003

- K. Jersey-Willuhn , M Soleimani, *Conductivity reconstruction based on inverse*

finite element measurements in a tissue monitoring system, US Patent application number 20030216630.

- K. Jersey-Willuhn, M Soleimani, *Film barrier dressing for intra- vascular infusion tissue monitoring system*, US Patent application number 20030216662.

- K. Jersey-Willuhn, M Soleimani, *Tissue monitoring system for intra-vascular infusion*, US Patent, application number 20030216663, filled International: Europe and Japan.

- M Soleimani, WRB Lionheart, *Reconstruction in 3D Eddy Current Imaging Using Vector Finite Element*, Report to Corus 2002

- M Soleimani, *Electric Network Method in Computation Electromagnetic in Direct and Inverse Problem in Electrical Impedance Tomography*, Presented and published in proceeding IEE Conference - Computation in Electromagnetics Fourth International Conference on Computation in Electromagnetics CEM 2002 The Cumberland Hotel, Bournemouth, UK: 8 - 11 April 2002.

- M Soleimani, *Electrodes Position Reconstruction in EIT Based on Genetic Algorithm from The Boundary Impedance Data*, Proceeding of 4th International Workshop on Biosignal Interpretation in Villa Olmo, Como, Italy on June 24-26th 2002.

- M Soleimani, *Hardware Assessment in Electrical Impedance Measurement and Tomography Systems by Optimization Technique*, Published in Proceeding of BIOSIGNAL 2002 , 16th International EURASIP Conference BIOSIGNAL 2002 26.06.2002 - 28.06.2002, Brno, Czech Republic (ISSN: 1211-412X).

- M Soleimani, A Movafeghi, *Image Reconstruction Methods for Electrical Impedance Tomography SUT-1 System,* Presented and published in proceeding in 23 th IEEE Conference on EMBC in 2001 (ISSN: 1094-687X).

- A Movafeghi, M Soleimani, A R Nateghi and A Mireshghi, *Introduction SUT-1 a Simple and Efficient EIT System,* Published in Proceeding of The XI International Conference on Electrical Bio-Impedance June 17-21 2001, pp 493-496, Oslo, Norway, (ISBN: 82-91853-05-3).

- M Soleimani, A Mireshghi, *Application of Finite Element Method in Medical Imaging,* Presented and published Proceeding 4th Int. Conf. Of Iranian Society of Mech. Eng., ISME, 2000, Tehran, Iran.

- M Soleimani, A Movafeghi, A Mireshghi, *Comparison of Various Applied Current Source Samples in Electrical Impedance Tomography,* Presented and published in proceeding 9th Annual Conf. on Biomed. Eng. Proc. Mar. 2000, Tehran, Iran, pp. 384-387.

- M Soleimani, A Movafeghi, A Mireshghi, *Consideration of Main Reasons for Artifacts in EIT Images,* Presented and published in Proceeding of 4th Iranian conference in Medical physics (1999).

- M Soleimani, *Design and fabrication of an Electrical Impedance Measurement (EIM) for Medical application,* M.Sc Seminar Sharif University of Technology (1997)

- A Mireshghi, M Soleimani, *Simulation, Design and Construction of an Electrical Impedance Tomography System,* SUT Research Bulletin, Vol. 4, 1999

- M Soleimani, *Design and fabrication of 32 electrodes Electrical Impedance Tomography system (SUT-1)*, M.Sc thesis under supervision of Prof. Mireshghi A, Sharif University of Technology (1999)

- A Mireshghi, M Soleimani, *Electrical Impedance Tomography and it's application in medicine*, Annual report on research activities in Sharif University of Technology (1998)

- M Soleimani and R Assareh, *Economic dispatch of power plants (Optimization)*, B.SC thesis under supervision of Dr. Aghasi A (1995)

Bibliography

[1] R. Albanese and G. Rubinacci,*" Integral formulation for 3D eddy-current computation using edge elements*," IEE Proceedings, Vol. 135, Pt. A, No. 7, pp. 457-462, September 1988.

[2] R. Albanese and G. Rubinacci, *"Solution of three dimensional eddy-current problems by integral and differential methods*," IEEE Trans. on MAG, Vol. 24, No. 1, pp. 98-101, January 1988.

[3] A. Arko , R.C. Waterfall, M.S. Beck, T. Dyakowski, P. Sutcliffe and M. Byars, *"Development of Electrical Capacitance Tomography for solids mass flow measurement and control of pneumatic conveying system*," 1st World Congress on Industrial Process Tomography, pp. 140-146, 1999.

[4] S. R. Arridge, *"Topical review: Optical tomography in medical imaging*," Inverse Problems 15(2), pp. 41-93, 1999.

[5] S. R. Arridge and J. C. Hebden, *"Optical imaging in medicine:II. Modelling and reconstruction*," Physics in Medicine and Biology, 42(5), pp. 841-853, 1997.

[6] J. Artola and J. Dell, *"Broyden quasi-Newton method applied to electrical impedance tomography*," Electronic Letter, vol. 30, No. 1, pp. 27-28, 1994.

[7] R. G. Aykroyd, M. Soleimani and W. R. B. Lionheart, *Bayes-MCMC reconstruction from ERT data with prior contraints from resistance matrix monotonicity,* Proc. of 3rd International Symposium on Process Tomography in Poland (ISBN: 8372831386)

[8] D. C. Barber and B. H. Brown, "*Imaging Spatial Distributions of Resistivity Using Applied Potential Tomography,*" Electronic Letters, 19:22, pp. 933-935, 1983.

[9] R.H. Bayford, A. Gibson, A. Tizzard , A.T. Tidswell and D.S. Holder, " *Solving the forward problem for the human head using IDEAS (Integrated Design Engineering Analysis Software) a finite element modelling tool*," Physiol. Meas., Vol. 22, No. 1., pp. 55-63, 2001.

[10] J. Besag, P. J. Green, D. Higdon and K. Mengersen "*Bayesian computation and stochastic systems*," Statistical Science, 10, pp. 1-41, 1995.

[11] R. Binns, A. R. A. Lyons, A. J. Peyton and W. D. N. Pritchard, "*Imaging molten steel flow profiles*," Meas. Sci. Technol., 12, pp. 1132-1138, 2001.

[12] O. Biro, "*Edge element formulations of eddy current problems.*," Computer methods in applied mechanics and engineering, 169, pp. 391-405, 1999.

[13] K. Boone, A.M. Lewis and D.S. Holder, "*Imaging of cortical spreading depression by EIT: implications for localisation of epileptic foci*," Physiolo. Meas., vol. 15, pp. A189-A198, 1994.

[14] EIDORS, "*http://www.eidors.org*"

[15] A. Borsic, C. N. McLeod and W.R.B. Lionheart, " *Total variation regularisation in EIT reconstruction*," 2nd World Congr. on Industrial Process Tomography (Hannover), pp. 579-587, 2001.

[16] A. Borsic, W.R.B. Lionheart and C. N. McLeod, " *Generation of anisotropic-smoothness regularization filters for EIT*," IEEE Trans Med Imaging, 21, pp. 596-603, 2002.

[17] A. Borsic,"*Regularisation Methods for Imaging from Electrical Measurements*,", Phd Thesis, Oxford Brookes University, 2002.

[18] A. Bossavit, "*Whitney forms: a class of finite elements for three-dimensional computations in electromagnetism*," IEE Proceedings, vol. 135, Pt. A., no. 8, pp. 493-500, November 1988.

[19] A. Bossavit "*Computational Electromagnetism*," Academic Press (Boston), 1998.

[20] W. R. Breckon , "*Image reconstruction in Electrical Impedance Tomography*," Ph.D. Thesis, Oxford Brookes Polytechnic, 1990.

[21] J.H. Bramble, "*Multigrid Methods*," Pitman Research Notes in Mathematics Series, 294, Longman 1993.

[22] A. Brandt, "Multigrid techniques: guide with applications to fluid dynamics GMD-Studien Nr 85," Gesellschaft fr Mathematik und Datenverarbeitung (Germany: St Augustin), 1984.

[23] W.L. Briggs, Van E. Henson and S.F. McCormick, "*A Multigrid Tutorial*," SIAM, 2000.

[24] B. Brandsttter, G. Holler and D. Watzenig, " *Reconstruction of Inhomogeneities in Fluids by means of Capacitance Tomography*," COMPEL, Vol. 22, No. 3, pp. 508-519, 2003.

[25] G. Boverman, M. Khames and E.L. Miller, "*Recent Work in Shape-Based Methods for Diffusive Inverse Problems*," Review of Scientific Instruments, vol. 74, no. 4, pp. 2580-2582, April 2003.

[26] M. Brühl, "*Explicit Characterization of Inclusions in Electrical Impedance Tomography*," SIAM J Math Anal, 32, pp. 1327-1341, 2001.

[27] A. P. Calderón, "*On an inverse boundary value problem*," Seminar on Numerical Analysis and its Applications to Continuum Physics , pp. 65-73, Soc. Brasil. Mat., Rio de Janeiro,, 1980.

[28] R. Casanova, A. Silva and A. R. Borges, "*MIT image reconstruction based on edge-preserving regularization*," Physiol. Meas., 25, pp. 195-207, 2004.

[29] R. Casañas, H. Scharfetter, A. Altes, A. Remacha, P. Sarda, J. Sierra, R. Merwa, K. Hollaus and J. Rosell, "*Measurement of liver iron overload by magnetic induction using a planar gradiometer: preliminary human results*," Physiol. Meas., 25, pp. 315-323, 2004.

[30] V. Cingoski, "*Study on Improved Three-Dimensional Electromagnetic Field Computations Utilizing Vector Edge Finite Elements*," Ph.D. Thesis, Graduate School of Engineering, Hiroshima University, 1996

[31] T. F. Chan and Xue-Cheng Tai, "*Level Set And Total Variation Regularization For Elliptic Inverse Problems With Discontinuous Coefficients*," Journal of Computational Physics, vol. 193, pp. 40-66, 2003.

[32] M. Cheney, D. Isaacson and J. C. Newell, "*Electrical Impedance Tomography*," SIAM Review., 41(1), pp 85-101, 1999.

[33] M. Cheney, D. Isaacson, J.C. Newell, S. Simske and J. Goble, "*NOSER: An algorithm for solving the inverse conductivity problem*," Int. J. Imaging Systems & Technology 2, pp.66–75, 1990.

[34] M.T. Clay and T.C. Ferree, "*Weighted regularization in Electrical Impedance Tomography with applicactions to acute cerebral stroke*," IEEE Trans. on Medical Imaging, vol. 21, no. 6, pp. 629-637, 2002.

[35] H. Dehghani, B. W. Pogue, J. Shudong, B. Brooksby and K. D. Paulsen, "*Three-Dimensional Optical Tomography: Resolution in Small-Object Imaging*," Applied Optics, Volume 42, Issue 16, pp. 3117-3128, June 2003.

[36] A. Dey and H.F. Morrison, " *Resistivity modelling for arbitrarily shaped three-dimensional structures*," Geophysics, vol. 44, pp.753–780, 1979.

[37] D.C. Dobson and F. Santosa, "*An image enhancement technique for electrical impedance tomography*," Institute for mathematics and its applicaation, University of Minnesota, 1993.

[38] O. Dorn, H Bertete-Aguirre, J. G. Berryman and G. C. Papanicolaou, "*A nonlinear inversion method for 3D electromagnetic imaging using adjoint fields*," Inverse Problems, vol. 15, no. 6, pp. 1523-1558, 1999.

[39] O. Dorn, E. L. Miller and C.M. Rappaport, "*A shape reconstruction method for electromagnetic tomography using adjoint fields and level sets*," Inverse Problems, 16, pp. 1119-1156, 2000.

[40] O. Dorn, " *Shape reconstruction in scattering media with voids using a transport model and level sets*," MSRI preprint http://www.msri.org/publications/preprints/online/2002-002.html, 2002.

[41] O. Dorn, H. Bertete-Aguirre, J. G. Berryman and G. C. Papanicolaou "*A non-linear inversion method for 3D electromagnetic imaging using adjoint fields*," Inverse Problems, 15, pp. 1523-1558, 2001.

[42] D. N. Dyck, D. A. Lowther and E. M. Freeman, " *A Method of computing the sensitivity of the electromagnetic quantities to changes in the material and sources*," IEEE Trans. MAG., vol. 3, no. 5, pp. 3415-3418, Sep 1994.

[43] T. Dyakowski and A.J. Jaworski, " *Tomographic Measurements of Solids Mass Flow in Pneumatic Conveying*," The 2nd World Congress on Industrial Process Tomography, pp. 353-362, 2001.

[44] T. Dyakowski, L.F.C. Jeanmeure, W.B. Zimmerman and W. Clark, "*Direct flow-pattern identification using electrical capacitance tomography*," Experimental Thermal and Fluid Science, Volume 26, Issues 6-7, pp. 763-773, 2002.

[45] R.G. Ellis and D.W. Oldenburg, "*The pole-pole 3D DC resistivity inverse problem: a conjugate gradient approach*," Geophysical Journal International, vol. 119, pp.187-194, 1994.

[46] FEMLAB:"*http://www.comsol.com*"

[47] M. J. Field, "*Differential calculus and its applications*", Van Nostrand Reinhold Company Limited, 1976.

[48] K. Fujiwara, T. Nakata and H. Fusayasu, *"Accelelation of convergence characteristics of the ICCG method,"* IEEE Trans. MAG, vol. 29, no. 2, pp. 1958-1961, 1993.

[49] J. B. Fraleigh and R. A. Beauregard, *"Linear algebra,"* Addison-Wesley publishing company 1995.

[50] P. A. Gaydecki, I. Silva, B. T. Fernandes and Z. Z. Yu, *"A portable inductive scanning system for imaging steel reinforcing bars embedded within concrete,"* Sensors and Actuators A: Physical 84, pp. 25-32, 2000.

[51] N.G. Gencer and M.N. Tek,*"Electrical conductivity imaging via contactless measurements,"* IEEE Trans. on Medical Imaging, vol. 18, Issue. 7, pp. 617-627, 1999.

[52] A. Gibson, *" Electrical impedance tomography of human brain function,"* PhD thesis, University College London 2000.

[53] G.H. Golub and C.F. Van Loan, *"Matrix Computations,"* John Hopkins University Press, 1989.

[54] S. Gomez, O. Michiyo, C. Gamio and A. Fraguela, *" Reconstruction of capacitance tomography images of simulated two-phase flow regimes,"* Applied Numerical Mathematics, 46, pp. 197-208, 2003.

[55] A. Greenbaum, *"Iterative Methods for Solving Linear Systems,"* SIAM, Philadelphia, 1997.

[56] B.D. Grieve , J.L. Davidson, R. Mann, W.R.B. Lionheart and T.A. York, *" Process Compliant Electrical Impedance Instrumentation for Wide Scale Ex-*

ploitation on Industrial Vessels," Proc. 3rd World Congress on Industrial Process Tomography, Banff, Canada, 2nd-5th September, pp.806-812, 2003.

[57] H. Griffiths, W. R. Stewart and W. Gough, "*Magnetic induction tomography: Measurements with a single channel*," X-ICEBI, Barcelona, pp. 361-364, 1998.

[58] H. Griffiths, "*Magnetic induction tomography*," Measurement Science and Technology, 12, 8, pp. 1126-1131, 2001.

[59] W. Hackbusch, "*Multi-Grid Methods and Applications*," Springer-Verlag, Berlin 1985.

[60] J. Hadmard, "*Lectures on Cauchy's problem in linear partial differential equations*," Yale University Press, New Haven, CT, 1923.

[61] M. Hanke-Bourgeois and M. Brühl, "*Recent progress in electrical impedance tomography*," Inverse Problems, 19, pp. S65-S90, 2003.

[62] P.C. Hansen, "*Rank-Deficient and Discrete Ill-Posed Inverse Problems*," SIAM, Philadelphia, PA, 1998.

[63] S.R. Higson, P. Drake, D.W. Stamp, A. Peyton, R. Binns, A. Lyons and W. Lionheart, "*Development of a sensor for visualization of steel flow in the continuous casting nozzle*," Revue De Metallurgie-cahiers D Informations Techniques, 100, pp. 629-632, 2003.

[64] D. S. Holder, "*Electrical Impedance Tomography: Methods, History and Applications*," Institute of Physics, 2004.

[65] K. Hollaus, B. Weiss, C.H. Magele and H. Hutten, *"Geometric multigrid to accelerate the solution of the quasi-static electric field problem by tetrahedral finite elements*," Physiol. Meas., vol. 25, no. 1, pp. 169-179, 2004.

[66] K. Hollaus, C. Magele, R. Merwa and H. Scharfetter, *"Fast calculation of the sensitivity matrix in magnetic induction tomography by tetrahedral edge finite elements and the reciprocity theorem*," Physiol. Meas., 25, pp. 159-168, 2004.

[67] K. Hollhaus, C. Magele, B. Brandstätter, R. Merwa and and H. Scharfetter, *"Numerical simulation of the forward problem in magnetic induction tomography of biological tissue*," In Proc. 10th IGTE Symposium, pp. 381-384, 2002.

[68] G. Holler, D. Watzenig and B. Brandsttter, *" A fast Gauss-Newton based ECT Algorithm with Automatic Adjustment of the Regularization Parameter*, Proceedings of the 3rd World Congress on Industrial Process Tomography, Banff, Alberta, Canada, pp. 415 -420, 2003.

[69] G. Holler, A. Fuchs, B. Schweighofer and G. Brasseur, *"Comparison of Measurement Results and Simulations Based on Finite Element Method for an Electrical Capacitance Tomography System*, To be published in the Proceedings of the Sensors for Industry Conference (Sicon/04), New Orleans, USA, 2004.

[70] H. Huang, T. Takagi and H. Fukutomi,*"Fast signal predictions of noised signals in eddy current testing.*," IEEE Trans. on MAG., vol. 36, Issue. 4, Part. 1, pp. 1719-1723, 2000.

[71] J.P. Kaipio, V. Kolehmainen, E. Somersalo and M. Vauhkonen, *"Statistical Inversion and Monte Carlo Sampling Methods in Electrical Impedance Tomography,*" Inverse Problems, 16, pp. 1487-1522, 2000.

[72] M. Kaltenbacher, S. Reitzinger and B. Vanrumste, "*Albegraic multigrid method for solving 3D nonlinear electrostatic and magnetostatic field problems*," Technical Report 00-07, SFB F013: Numerical and Symbolic Scientific Computing, 2000. Linz, Österreich, April 2000.

[73] A. Kameari, "*Three-dimensional eddy current calculation using edge elements for magnetic vector potential*," Applied Electromagnetics in Materials, K. Miya (Ed.), Pergamon Press pp. 225-236, 1988.

[74] Y. Kawase, T. Yamaguchi and N. Hayashi, "*3-D finite element analysis for molten metal shapes in an electromagnetic melting system*," IEEE Trans. on MAG, Vol. 29, No. 2, pp. 1554-1557, March 1993.

[75] D.S. Kershaw, "*The incomplete Cholesky-conjugate gradient method for the iterative solution of systems of linear equations*," J. comp. phys., vol. 26, pp. 43-65, 1978.

[76] V. Kolehmainen, S. R. Arridge, W. R. B. Lionheart, M. Vauhkonen and J. P. Kaipio, "*Recovery of region boundaries of piecewise constant coefficients of an elliptic PDE from boundary data*," Inverse Problems, 15, pp. 1375-1391, 1999.

[77] A. N. Kolmogorov and S. V. Fomin, "*Elements of rhe Theory of Funclions and Funcrional Analysis*," (Rochester. NY: Graylock Press) pp 1957-61.

[78] A. Korjenevsky, V. Cherepenin and S. Sapetsky,"*Magnetic induction tomography: experimental realization*," Physiol. Meas., vol. 21(1), pp. 89-94, 2000.

[79] A. V. Korjenevsky, V. A. Cherepenin, and S. A. Sapetsky, *"Visualization of electrical impedance by magnetic induction tomography,"* in Proc. of the World Congress on Industrial Process Tomography, pp. 240-246, Aug. 2001.

[80] A. Korjenevsky, *"Solving inverse problems in electrical impedance and magnetic induction tomography by artificial neural networks,"* Journal of Radioelectronics, No 12, December 2001.

[81] Y. Li, L. Udpa and S.S Udpa, *" Three-Dimensional Defect Reconstruction From Eddy-Current NDE Signals Using a Genetic Local Search Algorithm,"* IEEE Trans. MAG., vol. 40, no. 2, pp. 410-417, 2004.

[82] W.R.B. Lionheart, *"Review: Developments in EIT reconstruction algorithms: pitfalls, challenges and recent developments,"* Physiol. Meas. 25, pp. 125-142, 2004.

[83] W. R. B. Lionheart, M. Soleimani and A. J. Peyton, *"Sensitivity Analysis in 3D Magnetic Induction Tomography (MIT),"* In Proc. 3rd World Congress on Industrial Process Tomography, Banff Canada, pp. 239-244, 2003.

[84] W.R.B. Lionheart, *"Reconstruction Algorithms for Permittivity and Conductivity Imaging,"* In Proc. 2rd world congress on process tomography , Hannover, Germany pp. 4-10, 2001.

[85] A. Litman, D. Lesselier and F. Santosa, *"Reconstruction of a two-dimensional binary obstacle by controlled evolution of a level-set,"* Inverse Problems, 14, pp. 685-706 1998.

[86] M.H. Loke and T. Dahlin, *" A comparison of the Gauss–Newton and quassi–Newton methods in resistivity imaging inversion*," Journal of Applied Geophysics, 49, pp. 149-162, 2002.

[87] N. Ida and J. P. A. Bastos, *" Electromagnetics and calculation of fields*," 2^{nd} ed. , Springer- Verlag New York , Inc., 1997.

[88] H. Igarashi, K. Ooi and T. Honma, *"Magnetostatic permeability tomography*," Proc. COMPUMAG-Saratoga, CD-ROM, Paper Number 43142, 2003.

[89] H. Igarashi, K. Ooi and T. Honma, *"A Magnetostatic Reconstruction of Permeability Distribution in Material*," Inverse Problems in Engineering Mechanics IV, ed. M. Tanaka, pp. 383-388, 2003.

[90] H. Igarashi and T. Honma, *" On Convergence of ICCG Applied to Finite Element Equation for Quasi-Static Fields*," IEEE Trans MAG., Vol. 38, N0. , 2002.

[91] H. Igarashi, *"On the property of the curl-curl matrix in finite element analysis with edge elements*," IEEE Trans MAG., Vol. 37 Issue: 5 Part: 1 , pp. 3129 -3132, 2001.

[92] J. Jin, *"The Finite Element Method in Electromagnetics*," John Wiley & Sons, Inc., New York, 1993.

[93] Z. Jinchuang, F. Wenli, L. Taoshen and W. Shi, *"An image reconstruction algorithm based on a revised regularization method for electrical capacitance tomography*," Meas. Sci. Technol., 13, 638-640, 2002.

[94] X. Ma, A. J. Peyton, R. Binns and S.R. Higson, *"Imaging the flow of molten steel through the submerged pouring nozzel*," In Proc. 3rd World Congress on Industrial Process Tomography, Banff Canada, pp. 472-478, 2003.

[95] X. Ma, S.R. Higson, A. Lyons and A.J. Peyton, *"Development of a fast electromagnetic induction tomography system for metal process applications,"* In Proc. 4rd World Congress on Industrial Process Tomography, 2005.

[96] C. Maxwell, *"A Treatise on Electricity and Magnetism,"* Vols. I and II, Clarendon Press, England, 1904.

[97] J. A. Meijerink and H. A. Van Der Vorst," An iterative solution method for linear systems of which the coefficient matrix is a symmetric M-matrix," Math. Comp., vol. 31, no. 137, pp. 148-162, 1977.

[98] D. Menzel (Ed.). *"Fundamental Formulas of Physics,"* Vol. 2, 2nd ed. New York: Dover, p. 80, 1960.

[99] R. Merwa, K. Hollauhs, B. Brandstatter and H. Scharfetter, *"Numerical solution of the general 3D eddy current problem for magnetic induction tomography (spectroscopy),"* Physiol. Meas., Vo. 24, No. 2, pp. 545-554, 2003.

[100] R. Merwa, K. Hollaus, O. Bir and H. Scharfetter, *"Detection of brain oedema using magnetic induction tomography: A feasibility study of the likely sensitivity and detectability.,"* Physiol. Meas., 25, no 1, pp. 347-354, February 2004.

[101] P. Metherall, *"Three Dimensional Electrical Impedance Tomography of the Human Thorax,"* University of Sheffield, PhD thesis 1998.

[102] S. Mitchell, and S. Vavasis, *"Quality Mesh Generation in Higher Dimensions,"* SIAM J. Comput., 29, pp. 1334-1370, 2000.

[103] J. Mohamad-Saleh and B. S. Hoyle, *"Determination of multi-component flow process parameters based on electrical capacitance tomography data using artificial neural networks,"* Meas. Sci. Technol., 13, pp. 1815-1821, 2002.

[104] M. Mohr, B. Vanrumste, *"Comparing iterative solvers for linear systems associated with the finite difference discretisation of the forward problem in electroencephalographic source analysis,"* Medical and Biological Engineering and Computing, vol. 41, no. 1, pp. 75-84, 2003.

[105] V. A. Morozov, *"Methods for solving incorrectly posed problems,"* Springer-Verlag, New York, 1984.

[106] T. Murai and Y. Kagawa, *"Electrical impedance tomography bases on a finite element method,"* IEEE Trans. on Biomedical Engineering, vol. 32, pp.177-184, 1985.

[107] J. C. Nedelec, *"Mixed finite elements in R*3*,"* Numer. Math., Vol. 35, pp. 315-341, 1980.

[108] J. C. Nedelec,*" A new family of mixed finite elements in R*3*,"* Numer. Math., Vol. 50, pp. 57-81, 1986.

[109] J. Nocedal and S.J. Wright, *"Numerical Optimisation,"* Springer Series in Operational Research, Springer, Berlin, 1999.

[110] S. J. Norton and J. R. Bowler *"Theory of eddy current inversion,"* Journal of Applied Physics, Vol 73(2) pp. 501-512, January 15, 1993.

[111] P. Ola, E. Päivärinta, E. Somersalo, *"An inverse boundary value problem in electrodynamics,"* Duke Math. J. 70 pp. 617-653., 1993.

[112] S. Osher and J. Sethian, *"Fronts propagation with curvature dependent speed: Algorithms based on Hamilton-Jacobi formulations,"* Journal of Computational Physics, 56, pp. 12-49, 1988.

[113] S. Osher and R. Fedkiw, *"Level set methods and dynamic implicit surfaces"*, Springer, New York, 2003.

[114] D.M. Otten and B. Rubinsky, *"Cryosurgical monitoring using bioimpedance measurements- A feasibility study for electrical impedance tomography,"* IEEE Transactions on Biomedical Engineering, vol. 47, no. 10, pp.1376-1381, 2000.

[115] A. J. Peyton, S. D. Dickinson, W. R. B. Lionheart, M. soleimani, and W.D.N. Pritchard, *"Electromagnetic imaging and tomography - a review of recent advances,"* ON-LINE MEASUREMENTS FOR QUALITY IN THE METALS INDUSTRIES, 7-8, London, October 2003.

[116] A.J. Peyton, Z. Z. Yu, S. Al-Zeibak, N. H. Saunders and A.R. Borges, *"Electromagnetic imaging using mutual inductance tomography: Potential for process applications,"* Part. Syst. Charact., vol.12, pp. 68-74, 1995.

[117] M. Pham, Y. Hua and N. Gray, *"Imaging the solidification of molten metal by eddy currents - Part I,"* Inverse Problems, Vol 16, pp. 483-494, Apr 2000.

[118] M. Pham, Y. Hua and N. Gray *"Imaging the solidification of molten metal by eddy currents - Part II,"* Inverse Problems, Vol 16, pp. 469-482, Apr 2000.

[119] N. Polydorides and H. McCann, *"Electrode configurations for improved sensitivity i Electrical Impedance Tomography,"* Meas. Sci. and Tech., IoP Publishing, vol. 13, no. 12, pp. 1862-1870, December 2002.

[120] N. Polydorides and W. R. B. Lionheart, *" A Matlab toolkit for three-dimensional electrical impedance tomography: a contribution to the Electrical Impedance and Diffuse Optical Reconstruction Software project,"* Meas. Sci. Technol., 13, pp. 1871-1883, 2002.

[121] N. Polydorides, *"Image Reconstruction Algorithms for Soft-Field Tomography,"* PhD Thesis, UMIST, 2002.

[122] N. Polydorides, W.R.B. Lionheart and H. McCann, *"Krylov subspace iterative techniques: On the detection of brain activity with EIT,"* IEEE Trans. of Medical Imaging, vol. 21, no. 6, pp. 596-603, 2002.

[123] K. S. Paulson, W. R. Breckon and M. K. Pidcock*"Electrode modelling in Electrical Impedance Tomography,"* SIAM Journal of Applied Mathematics, Vol 52, pp. 1012-1022, 1992.

[124] PTL, *http://www.tomography.com*

[125] J. Qi-Nian, *" On the iteratively regularised Gauss-Newton method for solving nonlinear ill-posed problems,"* Mathematics of Computation, 69, 232, pp. 1603-1623, 2000.

[126] S. Quek, P. Gaydecki, B. Fernandes and G. Miller, *"Multiple layer separation and visualisation of inductively scanned images of reinforcing bars in concrete using a polynomial-based separation algorithm,"* NDT & E International, 35, pp. 233-240, 2002.

[127] M.M. Radai, S. Abboud and B. Rubinsky, *"Evaluation of the impedance technique for cryosurgery in a theoretical model of the head,"* Cryobiology, vol. 38, no. 1, pp. 51-59, 1999.

[128] P. Ramachandran. MayaVi: *"A free tool for CFD data visualization,"* 4th Annual CFD Symposium, Aeronautical Society of India, August, 2001

[129] Z. Ren, *"Influence of the R.H.S on the convergence Behaviour of the Curl-Curl Equation,"* IEEE Trans. MAG , vol. 32 , no. 3, pp. 655-658, May 1996.

[130] Z. Ren , A. Razek , *" Comparison of some 3D Eddy Current Formulation in Dual Systems, "* IEEE Trans. MAG., Vol. 36, N0. 4, pp.751-755, 2000.

[131] C. H. Riedel, M. Keppelen, S. Nani, R. D. Merges, and O. Dssel, *"Planar system for magnetic induction conductivity measurement using a sensor matrix,"* Physiol. Meas., 25(1): pp. 403-411, Feb. 2004.

[132] C. H. Riedel, *"Planare induktive Impedanzmessverfahren in der Medizintechnik,"* PhD thesis, Universitt Karlsruhe (TH), Institut fr Biomedizinische Technik, 2004.

[133] J. Rosell, R. Casañas and H. Scharfetter, *"Sensitivity maps and system requirements for Magnetic Induction Tomography using a planar gradiometer,"* Physiol. Meas. 22: pp. 121-130, 2001.

[134] G. Rubinacci, A. Tamburrino, S. Ventre and F. Villone, *"Shape identification in conductive materials by electrical resistance tomography,"* in E'NDE, Electromagnetic Non-destructive Evaluation (VI), F. Kojima et al. (Eds.), pp. 13-20, IOS Press, 2002.

[135] G. Rubinacci, A. Tamburrino and F. Villone, *"Shape identification of conductive anomalies by a new ECT data inversion algorithm,"* Proc. of the 4^{th} International Conference Computation in Electromagnetics (CEM 2002), Bournemouth (UK), 2002.

[136] G. Rubinacci and A. Tamburrino *" A non-iterative ECT data inversion algorithm,"* Proc. of the 8^{th} International Workshop on Electromagnetic Nondestructive Evaluation (ENDE 2002), Saarbruecken, Germany, 2002.

[137] J.W. Ruge and K. Stüben, "*Efficient solution of finite difference and finite element equations by algebraic multigrid (AMG),*" In: Multigrid Methods for Integral and Differential Equations, The Institute of Mathematics and its Applications Conference Series, D.J. Paddon, H. Holstein (Eds.), New Series 3, Clarendon Press, Oxford, pp.169–212, 1985.

[138] J.W. Ruge and K. Stüben, "*Algebraic Multigrid,*" In: Multigrid Methods, S.F. McCormick (Ed.), SIAM, Philidelphia, pp. 73–130, 1987.

[139] F. Santosa, "*A Level-Set Approach for Inverse Problems Involving Obstacles,*" ESAIM: Control, Optimization and Calculus of Variations 1, pp. 17-33, 1996.

[140] J. A. Sethian, "*Level Set Methods and Fast Marching Methods,*" (2nd ed) Cambridge University Press, 1999.

[141] H. Scharfetter, H. K. Lackner and J. Rosell, "*High resolution hardware for magnetic induction tomography (MIT) at low frequencies,*" in Proc. of the EIT Conference in London, 2000.

[142] H. Scharfetter, H. K. Lackner and J. Rosell, "*Magnetic induction tomography: hardware for multi-frequency measurements in biological tissues,*" Physiol. Meas., Vol. 22, no. 1, pp. 131–146, 2001.

[143] H. Scharfetter, P. Riu, M. Populo and J. Rosell, "*Sensitivity maps for low-contrast-perturbations within conducting background in magnetic induction tomography (MIT),*" Physiol. Meas., 23: pp. 195-202, 2002.

[144] H. Scharfetter, T. Schlager, R. Stollberger, R. Felsberger, H Hutten and H Hinghofer-Szalkay, "*Assessing abdominal fatness with local bioimpedance*

analysis: Basics and experimental findings," Int J Obes Relat Metab Disord. 25: pp. 502-511, 2001.

[145] H. Scharfetter, R. Casañas and J. Rosell, "*Biological Tissue Characterization by Magnetic Induction Spectroscopy (MIS): Requirements and Limitations*," IEEE Trans. on Biomedical Engineering, Vol. 50, No. 7, 2003.

[146] M. Soleimani, W. R. B. Lionheart, Claudia H. Riedel and Olaf Dossel, "*Forward Problem in 3D Magnetic Induction Tomography (MIT),*" In Proc. 3rd World Congress on Industrial Process Tomography, Banff Canada, pp. 275-280, 2003.

[147] M. Soleimani, W. R. B. Lionheart, A. J. Peyton and X. Ma, "*Image Reconstruction in 3D Magnetic Induction Tomography Using a FEM Forward Model*," In Proc. 3rd World Congress on Industrial Process Tomography, Banff Canada, pp. 252-255, 2003 (ISBN: 08531 62409).

[148] M. Soleimani and C. E. Powell, "*Black-box Algebraic Multigrid for the 3D Forward Problem Arising in Electrical Impedance Tomography,*" Presented and abstract published in Proc. 4th Conference on Biomedical Applications of Electrical Impedance Tomography, Apr. 2003.

[149] M. Soleimani and W.R.B. Lionheart, "*A nonlinear image reconstruction for electrical capacitance tomography using experimental data*," Submitted for Meas. Sci. Technol. 2005.

[150] E. Somersalo, D. Isaacson and M. Cheney, "*A linearized inverse boundary-value problem for Maxwell equation*," J comp appl math. 42, pp. 123-136, 1992.

[151] E. Somersalo, D. Isaacson and M. Cheney, "*Existence and uniqueness for a electrode models for electric current computed tomography*," SIAM Journal of Applied Mathematics, vol. 52, pp.1023–1040, 1992.

[152] P. P. Silvester and R. L. Ferrari, "*Finite Elements for Electrical Engineers*," Cambridge University Press, Cambridge, 1990.

[153] T. Takagi, H. Huang, H. Fukutomi and J. Tani , "*Numerical Evaluation of Correlation between Crack Size and Eddy Current Testing Signals by a Very Fast Simulator*," IEEE Trans. MAG., vol. 34, no. 5, pp. 2581-2584, 1998.

[154] K. Stüben, *Algebraic multigrid (AMG): An introduction with applications.* In: Multigrid, U. Trotenberg, C.W. Oosterlee, A. Schüller (Eds.), Academic Press, New York, 2000.

[155] A. Tamburrino and G. Rubinacci "*A new non-iterative inversion method in electrical resistance tomography*," Inverse Problems, vol. 18, pp.1809-1829 2002.

[156] A. Tamburrino, G. Rubinacci, M. Soleimani and W.R.B. Lionheart, *A Noniterative Inversion Method for Electrical Resistance, Capacitance and Inductance Tomography for Two Phase Materials*, In Proc. 3rd World Congress on Industrial Process Tomography, Banff, Canada, pp. 233-238, 2003.

[157] A.T. Tidswell, A. Gibson and R.H. Bayford, *Validation of a 3D reconstruction algorithm for EIT of human brain function in a realistic head-shaped tank*, Physiol. Meas., 22, pp. 177-185. 2001

[158] M. Vauhkonen, W.R.B. Lionheart, L.M. Heikkinen, P.J. Vauhkonen and J.P. Kaipio, "*A MATLAB package for the EIDORS project to reconstruct two-dimensional EIT images*," Physiol. Meas., 22, no. 1, pp. 107-111, 2001.

[159] P.J. Vauhkonen, M. Vauhkonen, T. Savolainen and J.P. Kaipio, "*Three dimensional electrical impedance tomography based on the complete electrode model*," IEEE Trans. on Biomedical Engineering, vol. 46, pp.1150–1160, 1999.

[160] M. Vauhkonen,"*Electrical Impedance Tomography and piror information*," PhD Thesis, Koupio University, Finland, 1997.

[161] Curtis R. Vogel, "*Computational Methods for Inverse Problems*," SIAM, Frontiers in Applied Mathematics, 2002.

[162] S. Watson, R. J. Williams, H. Griffiths, W. Gough, and A. Morris, "*Frequency downconversion and phase noise in MIT*," Physiol. Meas., Vol. 23, pp. 189-194, Feb. 2002.

[163] S. Watson, R. J. Williams, H. Griffiths, W. Gough, and A. Morris, " *Magnetic induction tomography: phase versus vector-voltmeter measurement techniques*," Physiol. Meas., Vol. 24, pp. 555-564, 2003.

[164] W. Warsito and L.S. Fan, "*Neural network based multi-criterion optimization image reconstruction technique for imaging two- and three-phase flow systems using electrical capacitance tomography*," Meas. Sci. Technol. **12**, pp. 2198-2210, 2001.

[165] D. Watzenig, B. Brandsttter and G. Holler, "*Adaptive Regularization Parameter Adjustment for Reconstruction Problems*," IEEE Trans. on MAG, Vol. 40, Issue: 2, pp. 1116 - 1119, 2004.

[166] J.P. Webb and B. Forghani , "*A single scalar potential method for magnetostatics using edge elements*," IEEE Trans. On MAG, Vol.25, No.5, pp. 4126-4128, 1989.

[167] J. B. Webb, "*Edge elements and what they can do for you*," IEEE Trans. on MAG, Vol. 29, No. 2, pp. 1460-1465, 1993.

[168] J. G. Webster,"*Electrical Impedance Tomography* ," Adam Hilger Pub., 1990.

[169] P. Wesseling, "*An Introduction To Multigrid Methods*", John Wiley & Sons, 1992.

[170] R.M. West, R. G. Aykroyd, S. Meng and R.A. Williams, "*Markov chain Monte Carlo techniques and spatial-temporal modelling for medical EIT*," Physiol. Meas., Intstitute of Physics, vol. 25, pp.181-194, 2004.

[171] R.M. West, S. Meng, R.G. Aykroyd and R.A. Williams , "*Spatial-temporal Modelling for EIT of a Mixing Process.*" In Proceeding of the 3rd World Congress in Industrial Process Tomography, Banff, Canada, 2003.

[172] A. Wexler, B. Fery and R. Neuman, " *Impedance-computed tomography algorithm and system*," Applied Optics, 24, pp. 3985-3992, 1985.

[173] H. Whitney, "*Geometric Integration Theory*," Princeton University Press, 1957.

[174] W.Q. Yang , "*Calibration of capacitance tomography systems: a new method for setting system measurement range*," Meas. Sci. Technol., **7** , pp. L863-L867, 1996.

[175] W.Q. Yang and L.H. Peng, " *Image reconstruction algorithms for electrical capacitance tomography*," Meas. Sci. Technol. (Review Article), 14, pp. R1-R13, 2003.

[176] W. Q. Yang, D. M. Spink, T. A. York and H. McCann, "*An image-reconstruction algorithm based on Landweber's iteration method for electrical-capacitance tomography*," Meas. Sci. Technol., 10, pp. 1065-1069, 1999.

[177] W. Q. Yang and T.A. York, "*A New AC-based Capacitance Tomography System*," IEE Proc. Sci., Meas. and Technology : 146, 1, 1999.

[178] T. J. Yorky, "*Comparing reconstruction methods for electrical impedance tomography*," PhD thesis, University of Wisconsin, Madison, 1986.

[179] O.C. Zienkiewicz, "*The finite element method*," McGraw-Hill, London, 1997.